High Quality Graphene Membranes as a Coating for Plasma Facing Components in a Nuclear Fusion Environment

By

Marcos X. Navarro González

A dissertation submitted in partial fulfillment of

the requirements for the degree of

Doctor of Philosophy

(Nuclear Engineering and Engineering Physics)

at the

UNIVERSITY OF WISCONSIN – MADISON

2018

Date of oral examination: 9/20/18

This dissertation was approved by the following members of the Final Oral Committee:

Gerald L. Kulcinski, Professor Emeritus, Engineering Physics
Douglass L. Henderson, Professor, Engineering Physics
Max G. Lagally, Professor, Materials Science and Engineering
Oliver Schmitz, Associate Professor, Engineering Physics
Adrien Couet, Assistant Professor, Engineering Physics
John F. Santarius, Research Professor Emeritus, Engineering Physics

This page is intentionally left blank.

Abstract

This research explores the performance of graphene as a coating for plasma facing components (PFC's) irradiated by energetic ions leaving the plasma and the construction of a new linear Inertial Electrostatic Confinement (IEC) fusion device at the University of Wisconsin-Madison. A few studies have shown that graphene can act as a protective layer against sputtering due to energetic ions leaving from a plasma. In the presence of such irradiation, PFC's tend to develop surface morphologies that lead to mass loss of the wall material, potentially diminishing their lifetime, plasma performance and safety of a fusion reactor.

It has been shown that graphene can reduce and slow down changes of surface morphology due to energetic helium bombardment over a wide range of energies, as tested in the MITE-E facility at UW-Madison, PISCES at UC-San Diego, and the C-2W device at TAE Technologies. Insight has been gained about the interaction of graphene with high and low energy ions using Raman Spectroscopy as a diagnostic for determining the damage and lifetime of the membrane. Graphene was also shown to reduce secondary electron emission from tungsten, decreasing the yield by as much as 50%. In addition, heating tests were performed on tungsten in a variable pressure neutral deuterium environment to determine the survivability and chemical stability of graphene coatings. Although, the deuterium appears to etch some of the carbon atoms, the increase in vacancies is minor enough that the graphene still retains its structure, and at pressures expected in the plasma edge, the deuterium seems to have little effect on damage in W.

Graphene half-coated tungsten samples were exposed in the PISCES facility, and through surface analysis techniques it was found that the tungsten fuzz growth can be reduced by about

30% for high fluences (10^{20}-10^{21} He-D/cm^2). In these high fluence cases, embrittlement of materials can be an issue and a residual stress analysis found that the membrane does not have much of an effect on the internal stresses in W for the helium irradiation, but it reduces these stresses by deuterium in the tungsten substrate. Additionally, it appears that graphene does not perform as well at bombarding ion energies close to sp^2 carbon binding energy of 20 eV, as seen across the different exposures.

Lastly, two samples were exposed in the C-2W device at TAE and it was shown that the slower ions ($E<200$ eV) interact more strongly with the graphene, introducing vacancies into the membrane. It also found that graphene reduces the collection of impurities on the material surfaces.

A linear IEC device was also built in order to find optimal regimes for neutron generation. The ease in making geometric changes to the chamber configuration makes these systems more desirable over conventional IEC devices. This study showed that the optimal pressure of operation occurs at 2.25 mTorr, for a wide range of cathode high voltage and ion currents in a DD plasma environment.

Acknowledgements

I would like to thank Professor Gerald Kulcinski for allowing me to pursue my PhD with the IEC group at UW-Madison, but also, for believing in my ideas and allowing me the flexibility to perform my own experiments and collaborations with different research groups across the United States. I would also like to thank Professor John Santarius for his extremely helpful conversations regarding all my research topics, his advice on how to proceed with experiments, as well as his encouragement of me keeping an active life outside the office.

I would like to thank my entire IEC group for assisting me during my stay here; Karla Hall for helping me start this graphene revolution in the MITE-E experiment and all the long hours staying in the laboratory irradiating samples, Aaron Fancher for helping me put together the LUNA experiment, both vacuum and electronics equipment, Matthew Jasica for his input in material damage interpretation and for having me collaborate in his materials analysis as well, Nolan van Rossum for his assistance in constructing some of LUNA's crucial components and improving the experiment's performance, Kevin Johnson for assisting in any machining I needed done, Aaron Olson for his helpful advice for experimental design, and Matt Michalak, Aaron McEvoy, Gabriel Becerra, and Lauren Garrison for their senior advice and helping me get started in graduate school.

I am extremely proud to have been able to work with Professor Max Lagally, our surface science and thin film expert, without whom, I never would have been able to get started in this graphene research, learned as much as I have, or finished this project. The conversations with his research group and their assistance have been crucial to this research. I'd like to thank Richard Rojas for jumping into my crazy ideas and helping me start this graphene coating program,

Marziyeh Zamiri for all the hours we put into growing graphene and all her effort in helping me achieve this work, Don Savage for training me on XRD techniques that have made this work possible, RB Jacobson for helping me scavenge for vacuum equipment for my experiments, and Frank Flack, Shelley Scott, Abhishek Bhat, Xiaorui Cui, and Gabriel Jaffe for their input in their interpretation of data.

Much of this research could not have been done without Professor Oliver Schmitz's support. I am extremely grateful he put me in contact with Professor Russ Doerner and allowing me to test my experiments in the PISCES facility in UCSD. Thank you to both for using your own resources and time to make this work possible, and for the discussions which helped my interpretation of these results.

Thank you to Professor Adrien Couet for his insight into data analysis for some of this work and in giving direction on how to proceed forward, as well as having me as his teaching assistant for both Radiation Damage in Metals and Nuclear Engineering Materials courses. I learned a lot from him about being a good educator, and the lessons I taught during these courses helped me in becoming a better presenter.

I would like to thank Professor Douglass Henderson for having me here at the UW and helping me join the Graduate Engineering Research Scholars, as well as Kelly Burton for all her support throughout the years and having me lead the recruitment committee for the group for so long. I've built many long-lasting friendships in this group, and my experience at UW-Madison has been all the better for it; I sincerely hope the group continues to grow over the years and minority presence at UW-Madison increases and we all eventually become equal parts of a whole.

I am very thankful to the TEAM-Science program here at UW-Madison for assisting me in funding some of my research, but I'm especially grateful for having met Dr. Angela Byars-Winston. Angela has taught me about time management, research management, improving my confidence, and stop thinking of myself as just a grad student. She has also taught me how to manage difficult conversations in the office setting and how to negotiate with collaborators. Her advice has been invaluable to me since I met her, and I thank her for that.

I first met Dr. Ales Necas of Tri Alpha Engineering when he came to UW-Madison to give a talk about their company experiments. It was here that we talked about my graphene experiments and his interest led to meeting Professor Toshiki Tajima over in California. Thank you to both for your support and collaboration in some of the experiments that made this thesis possible, as well as the assistance of the TAE team. Thank you to Martin Griswold for installing and monitoring and handling the samples, as well as the rest of the team for assisting in the discussions and interpretation of the resulting data.

I would like to thank my family for providing me with the emotional support I needed throughout my years here. To my mom, my dad, and my sister, thank you for all your messages of encouragement; I love you all very much. Thanks to my grandparents, aunts, and cousins for always believing in me and listening when I needed to vent, I hope I've made you all very proud. I would like to thank my friends that I've made here at UW-Madison. You've made such an impact in my life, and made this experience so much better, I don't think words could ever describe how much I've grown and love you for it. Thanks to Nayomi, Suehelay, John, Florian, Ryan, Kyle, Tyler, Jeff, Nestor, all the Carlos', Matt, Victoria and everyone else who've improved my life here.

Lastly, I'd like to thank the best person I've ever known in my life, my best friend, Torrin Bechtel, without whom, I would not have had the strength to keep going. Thank you for always being like family to me, for always having time to hang out together, for your advice, and for always being there for me. I would not be where I am today without you.

To everyone else, thank you, and as F. D. Roosevelt said: "courage is not the absence of fear, but rather the assessment that something else is more important than fear". To better humanity, we need to be bold, resolute, and challenge the norm.

Table of Contents

Table of Figures

List of Tables

Chapter 1 – Introduction

Ever since its discovery in 2004, graphene has been a source of interest due to its unique thermal, electronic, and structural properties. Up to that point, it was believed that there were no thermodynamically stable 2-D materials at any finite temperature as the theory by Landau and Peierls, and extended by Mermin stated [1–3]. The thermal fluctuations in a low dimensional crystal lattice would lead to atomic displacements comparable to the interatomic distance between them. This is still true for many materials since it has been observed that the thickness of a material and its melting temperature are directly proportional to each other. Graphene was found not only to exhibit extraordinary stability and properties, it was also found to have a high crystalline defect-free quality [4,5]. It is believed that due to its strong interatomic bonds (with a lattice parameter α=1.43 Å), even at elevated temperatures, these can prevent thermal fluctuations from leading to defects in the crystal structure [3]. This stability achieved by graphene, or 2D crystals in general, is due to a gain in elastic energy due to 3D warping of the film. In turn, this elastic energy suppresses thermal vibrations which are large in 2D planes and above certain temperatures can minimize the total free energy of the system [6]. Geim and Novoselov, stated that we are in a graphene "gold rush" [7], and although there is a vast amount of studies being performed in the area, this thesis will only include the properties most relevant to ion irradiation and plasma exposure.

For over 50 years, researchers have been attempting to find the optimal material for fusion applications due to the extreme conditions they experience [8–12]. None of the proposed materials function perfectly under this environment, as each is plagued with their own problems. Graphite absorbs hydrogen isotopes to form hydrocarbons, as well as retaining large quantities of these isotopes in its bulk [13–16]. Tungsten, while it has a high melting temperature and low sputter yield, erodes under helium exposure and, since the bremsstrahlung radiation scales as Z^4, it cools down the plasma quite quickly, making it more difficult to sustain a high temperature plasma [17–19]. Beryllium is extremely toxic, has a high sputter yield, and handling of any components that include it needs to be closely regulated [20–23]. Lithium is not very well understood and is difficult to control due to it being a liquid state. It forms hydrides which can solidify the flow and prevent cool down. It is also is reactive with air [24–29]. Because none of these components have shown the capability to survive over a long time, replacing these components would require significant shutdown times for commercial reactors.

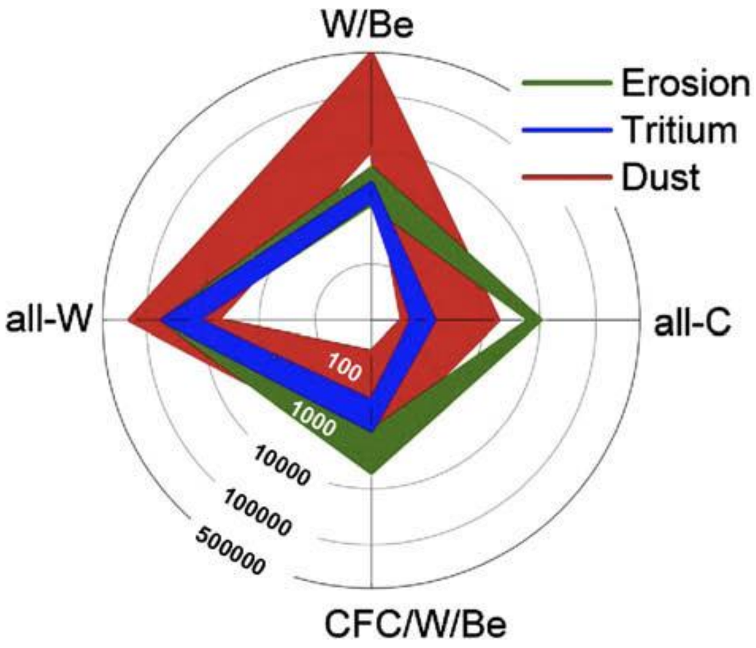

Figure 1-1. Number of discharges required for reaching the safety limits due to erosion, dust generation and tritium inventory for the four material options for ITER [12].

Tungsten and graphite are the most popular choices for these fusion reactors. As the mother of all graphitic materials, graphene has been shown to have even better properties than bulk graphite overall, and even better thermal and physical properties than tungsten [30,31]. The question then arises, is graphene a suitable candidate as a plasma facing component? Extensive work has gone into modeling ion and electron bombardment of graphene and shown it to be quite robust to such an interaction [32,33]. This has been confirmed as well in some experimental work, showing that the interaction between graphene and incoming charged particles becomes stronger the lower the particle energy, causing defects in the carbon membrane [34–36]. Future fusion reactors are expected to operate at higher edge temperatures which would allow graphene to perform better. This thesis research encompasses several uses of graphene for applications which are relevant not only to the devices under study but to other fusion/plasma experiments.

The LUNA inertial-electrostatic confinement (IEC) experiment is versatile in that it is able to produce DD fusion neutrons (2.45 MeV) in a linear configuration which can be used for neutron activation to detect radioactive materials; it can also be used to create high energy (14.7 MeV) DT protons which could be used to make radioisotopes when implanted into a gas such as nitrogen or oxygen. The chamber configuration is such that it is possible to use a graphene layer on a meshed surface to take advantage of graphene's ability to sustain a pressure difference between two different surrounding conditions [37–39]. In order to first characterize and optimize the experiment, D-D fusion was used to study ion and neutron physics in LUNA.

The main aspect of this research involves the use of graphene as a coating for plasma facing components (PFC's). Graphene coated tungsten samples have been tested under intense ion irradiation in the MITE-E [40,41], PISCES [42,43] and C2-W [44] facilities and characterized via several surface and bulk diagnostics. The idea behind this is that the graphene will act as a barrier against sputtering of the metal and, in the case of helium irradiation on tungsten in a fusion reactor, prevent "fuzz" or "grass" structures [40,43,45–47] from forming on the surface, which is indicative of very high erosion yields into the core plasma. This would lead to large radiative losses due to bremsstrahlung and, potentially, termination of the plasma discharge. On larger plasma physics experiments such as DIII-D [48,49], ASDEX [50,51], ITER [12,48,52] and W7-X [53], this materials concern is of high importance due to the relatively short lifetimes that the plasma facing components have at their operating conditions.

There are three main goals addressed in this thesis: 1) implementation of a graphene membrane for the reduction of plasma induced damage in tungsten (W) in a DT fusion reactor, 2) exploring the effect of energetic helium and deuterium particles passing through graphene membranes and its durability, and 3) optimize the neutron rates in the first UW-Madison linear inertial electrostatic confinement fusion device. The structure of this thesis document contains a section of previous work detailed in Chapter 2. It will include background information on graphene as well as studies performed by other groups on the different aspects (neutronics, membrane and tungsten studies) that encompass the scope of the thesis work. Chapter 3 will focus on the experimental procedures and experiments (i.e. Graphene growth and ion bombardment facilities). Chapter 4 will include the methods and diagnostics used to characterize the samples that were exposed to ion bombardment. Because the drive for testing graphene as a PFC originated from its use as a membrane, chapter 5 will detail IEC theory, the construction of the LUNA experiment and initial results, while Chapter 6 will go through the results for the use of graphene as a coating for tungsten. The results will be discussed in chapter 7 and conclusions from this work in chapter 8. Lastly, chapter 9 discusses some suggestions for potential future work that appears worthwhile for extending the results of the present thesis research.

This page is intentionally left blank.

Chapter 2 – Previous Work by Others

2.1 – Graphene Properties

It is of no surprise that the discovery of a 2D stable material has led to scientific breakthroughs in many areas; in graphene's case, it has proven to be particularly effective in the semiconductor industry. Graphene is a 2-dimensional carbon allotrope that has a very tightly packed sp^2 honeycombed structure which leads to the smallest bond distance between carbon atoms of 1.42 Å [7]. These atoms are bonded together by three single σ bonds (strong along axis) and one π bond (weak parallel axes) [54]. This structure has demonstrated extraordinary properties which have led to a "golden age" for graphene [55], having generated a significant amount of studies, both theoretical and experimental in many areas of science and engineering. Figure 2-1 demonstrates how graphene can be used to generate other carbon dimensionalities. There are many excellent properties inherent to graphene, but this document will only go over the ones most relevant to the thesis studies.

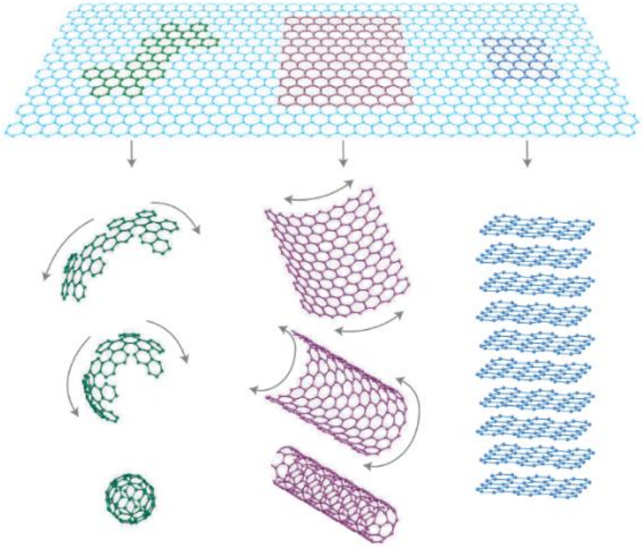

Figure 2-1. The mother of all graphitic forms, graphene is a 2D building material for carbon materials of all other dimensionalities. It can be wrapped into 0D buckyballs, rolled into 1D nanotubes or stacked into 3D graphite [7].

2.1.1– Thermal and Chemical Stability

A free-standing sheet of graphene has an extremely high thermal conductivity of ~5000 W/(m-K) at room temperature [30,31,56], larger than copper by over a factor of 10. Graphene's "fingerprints" are measured via Raman spectroscopy [57,58] (Figure 2-2) with the main phonon mode's intensity I_G found at ~1550 cm^{-1} and I_D found at ~1350 cm^{-1}. These correspond to the sp^2 vibrational mode of the carbon membrane, and the defect breathing mode, respectively. Defect free graphene is considered that which has I_D/I_G~0. The 2D peak can be used to determine a number of electronic and thermal properties of the material.

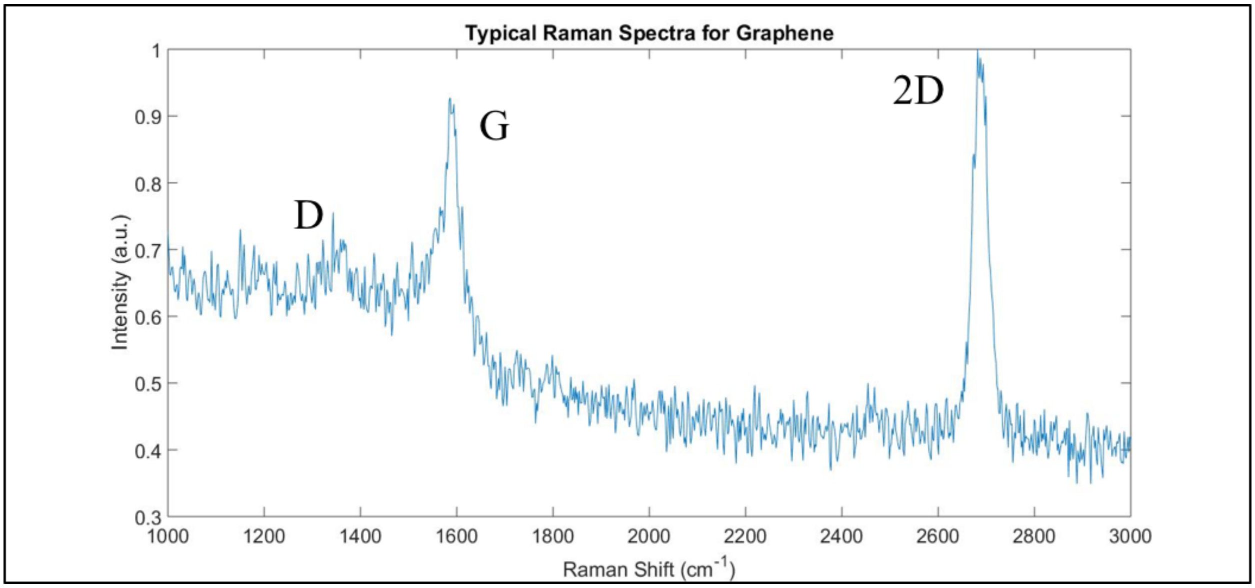

Figure 2-2. Typical low defect graphene Raman spectrum.

Graphene has been shown to have superb chemical and thermal stability, which in an inert and ultra-high vacuum environment, is stable up to 2600 K [59]. Due its chemical stability, it can be removed from a growth substrate after being grown via chemical vapor deposition and transferred onto other substrates without chemically damaging it during these processes [60–63]. One well studied property is graphene's resistance to corrosive environments [64–70]. These properties make it an ideal candidate for use in environments with harsh conditions, such as damage preventive coatings and high temperature applications.

2.1.2– Mechanical Properties

So far, graphene is the strongest material to be tested, with an intrinsic tensile strength of 130 GPa and a Young's Modulus of 1 TPa, which leads to an extremely high fracture strength of 120 GPa [71]. The closely packed hexagonal structures formed by the tightly bound sp^2 orbitals that make up the graphene lattice have been shown to give it these exceptional mechanical properties [72–76] as well as make it impenetrable to atomic and molecular neutral species as small as helium [77]. Figure 2-3 shows experimental tests of graphene as a membrane for sustaining a pressure differential. Experimentally, its success as a pressure barrier is limited by scaling pristine graphene for larger applications and reproducing positive results from these proof of concept studies [78–81]. This property along with its chemical stability can be advantageous for manufacturing size selective transport membranes. Due to selective etching processes, it is possible to introduce nanopores into the graphene sheet, which allows it implementation for gas separation [37,77], water desalination [82–84] or drug delivery [85–87]

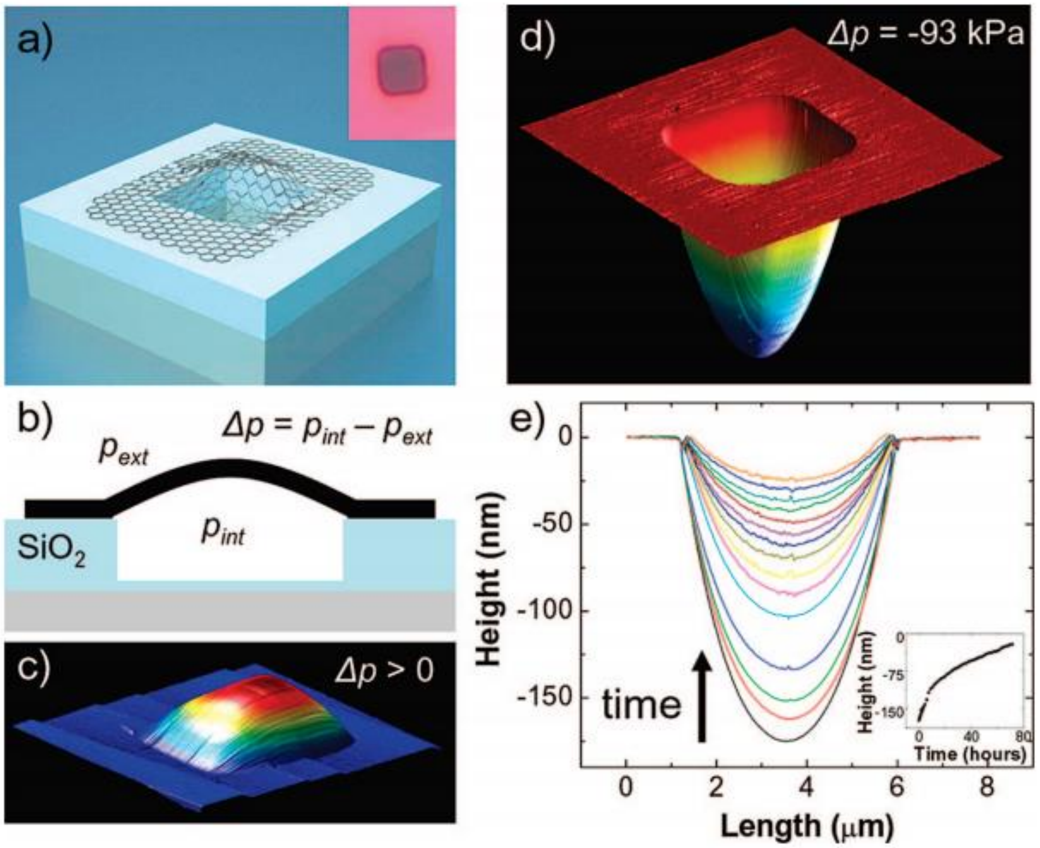

Figure 2-3. Schematic of a graphene sealed microchamber. a) Optical image of a single atomic layer graphene drumhead on 440 nm of SiO2. The dimensions of the microchamber are 4.75 μm × 4.75 μm × 380 nm. (b) Side view schematic of the graphene sealed microchamber. (c) Tapping mode atomic force microscope (AFM) image of a ~9 nm thick many layer graphene drumhead with $\Delta p>0$. The dimensions of the square microchamber are 4.75 μm × 4.75 μm. The upward deflection at the center of the membrane is 90 nm. (d) AFM image of the graphene sealed microchamber of Figure 1a with $\Delta p = -93$ kPa across it. The minimum dip in the z direction is 175 nm. (e) AFM line traces taken through the center of the graphene membrane of (a). The images were taken continuously over a span of 71.3 h and in ambient conditions. Deflection is measured at the center of the graphene membrane vs time. The first deflection measurement (z=175 nm) is taken 40 min after removing the microchamber from vacuum [77].

2.1.3 – Optical Transparency

The electronic band-structure of single layer graphene makes it extremely transparent (~97.7%), which is uniform over the visible range to the IR range of the electromagnetic spectrum [54,79-80]. It also has a greater transmittance of light over a wider wavelength range compared to single walled nanotubes or thin metal films due to its extremely high conductance [88] for visibility. While this has a huge potential for the construction of semiconducting devices, it allows one to easily characterize surface damage of materials used in nuclear environments.

2.1.4 – Ultra-Low Secondary Electron Emission

Secondary electrons (SE) cause problems for many devices ranging from small gauges, detectors and Langmuir probes to charged particle accelerators and any device that relies on usage of positive ions but is limited by electron buildup [90,91]. These SE's can cause pressure buildup and electron beam instabilities and it can limit performance of vacuum electronic devices [90]. A model of the effective surface barrier is used to explain the effect of graphene on secondary electron yield (SEY) [92]. The energetic primary electrons penetrate through the graphene, but the secondary inner electrons have difficulty passing through the compact graphene atomic layer due to its local electron space charge. Those that have lower energies (few eV) cannot enter the material, leading to less internal electrons that can be excited. This suppressant effect of graphene has been proven on various materials, including stainless steel [91], copper [92], SiC [93], and nickel [94], allowing for use of this technology for various applications.

2.1.5 – Low Hydrogen Reaction Rate

One particular concern for fusion plasma devices is the hydrogen bonding between the fuel (deuterium and tritium) and the carbon atoms. Density functional theory and molecular dynamics have been used to determine transmission, absorption and reflection of hydrogen on a graphene layer as a function of temperature and energy [86-87]. Figure 2-4 shows this dependence, with reflection dominating at very low (eV) energies due to the existence of a sticking resistant barrier from an electronic sheet. As the hydrogen energy increases, adsorption is a concern since chemisorption can occur. At low energies, the hydrogen atoms experience a repulsive force due to the π electrons, which prevent absorption on graphene; this is then overcome as hydrogen increases in energy. Penetration becomes dominant for high energies (>20 eV).

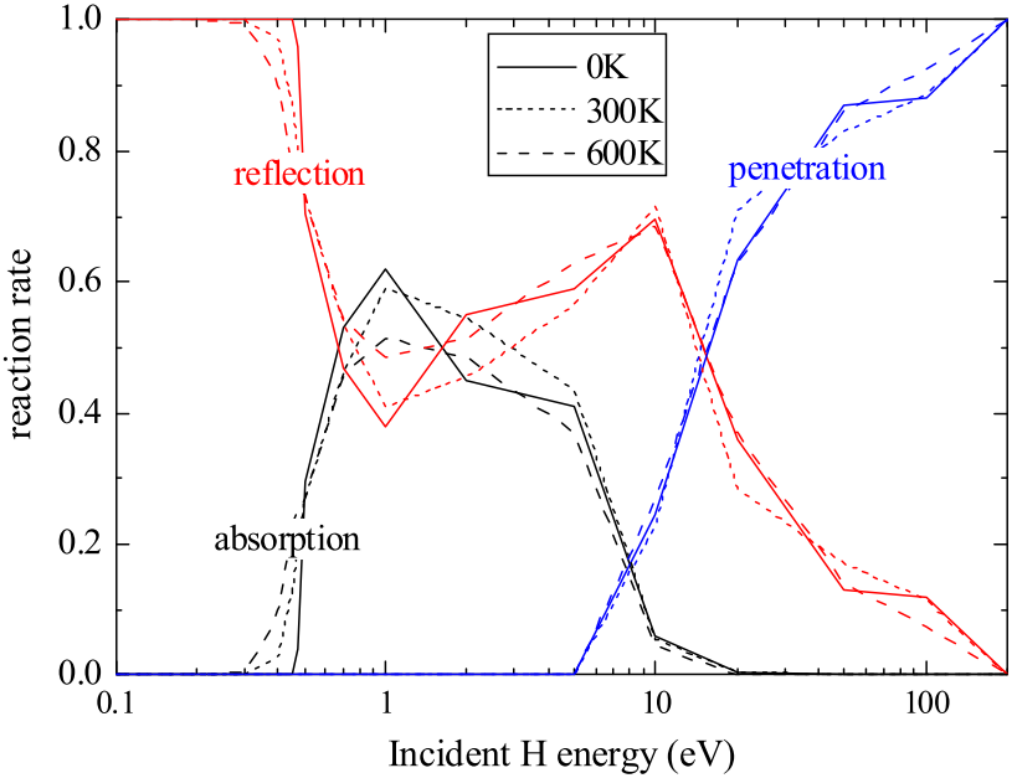

Figure 2-4. Influence of H incident energy and graphene surface temperature on adsorption (black), reflection (red), and penetration (blue) probabilities from computational molecular dynamics statistical calculations of atomic H impinging normally to the surface at random locations [95].

Another thing to note is that the reaction rates for absorption decrease as a function of temperature, which is also supported by other experimental studies [88-89]. Figure 2-5 shows that etching of graphene at its edges and defect sites peaks at relatively low plasma temperatures (between 300-500 °C), with etching entirely suppressed at temperatures above 700 °C. These etch rates are also suppressed by multi-layer graphene, and only depend on lattice defects. Since the temperatures under study will be much greater than the peak reaction rate temperatures, graphene is an appropriate candidate for coating the plasma facing components laid out in the future work section.

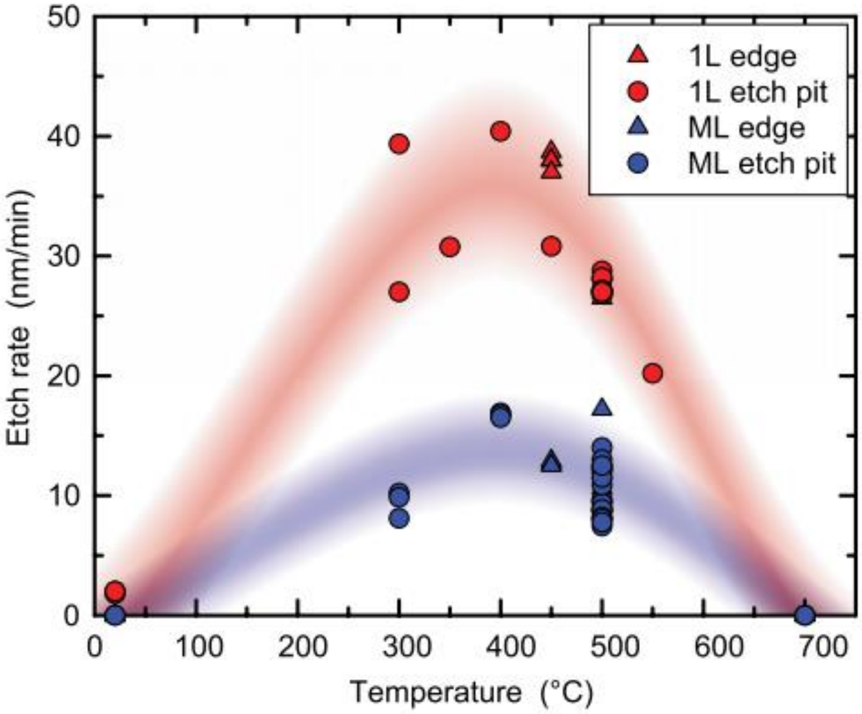

Figure 2-5. Dependence of etch rate on furnace temperature, for 10 min of hydrogen plasma exposure. The etch rate is calculated as half the etch pit diameter divided by treatment duration. For monolayer (1L) graphene uniform etching from the sheet edges (red triangles) and circular etch pit formation within the basal plane (red circles) proceed at very similar rates, suggesting that the same isotropic etch mechanism controls both processes. For circular etch pits, only the diameter of the largest hole found in each sample is shown. For multilayer (ML) graphene, uniform etching from the sheet edges (blue triangles) occurs alongside anisotropic etching in the basal plane (blue circles). The diameter of hexagonal etch pits is taken as the distance between opposing sides. All etch pit dimensions are determined from AFM images. Red and blue swathes are guides to the eye.

2.1.6 – Negative Thermal Expansion

Raman Spectroscopy is a useful tool in that it can distinguish between graphene or any other thin layer material for up to three atomic layers. It also allows for the study of in-situ measurements for temperature effects on graphene due to the Raman laser heating. It has been estimated from first principle calculations that the thermal expansion coefficient for graphene as a function of temperature has a negative value for temperatures up to at least 2500 K, which is caused by bending acoustic modes [90-91]. Experimentally, it has been demonstrated that for various temperature ranges, graphene also exhibits a negative thermal expansion coefficient [92-93], which leads to ripples on the graphene sheet [103].

2.1.7 – Radiation Resistance

This property has been studied both experimentally and numerically, over a wide range of energies and ions [32-33,35,95–97]. All these prior studies agree on the resilience of graphene under these extreme conditions. Åhgren, et al. showed that by introducing vacancies (prior to bombardment) and increasing the energy of the incoming ions, the sputtering yields of free standing graphene become close to zero [104] for helium, which is one of the species used for these studies. These results are summarized in Figure 2-6.

The free-standing aspect is of particular interest for using graphene as a membrane to separate a low-pressure plasma region from a high-pressure neutral gas, as is the case explored in one of the following chapters of the thesis. However, its relevance as a pressure barrier also applies to the case of irradiation of surfaces with graphene coatings. Tungsten itself requires high particle energies for sputtering, so even if the graphene is not suspended, ejected particles should not contribute much damage to the monolayer as seen in other studies with non-refractory metals as a substrate [32,35,106].

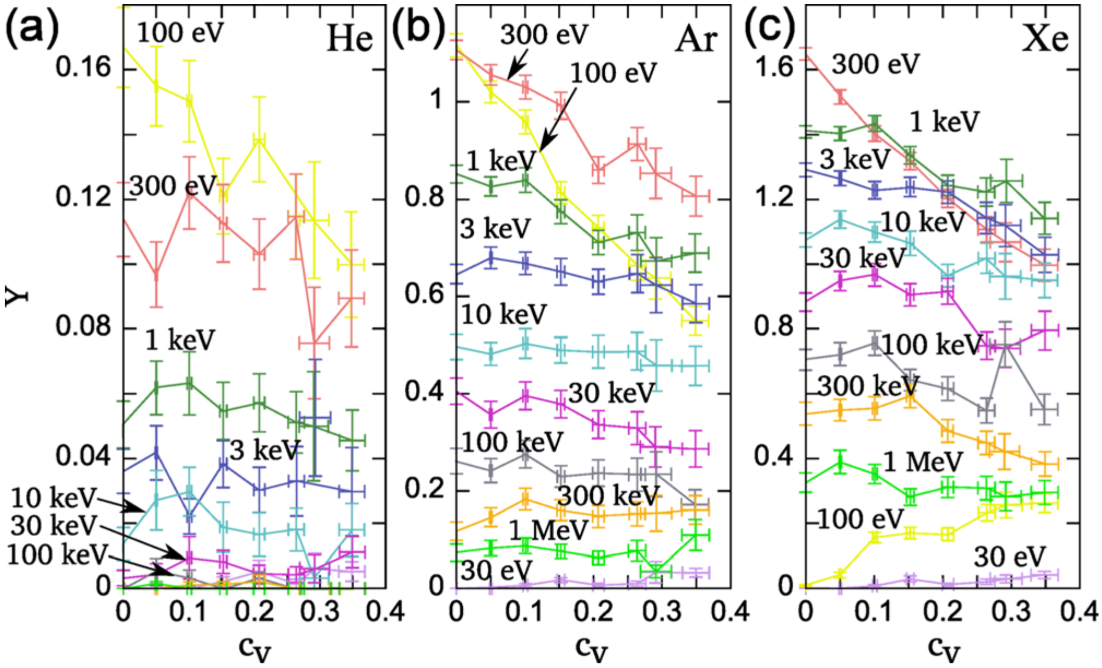

Figure 2-6. Sputtering yield (Y) as a function of vacancy concentration (cv) for (a) He, (b) Ar, and (c) Xe ions. Each data point is an average Y for all simulations for the same ion species, ion energy and cv. The error bars corresponding to Y show the standard deviation and the error bars corresponding to c_v are caused by the removal of unconnected fragments after randomly removing atoms from pristine graphene. Increasing incoming ion energy decreases the sputtering yields of graphene, as does introducing defects to the film for most cases [104].

More recently, Herbig and Michely [107] determined that for ionized noble gases with energies between 200-500 eV, a single layer graphene coating on single crystalline iridium can suppress the sputtering of the substrate metal by about two orders of magnitude for substrate bulk temperatures above 1000 K. At room temperature, the physical sputtering yield only decreases by one order of magnitude. They concluded that this protection mechanism is dominated by self-repair of the radiation damage in graphene, which occurs at temperatures where CVD growth is performed, and can be maintained as long as there is a partial hydrocarbon partial pressure in the chamber.

Ahlberg, et al. were able to study defect formation in graphene during low energy argon ion bombardment [108]. In this study, single layer graphene was placed on SiO_2 and bombarded with an argon ion beam at energies ranging from 5-200 eV. Figure 2-7 demonstrates some of the major results of this study. Due to the energy transfer mechanism, ions with energies below 25 eV will not impart enough energy into a graphene carbon atom in order to knock it off its lattice and introduce single vacancy defects. As the energy is increased beyond this minimum threshold for sputtering, defects are introduced into the membrane up to certain energies, at which point, a smaller quantity of ions interact with the graphene atoms and lowers the defect ratio.

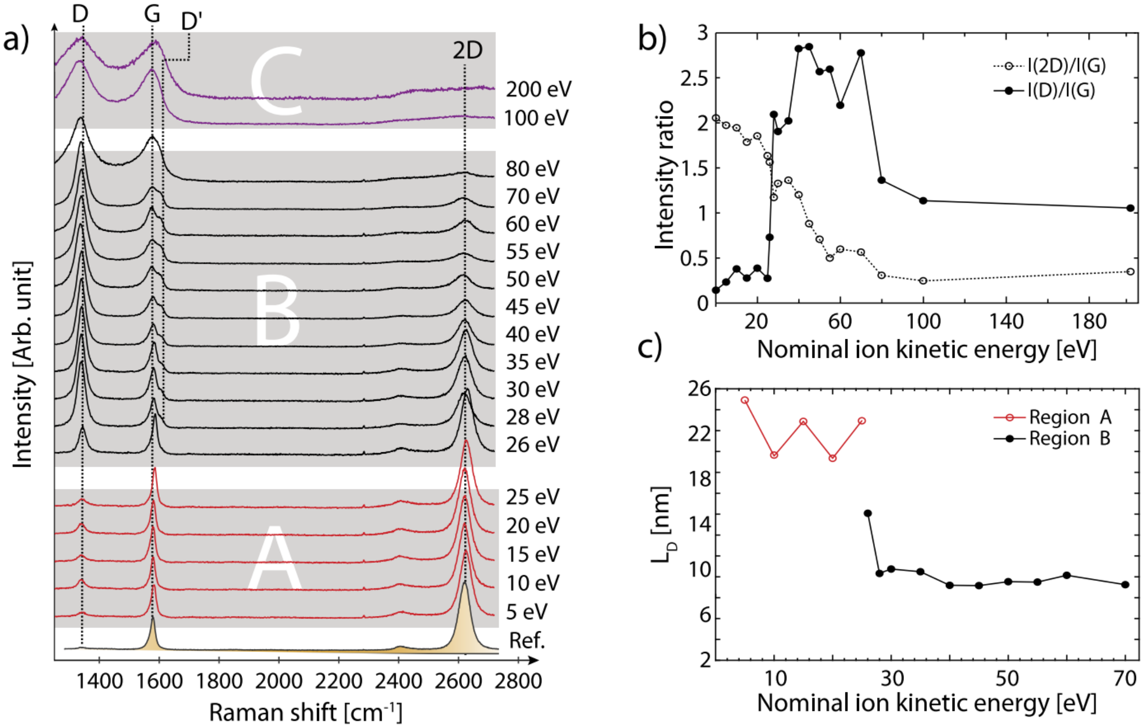

Figure 2-7.(a) Raman spectra of graphene exposed to same Ar+ ion dose but at different ion energies. (b) Intensity ratios of 2D to G and D to G Raman peaks vs. kinetic energy of the ions bombarding the graphene sample seen in (a). (c) LD calculated from the I(D) [108].

This study has also found that there is a trend of increasing I(D)/I(G) vs dose and kinetic energy (Figure 2-8) which illustrates that there is a potential for developing sputter deposition processes of graphene, but that this could be difficult to implement. This dependence of the defect ratio on dose also suggests that at high fluences, the membrane will eventually fail, though this could be highly dependent on the underlying substrate and process temperature, such as that observed by Herbig and Michely [107].

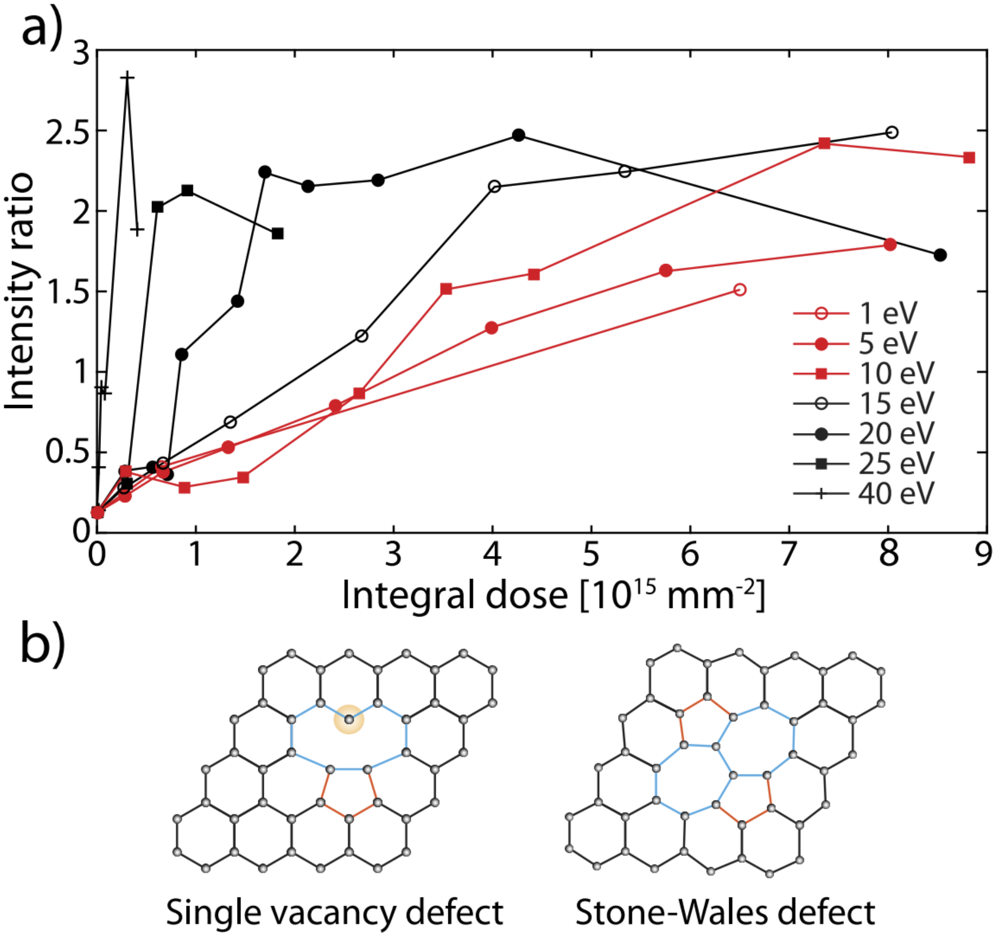

Figure 2-8. (a) I(D)/I(G) vs ion dose (exposure time) for different energies illustrating the two separate regions, 1-15 eV being the low energy region and 20 and upward being the high energy region, correlating to the two different dominant defect formation mechanisms. (b) Illustrations depicting different types of defects from energetic ion bombardment, displacement defects from high energy impact (left) and isomerization from low energy impact (right) [108].

2.2 – Helium Irradiation of Tungsten

Tungsten has become a leading candidate for plasma-facing components in future fusion reactors due to the properties of a refractory metal. Many groups across the world have studied sputtering of tungsten due to helium over a various wide range of energies and temperatures [42,109–114], including energies ranging from eV to keV, temperatures extending from 30-2700 °C and fluences up to $1x10^{23}$ He^+/cm^2. This study will only focus on polycrystalline samples.

Due to irradiation with helium, vacancies are created, and interstitials are introduced into the tungsten lattice, which eventually lead to changes in surface morphology, erosion and mass losses. Diffusion of helium eventually leads to clusters and helium bubbles which can lead to blistering [112,114–116], tungsten fuzz [42,45,46,117] or other morphology changes [43,108-109] forming on the surface of the material. Figure 2-9 summarizes important temperature and fluence effects on surface changes to polycrystalline tungsten samples.

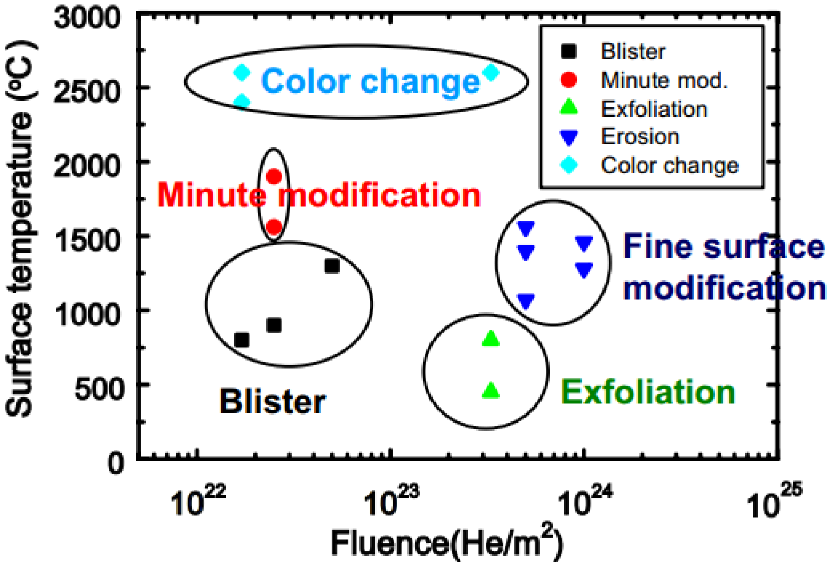

Figure 2-9. Schematic diagram of the relation of surface modifications to fluence and peak temperature irradiated with 19 keV He [115].

Tokunaga [115] was able to observe the effects of He bubble formation as a function of fluence and temperature at the JAERI (Japan Atomic Energy Research Institute), Particle Beam Engineering Facility. At 800 ºC and the lowest fluence, blisters of around 1µm diameter formed on the surface, as seen in Figure 2-10. With increasing fluence, pinholes started to form inside of the blisters and as the temperature increased to 1400 ºC, a wavelike structure formed at the surface, similar to results published by Zenobia [40]. As temperature was raised to a 2600 ºC, a coral-like structure formed at the surface; a darkening of the surface was also seen due to surface oxidation. Figure 2-11 shows these structures on the surface.

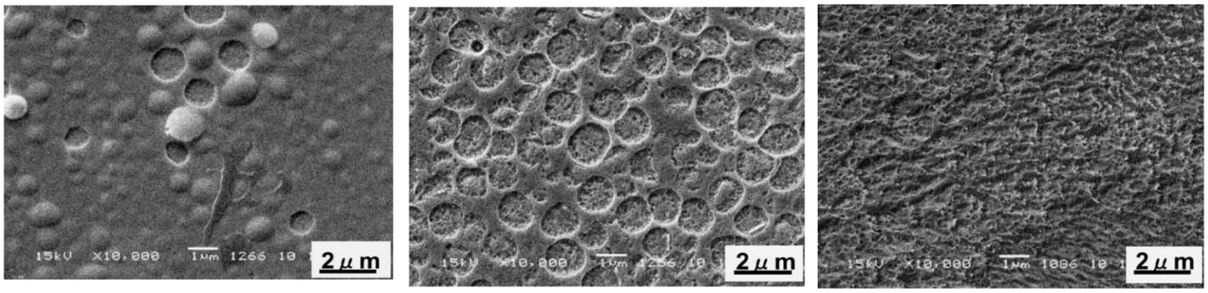

Figure 2-10. W irradiated with 19 keV He+ at 800 ºC. (a) Blisters and bumps formed on the W surface at a fluence of 1.7x10^{19} He^{+}/cm^{2}. (b) As the fluence was increased to 3.3x10^{19} He^{+}/cm^{2} blister bumps appear to have erupted and holes formed inside of the blisters. (c) Surface morphology changed to a wavy structure, most likely from surface erosion, at a fluence of 5x10^{19} He^{+}/cm^{2} and a temperature of 1400 ºC [115].

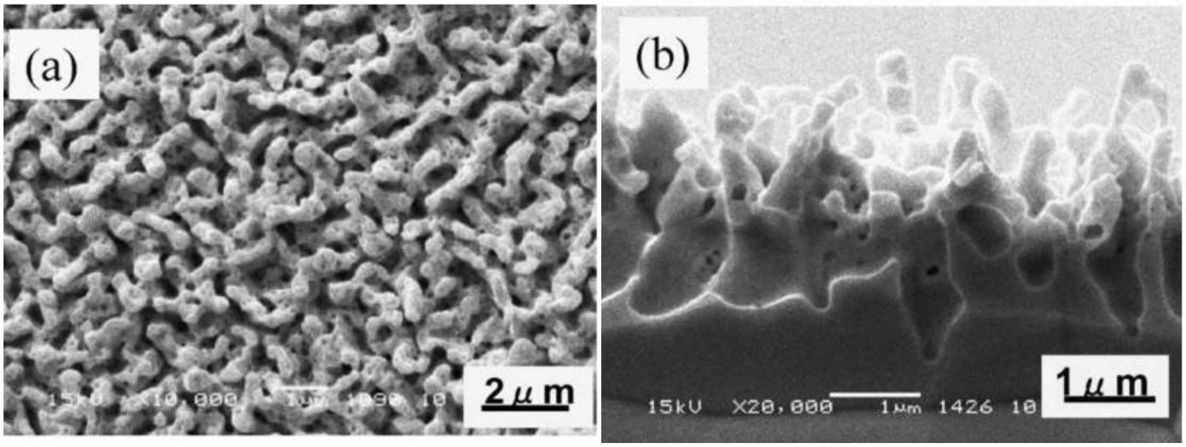

Figure 2-11. (a) Coral structure forming on the W surface after being irradiated with 19 keV He^{+} at a fluence of 3.3x10^{19} He^{+}/cm^{2} and a temperature of 2600 ºC. (b) Cross section of the sample surface showing holes in the extending coral structures [115].

Iwakiri et al [116] performed a study on low and high energy helium implanted in tungsten. At high ion energies they found that the implanted helium and radiation-induced vacancies act as nucleation sites for helium bubbles to form, as well as enhance nucleation of interstitial loops. This was observed over a wide range of temperatures (293-1073 K), in which they also observed that the density and the size of these defects increased with temperature as seen in Figure 2-12. At low temperatures, there are still bubbles, platelets and interstitial loops observed. Any impurities act as traps for helium and this forms bubbles that displace tungsten ions from their lattice sites.

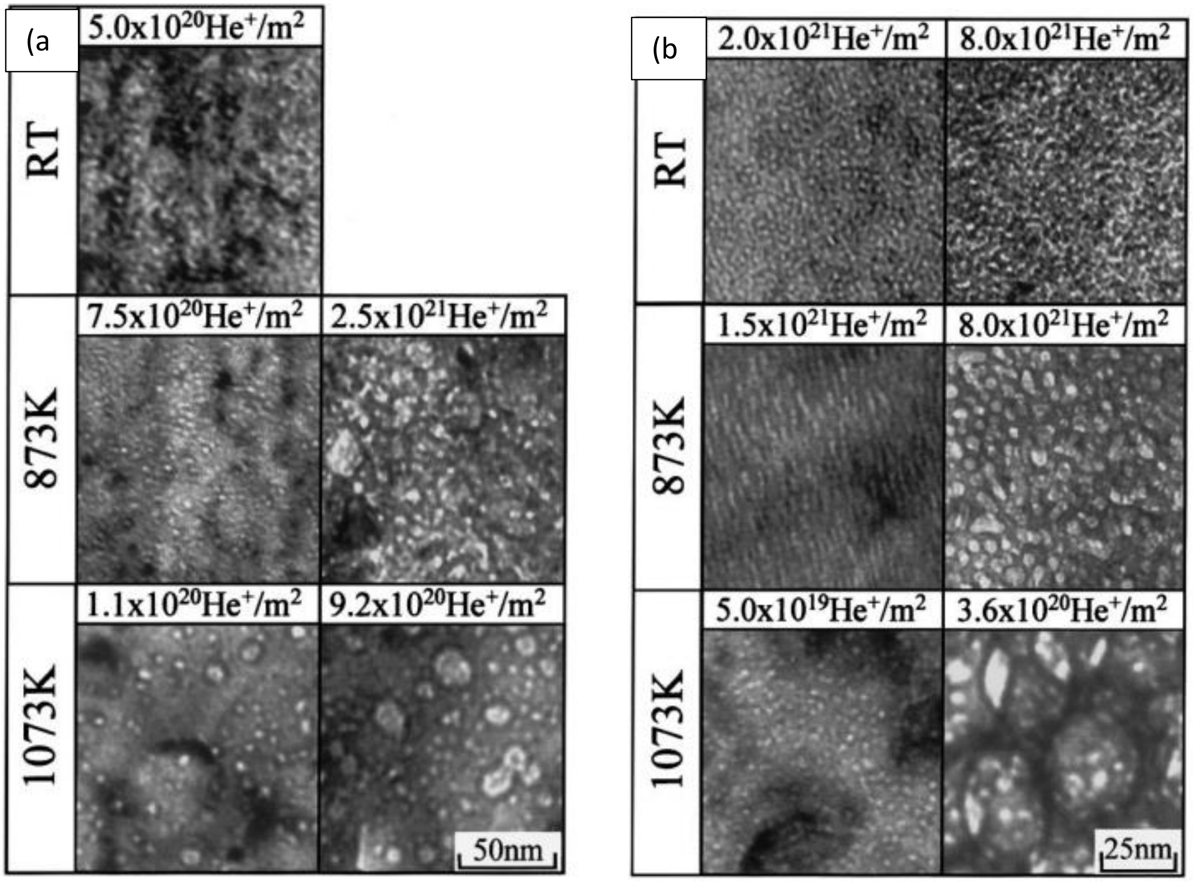

Figure 2-12. Temperature dependence of bubble formation during irradiation with (a) 0.25 keV He$^+$ ions, (b) 8 keV He$^+$ ions [116].

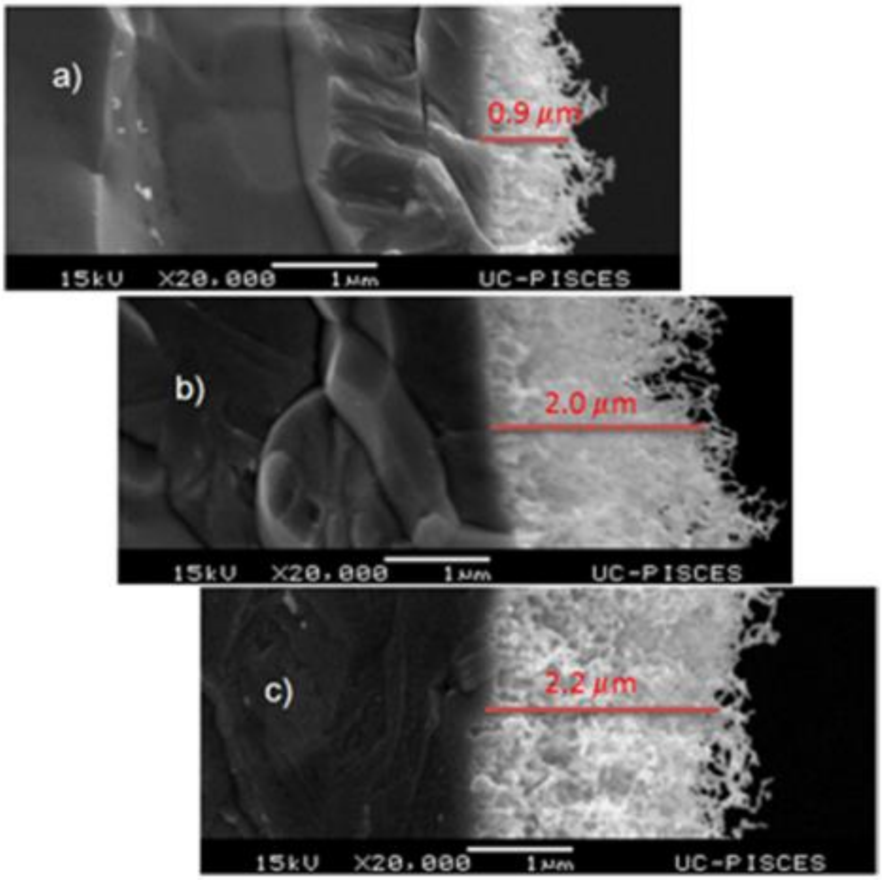

Figure 2-13. Estimated tungsten fuzz surface layer thicknesses resulting from exposure to He$^+$ ions at (a) 250 eV, (b) 200 eV, and (c) 60 eV [45].

Baldwin, Doerner and Stangeby [45] were able to show that in a steady-state plasma, and at the right conditions, it is possible to predict the thickness of the tungsten fuzz layers forming at the surface of the samples. Figure 2-13 shows this fuzz evolution as a function of energy, and it was also determined that it is strongly a function of time, $\sqrt{t}$. They later found that varying the fluence revealed a more general form of growth dependence and reconciled different rates of growth observed at different fluxes [46]. There are still many ongoing studies on the effect of these high tungsten erosion yields in a large fusion device, but the general consensus is that this will greatly limit performance of these devices unless mitigation techniques are found.

Recent studies at the Materials Irradiation Experiment (MITE-E) at the University of Wisconsin-Madison have shown the dependence of surface morphology on temperature and ion fluence. There are different regimes for surface damage structures in tungsten and these are summarized in Figure 2-14. Zenobia [40] demonstrated the formation of grass structures forming at 900 ºC above fluences of 1×10^{18} He/cm^2 as seen on Figure 2-15 and Figure 2-16. This also allowed quantification of the diffusion coefficient for helium in tungsten to be 9×10^{-7} cm^2/s [40]. Following the discovery of the dependence of grain erosion on grain orientation, Garrison [118] found that grains in the (001) orientation were more resistant to radiation; see Figure 2-17. This grain orientation of single crystalline tungsten has not been tested yet on the MITE-E facility, but it is expected that this should greatly reduce the mass losses.

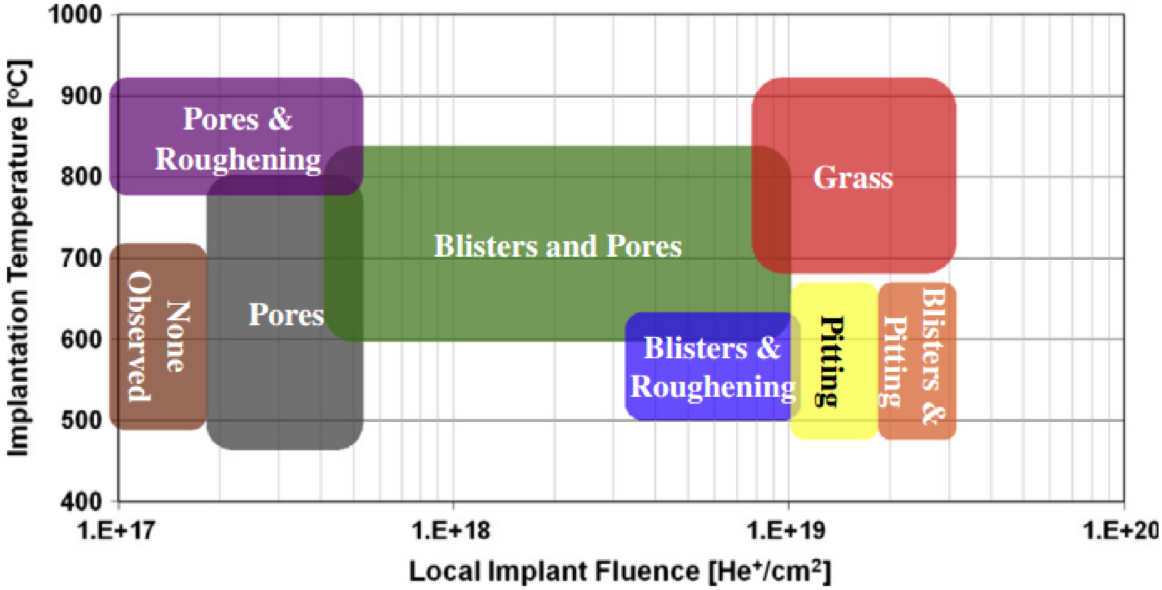

Figure 2-14. Compilation of the temperature and fluence regimes where different surface morphologies are observed [118].

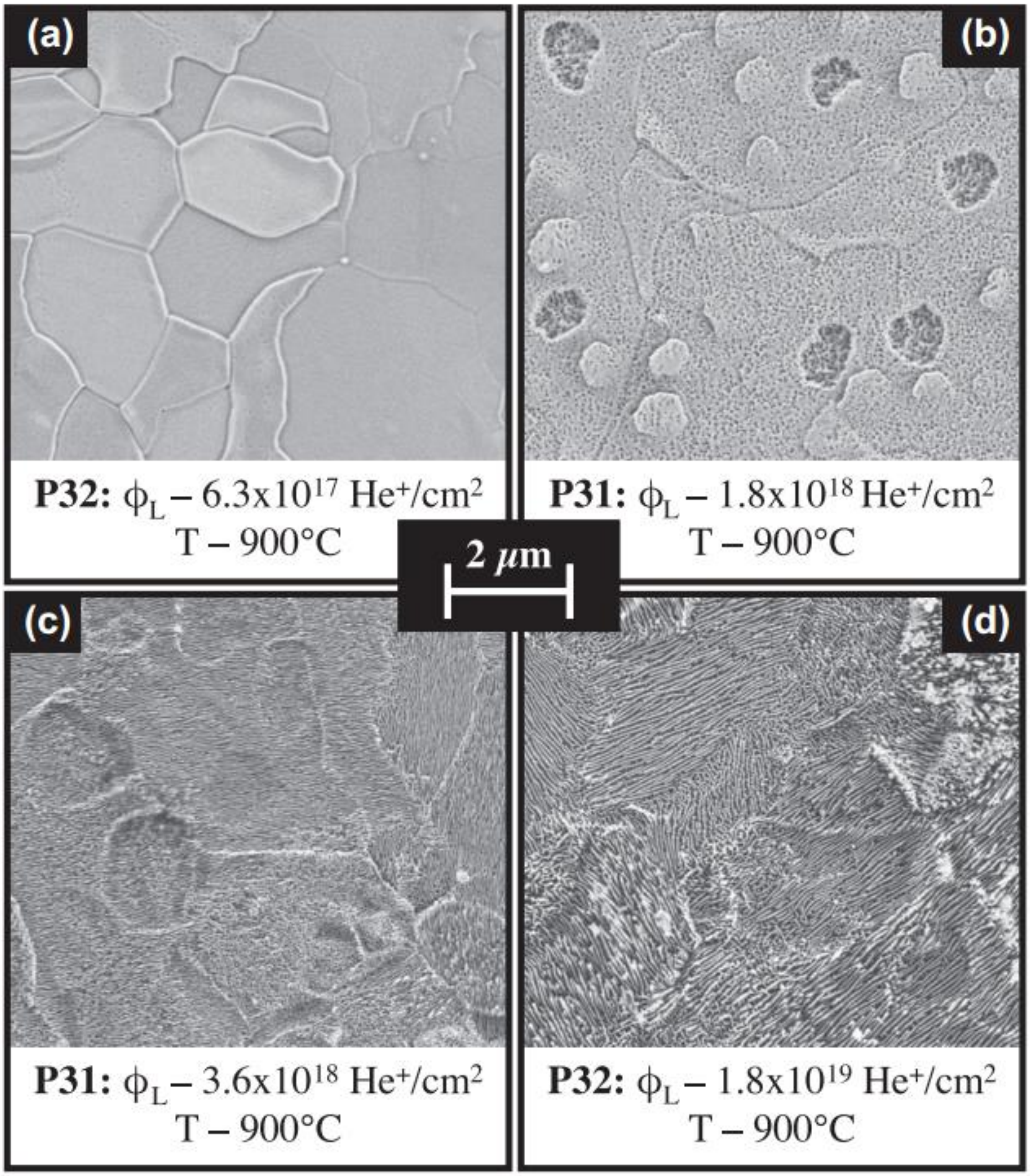

Figure 2-15. As fluence was increased on PCW samples irradiated with 30 keV He+ the surface morphology changes became more severe-starting with (a) small pores and grain shifting, evolving to (b) blisters and pores, then (c) blister remnants and grass, and finally (d) grass only [40].

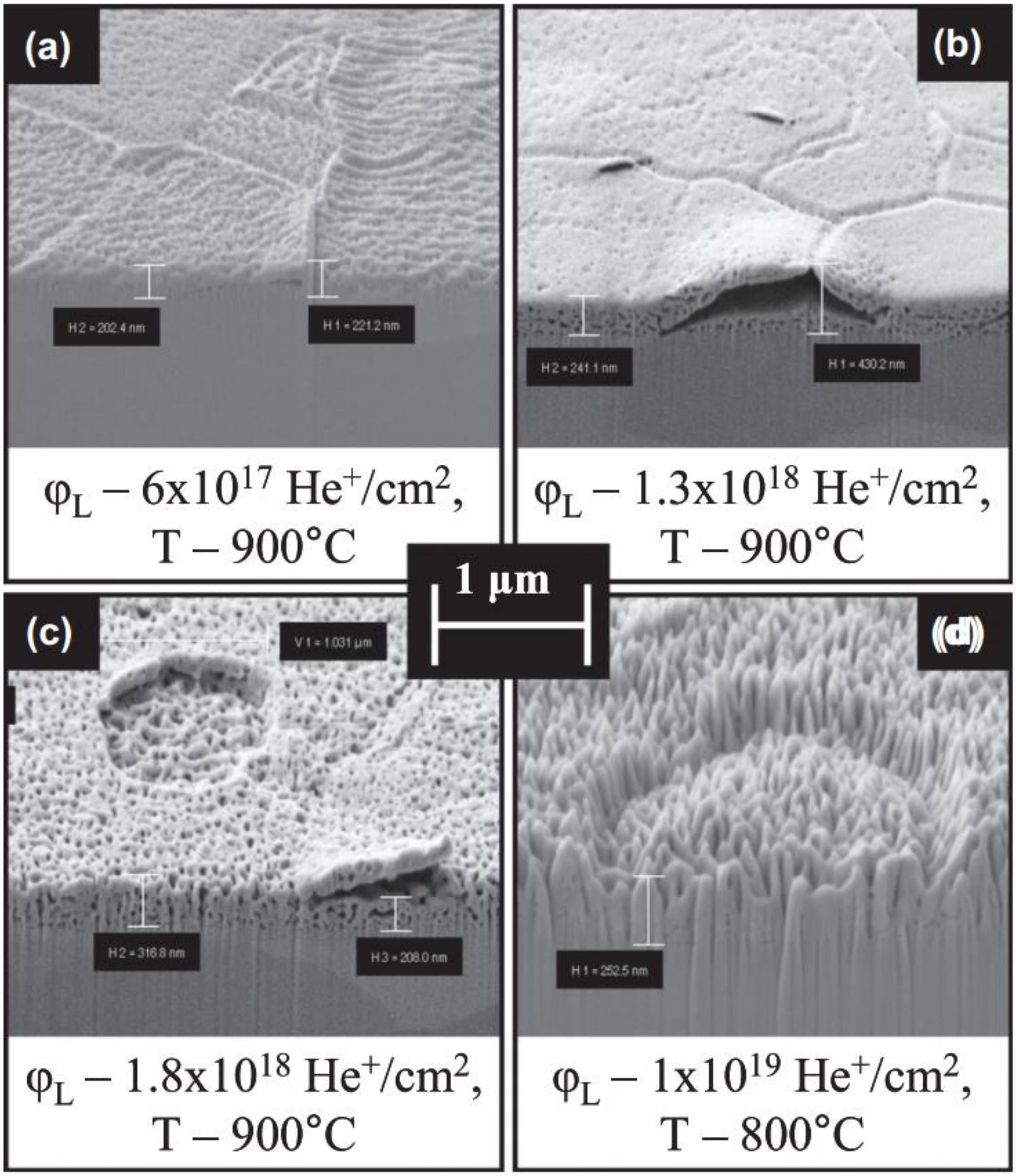

Figure 2-16. Progression from blisters to grass structure: (a) initial sub-surface bubbles form, (b) trapped gas raises blister cap, (c) blister cap ruptures or erodes completely, and (d) grass morphology overwhelms depression left by blisters [40]*.*

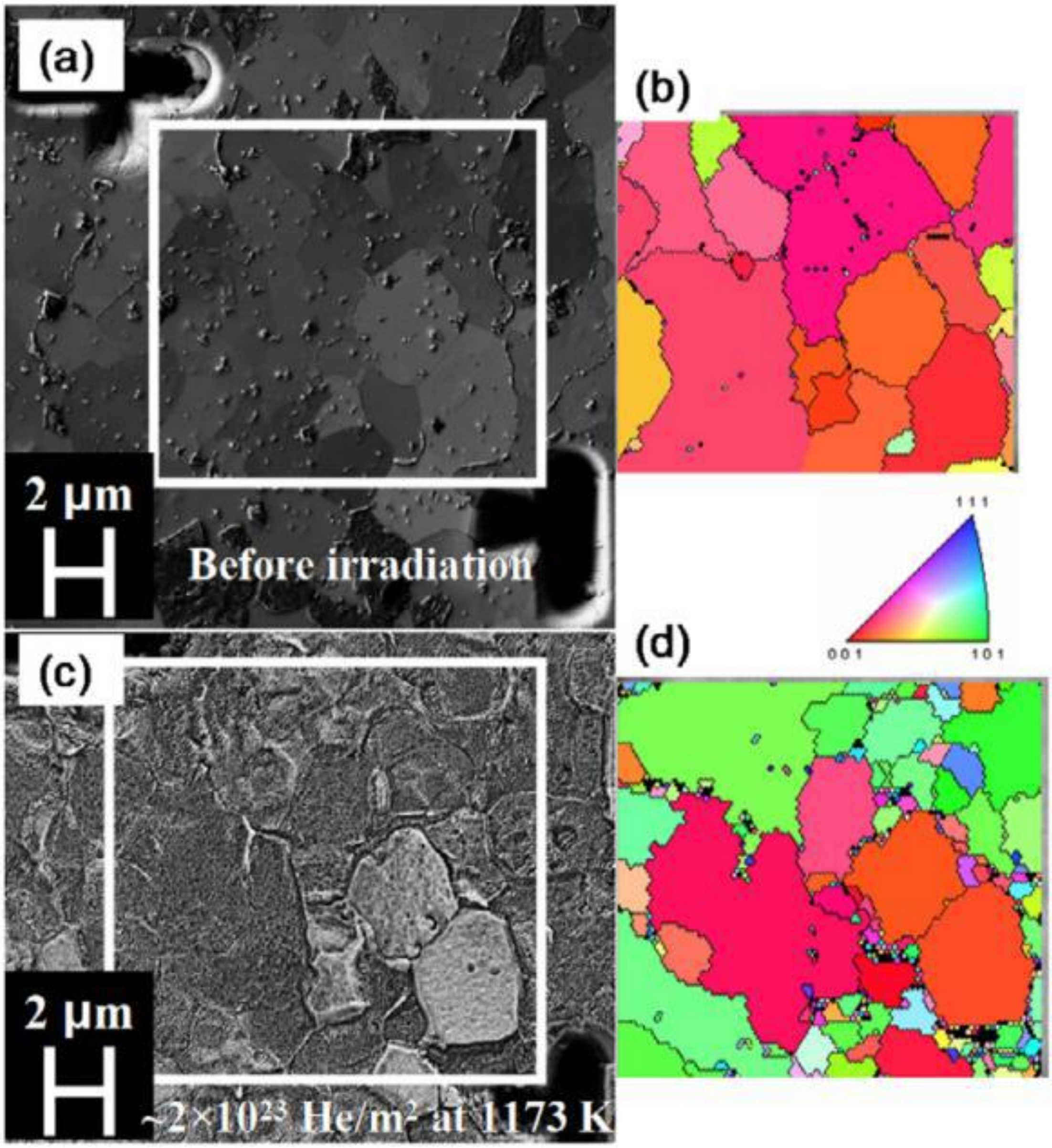

Figure 2-17. Left: SEM image of a PCW sample (a) pre- and (c) post-irradiation to an average fluence of $6x10^{18}$ He^+/cm^2 with 30 keV He^+ at 900 ºC. Fluence values are local fluences for images taken from the center of the sample, corresponding to the center of the beam. Right: (b) and (d) correspond to the images at left and are an EBSD map of the grains taken at the same location on the sample surface [50].

2.3 – Neutron Production and IEC Work

At the University of Wisconsin-Madison, Inertial Electrostatic Devices are used for a myriad of purposes (see Figure 2-18), ranging from materials damage studies, to the production of short lived radioisotopes and neutrons for the detections of clandestine materials [120,121].

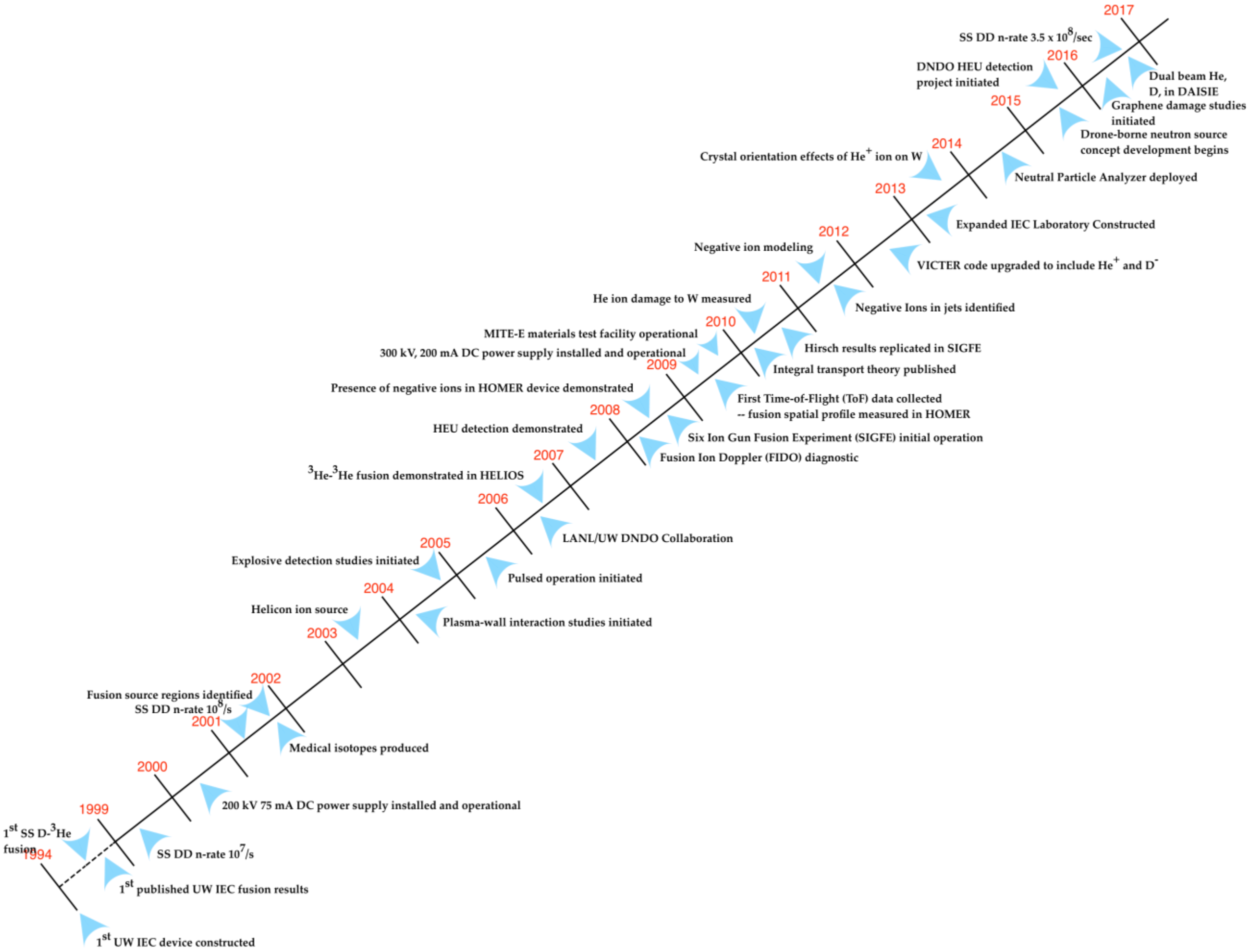

Figure 2-18. Brief History of the University of Wisconsin IEC program over the past 18 years [120].

IEC devices function by ionizing fuel in the region outside of a grounded anode, and a negative bias is applied to the central cathode, towards which the ions drift and converge, causing fusion mainly with the background gas. Significant effort has been made to explain IEC physics, particularly by researchers in the U.S., Japan and Australia. At UW-Madison, Emmert and

Santarius developed the VICTER code [122,123], which takes into account charge exchange, ion impact ionization and other atomic and molecular processes for ion flow through a neutral background gas. The code also accounts, through post-processing of the ion flow results, for negative ion currents and fast neutral production, along with the consequent fusion reactions in the devices. While the code has been able to show a general agreement with experimental neutron rates for other IEC devices, there are still some differences that need to be accounted for as seen in Figure 2-19 and Figure 2-20.

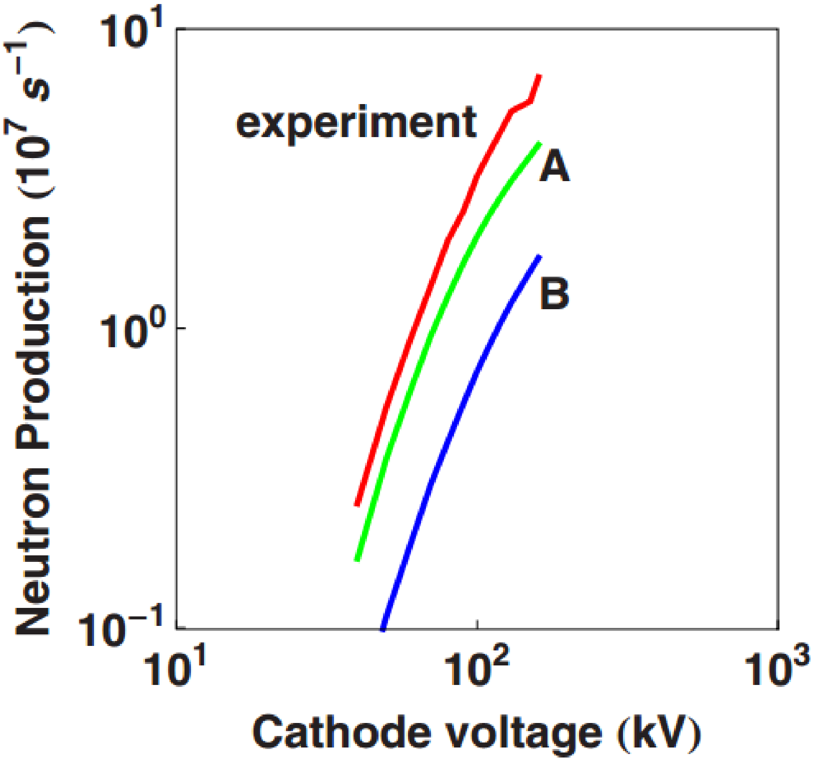

Figure 2-19. Comparison between experimental and calculated DD neutron production rates as a function of cathode voltage. (a) Model with cold ions in cathode region not included. (b) Model with cold ions in cathode region included [122]*.*

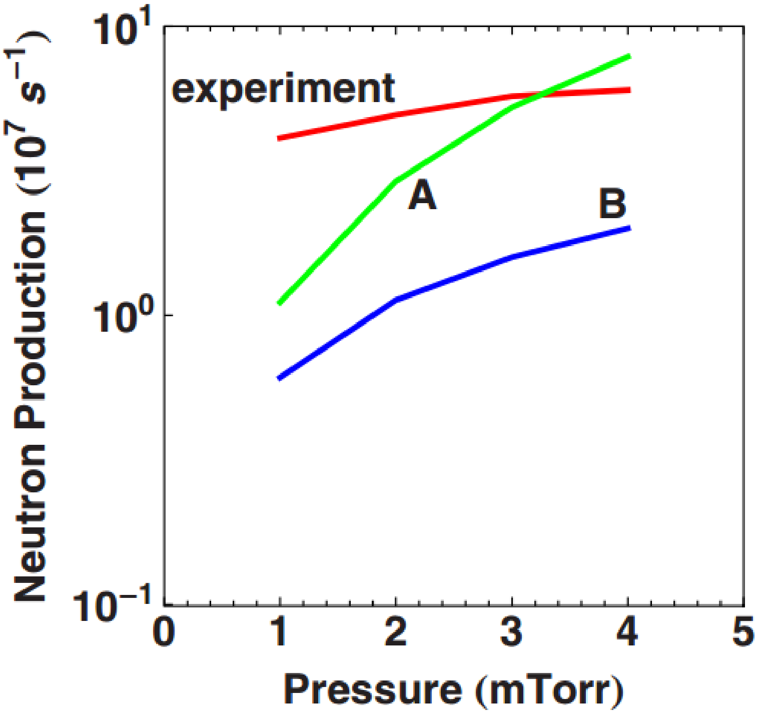

Figure 2-20. Comparison of experimental and calculated DD neutron production rates as a function of background pressure. (a) Model with cold ions in cathode region not included. (b) Model with cold ions in cathode region included [122].

Current IEC devices are relatively inflexible in that the chamber size limits cathode and anode sizes, and constructing spherical grids is time consuming, which makes parametric exploration of grid sizes and spacings difficult. Figure 2-21 shows the traditional experimental setup for these devices, while the new device breaks away from conventional IEC experiments at the University of Wisconsin-Madison. The novelty of the LUNA device is that has fixed cathode and anode areas, but they are movable along the chamber axis, which allows for optimization of the neutron rates in differently sized target and charge exchange regions as well as performing parametric studies varying ion energies and chamber pressure.

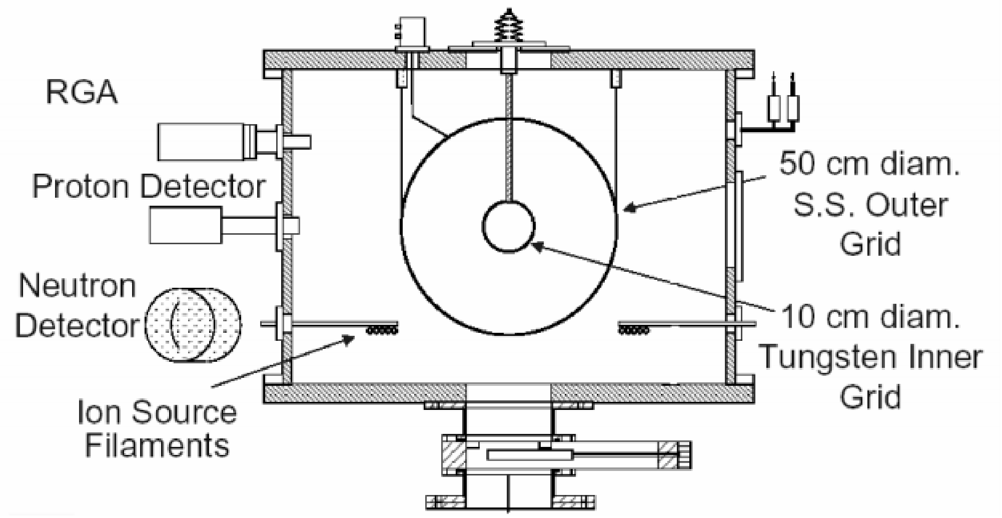

Figure 2-21. Experimental Setup of HOMER IEC Device at UW-Madison [120].

Chapter 5 will explain how these different aspects will be integrated in the LUNA device in order to optimize the fusion neutron rates. Success of the experiment could permit commercializing this technology for use in non-proliferation, detection of clandestine materials and other applications.

This page is intentionally left blank.

Chapter 3 – Experimental Procedures

3.1 – Graphene Synthesis

There are multiple ways to obtain graphene, the most famous one being mechanical exfoliation [7], which along with further elaboration of the experimental and theoretical details was awarded a Nobel Prize to Geim and Novoselov. In order for this thesis project to come to fruition, all the graphene was grown via Chemical Vapor Deposition (CVD), which can be used to grow on different substrates such as copper [51,114-115], nickel [124,126], stainless steel [118-119], and even tungsten [130]. The graphene used in this study was grown and transferred at UW-Madison in Professor Max Lagally's laboratories.

3.1.1 – Graphene Synthesis on Copper

Graphene was grown on copper foil by CVD (Figure 3-1). First, the copper must be cleaned in an ultrasonic cleaner in an isopropanol solution for 5 minutes to remove any impurities from the surface (e.g. copper oxide). Afterwards, the surface is dried with nitrogen. The quartz tube furnace used for these growths was set to a temperature of 1030 ˚C, and once this temperature is reached, hydrogen is introduced (5% H_2, 95% Ar) at 500 sccm for 30 minutes to purge the system from any oxygen. The end of the furnace is opened, and the copper foil is placed on a quartz boat in one of the heating zones, close the system and keep purging for an additional 30 minutes before growth. Growth is then initiated by flowing methane (5% CH_4, 95% Ar) and hydrogen, CH_4:H_2 at gas flows of 1.35 sccm:500 sccm at atmospheric pressure for 2 hours. After growth, the foil is left in a cooler zone in the furnace for 30 minutes in order to avoid it turning to oxide if it were removed too quickly. After cooling, the hydrogen is turned off and the samples are removed for transfer.

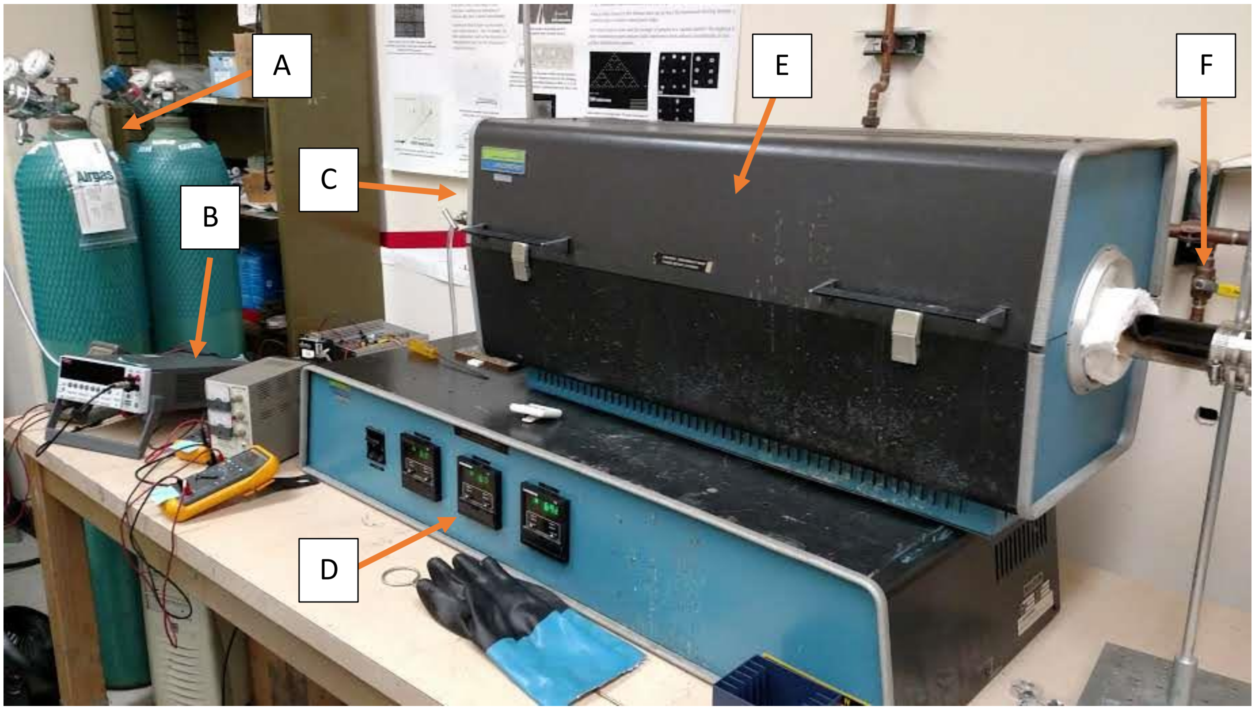

Figure 3-1. Quartz tube furnace setup at UW-Madison for graphene growth. (A) Hydrogen and methane tanks, (B) Flow control system, (C) Furnace gas inlet, (D) Temperature controller, (E) Furnace heater, (F) Furnace gas outlet.

3.1.2 – Graphene Transfer

In order to prepare the sample for transfer (Figure 3-2), one of the surfaces of the film is spin-coated with poly methyl methacrylate (PMMA). The sample is then put in an ozone cleaner for 20 minutes at a temperature of 85 °C to remove all the graphene from the uncoated surface. Once finished, the sample is immersed in a $FeCl_3$ solution to etch the copper for at least 8 hours to remove all traces of the metal. Once the substrate for transfer is ready, the suspended graphene on PMMA is scooped up with it and transferred into a de-ionized water bath three times to remove any traces of $FeCl_3$. After this, the sample can finally be placed on the substrate, and placed on a hot plate for 30 minutes at 85 °C to bind the graphene to the surface. The PMMA is then cleaned off in an acetone bath, an IPA bath and finally treated with nitrogen.

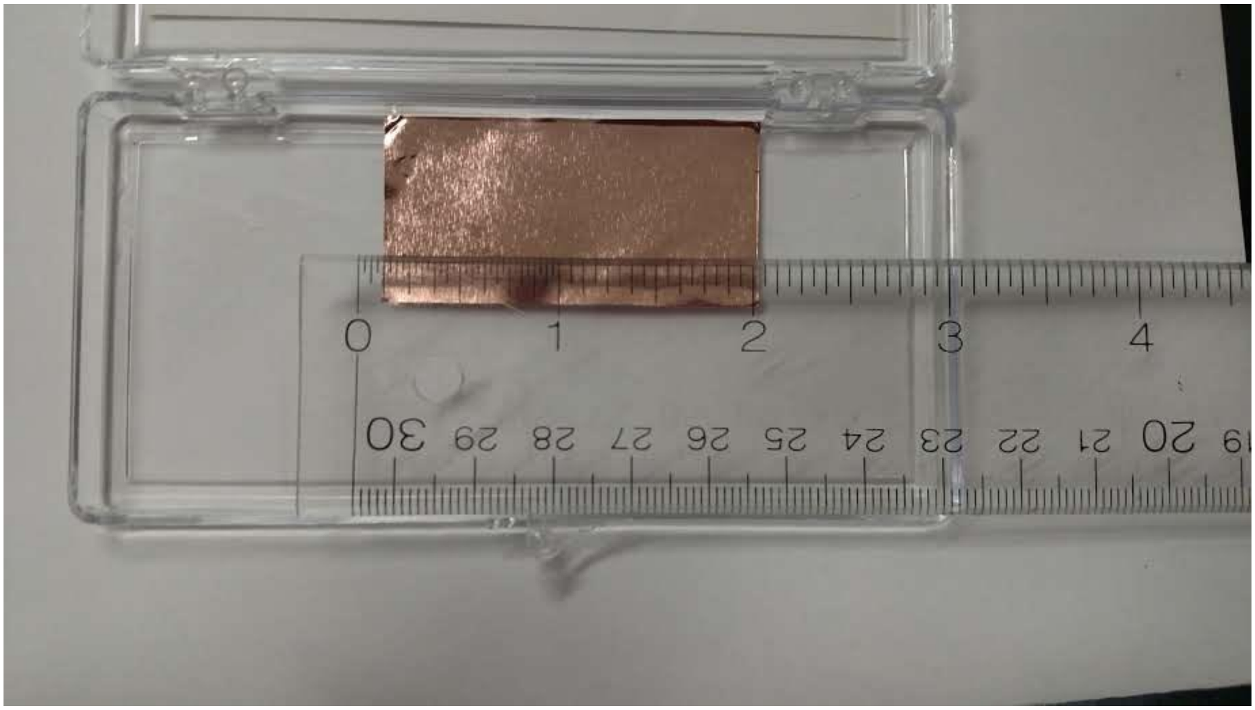

Figure 3-2. Graphene grown on copper foil. This is the largest full area sample grown in the laboratory up to date.

3.2 – Tungsten Substrates for Exposures

The samples used for this study are polycrystalline tungsten (PCW) since it is the most common type used for fusion applications. The sample sizes are 10 mm x 10 mm x 1 mm as well as 2.54 cm disks with a 2 mm thickness, and they were mechanically polished to a mirror finish and electropolished. The procedure for sample preparation and testing can be broken down into several parts, described in the subsections below.

3.2.1 – Mechanical Polishing

These were mechanically polished sequentially with 20.3 cm diameter 60, 120, 180, 320, 600, and 800 grit SiC discs. They were then polished with a 3µm water-based polycrystalline diamond solution on a white label polishing cloth and a final polishing with a 1µm water-based polycrystalline diamond solution with an Imperial cloth disk. Finally, the samples were rinsed with filtered water and then ethanol.

3.2.2 – Electropolishing

The solution used is 2 wt.% KOH dissolved in deionized water. The samples are dipped for 20 seconds at different voltages (i.e. 17, 20, 25 V). A graphite rod is used as a cathode and the metal sample acts as the anode. A magnetic stirrer is used for even etching. The solution ions are attracted to the metal surface and preferentially etch away surface atoms, revealing the material grains and boundaries. The samples are then rinsed with deionized water and ultrasonically cleaned in ethanol to rid the surface of any impurities on the surface. These are then characterized via Scanning Electron Microscopy (SEM), X-Ray Photoelectron Spectroscopy (XPS), Raman Spectroscopy (RS), X-Ray Diffraction (XRD), and weighed.

3.3 – Irradiation Experiments

In order to gain some understanding into the interactions of graphene as a coating for a plasma facing component, numerous samples were exposed in different experiments: the MITE-E Irradiation Facility at the University of Wisconsin-Madison, the PISCES Facility at the University of California-San Diego, and the C-2W Field Reversed Configuration Facility at TAE Technologies in Lake Forest, California.

3.3.1 – MITE-E Ion Beam Facility

The irradiation device used in this study was designed to deliver a high energy (5-150 keV) ion beam to a material in order to study surface damage. It utilizes an ion gun that can use gases such as deuterium, helium and nitrogen. An external laser is used to heat the samples on the stage to fusion relevant temperatures (~550-1200 °C). Figure 3-3 depicts the MITE-E experimental chamber as constructed by Zenobia [40]. Figure 3-4 illustrates the ion beam gun used to irradiate samples inside the chamber as well as the setup for laser heating and temperature measurements via a pyrometer, built by Egle [131] and Zenobia respectively.

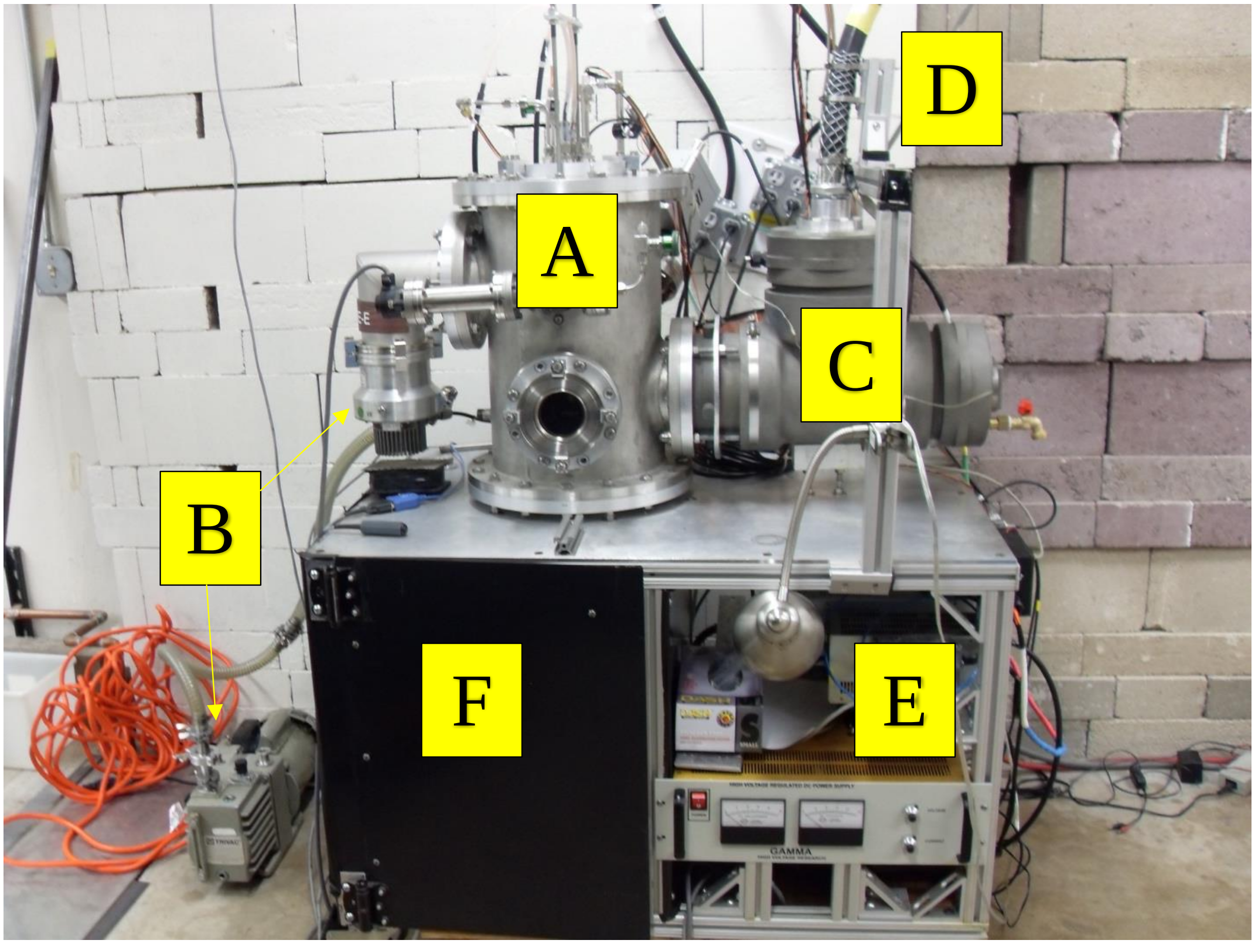

Figure 3-3. The MITE-E facility. (A) Vacuum chamber and ion gun housing, (B) Roughing and turbomolecular pumps, (C) High Voltage (HV) feedthrough, (D) HV cable, (E) Ion gun HV supplies, (F) laser cage.

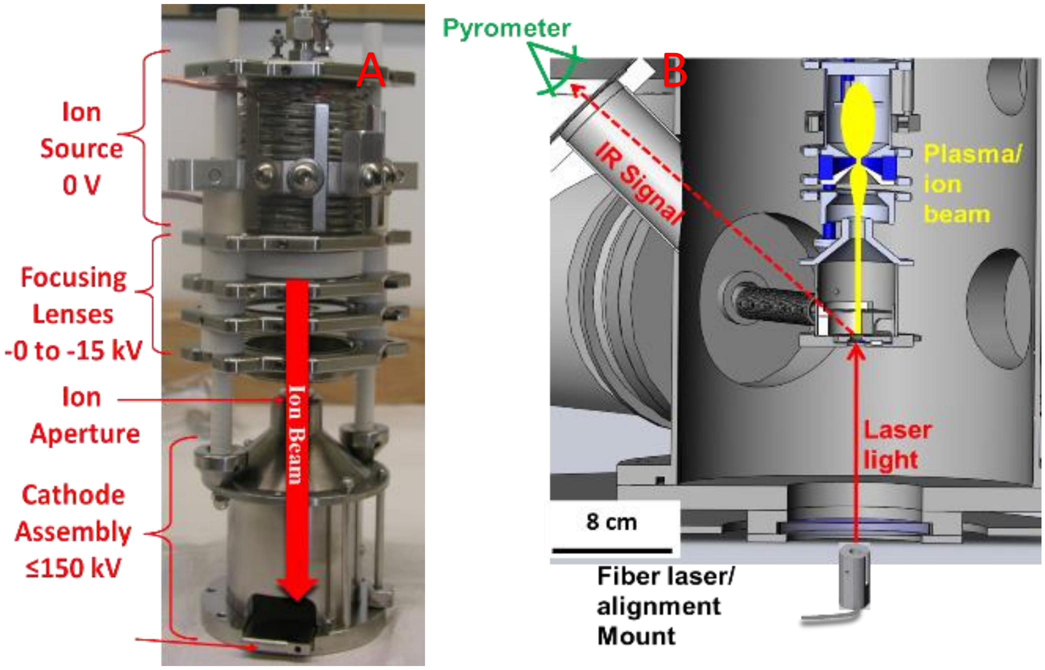

Figure 3-4. (A) Ion gun utilized in the MITE-E experiment. The samples are mounted at the bottom of the cathode assembly. (B) Sample and laser setup. Temperature readings are taken with an external pyrometer [41].

The samples were then irradiated with energetic helium at different conditions and characterized via the same techniques used prior to irradiation. In order to track the fluence received by the sample, the current to the sample is measured and transmitted using fiber optics. Secondary electron emission is an issue when trying to measure an accurate current. The samples are normally corrected for the secondary electron yields for tungsten using a coefficient of 1.8; the coated samples use the same correction for the yield. The correction used for the graphene coated samples is the same due to not having the data available for graphene on tungsten. This leads to the expected actual fluences for these samples to be higher by perhaps 1.8 times higher than what will be reported since we do not have an accurate way of measuring these electron yields.

3.3.2 – PISCES Linear Divertor

The Linear Divertor Experiment PISCES [42] at the University of California-San Diego allows exploration of low energy ions ranging from 40-250 eV, fluences ranging from 10^{19}-10^{22} ions/cm^2, and temperatures ranging from 500-1000 °C, for various ion species, in this study, deuterium and helium. It utilizes a dense plasma column with electron temperatures of approximately 50 eV, and ion temperatures of 20 eV which are then accelerated by biasing the target plate to the desired potential. Figure 3-5 shows the PISCES-A configuration with its plasma column. The target plate holds samples of 2.54 cm diameter disks that are 2 mm thick. These samples are actively cooled, and their temperature of them can be set by manipulating the cooling parameters. The plasma flux is also measured via fiber optics connected to the target plate. Figure 3-7 and Figure 3-8 show typical deuterium and helium discharges respectively in the PISCES-A facility. The samples were then characterized in the same manner as prior to the exposure, with the addition of a residual stress analysis performed on them due to each sample being only half-coated with graphene.

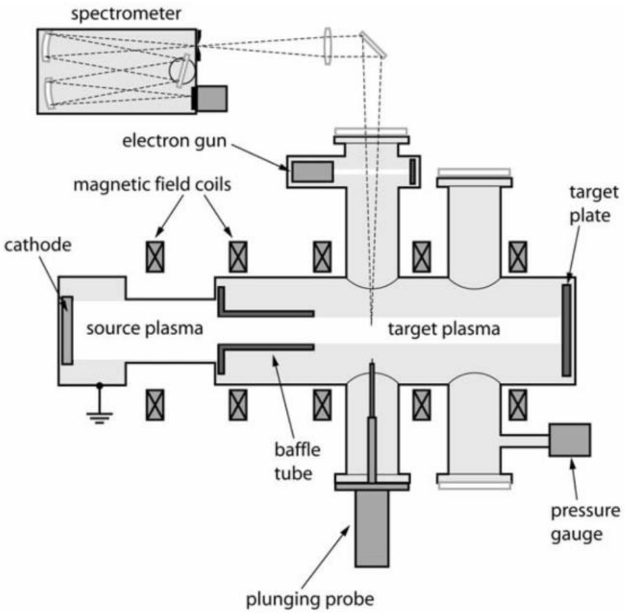

Figure 3-5. Schematic of experimental setup used in PISCES-A for spatial decay measurement [132].

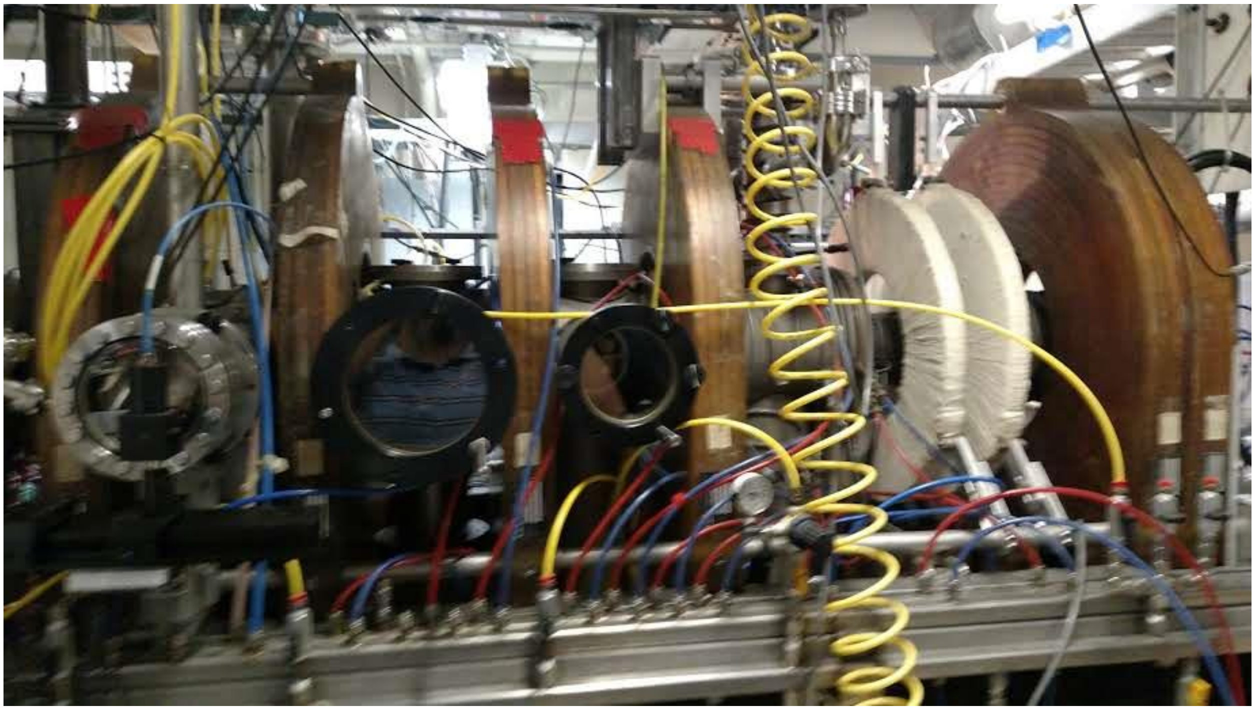

Figure 3-6. PISCES-A vacuum chamber and magnetic coils at the University of California-San Diego.

Figure 3-7. Deuterium plasma exposure to tungsten disks in PISCES-A for 30 minutes.

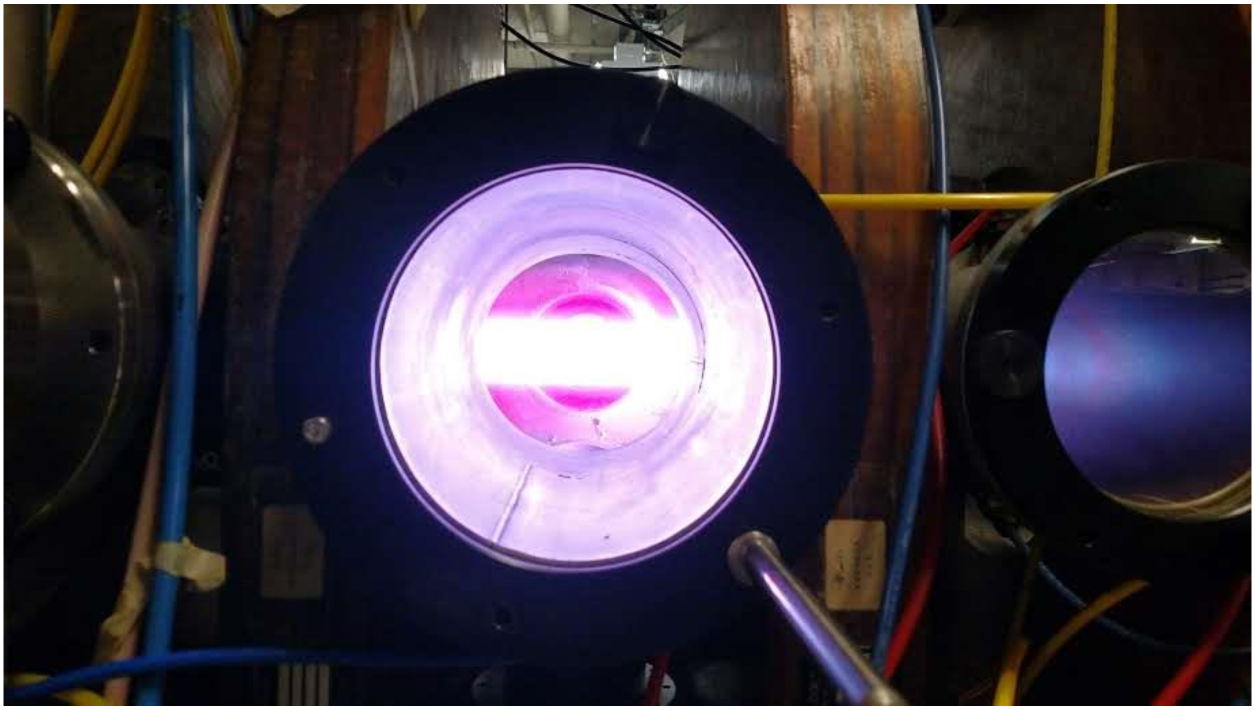

Figure 3-8. Helium plasma exposure to tungsten disks in PISCES-A for 30 minutes.

3.3.3 – C-2W Field Reversed Configuration

An excellent balance between potential reactor attractiveness and technical development risk motivates the development of field-reversed configuration (FRC) fusion power plants [133–135]. The linear, cylindrical FRC geometry facilitates the design of shields, magnets, input-power systems, and tritium-breeding blankets, while the high FRC β (≡plasma pressure/magnetic field pressure) increases the plasma power density and allows a compact fusion core. The surface heat flux to the divertor is moderate despite a high power density, because the plasma flowing to the end chamber walls carries much of the fusion power. The CAD design of the Tri Alpha Energy FRC experimental facility known both as C-2W and Norman is shown in Figure 3-9. The FRC is an ellipsoidal magnetic configuration immersed inside the magnetic field lines of an open-ended magnetic geometry. The open field lines guide charged particles toward the inner or end divertors for carrying heat and removing impurities from the system. Because of the β^2B^4 scaling of the fusion power density, where β is the plasma pressure divided by the magnetic field pressure and B is the magnetic field, the FRC (typical β~0.9) can be an extremely high power density system.

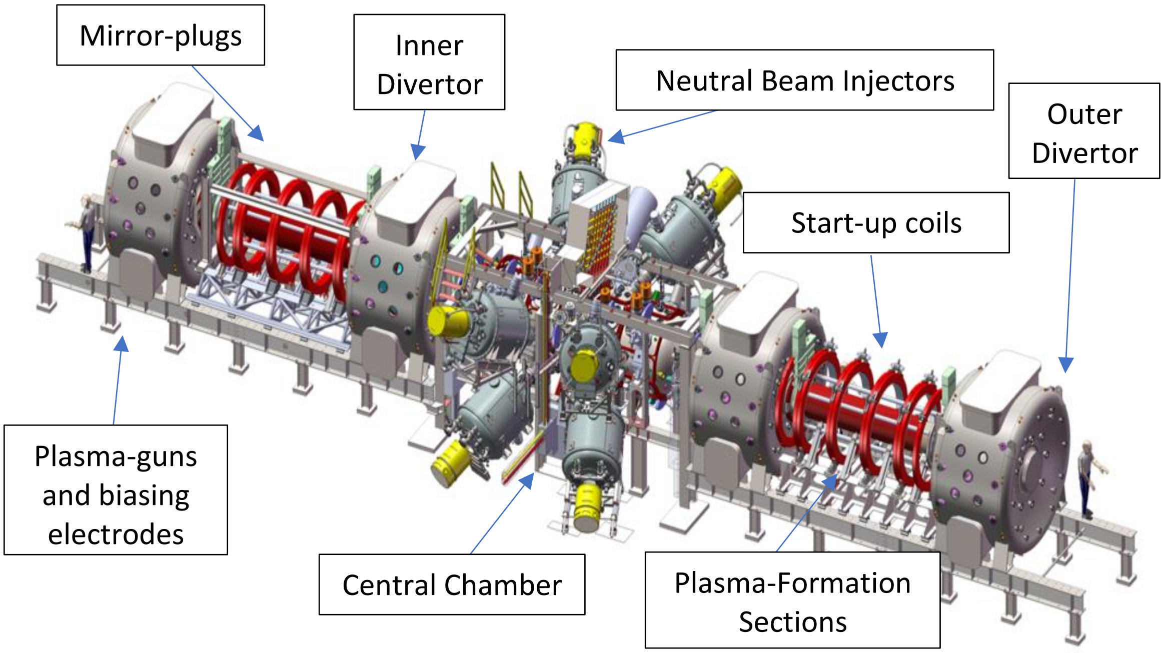

Figure 3-9. CAD design of an FRC experimental device at Tri Alpha Energy [44].

This is the first large scale fusion experiment where the graphene coating was tested, and samples were placed in the outer southern divertor (as seen in Figure 3-10). Core ion temperatures of 1 keV (of deuterium) are achieved in this experiment and all flux and heating data is extracted through the use of bolometers and fiber optics. The samples were installed in the southern divertor as indicated on Figure 3-11 and exposed to over 1,000 plasma shots over a period of 2 months and then sent back to the University of Wisconsin-Madison for subsequent analysis. Four additional samples were installed in the inner divertor; however, they will not be a part of this thesis.

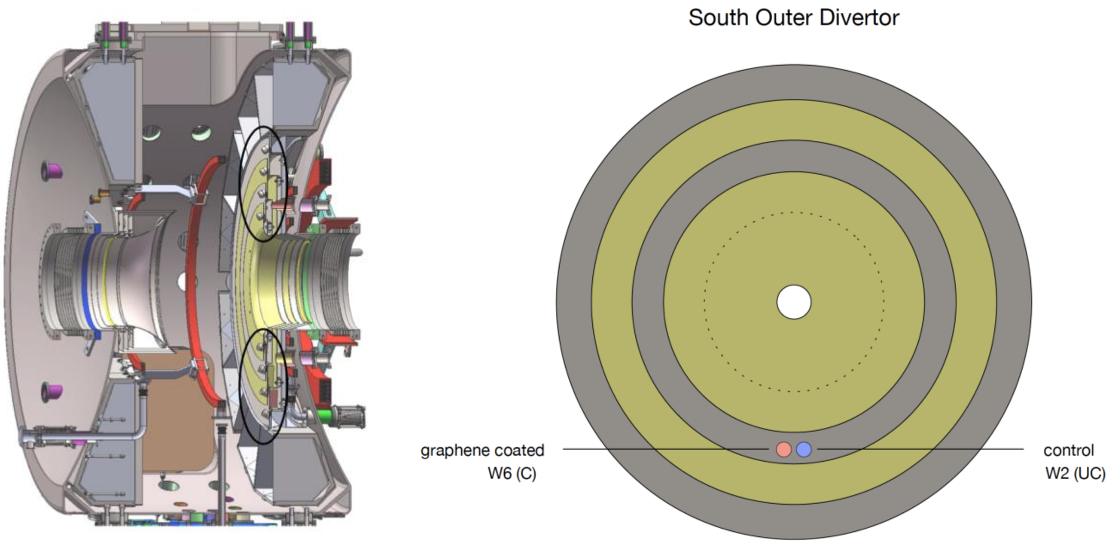

Figure 3-10. Cross sectional views of southern divertor in C-2W and placement of tungsten-graphene samples. Courtesy of TAE Technologies team.

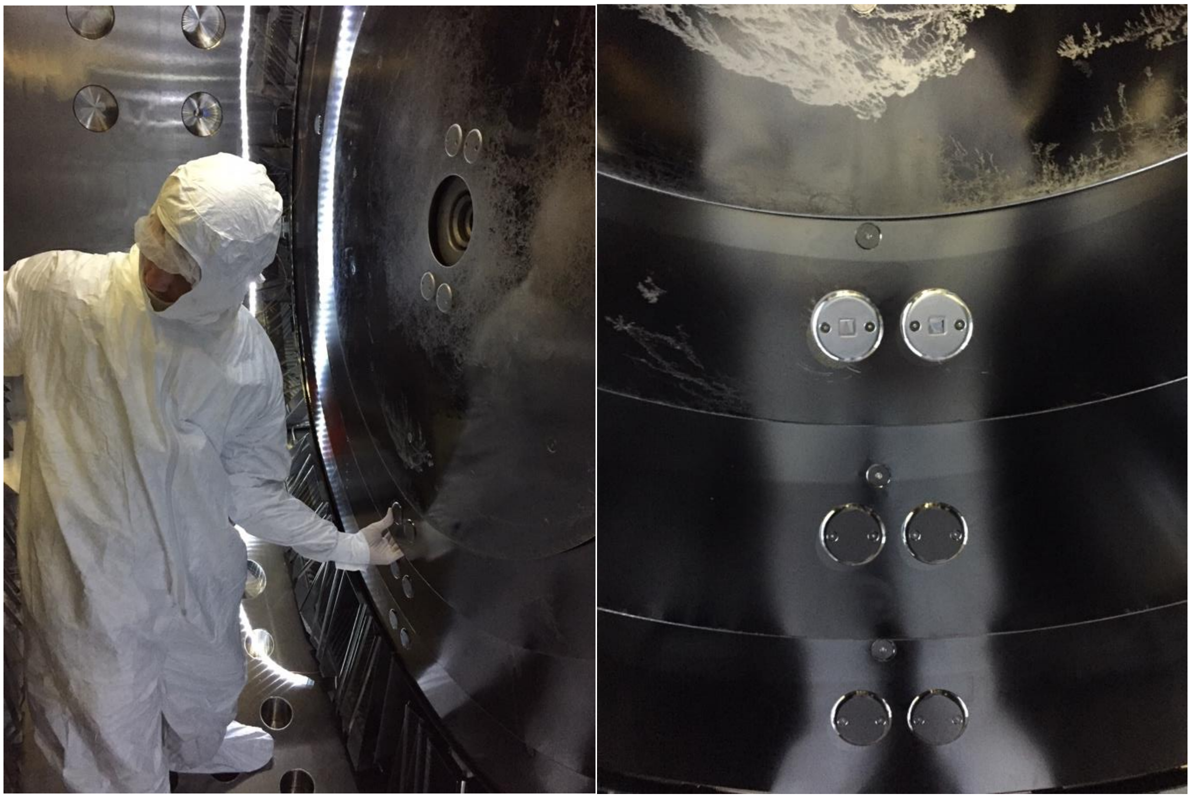

Figure 3-11. Installment of graphene coated and uncoated samples in C-2W. Courtesy of TAE Technologies team.

This page is intentionally left blank.

Chapter 4 – Characterization Techniques for Graphene and Tungsten

In order to study the graphene/W systems, the surfaces of these materials were examined at different exposure conditions (energy, sample temperature, fluences). Raman Spectroscopy was used to characterize the properties of graphene, including defects. X-ray photoelectron spectroscopy was used to analyze oxidation and impurity composition on the surface of the samples. For some high fluence cases, embrittlement due to ion exposure can become an issue, therefore, X-ray diffraction was used to perform a residual stress analysis in the subsurface of these systems. Finally, Scanning Electron Microscopy was employed to determine any morphology changes on the surface due to these exposures. Because no one technique can tell all the information needed about these samples, multiple methods are employed to better understand the effects of ion bombardment on these nuclear materials. This information was used to further the University of Wisconsin Inertial Electrostatic Confinement (UW-IEC) materials irradiation program's understanding and contribution to PFC candidates.

4.1 – Raman Spectroscopy

Raman Spectroscopy is a technique used to observe the vibrational, rotational and other low-frequency modes in materials [58]. The Raman effect is a non-destructive process which consists of illumination using monochromatic light as in Figure 4-1, from a laser with wavelength in the near-infrared to near-UV range, and the light interacts with molecular vibrations, phonons, and other excitations in the system without damaging its structure. Any interaction will result in a shift of the incident phonons, positive or negative, and is caused by the excitation and de-excitation of a vibrational mode, which gives us information about the system. When the incident light shines on the surface, it excites an electron from a full state in its valence band to a higher-energy empty state and this excited electron interacts with a phonon, reducing or increasing its energy by the amount needed to either excite or de-excite the phonon mode as shown in Figure 4-2.

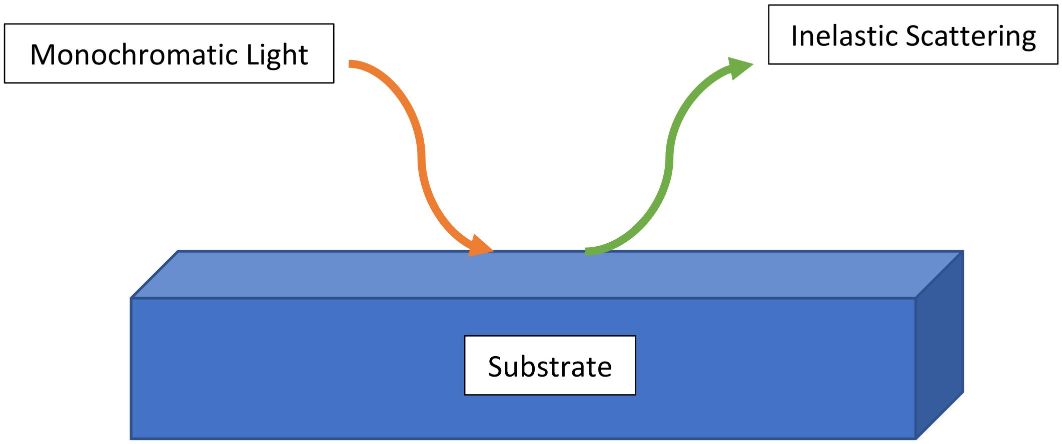

Figure 4-1. Monochromatic light interacts with the sample and inelastically scatters by the energy of a vibrational phonon.

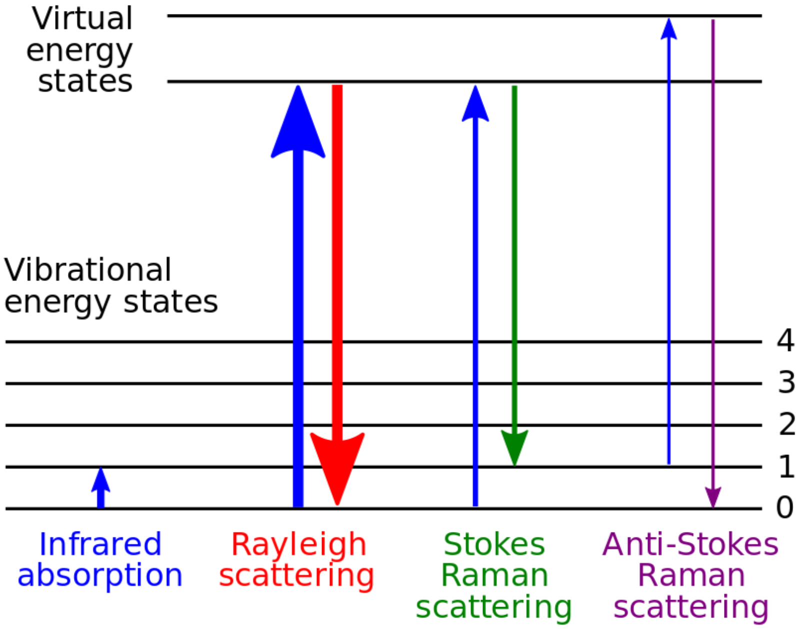

Figure 4-2. Energy level diagram showing the states involved in the Raman signal. The thicknesses of these lines are roughly proportional to the signal strength from the different transitions. Taken from Wikipedia.

These samples were analyzed on a DXR2 Thermo Scientific Raman microscope using a 532 nm wavelength laser. The settings for the instrument ranged from 7-10 mW of power with a 50x objective. Ten sites are probed multiple times with a 0.125-2 second exposure. Graphene quality is determined from the Raman shifts of the D band (~1350 cm^{-1}), G band (~1550 cm^{-1}) and 2D band (~2700 cm^{-1}), such as the sample spectra in Figure 2-2. In order to better understand the meaning of these bands, it is necessary to describe some of graphene's structure first.

4.1.1 – Graphene Crystal Structure

Because it is a 2D material, graphene's crystal structure is not considered a Bravais lattice, but rather it is called a honeycomb lattice, with 3 sp^2 orbitals angled at 120° from each other. Figure 4-3 shows the honeycomb lattice and its reciprocal lattice [136].

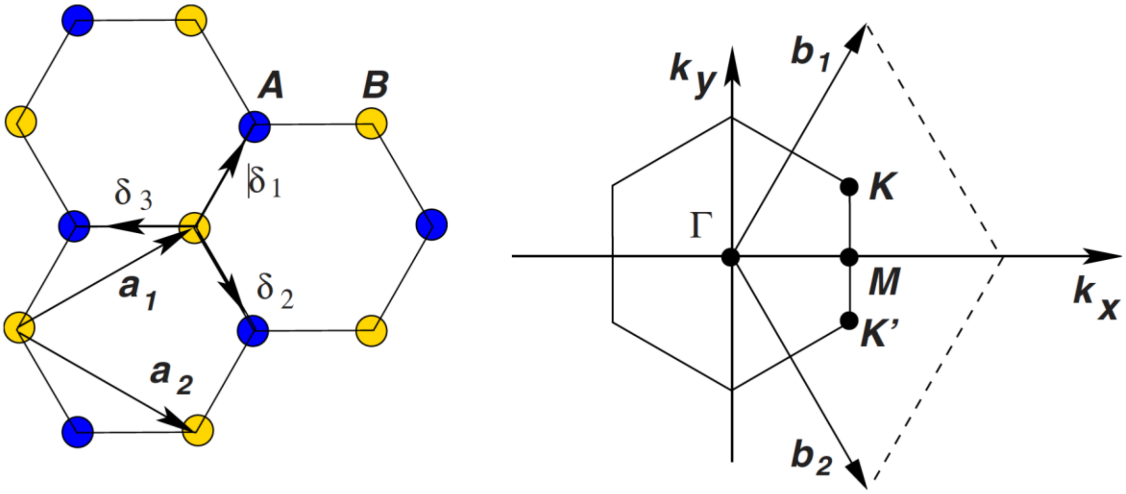

Figure 4-3. Honeycomb lattice and its Brillouin zone. Left: lattice structure of graphene, made out of two interpenetrating triangular lattices ($\mathbf{a}_1$ and $\mathbf{a}_2$ are the lattice unit vectors, and δ_i, i=1,2,3 are the nearest-neighbor vectors). Right: corresponding Brillouin zone. The Dirac cones are located at the K and K' points [134].

Its structure is seen as a triangular lattice with a basis of two atoms per unit cell where its vectors are written as:

$$\boldsymbol{a}_1 = \frac{a}{2}\left(3, \sqrt{3}\right) \qquad \boldsymbol{a}_2 = \frac{a}{2}\left(3, -\sqrt{3}\right)$$

where $a \approx 1.42$ Å is the distance between carbon atoms. The reciprocal lattice vectors are:

$$\boldsymbol{b}_1 = \frac{2\pi}{3a}\left(1, \sqrt{3}\right) \qquad \boldsymbol{b}_2 = \frac{2\pi}{3a}\left(1, -\sqrt{3}\right)$$

The two Dirac points are important because the conduction and valence bands meet at them, granting graphene its zero bandgap. These originate at Γ (see Figure 4-3) and are located at:

$$\boldsymbol{K} = \left(\frac{2\pi}{3a}, \frac{2\pi}{2\sqrt{3}a}\right) \qquad \boldsymbol{K'} = \left(\frac{2\pi}{3a}, -\frac{2\pi}{3\sqrt{3}a}\right)$$

Meanwhile, the three nearest neighbors to K in real space are given by:

$$\boldsymbol{\delta}_1 = \frac{a}{2}\left(1, \sqrt{3}\right) \qquad \boldsymbol{\delta}_2 = \frac{a}{2}\left(1, -\sqrt{3}\right) \qquad \boldsymbol{\delta}_3 = -a(1,0)$$

These can be used to find the area of the unit cell with the modulus of the lattice vectors, equating all to an area of 0.051 nm^2. With the number of atoms per unit area and knowing that there are two atoms per unit cell, the density of atoms in graphene is,

$$n_G = \frac{2}{A_{unit}} = \frac{2}{0.051\, nm^2} = 39\, nm^{-2} = 3.9 \times 10^{15}\, cm^{-2}$$

4.1.2 – The D Band

Whenever there are defects in the lattice, this corresponds to an increase in the D band. This is a one-phonon resonance mode that comes from the second order Raman Scattering process, which involves K and K' and involves the scattering of an in plane transversal optical mode (iTO) phonons and a crystal defect. Initially, an electron around the K point is elastically scattered by some defect to a point near K' via a process called the inter-valley mechanism [137]. This shifts the band towards a higher or lower Raman wavelength, indicating the disorder in the crystal. The ratio of this band to the G band can give an estimate of the crystal damage in the graphene.

4.1.3 – The G Band

Graphene's G band comes from a single-resonance process with double degeneracy in the plane transversal optical (iTO) mode phonons as well as lateral optical (LO) mode phonons at the Brillouin zone center Γ. It is the only band coming from a normal first order Raman scattering process in graphene.

4.1.4 – The 2D Band

Graphene's 2D band gets its name because it is located approximately at twice the D band frequency ($\omega_{2D} = 2\omega_D$). It originates from a second order process involving two iTO phonons near the K point through a double resonance scattering process. Unlike the D band, this one is allowed in the second order Raman spectra of graphene without any disorder or defects in its lattice because it replaces the crystal defect which is involved in the D band with another phonon. With this band we can determine the number of layers of graphene in the area measured through the ratio of the height of this band to the G band [58,136], with $I_D/I_G \sim 2$ corresponding to single layer graphene, and $I_D/I_G \sim 1$ to bilayer graphene.

4.1.5 – Amorphization Theory of Graphitic Materials

To recall, whenever the term “damage ratio” is mentioned, it refers to the intensity ratio between the D and G bands of graphene’s Raman spectrum (I_D/I_G). These are derived from different carbon motions in the atomic level as seen in Figure 4-4. The G mode takes into account the in-plane bond-stretching motion of pairs of C sp^2 atoms and does not require the presence of six-fold carbon rings, and therefore occurs at all sp^2 sites [138]. The D peak is a breathing mode of the carbon symmetry and only becomes active in the presence of disorder. Due to the nature of this mode, any defect site contributes to one breathing mode for each of its three neighbors. This can be used as an estimate of defect concentrations in the sheet.

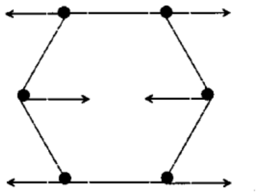

A) E_{2g} G Mode

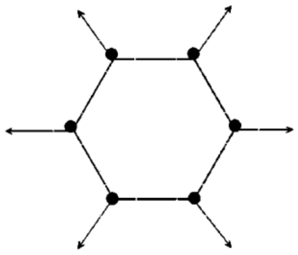

B) A_{1g} D breathing mode

Figure 4-4. Carbon motions in the (A) G and (B) D modes. Note that the G mode is just due to the relative motion of sp^2 carbon atoms and can be found in chains as well [138].

The description of graphene's state will be loosely based on a phenomenological three-stage model called "Amorphization trajectory" (Figure 4-5) developed by Ferrari and Robertson [138]. The model considers introduction of defects such as hybridization and different types of disorders, ignoring hydrogen bonds since they don't significantly affect the G or D peaks and assumes the Raman spectrum depends on (1) clustering of the sp^2 phase, (2) bond disorder, (3) presence of sp^2 rings and (4) the sp^2/sp^3 ratio.

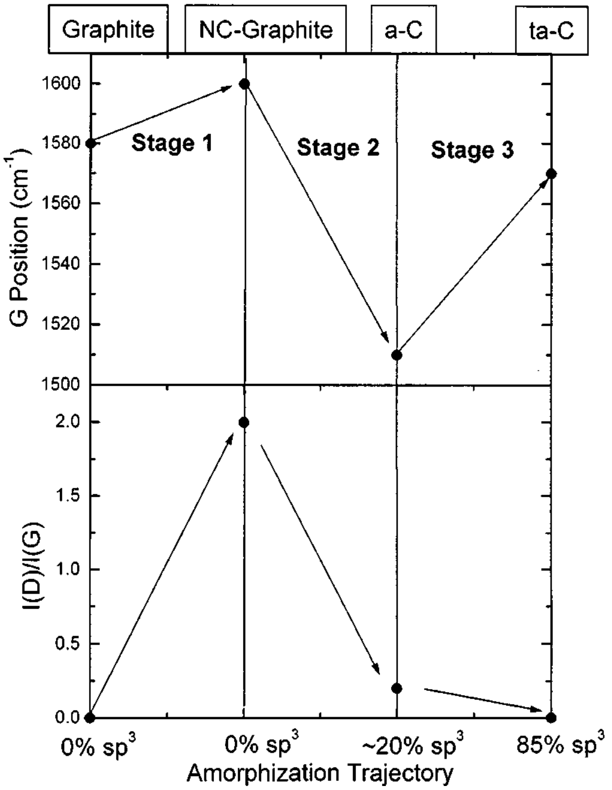

Figure 4-5. Amorphization trajectory, showing a schematic variation of the G position and I(D)/I(G) ratio. The three stages range from graphite to nanocrystalline graphite (NC-G), nanocrystalline graphite to amorphous carbon (a-C) and amorphous carbon to diamond (ta-C) [138].

Lastly, one parameter other parameter for Raman characterization is the cluster diameter or in plane correlation length (L_a), which describes the cluster size of sp^2 bonds of the graphene structures. The main consequence of the Raman spectrum is that the origin from the D peak comes from disorder in the aromatic rings (C-C, C=C). The D peak is dispersive, and therefore we assume a fixed wavelength λ on the nanocrystalline structure, the I_D/I_G ratio will increase with disorder, and as this grows, the ring clusters decrease in number, become smaller and more distorted until they eventually spread out. Because the G peak is related to the sp^2 motion of the carbon atoms, the D peak will now decrease, and a different cluster regime is attained for amorphous carbon. Figure 4-6 shows the transition across these two regimes as a function of the cluster diameters of the six-fold rings.

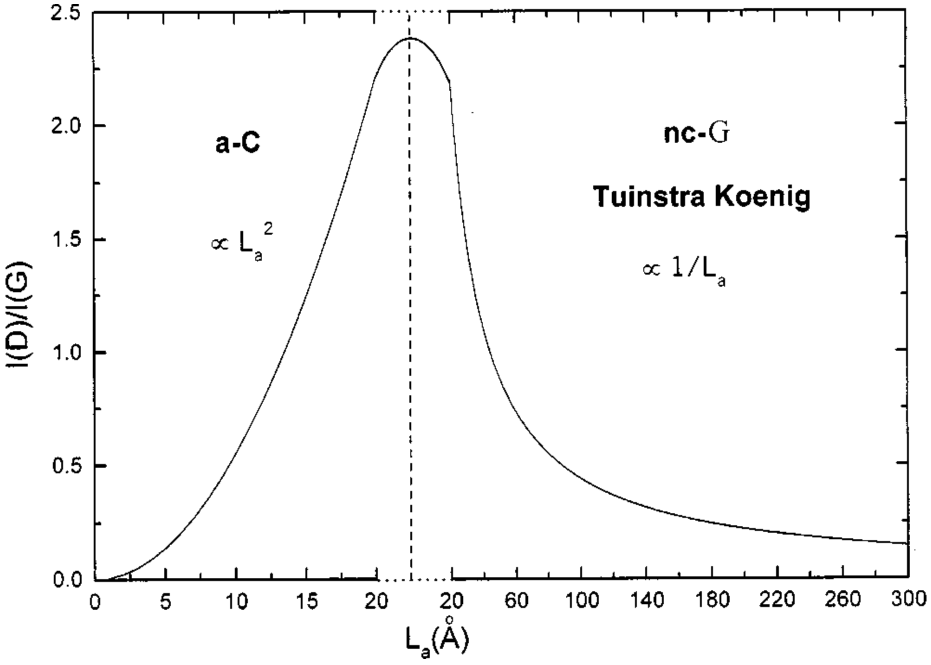

Figure 4-6. Variation of the I(D)/I(G) ratio with the in-plane correlation length, L_a. The broad transition between the two regimes is indicated [138].

While the model still describes the disorder and transformation of the hybridization in graphene structures, more recent results [155-156] have demonstrated that graphene behaves somewhat differently as a function of correlation length. The original model relies on a monotonic increase of the defect ratio, and in the case of ion irradiation, graphene exhibits three different removal regimes (Figure 4-7). In the first regime, for large in-plane correlation lengths (L_D), (L_D

= L_A from the Tuinstra-Koenig model), single vacancies are produced, leading to disorder in the lattice and increasing the D peak intensity while the G peak remains constant, increasing the defect ratio. Once the graphene has been severely damaged, the model moves for graphene sputtering proceeds to the second regime. Here, as more carbon atoms get removed from the graphene, the hexagonal lattice is destroyed and the radial breathing mode, or D peak, decreases. This is due to the multiple smaller islands of intact benzene rings, leaving a much smaller membrane comprised of sp^2 amorphous carbon chains. The last regime in the model shows a sharp decrease in damage ratio. Here, the remaining loose network of carbon atoms is removed slowly as it is being irradiated, without significant changes in the bond structure (sp^2 or sp^3) until all the atoms are removed.

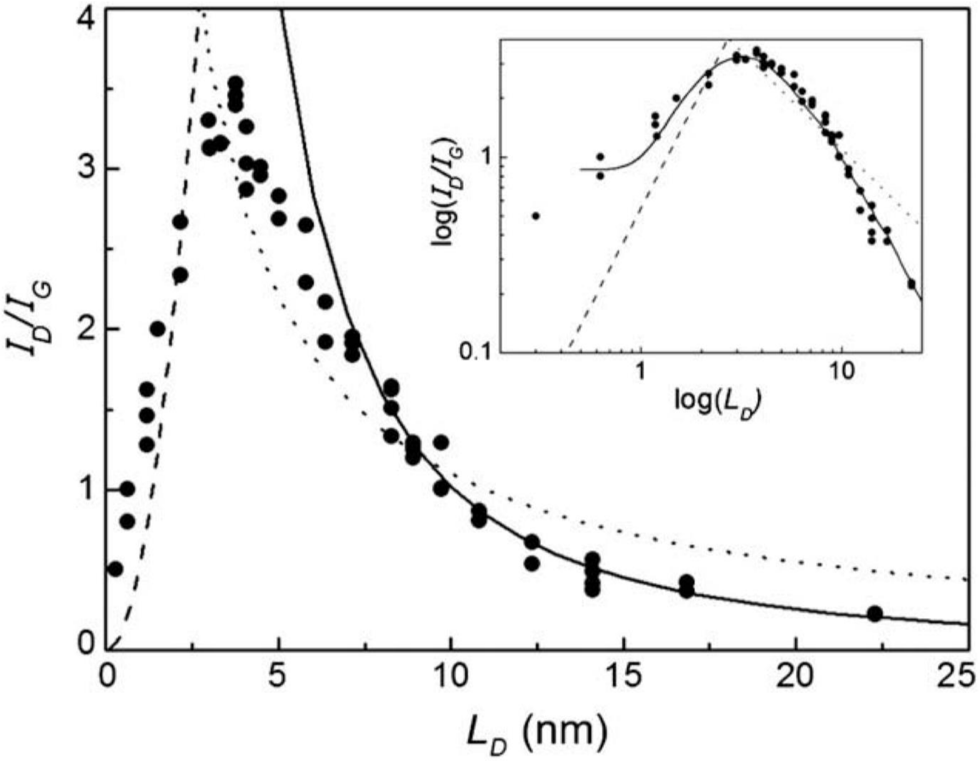

Figure 4-7. Comparison of the I_D/I_G data points with the amorphization trajectory proposed by Ferrari and Robertson [140].

Some studies have even gone as far as using this correlation length to determine the defect density [34] for the membrane. This behavior of the damage ratio holds for different exposure conditions and ion species used for irradiating graphene membranes [34,155-156].

4.2 – X-Ray Photoelectron Spectroscopy

X-Ray Photoelectron Spectroscopy (XPS) is a popular surface analysis technique due to its accessibility and simplicity of use. It is used for analyzing the surface chemistry of materials as well as being able to measure the elemental composition and valence state of the elements at or near the surface of a material. XPS relies on the photoelectric effect, which produces free electrons and other carriers when light interacts with a material. The spectrum is then formed by measuring the electron current emitted from the surface as a function of their kinetic energy. By using the intensities of these peaks, it is possible to identify and quantify all the surface elements with the exception of hydrogen and helium.

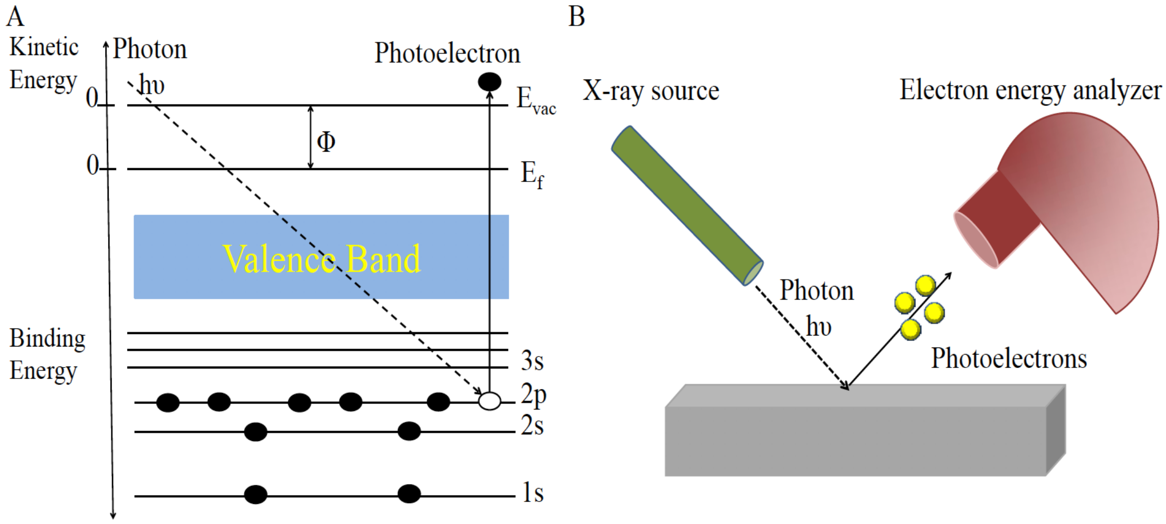

Figure 4-8. X-ray photoelectron spectroscopy. (A) A photon from and x-ray source interacts with the sample, where electrons are ejected from the core of the material with a kinetic energy (K.E.) =hv-(binding energy + Φ_{sample}*) and the spectrometer will measure a binding energy (B.E.) = hv – (K.E.+* $\Phi_{spectrometer}$*). (B) XPS experiment setup diagram showing the main components of the system. Photons are directed from the x-ray source on to the sample, followed by ejections of electrons with a given kinetic energy entering the electron energy analyzer. The electron analyzer directs the electrons (with a distinctive K.E.) from the entry area following a semicircular path to the end of the analyzer where a target counts the electrons completing the distance by adjusting an electric field in the path (pass energy)* [141].

Data for these samples were taken in a Thermo Scientific K-Alpha instrument using an Al Kα over a range of 0-1400 eV energies. The analyzer pass energy was set to 50 eV, for a step size of 0.82 eV, and 20 scans were taken per sample on 3 separate regions. These were then analyzed using the *AVANTAGE™* software.

4.3 – X-Ray Diffraction

This technique relies on the interactions of the x-ray beam and the crystal lattices and are all based on Bragg's law. If we consider a crystalline material made up of many crystals, the many planes of atoms cause constructive and destructive interference patterns by diffraction. This interference depends on the inter-planar spacing *d*, and the wavelength of the x-rays λ.

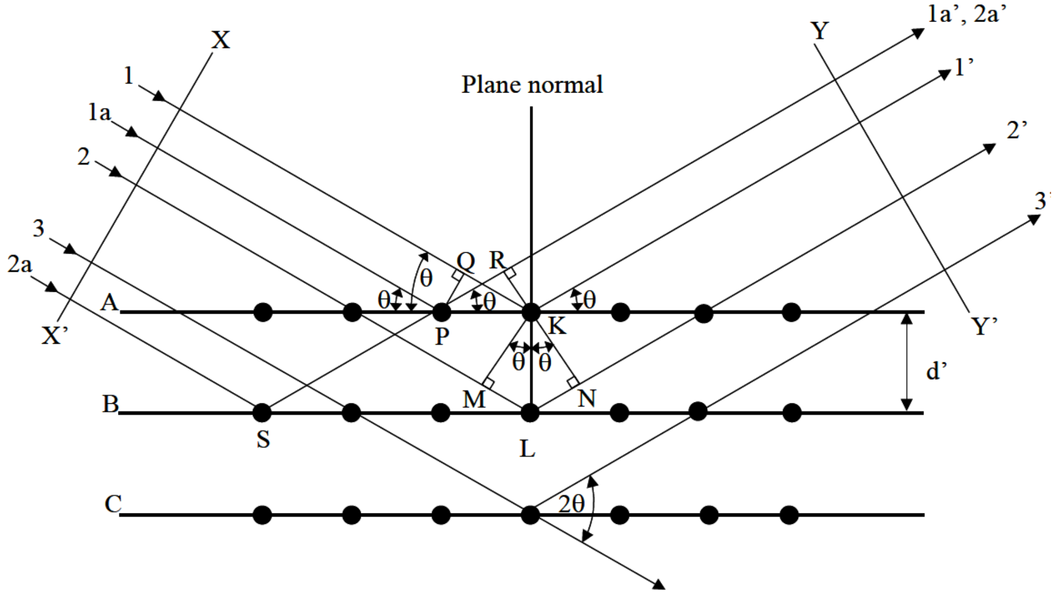

Figure 4-9. Diffraction of X-rays by a crystal lattice [142].

In Figure 4-9, rays 1 and 1a strike atoms K and P in the first plane and are scattered in all directions, but the only ones in phase are 1a' and 1, and they interfere constructively. This kind of interference occurs because the difference in path length between the wave fronts XX' and YY' is equal to zero, or

$$QK - PR = PK\cos\theta - PK\cos\theta = 0$$

Any other rays scattered that are parallel to 1' will also be in phase and their contributions are added to the diffracted beam, increasing the intensity. Now, in order for constructive interference to occur by rays scattered by atoms in different planes the rays 1 and 2 scattered by K and L are considered. The path difference for 1K1' and 2L2' is,

$$ML + LN = d'\sin\theta + d'\sin\theta = 2d'\sin\theta$$

Therefore, the scattered rays 1’ and 2’ will be in phase only if their path difference is equal to a whole number n of wavelengths, well known as Bragg’s Law:

$$n\lambda = 2d' \sin\theta$$

4.3.1 – Residual Strain Measurements

The specimens for this measurement are placed on an X-ray diffractometer and exposed to a beam to cause diffraction patterns (in the case of tungsten, at a diffraction angle close to normal to the surface, ~130°). Many studies have shown the relationship between diffraction patterns and atomic plane separation of a material [143–145]. When the material is strained, compression or tension in the lattice will change the interplanar spacing, which in turn shifts the diffraction pattern. By precisely measuring the shift, the strain in the material can be determined.

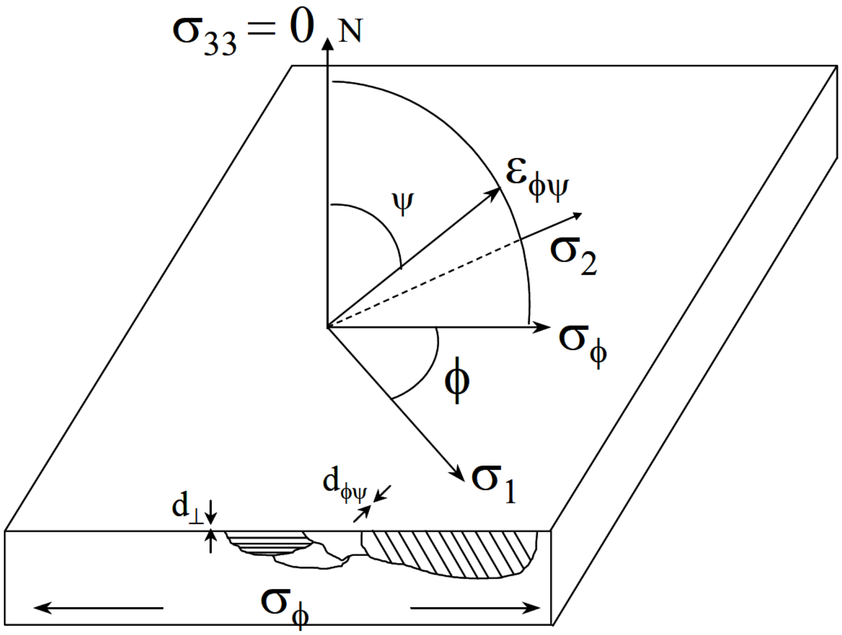

Figure 4-10. Schematic showing diffraction planes parallel to the surface and at an angle $\phi\psi$. Note σ_1 and σ_2 both lie in the plane of the specimen surface [140].

The derivation involved with the residual stress measurement requires knowledge of elasticity theory and can be found in numerous papers [142,146]. It is possible to evaluate the engineering stresses in any chosen direction from the inter-planar spacings determined from two measurements, made in a plane normal to the surface (ψ) and containing the direction of the stress to be measured (ϕ). The most commonly used method is the $\sin^2\psi$ method, in which XRD measurements are made at different psi tilts (as seen in Figure 4-10) and the inter-planar spacing (d) or 2-theta (2θ) peak position is extracted and potted as a function of $\sin^2\psi$. The stress is then found by determining the gradient of the line, knowing the elastic properties of the materials:

$$\sigma_\phi = \left(\frac{E}{1+\nu}\right) m$$

where m is the slope of the curve, E is the elastic modulus of the material and ν is its Poisson ratio. Different ϕ measurements are taken (0°, 45° and 90°) in order to determine if the material is similar in all directions (biaxial stress state). Otherwise, a different approach must be used to accurately determine the residual stresses in the lattice.

4.4 – Scanning Electron Microscopy

Scanning Electron Microscopes (SEM) uses a Schottky field-emission electron source, with a beam of electrons capable of achieving energies from 1 keV-30 keV, and few energies below 1 keV. These contain three types of detectors, a secondary electron detector, an in-lens detector and a backscatter detector. Each of these collect a different portion of the electrons emitted from the sample surface, achieving different types of images and information. When the energetic primary electrons hit the surface, three processes happen, leading to emission:

1) Primary electrons are elastically scattered from the surface and return at the same energy as when they entered. The probability of this occurring decreases with distance traveled into the material, and therefore measured full-energy electrons mostly occur from the near surface.
2) Primary electrons penetrate into the material, have inelastic scattering events and return out of the sample with less energy than when they started.
3) Primary electrons knock out an electron that was in a bound state, and if this electron escapes successfully from the surface, it is called a secondary electron. These have much lower energies than any of the other events, so they are more likely to escape from the near surface. Their yield also depends on the material, since some are more likely to emit secondaries with high energy primary electrons, which leads to a higher or lower materials contrast, as shown in Figure 4-11.

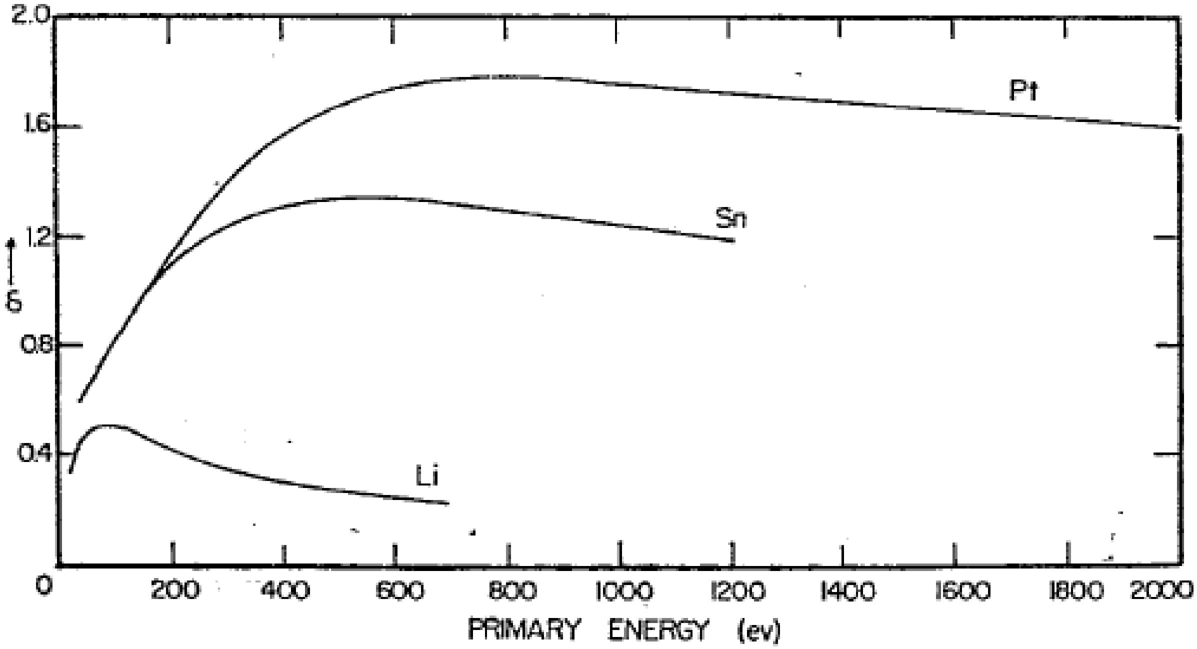

Figure 4-11. Secondary electron yield versus primary electron energy (incident beam energy) for three different metals [147].

These three types of emitted electrons (elastically scattered, backscattered and secondaries) will always be present in an SEM. The yield of these electrons is plotted in Figure 4-12 as a function of energy. This figure shows that elastically scattered electrons have energy equal to the energy of the primary beam of electrons, secondary electrons are at much lower and backscattered are in between both as demonstrated in Figure 4-12. It is with this understanding that we can choose the appropriate SEM detector to generate images. This study will not focus on the InLens detector (used for detecting elastically scattered electrons) due to its low information on material contrast and will not be useful in studying the effect of graphene on secondary electrons later on. The backscattered electron detector is not used either because it focuses mostly on high energy electrons in the near surface region, and the interest of this work is focused in the secondary emission.

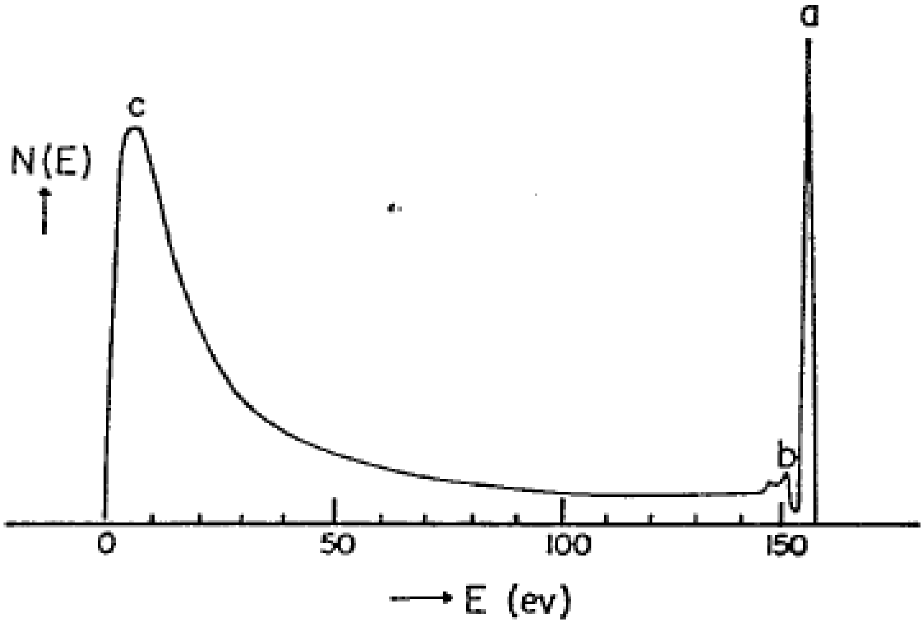

Figure 4-12. Yield of emitted electrons versus their kinetic energy for a 155 eV primary beam (incident beam) energy on a silver target. (a) Elastically scattered electrons emitted near the primary beam energy. (b) Between regions a and c are the backscattered electrons which have had inelastic collisions in the sample and lost some energy. (c) True secondary electrons originate from bound states in the material and are emitted at low energy [147].

The SE2 detector takes advantage of electrons being emitted at different energies. It has a grid in front of it that can be biased from +400 V down to -250 V. For an SEM, the primary electron energy is typically 3 keV for imaging, and although Figure 4-12 shows the trend for a primary energy of 155 eV, the trend would still be the same. Therefore, for a bias of -250 V all the secondary electrons would be turned away from the SE2 detector and only higher energy backscattered electrons would be collected, and at +400 V, all the electrons emitted from the sample will be attracted to the detector, and it will collect electrons with all kinds of kinetic energies. The bias used for the SEM in this study was +300 V, meaning that it will still attract all types of electrons as well, which will become significant as we go down in primary electron energies, where we will see graphene's effect on substrate emission.

4.5 – Microbalance

Because there is material being sputtered off in plasma-facing components, these could lead to disruptions in the plasma. This work is interested in measuring if the graphene coating reduces sputtering of material from the surface, and these mass losses are measured with a Sartorius Micro Balance CPA26P. This balance has an error of $\pm 2 \times 10^{-6}$g. The samples were all measured 5 times, with a minute between measurements for equilibration of the scale. From this, the standard deviation can be used for the error of the measurements.

This page is intentionally left blank.

Chapter 5 – The LUNA Experiment

To better understand the functionality of the linear inertial-electrostatic confinement (IEC) experiment LUNA, we first need a better understanding of the physics in an IEC fusion device and high voltage engineering. During an IEC discharge, particles become ionized, get accelerated, and collide with the background gas molecules each other, sometimes resulting in fusion reactions. Different processes occur throughout deuterium particle trajectories, including charge exchange, ion impact ionization and molecular dissociation. In order to predict the results of these processes and the neutron rates corresponding to them, the VICTER code was written [120-121] to account for the spatial and energy distribution of ions throughout the IEC device. Lastly, the construction of the LUNA experiment, which was created to explore the physics of linear IEC device operation, will be discussed as well as some results of the operation of the device.

5.1 – Inertial Electrostatic Confinement Theory

Most Inertial Electrostatic Confinement (IEC) devices used at the University of Wisconsin-Madison operate by ionizing a gas, usually deuterium, and accelerating the ions radially inwards through the use of electric fields between concentric spherical grids. Cathodes are biased to a high negative voltage and the outer larger anode is grounded. These grids are typically 92-96% transparent to ion and electron flow, and it is this property that allows the ions to travel multiple trajectories until they are neutralized, lost to the grid wires or the walls, or collide with another particle and generate a fusion reaction. A schematic of a typical spherical IEC device is shown in Figure 5-1 and that of a linear IEC device is shown in Figure 5-2.

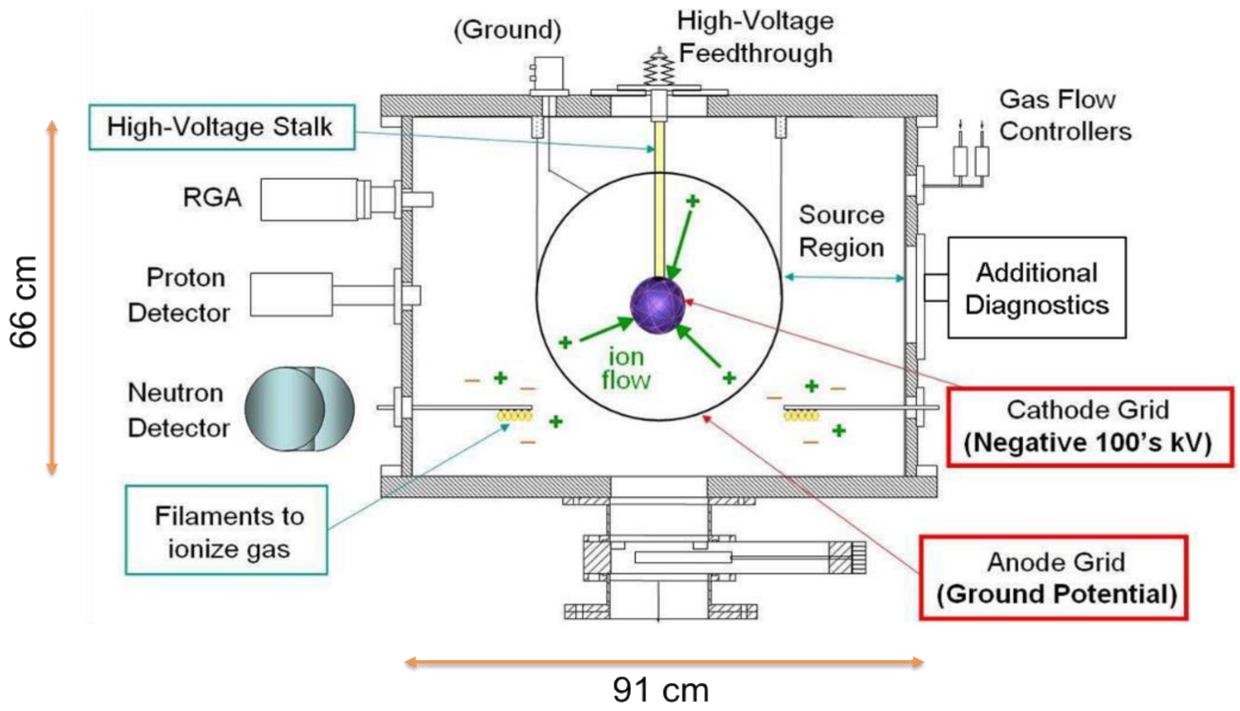

Figure 5-1. Schematic of the UW IEC HOMER device and several diagnostic capabilities at the University of Wisconsin-Madison.

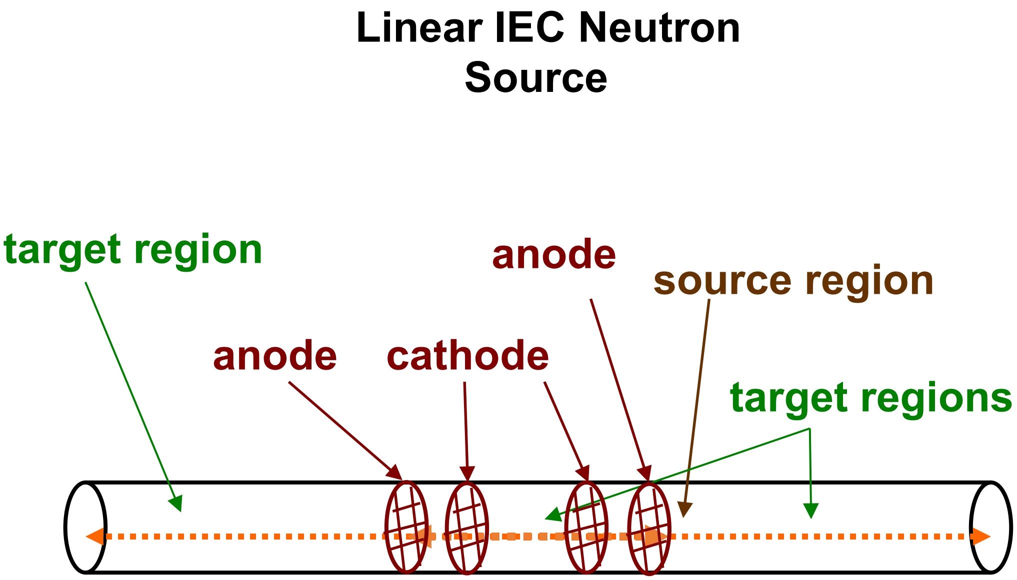

Figure 5-2. Schematic of UW IEC LUNA device depicting the different regions and components at the University of Wisconsin-Madison.

One can use Poisson’s equation to solve for the vacuum potential in an IEC device for any geometry. A standard spherical IEC device has the following potential, with r_a and r_c represent the anode and cathode radii respectively, and V_c is the cathode voltage:

$$\phi(r) = \begin{cases} -V_c & (r < r_c) \\ -\frac{r_c}{r_a - r_c}\left(\frac{r_a}{r} - 1\right) V_c & (r_c < r < r_a) \\ 0 & (r > r_a) \end{cases} \qquad (5-1)$$

For a linear IEC device, the vacuum potential is linear:

$$\phi(r) = \begin{cases} -V_c & (0 < r < r_c) \\ -\left(\frac{r - r_a}{r_c - r_a}\right) V_c & (r_c < r < r_a) \\ 0 & (r > r_a) \end{cases} \qquad (5-2)$$

The electric field is therefore found by taking the gradient of these potentials and as such,

$$\boldsymbol{E}(r) = \begin{cases} \frac{r_a r_c}{(r_a - r_c) r^2} V_c \, \hat{e}_r & (r_c < r < r_a) \\ 0 & (r < r_c, r > r_a) \end{cases} \quad (Spherical) \qquad (5-3)$$

$$\boldsymbol{E}(r) = \begin{cases} \frac{1}{(r_a - r_c)} V_c \, \hat{e}_r & (r_c < r < r_a) \\ 0 & (r < r_c, r > r_a) \end{cases} \quad (Linear) \qquad (5-4)$$

The main feature here being that the electric field is constant for a linear configuration and varies as $1/r^2$ for a spherical configuration. For planar electrodes aligned in a linear configuration, edge effects begin to become significant when the anode-cathode separation approximately equals the electrode dimensions in the transverse direction.

5.1.1 – Fusion Reaction Regimes in IEC Devices

Nuclear fusion can be achieved with different fuels, but in order for this to occur, the two reacting particles need to have sufficient kinetic energy to overcome the Coulomb forces. IEC devices enable this process by having the ions move into a large electrostatic potential difference (well), held between the anode and cathode grids, capable of generating ion energies up to hundreds of keV, and fusion of those ions with background gas emits high energy fusion products. The probability of these reactions occurring is described by fusion cross sections, which vary with the center of mass energies between colliding particles as well as the type of particle, illustrated in Figure 5-3.

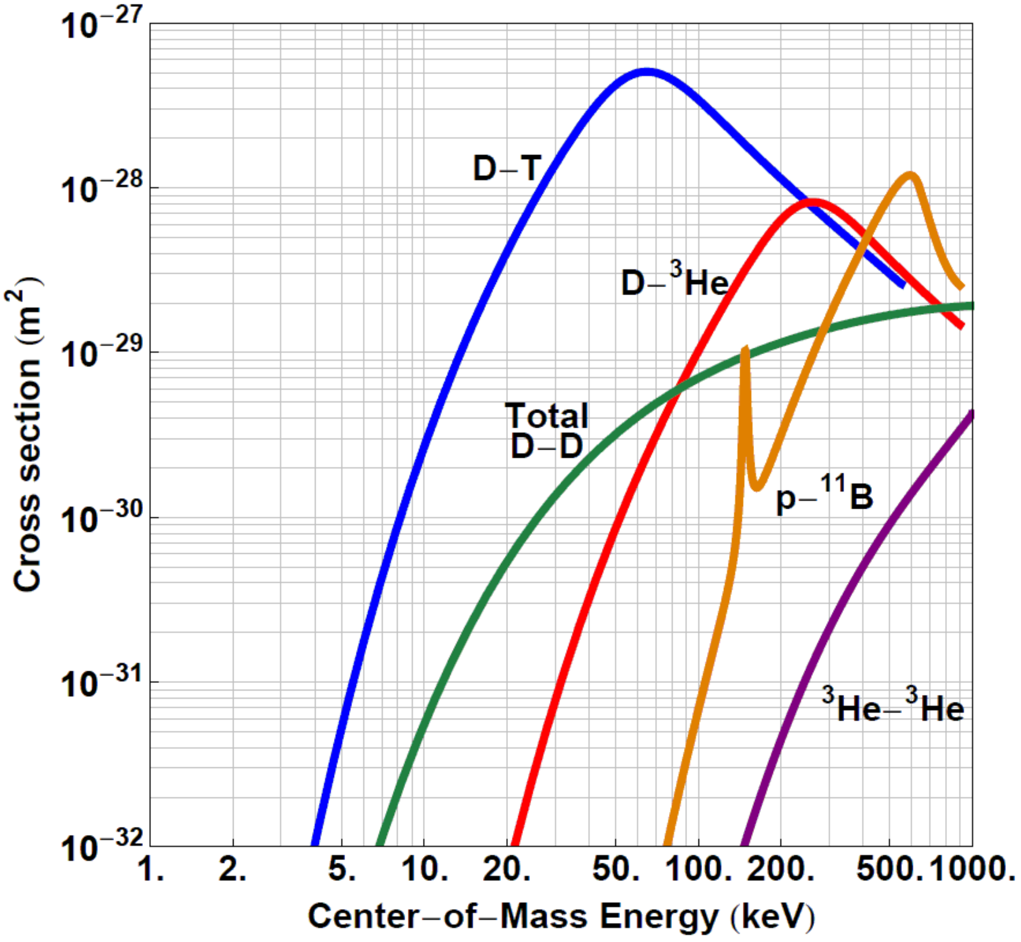

Figure 5-3. Center of Mass reaction cross-sections for fusion fuels of interest in an IEC device. Courtesy of J.F. Santarius.

The corresponding reactions are summarized in Table 5-1. These fuels are classified as first, second and third generation due to the input reaction energy needed as well as the low neutron production which could prove useful for advanced fusion energy concepts.

Table 5-1. Fusion fuel reactions of interest to IEC devices [148].

First Generation	$D + T \rightarrow {}^4He\ (3.52\ MeV) + n\ (14.07\ MeV)$ $D + D \rightarrow \begin{cases} {}^3He\ (0.82\ MeV) + n\ (2.45\ MeV) \\ T\ (1.01\ MeV) + p\ (3.02\ MeV) \end{cases}$
Second Generation	$D + {}^3He \rightarrow {}^4He\ (3.67\ MeV) + p\ (14.68\ MeV)$
Third Generation	${}^3He + {}^3He \rightarrow \begin{cases} {}^4He + 2p\ (12.86\ MeV\ total) \\ {}^5Li^{(g.s.)} + p \rightarrow \underbrace{{}^4He + p}_{(3.79\ MeV\ total)} + p\ (9.07\ MeV) \end{cases}$ $p + {}^{11}B \rightarrow 3\ {}^4He\ (8.68\ MeV\ total)$

The two reacting species fuse at a certain rate, called the reaction rate per unit volume R_{ij}, and it is different for every reaction. It is proportional to the density of both species (n_i, n_j), and the two properties extracted from Figure 5-3, the reaction cross section (σ_{ij}) and the velocity in the center of mass frame (v) which can be calculated from the center of mass energy. In the lab frame, for essentially stationary neutral gas targets, projectile-target cross sections can be calculated by translating into the center of mass frame; these cross sections are shown in Figure 5-4.

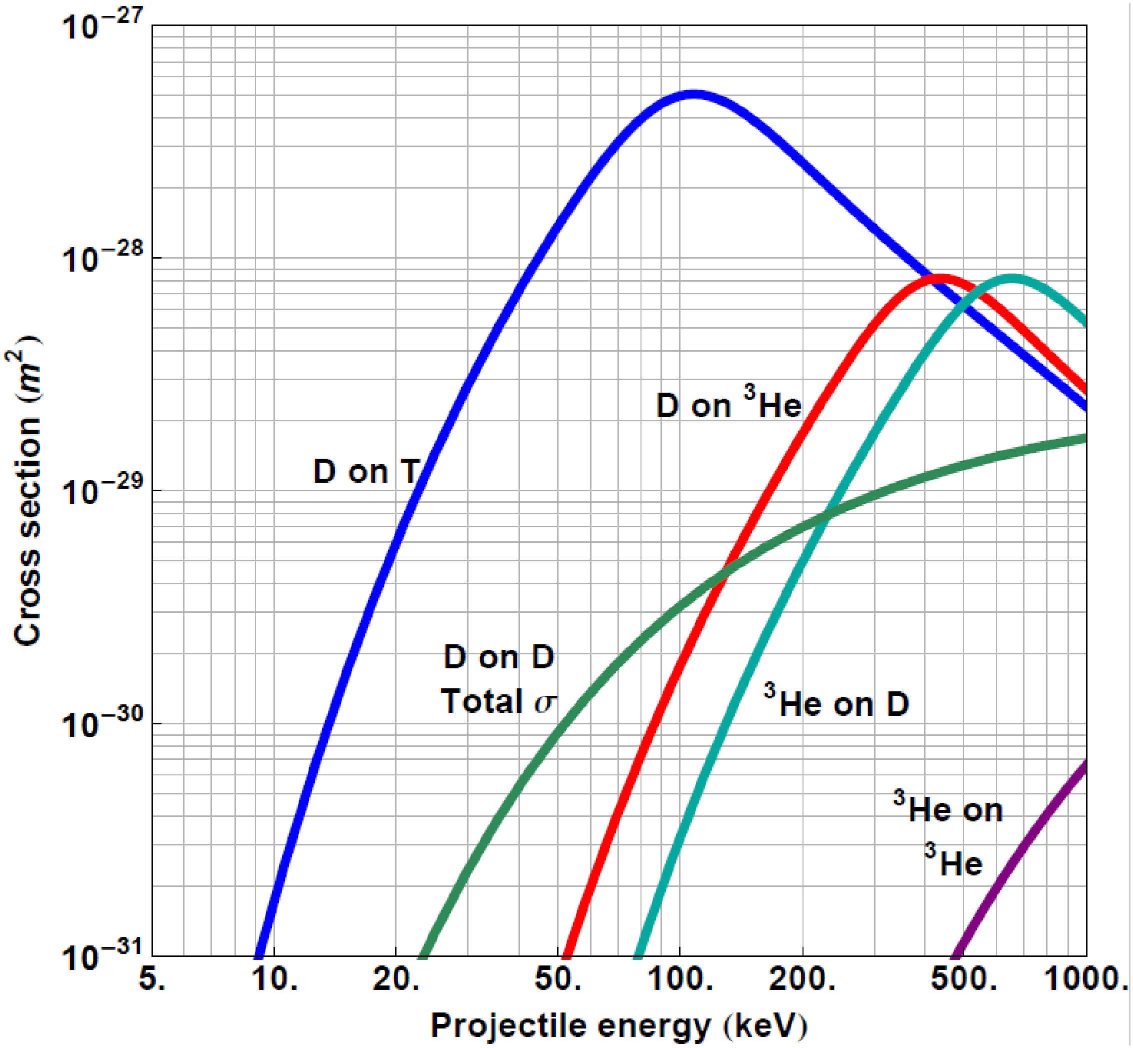

Figure 5-4. Projectile-target fusion cross-sections for fusion fuels of interest in an IEC device. Courtesy of J.F. Santarius.

The following formula gives the local relationship between these quantities, which in general must be weighted by the velocity distribution and the energy dependence of the fusion cross section. To calculate the total fusion production in a given device, the local reaction rate must be integrated also using the appropriate densities of the species.

$$R_{ij} = n_i n_j \sigma_{ij} v \qquad (5-5)$$

Because of the complicated orbits and processes occurring in IEC chambers, particles collide with each other in three main ways: beam-beam collisions, beam-background collisions, and beam-embedded collisions.

5.1.2 – Beam-Beam Fusion

These interactions between energetic particles are the ones with the highest available energy. This is because both particles involved are moving at high velocities towards each other, so their maximum center of mass (CM) energy, assuming deuterons colliding head-on, is $2E_{lab}$, which Figure 5-3 shows will give a very small fusion reaction rate increase compared to the effect of the background gas density being ~10^4 times larger than the deuteron "beam" density.

5.1.3 – Beam-Background Fusion

Due to the high background gas density in IEC systems, this is the dominant mode of operation of IEC devices at the University of Wisconsin-Madison and elsewhere. The center of mass energy available for fusion of the energetic particles can be calculated, approximating the energy of the background gas particles (< 1eV) as zero, to be

$$E_{COM} = \frac{m_i E_i + m_j E_j}{m_i + m_j} = \frac{m_i E_i + m_b(0)}{m_i + m_b} = \frac{m_i}{m_i + m_b} E_{Lab} \qquad (5-6)$$

where m_i is the beam ion mass and m_b is the background atom mass. One insight gained from this equation is that if we are only using one species to generate the discharge, the maximum center of mass energy is half of the laboratory energy, or the voltage set by the high voltage supply to the cathode.

Throughout the years, the IEC laboratory has been using neutron rates as a measure of the reaction rates as well as a way to gain insight on the particle interactions during discharges. For different operating regimes, one result has always been consistent, the scaling of neutron rates is proportional to the ion current. This suggests that while beam-beam interactions could still be taking place, most neutrons are generated by this type of reaction (beam-background fusion), and since the background particles essentially stationary (i.e. gas thermal energies are far below the 10s of keV energies to which the ions are accelerated and at which fast neutrals are created), the reaction rate can be rewritten as,

$$R_{beam-background} = n_b I_i \sigma_{b-i} v_{COM} = n_b I \sigma_{b-i} \sqrt{\frac{2E_{COM}}{M}} = n_b I \sigma_{b-i} \sqrt{\frac{2m_i E_{Lab}}{(m_i + m_b)^2}} \qquad (5-7)$$

thus, demonstrating the linear scaling with current I that we observe through neutron acquisition for fast particles colliding with background particles.

5.1.4 – Beam-Embedded Fusion

This type of interaction occurs because the fast particles are hitting chamber surfaces which over time have become loaded with trapped fuel. As the fast particles hit the surface they slow down, and their energy is reduced according to the stopping power relation for the wall material and the mean free path through the fuel particles. The reaction rate for this type of interaction is given by,

$$R_{embedded} = \int_0^{x_f} n_{embedded}(x) \phi_i \sigma_{ij}^{p-t} [E_P(x)]\, dx \qquad (5-8)$$

where the density of the embedded fuel particles can vary with penetration distance, $n_{embedded}(x)$, ϕ_i is the flux of the incoming energetic particles hitting the material wall, σ_{ij} is the projectile-target fusion reaction cross section which varies with the projectile energy $E_P(x)$, which in turn varies with depth since the particle loses energy as it interacts with charged particles during it traverse through the material. As seen in the SIGFE experiment [131], enough fuel can be stored in the chamber wall such that it will give rise to significant neutron production, and the origin of these particles arises from different molecular processes occurring in a plasma discharge.

5.2 – Atomic and Molecular Processes occurring in an IEC Device

While using deuterium for a fusion device is the most widely used fuel in current IEC devices, analysis of it comes with its set of obstacles due to the atomic and molecular processes occurring with the background gas. During such a plasma discharge, the deuterium molecules dissociate and give rise to fast neutral particles which are unconfined. Fast ions or neutrals can interact with background neutrals to give negative ions, which can shift the population distribution across the chamber. Source ions are referred to as first generation ions, and these are generated through electron impact ionization by electrons produced by voltage-biased, heated tungsten-rhenium wires. These ions drift throughout the ion source region between the anode and wall, and some of them cross the anode plan and are then accelerated by the electrostatic potential difference between the anode and cathode. As they traverse the space from anode to anode, they give rise to subsequent generations of ions that, if positive, are trapped within the potential. Deuterium can dissociate into multiple atomic and molecular species, and the multiple processes taking place with these particles are summarized in Table 5-2.

Table 5-2. Atomic and molecular processes in the formation of ions in the plasma source region external to the anode grid [149].

Process	Interaction
1. Ionization of D_2	$e+D_2 \rightarrow D_2^+ + 2e$
2. Dissociation of D_2	$e+D_2 \rightarrow 2D + e$
3. Ionization of D	$e+D \rightarrow D^+ + 2e$
4. Dissociation of D_2^+	$e+D_2^+ \rightarrow D^+ + D + e$
5. Dissociative ionization of D_2	$e+D_2 \rightarrow D^+ + D + 2e$
6. Dissociative recombination of D_2^+	$e+D_2^+ \rightarrow 2D$
7. Interchange reactions producing D_3^+ ions	$D_2 + D_2^+ \rightarrow D_3^+ + D$
8. Dissociative recombination of D_3^+ ions	$e+D_3^+ \rightarrow D_2 + D$

All these interactions result in redistributions of energy among between particle species. Fast neutrals, for example, are produced by charge exchange between fast ions and slow neutrals,

$$X^+(fast) + Y(slow) \rightarrow X(fast) + Y^+(slow) \qquad (5-9)$$

A fast ion interacts with a slow neutral and this creates a fast neutral and a slow ion. The fast neutrals can now be lost to the wall, because they are not confined by the potential structure. The slow ion created by the charge exchange reaction will be accelerated by the electrostatic potential but is trapped in the well until it collides with something else, recombines, or cascades down into creating multiple generations of ion species. All the different possibilities for the ions are summarized in Table 5-3.

Table 5-3. Fast deuterium ion interactions with the background gas by atomic or molecular collisions resulting in ion destruction, stationary ion formation, or fast ion species formation [123].

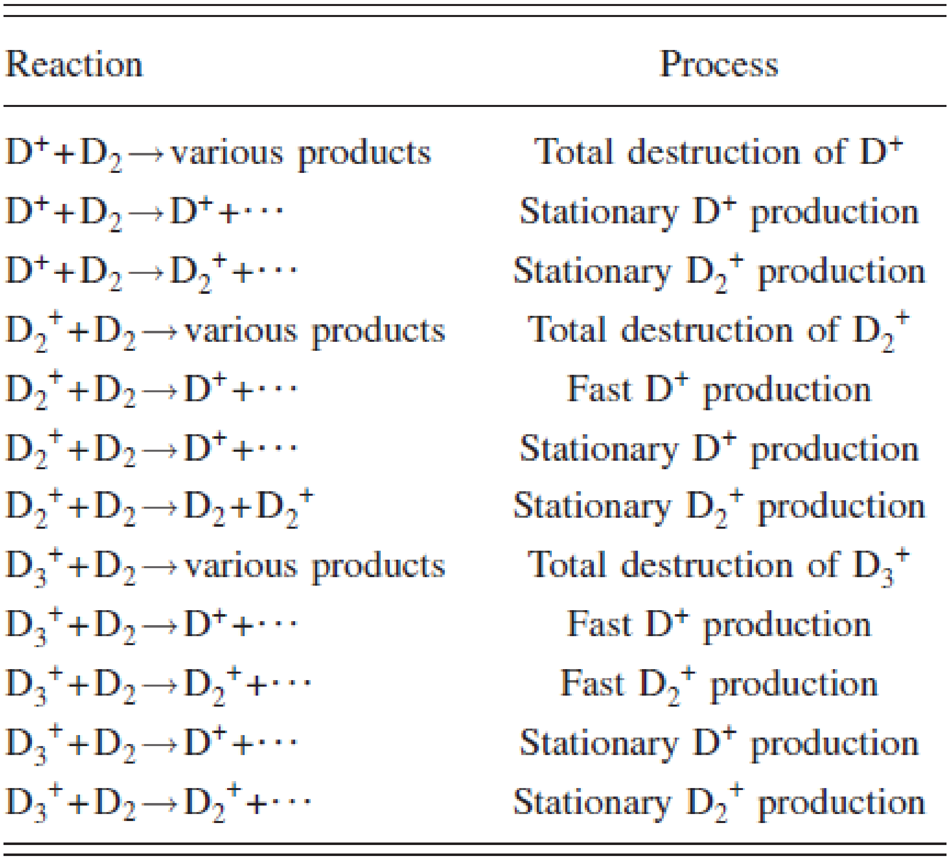

Reaction	Process
$D^+ + D_2 \rightarrow$ various products	Total destruction of D^+
$D^+ + D_2 \rightarrow D^+ + \cdots$	Stationary D^+ production
$D^+ + D_2 \rightarrow D_2^+ + \cdots$	Stationary D_2^+ production
$D_2^+ + D_2 \rightarrow$ various products	Total destruction of D_2^+
$D_2^+ + D_2 \rightarrow D^+ + \cdots$	Fast D^+ production
$D_2^+ + D_2 \rightarrow D^+ + \cdots$	Stationary D^+ production
$D_2^+ + D_2 \rightarrow D_2 + D_2^+$	Stationary D_2^+ production
$D_3^+ + D_2 \rightarrow$ various products	Total destruction of D_3^+
$D_3^+ + D_2 \rightarrow D^+ + \cdots$	Fast D^+ production
$D_3^+ + D_2 \rightarrow D_2^+ + \cdots$	Fast D_2^+ production
$D_3^+ + D_2 \rightarrow D^+ + \cdots$	Stationary D^+ production
$D_3^+ + D_2 \rightarrow D_2^+ + \cdots$	Stationary D_2^+ production

The subsequent ion generations can also be generated by stripping electrons from slow background molecules through electron or ion impact ionization. These electrons will be lost away from the cathode due to the large negative bias, and this has a high probability of occurring at higher energies due to the large reaction cross sections. Figure 5-5 summarizes the regions where these processes occur for a linear IEC device.

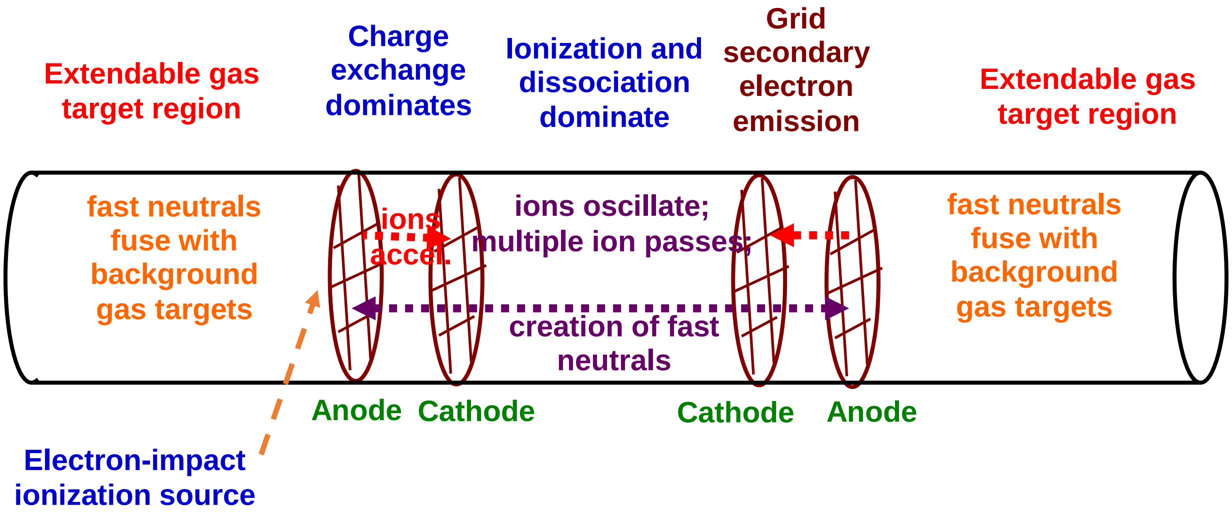

Figure 5-5. Regions of dominant atomic and molecular physics effects for a LINEAR IEC device.

These processes also give rise to negative ions which can contribute as much as 5% of the total ion current in the device [150]. Formation of this type of ion can occur from electron attachment or dissociation processes. Different molecular processes for negative ions are summarized in Table 5-4.

Table 5-4. Table of reactions involving the formation or destruction of negative ions [150].

Reaction	Process
$D + D_2 \rightarrow D^- + D^+ + D$	Dissociative
$D_2 + D_2 \rightarrow D^- + D^+ + D_2$	Dissociative
$D^+ + D_2 \rightarrow D^- + 2D^+$	Dissociative
$D_2^+ + D_2 \rightarrow D^- + 2D^+ + D$	Dissociative
$D_3^+ + D_2 \rightarrow D^- + 2D^+ + 2D$	Dissociative
$D_2 + e^- \rightarrow D_2^- \rightarrow D^- + D$	Electron attachment
$D^- + D_2 \rightarrow D + D_2 + e^-$	Electron stripping
$D^- + D_2 \rightarrow D^+ + D_2 + 2e^-$	Electron stripping

Insight into the neutron production is crucial to optimizing IEC devices, which is why the VICTER code (Section 5-3) was written and includes many of these molecular processes.

5.3 – VICTER Code

The Volterra Integral Code for Transport in Electrostatic Reactors (VICTER) was developed by Emmert and Santarius to model the different atomic and molecular processes taking place in IEC devices [123,151]. The code uses several definitions and assumptions to model the flow of ions through a background gas for multiple IEC geometries in 1D:

1) The geometry is treated as a spherical, cylindrical, or linear symmetric device.
2) The cathode is set at a radius a, anode at b, and wall at c, and the cathode and anode transparencies are set as T_C and T_a respectively.
3) The electrostatic potential is typically defined instead of solved self-consistently, although the Child-Langmuir electrostatic potential solution is implemented for use with high current operation, such as pulsed modes.
4) The cold neutral gas density n_g is uniform and only a single neutral species is considered with a charge $q = 1$ for the molecular version of the code that is used for deuterium.
5) The plasma is weakly ionized.
6) Elastic scattering between ions and the background gas is negligible.
7) The atomic and molecular processes occurring are those described in 0 for interactions between ions and the cold background gas. Fast neutrals are neutralized at the walls and ionization by ion impact imparts negligible momentum transfer to the ions involved.
8) Cold ions produced in the cathode region due to ionization and charge exchange are trapped and neutralized by the electrons created with them or by secondary electrons from ion impacts with the cathode.

The mix of first generation ions is also defined for D^+, D_2^+, and D_3^+ as 6%, 23% and 71% respectively [149]. The neutron rates are calculated from a set of equations that takes the form of a Volterra integral [120-121] when summed over an infinite number of radial passes:

$$S^1 = A^1 + \int_r^b K^{11} S^1 dr' + \int_r^b K^{12} S^2 dr' \qquad (5-10)$$

$$S^2 = A^2 + \int_r^b K^{21} S^1 dr' + \int_r^b K^{22} S^2 dr' \qquad (5-11)$$

The A terms in these equations include the first-generation ions which are born outside the anode radius, whereas the S term includes sources from subsequent ion generations which are generated within the anode region. In order to relate the source term from one location to the next one, the kernel, K, accounts for the various atomic and molecular reaction cross sections and energy loss mechanisms as the ions travel across the device. Solving these equations provides information on ion, anion, and electron currents, species lost to the walls, as well as neutron rates and spatial distribution. VICTER was used to estimate optimal parameters for operation.

5.4 – Construction of Linear IEC Device (LUNA)

5.4.1 – Experiment Setup

In order to optimize the neutron rates in a linear setup, the LUNA experiment was operated over a wide range of conditions. The setup is simple: a long cylindrical chamber with tungsten-rhenium cathodes and anodes along its axis, which allows for large charge exchange regions. Depending on the voltage, the fast, charge-exchange neutrals may dominate the fusion rate, in which case most of the fusion reaction will occur beyond the anodes in the target region. Figure

5-5 and Figure 5-6 highlight the main physics effects and the setup of the experiment. The regions between the anodes and cathodes shows the negatively falling potential that will accelerate the deuterium ions in the chamber. Between the anodes at each end of the acceleration region, some of these fast ions will go through different atomic and molecular processes and exit the region as fast neutrals.

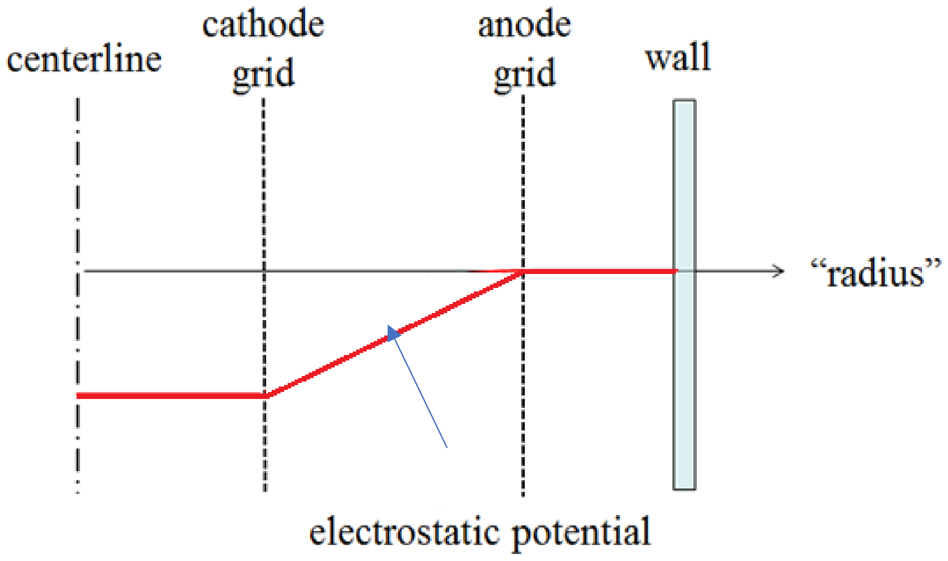

Figure 5-6. Half view of the electrostatic potential arrangement in the LUNA device as set up on the VICTER code.

These components translate into the LUNA device shown in Figure 5-7. It comprises (A) the cylindrical vacuum chamber, (B) an RV206 Kurt J. Lesker roughing pump, (C) a Pfeiffer TPU-1500 Turbopump, (D) a 100 kV rated High Voltage feedthrough, (E) a turbopump controller, (F) Pressure gauge monitors for both the foreline Convectron gauge and the chamber ionization pressure gauge, (G) Anodes, (H) Cathode, (I) and an electron filament supply at the top of the experiment.

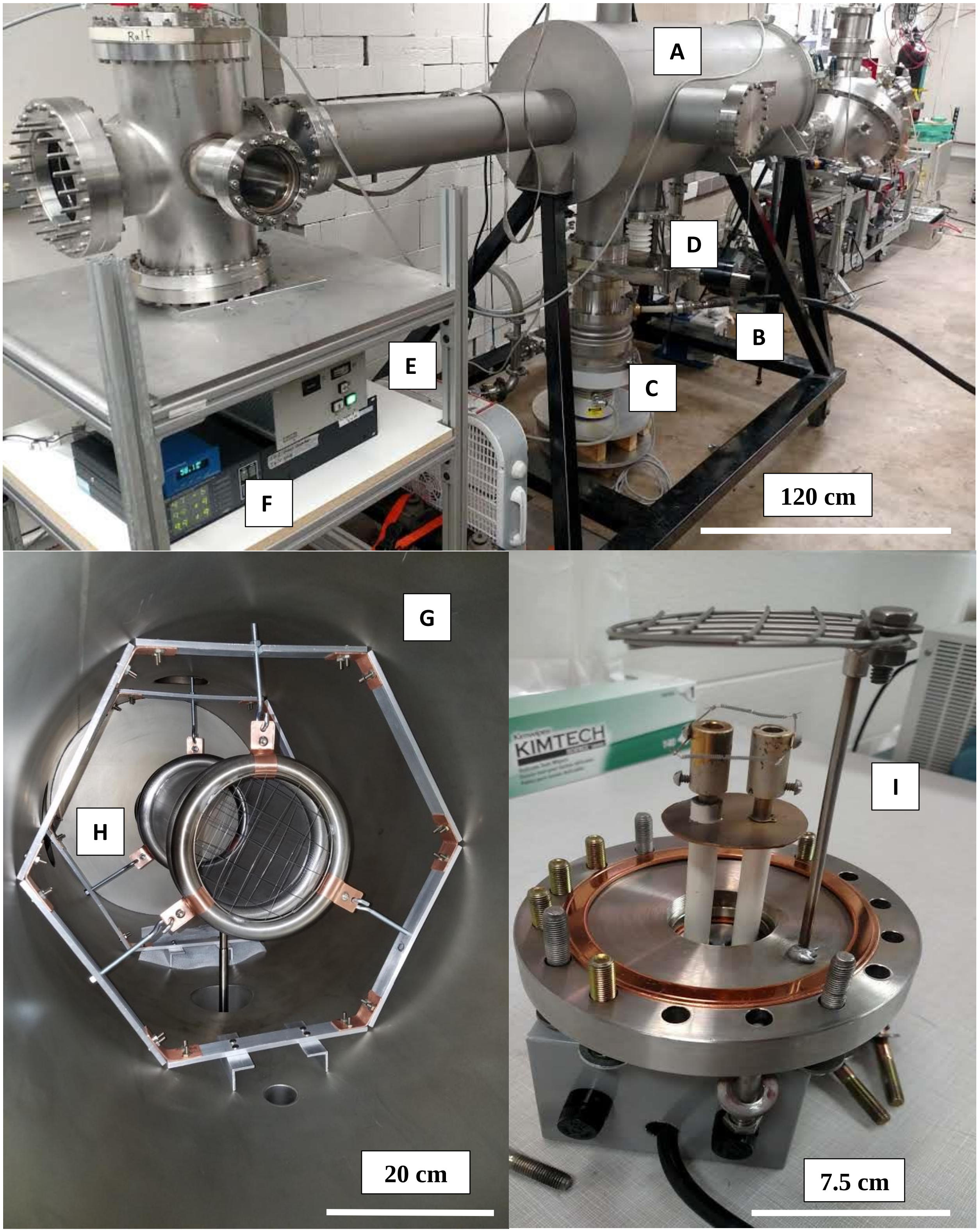

Figure 5-7. Major components of the LUNA Experiment: (A) cylindrical vacuum chamber, (B) roughing pump, (C) Turbopump, (D) High Voltage feedthrough, (E) turbopump controller, (F) Pressure gauge monitors, (G) Anodes, (H) Cathodes, and (I) an electron filament supply.

5.4.2 – High Voltage Feedthrough

The vacuum chamber was repurposed for LUNA and required a face seal O-ring design. After installing the original feedthrough design, the high thermal load due to the high voltage destroyed the vacuum seal causing the cathode to collapse but left the ceramic insulation intact. We manufactured a new 16.5 cm diameter flange and vacuum welded it to the feedthrough. The connection to the high voltage supply needed to be replaced for ease of access as well as to avoid edges that would cause the system to arc to the turbopump due to its close proximity. In order to achieve this, a 5 cm diameter bronze sphere was manufactured, shown in Figure 5-8.

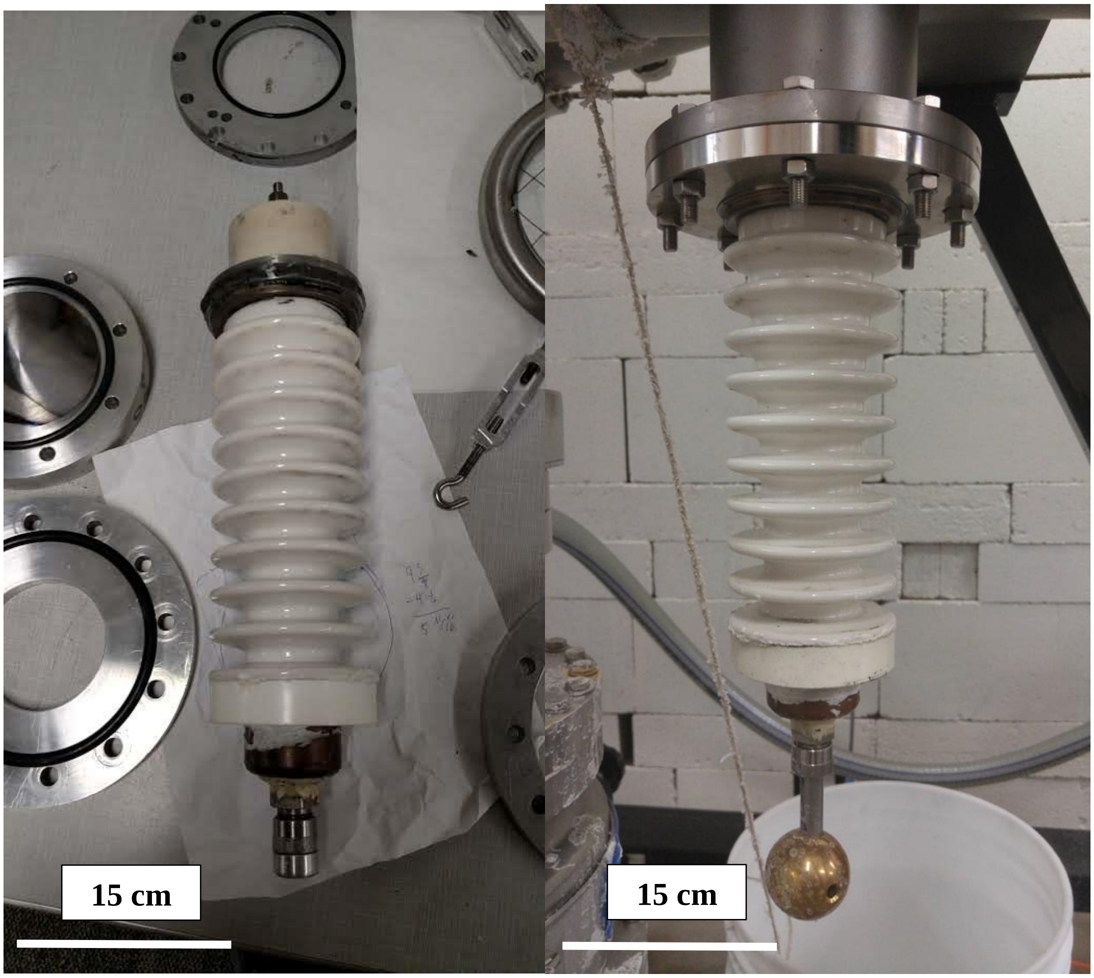

Figure 5-8. Left: high voltage feedthrough as received. Right: Upgrade to high voltage feedthrough.

5.4.3 – Cathode and Anode Design

The wires for both the cathodes and anodes were made out of a tungsten-rhenium (74:26) alloy and spot welded together. Afterwards, these were silver soldered onto 21.5 cm outer diameter (16.5 cm inner diameter) annular rings. Due to poor performance of the initial anode, we upgraded to a different design which consists of an aluminum and copper hexagonal support structure for the anode ring. The new anode provided improved hardware stability and ease of movement, as well as improved neutron rates.

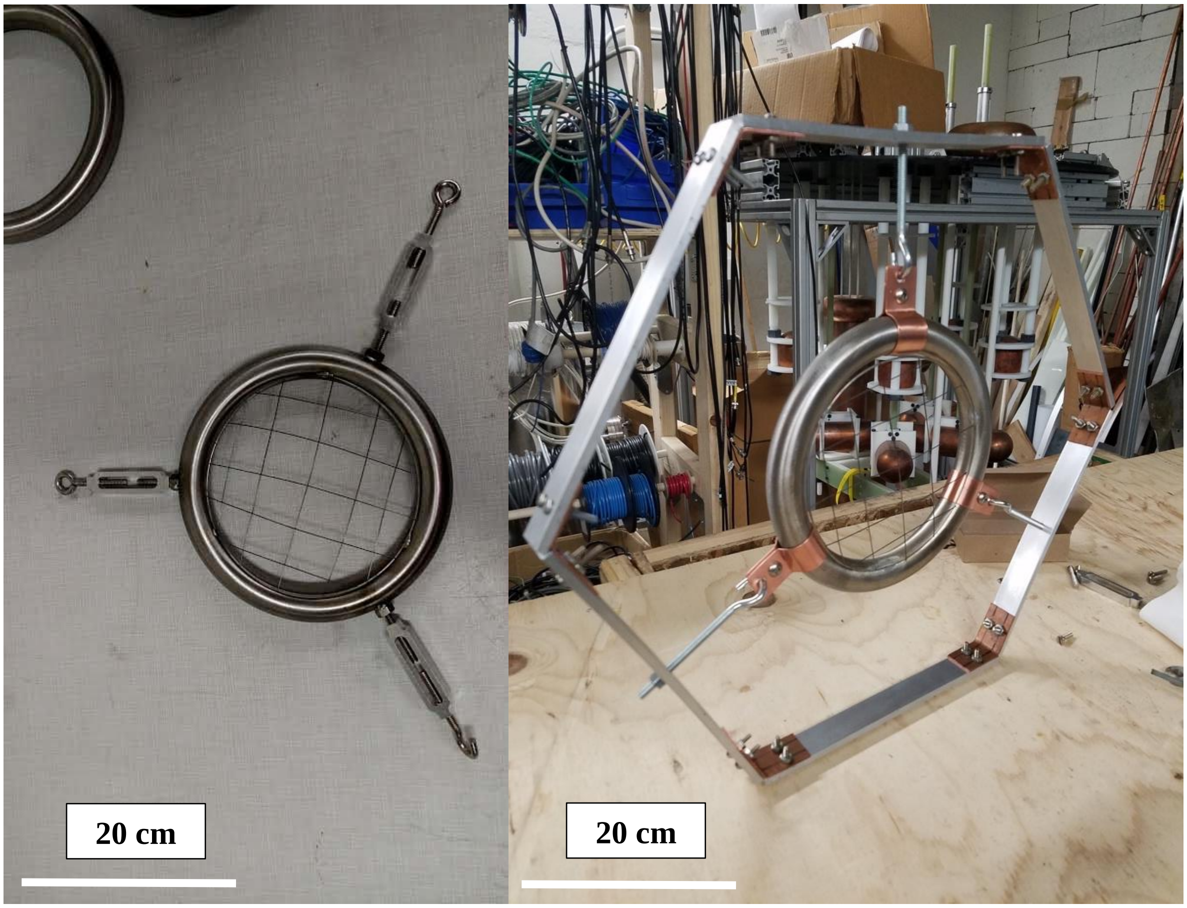

Figure 5-9. Left: Initial anode design for LUNA. Right: Anode upgrade courtesy of Graduate Student Nolan Clay van Rossum.

The cathode consists of a 12” long, 6” diameter stainless steel tube which supports the annular rings and wire meshes used for ion acceleration. Mechanical polishing of the surface with 180, and 320 grit SiC papers smoothed the surface and got rid of undesired imperfections to provide a clean surface for silver soldering the rings with the wire meshes. After this was done, many edges required smoothing out with SiC by mechanical polishing. The tube was then ultrasonically cleaned in an ethanol bath for 30 minutes to remove any impurities introduced by the soldering process. In order to support the structure and connect to the high voltage feedthrough, a stainless-steel fitting was manufactured and installed as well, as seen in Figure 5-10.

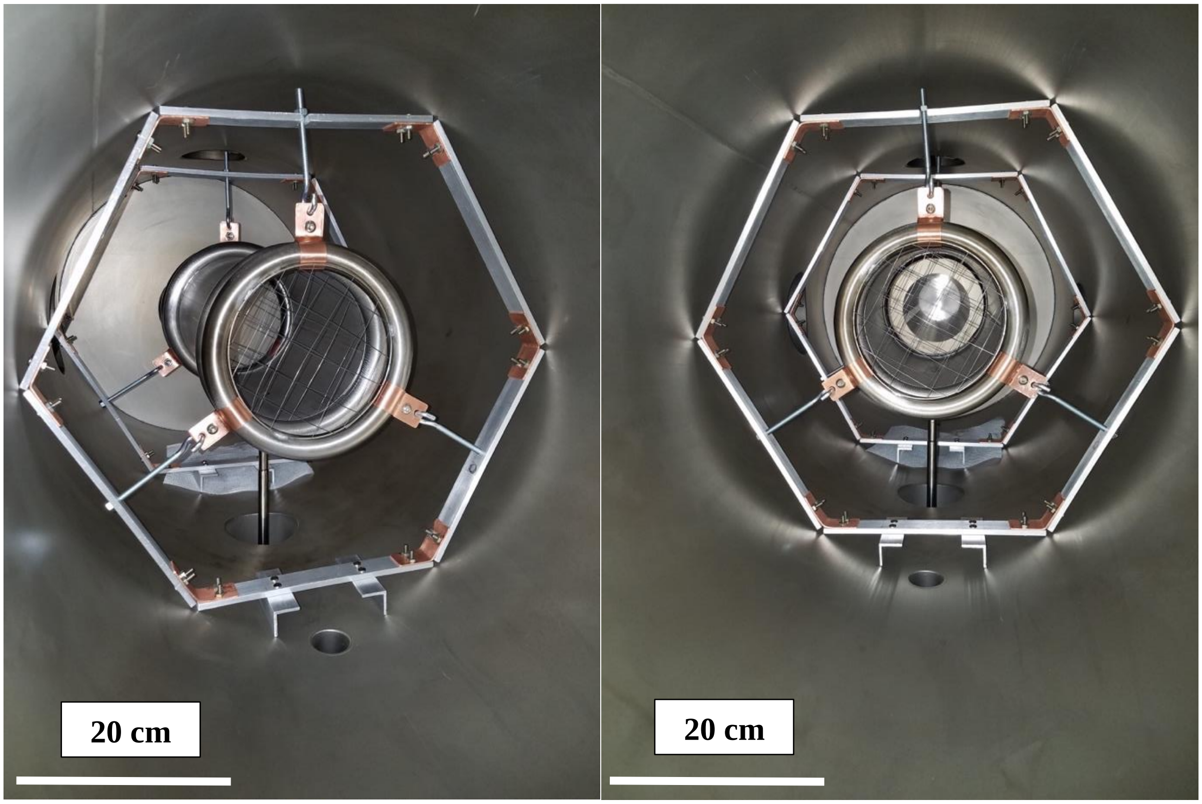

Figure 5-10. Left: Isometric view of high voltage configuration. Right: Front view of high voltage configuration.

5.4.4 – Electron Filament Supply

The filament supply offers a simple structure and mode of operation (Figure 5-11). The filaments (A) were taken from a 250 W incandescent light bulb and installed on a biasing feedthrough. In order to prevent electrons from drifting towards the grounded flange, a copper plate (B) was installed and electrically connected to one of the feedthrough prongs in order to negatively bias it. A stainless-steel rod and grid (C) were installed to accelerate the electrons into the chamber. In order to have current flow, the second feedthrough prong was isolated using boron nitride rods. Two fuses (D) were installed at the bottom to prevent damaging any equipment.

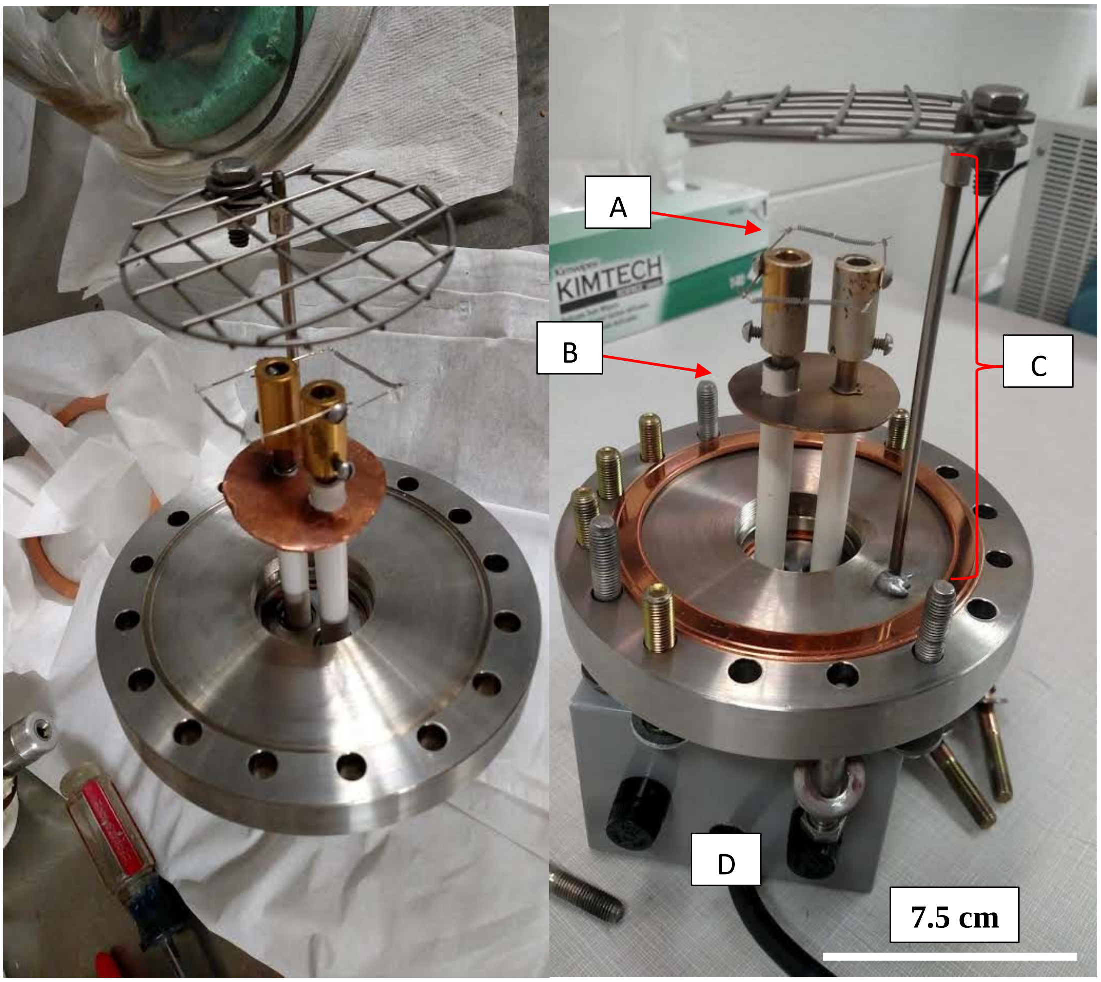

Figure 5-11. Electron filament supply for LUNA. Left: Before operation. Right: After operation.

5.5 – VICTER Optimization Results

Calculations were carried out using the VICTER integral equation code in order to determine the neutron rates due to DD fusion in a linear and a spherical IEC device, mimicking the geometric and input parameters summarized in Table 5-5. The reason for performing these was to predict the optimized parameters for the neutron rates in the LUNA device.

Table 5-5. LUNA Optimization Parameters.

$L_{C\text{-}C}$ (m)	Cathode-Cathode Separation
Δ (m)	Cathode-Anode Separation
V_C (kV)	Cathode Voltage
P (mTorr)	Chamber Pressure

The current steady-state IEC DD neutron record is $3.8\text{x}10^8$ n/s at 200 kV, 100 mA cathode current and 1 mTorr D_2 [148]. As presented in Figure 5-12 through Figure 5-14, the LUNA device has not been sued to pursue cathode voltages of such magnitude because the filament position limits the anode-cathode spacing to small values (<4cm), so wire-to-wire arcing limits the achievable voltage. One disadvantage to the VICTER code is that it does not include the physics for transition to a glow discharge. In practice, the LUNA experiment transitions into glow discharge at pressures past 3 mTorr. All the following calculations were performed for a 30 mA discharge.

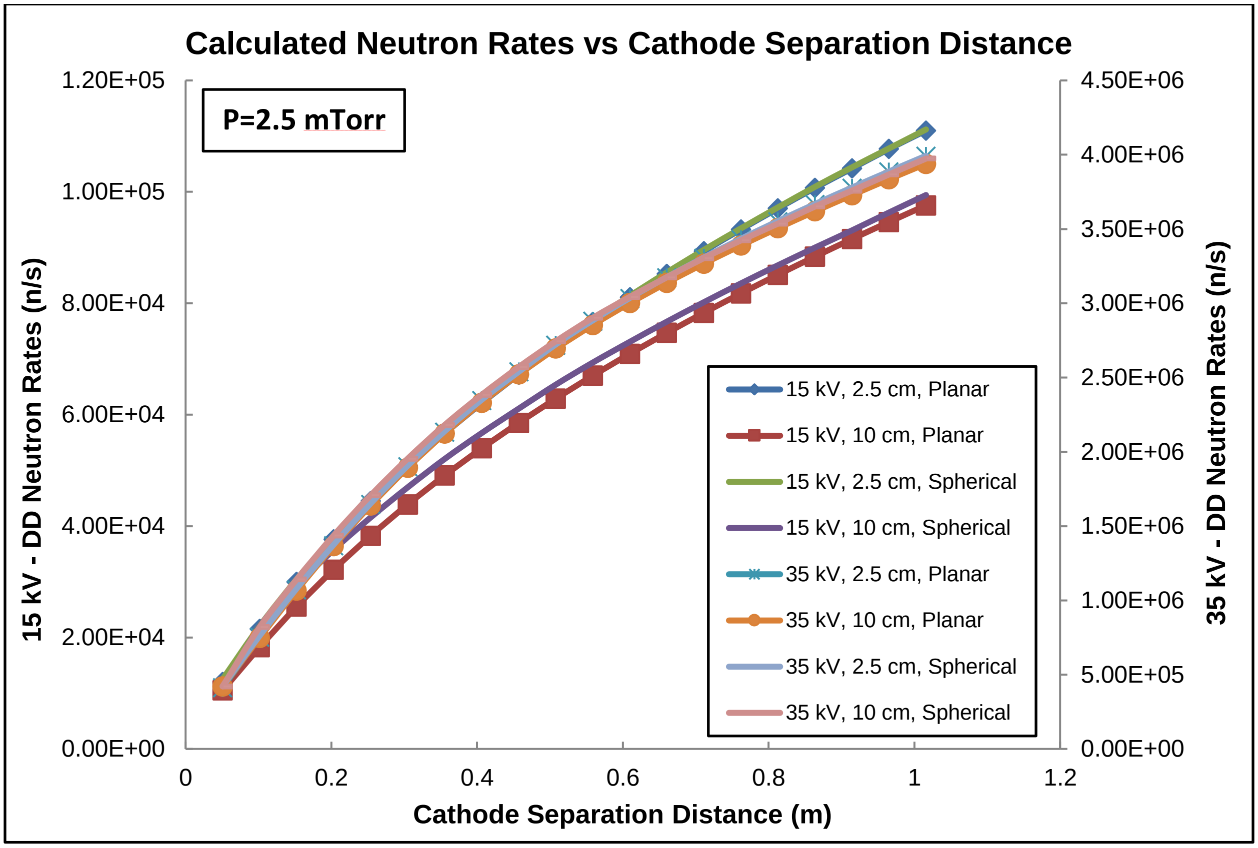

Figure 5-12. Comparison of calculated neutron rates for a chamber pressure of 2.5 mTorr at different cathode-anode separation for both a linear and a spherical geometry of equal dimensions.

A comparison between two different geometries was performed to compare neutron rates. It is seen that the neutron production rate is highly dependent on all the optimization parameters. Figure 5-12 suggests that the neutron rates for both a linear (Figure 5-5) and a spherical geometry (Figure 5-1) are comparable. However, there is a problem to having a spherical geometry, because the size of these IEC devices would be much larger and multiple-sized spherical cathodes and anodes would need to be manufactured to perform parametric variations of the cathode-anode spacing test, which could be done in linear geometry by moving the axial positions of two cathode/anode sets.

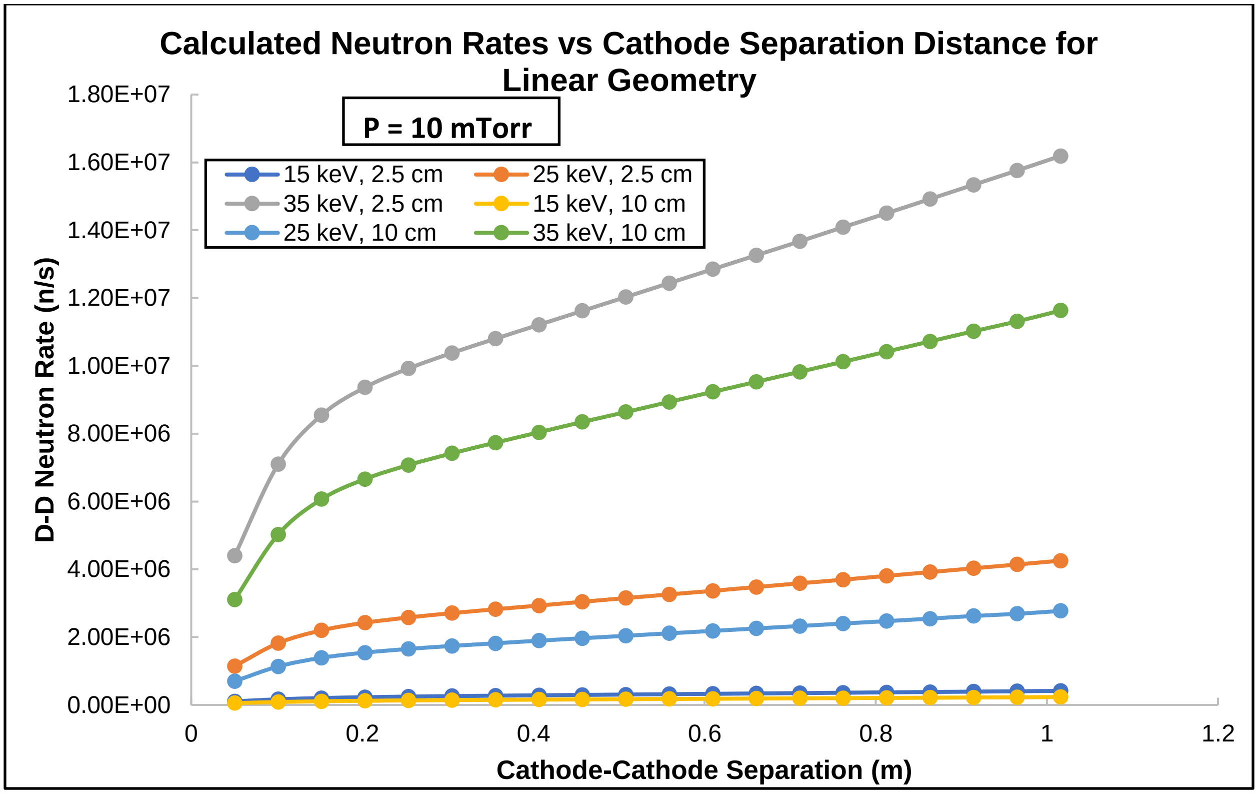

Figure 5-13. Calculated neutron rates for a linear geometry with a fixed chamber pressure of 10 mTorr for different cathode-anode separation distances at various cathode voltages. The data was collected for anode-cathode separations (Δ) of 2.5 cm and 10 cm.

Neutron rates were shown to have a strong dependence on cathode-anode separation and pressure as seen on Figure 5-13. One of the main conclusions to come from these results is that the larger the separation distance between cathode and anode, the lower the neutron rates, possibly due to the high collisionality (elastic collisions, charge exchange, ionization, dissociation, etc.) and energy losses between ions and neutrals between the cathodes and anodes in the significantly smaller target regions which also lead to enhanced ion losses to the walls. An increasing cathode-cathode separation leads to a corresponding increase in the neutron rates. As this distance is increased, there is a much larger target exchange region between the cathodes, reducing wall losses, and enhancing the neutron rates.

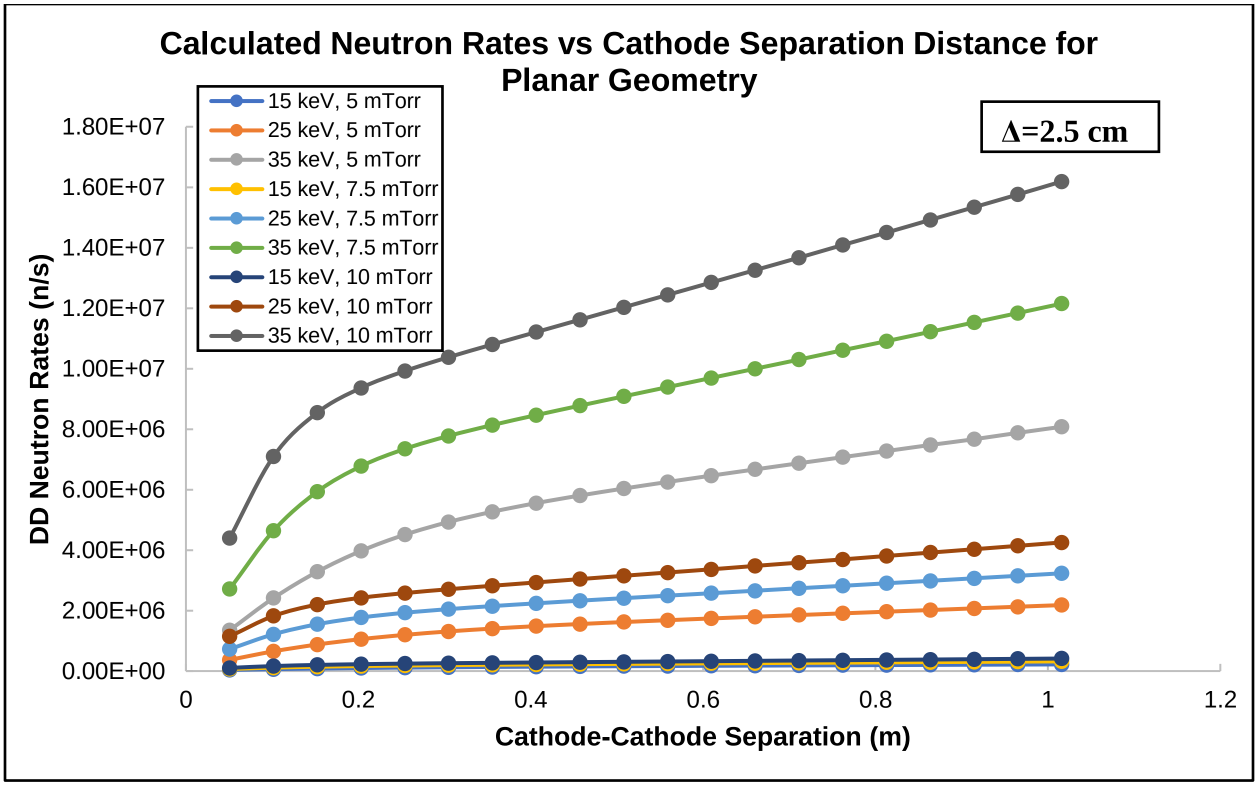

Figure 5-14. Calculated neutron rates for a linear geometry with a fixed chamber cathode-anode separation (Δ) distance of 2.5 cm for different chamber pressures at various cathode voltages.

On Figure 5-14, we see that neutron rates increase with fuel pressure due to the higher density of target gas atoms, as well as cathode voltage. Current IEC devices are run at similar pressures (~1-2 mTorr), and as mentioned before, experimental results show that at pressures somewhat higher than these, the neutron rates are reduced, therefore, the LUNA device could not be pushed to more intense neutron rates than these. These results were tested after the construction of the device, which is the first phase of the linear neutron source concept.

5.6 – LUNA Optimization Results and Discussion

After construction, the system was baked with heating tape for 24 hours at 150 °C in order to reach a base chamber pressure of 2×10^{-7} Torr. Deuterium gas was fed to the system at this point as a discharge fuel. For a given electrode geometry, gas breakdown (a plasma or “glow discharge”) that serves to help clean surfaces in the chamber spontaneously occurs within a range of pressures and voltages.

All the data collected shows the same linear dependence seen in a spherical IEC device [148], which corresponds to beam-background fusion interactions. The neutron production for LUNA is weighted towards the center of the cathode region (Appendix A), but an experimental spatial distribution of the neutrons cannot be determined until a neutron detector array is installed near the device. As opposed to the HOMER IEC device [148], LUNA only relies on one ionization source to generate the electrons that create the ions source needed to achieve the desired operating current. Chamber pressure buildup was a limiting factor, which led to an increased population of electrons in the chamber, creating a glow discharge and drastically decreasing the neutron rates, with the meter current increasing to excessive values. The chamber also utilizes an annular tube which connects the cathode grids and negatively and biases them. This geometry could be a large contributor to the large electron currents due to secondary electron emission caused by deuterium ions. HOMER only utilizes nearly transparent grids for the anode and cathode, which is potentially also a factor in its higher neutron rates. The data collected in this thesis shows comparable neutron rates to the HOMER IEC device at UW-Madison. However, optimization of this linear device cannot be directly correlated with HOMER due to the large difference in path lengths of the particles between the anodes and cathodes in both devices. In the linear device, these are 3.75 cm and in the spherical device, close to 20 cm. The optimization data collected in the odd-numbered Figures from 5-15 through 5-23. VICTER results for the same run parameters as the optimization data are presented in the even-numbered Figures from 5-16 through 5-24.

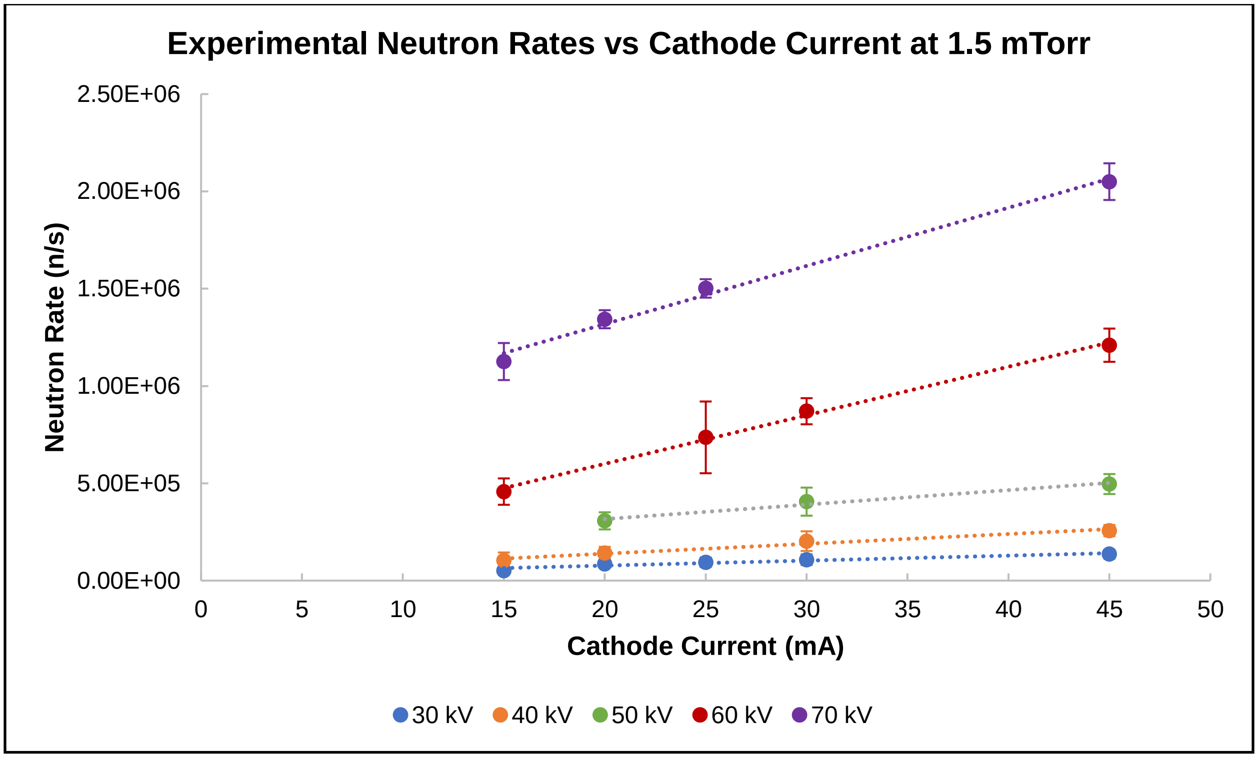

Figure 5-15. Experimental optimization for a cathode-anode separation of 3.75 cm, a cathode-cathode separation distance of 0.305m and a set deuterium pressure of 1.5 mTorr.

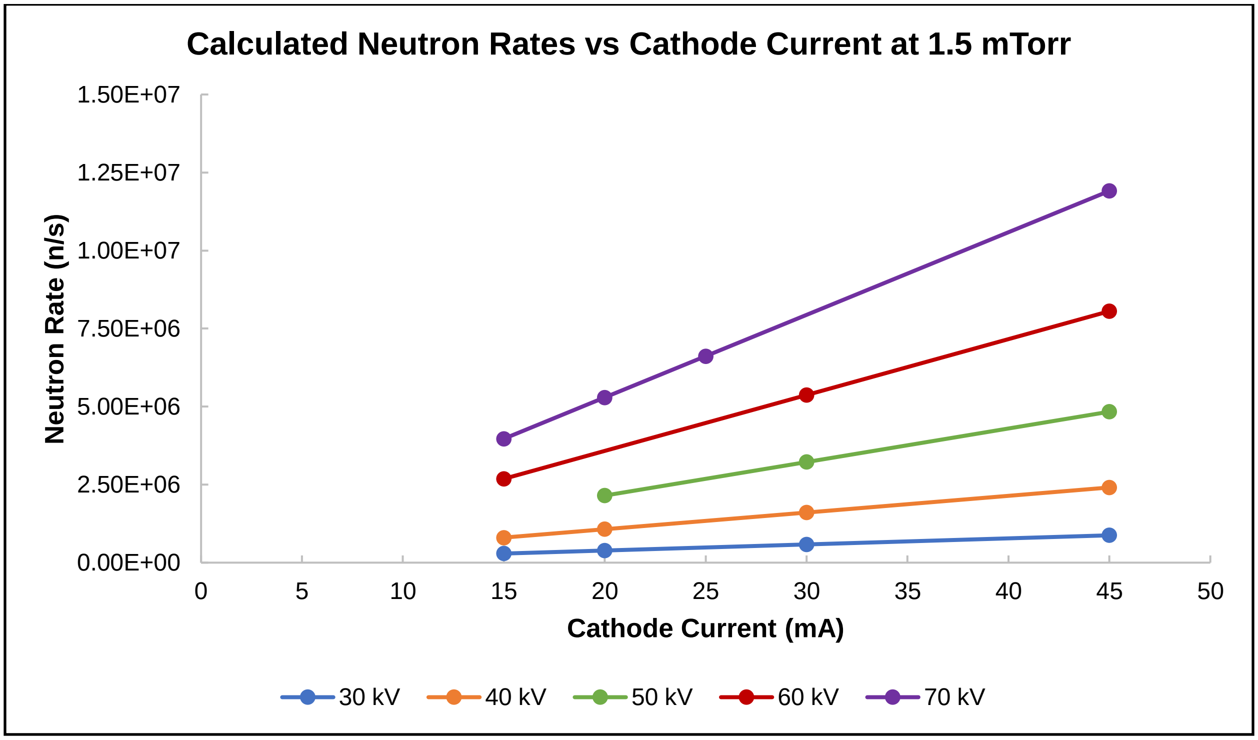

Figure 5-16. VICTER discharge predictions for the same run conditions as in Figure 5-13.

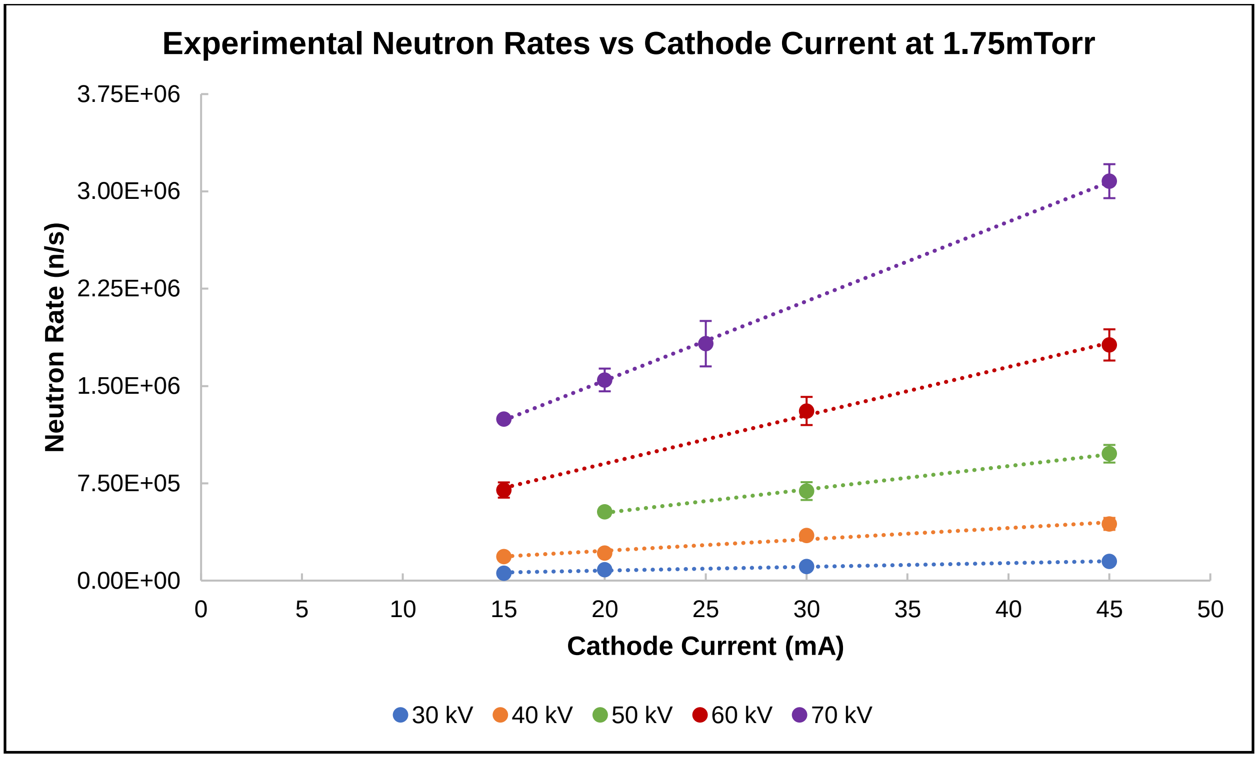

Figure 5-17. Experimental optimization for a cathode-anode separation of 3.75 cm, a cathode-cathode separation distance of 0.305m and a set deuterium pressure of 1.75 mTorr.

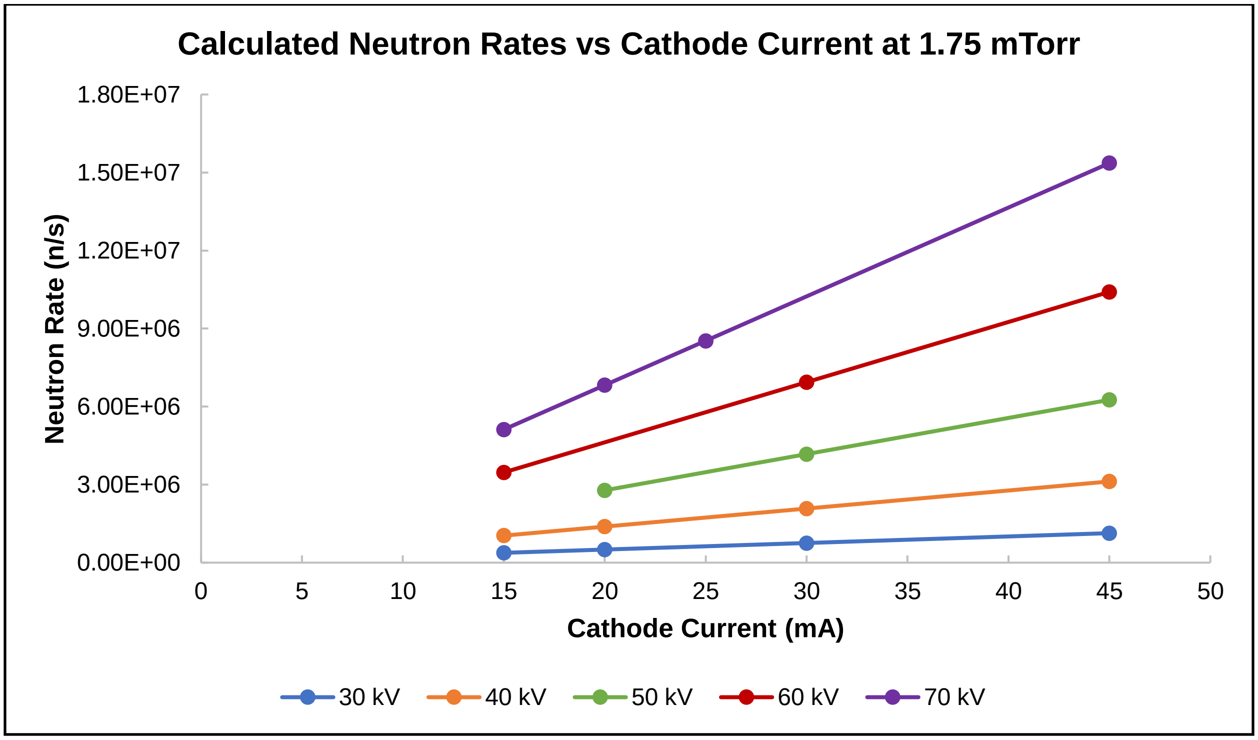

Figure 5-18. VICTER discharge predictions for the same run conditions as in Figure 5-15.

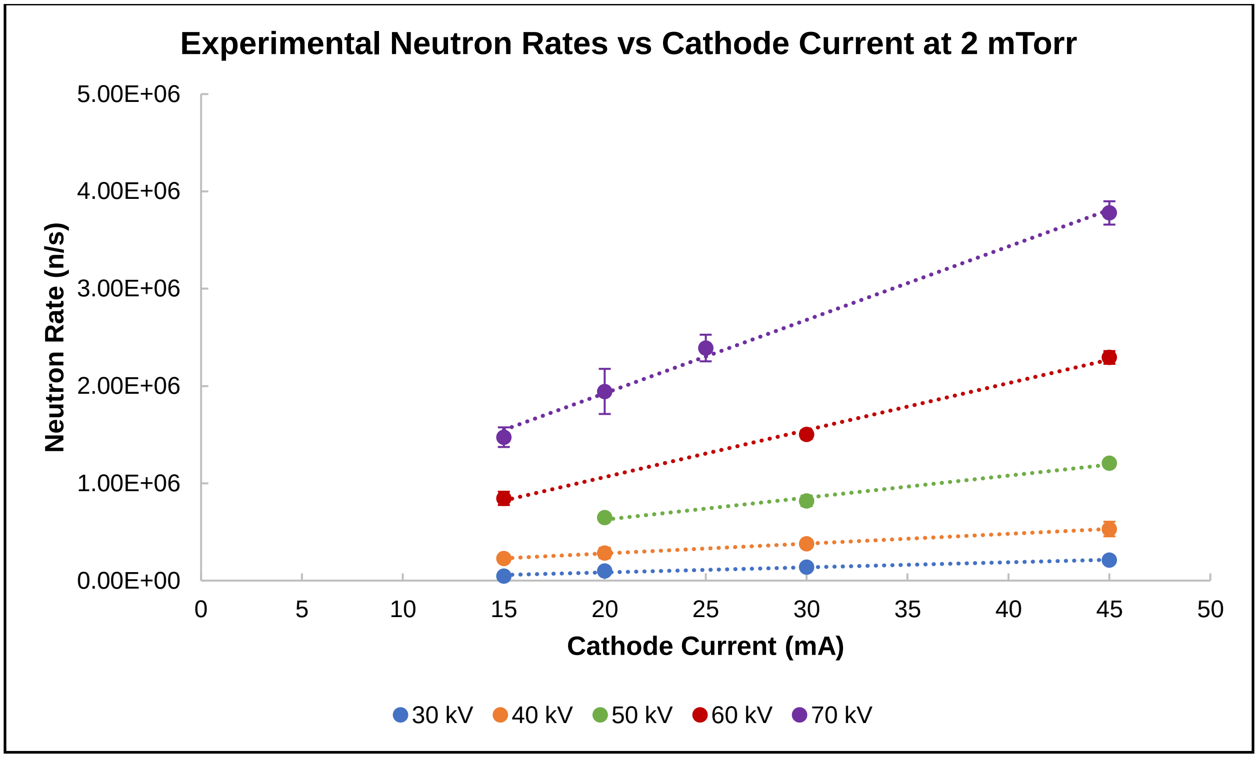

Figure 5-19. Experimental optimization for a cathode-anode separation of 3.75 cm, a cathode-cathode separation distance of 0.305m and a set deuterium pressure of 2 mTorr.

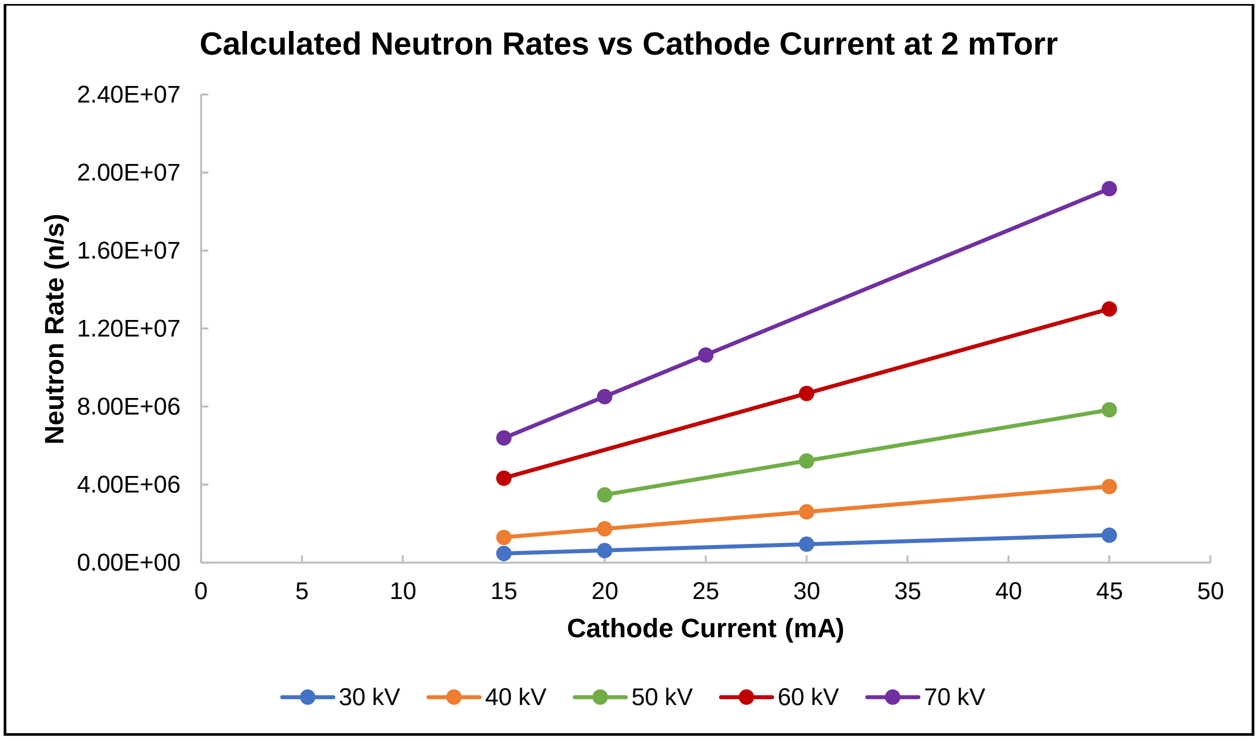

Figure 5-20. VICTER discharge predictions for the same run conditions as in Figure 5-17.

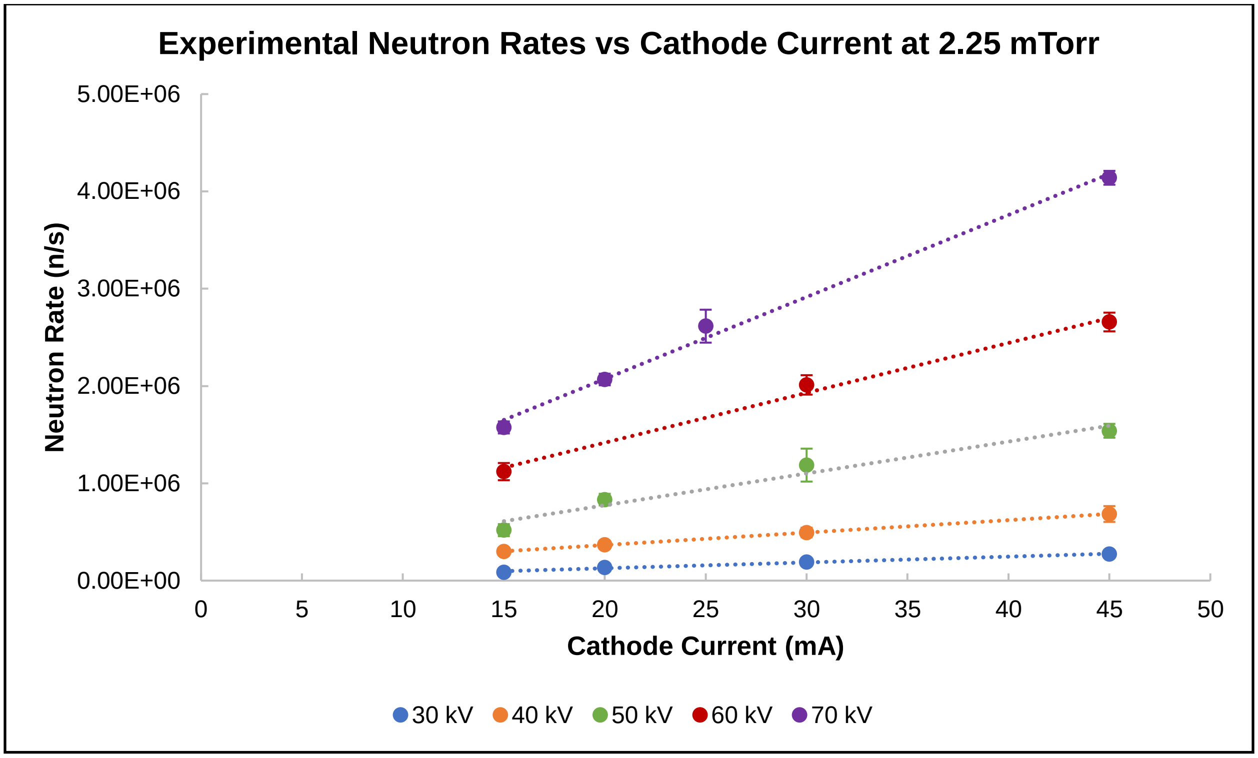

Figure 5-21. Experimental optimization for a cathode-anode separation of 3.75 cm, a cathode-cathode separation distance of 0.305m and a set deuterium pressure of 2.25 mTorr.

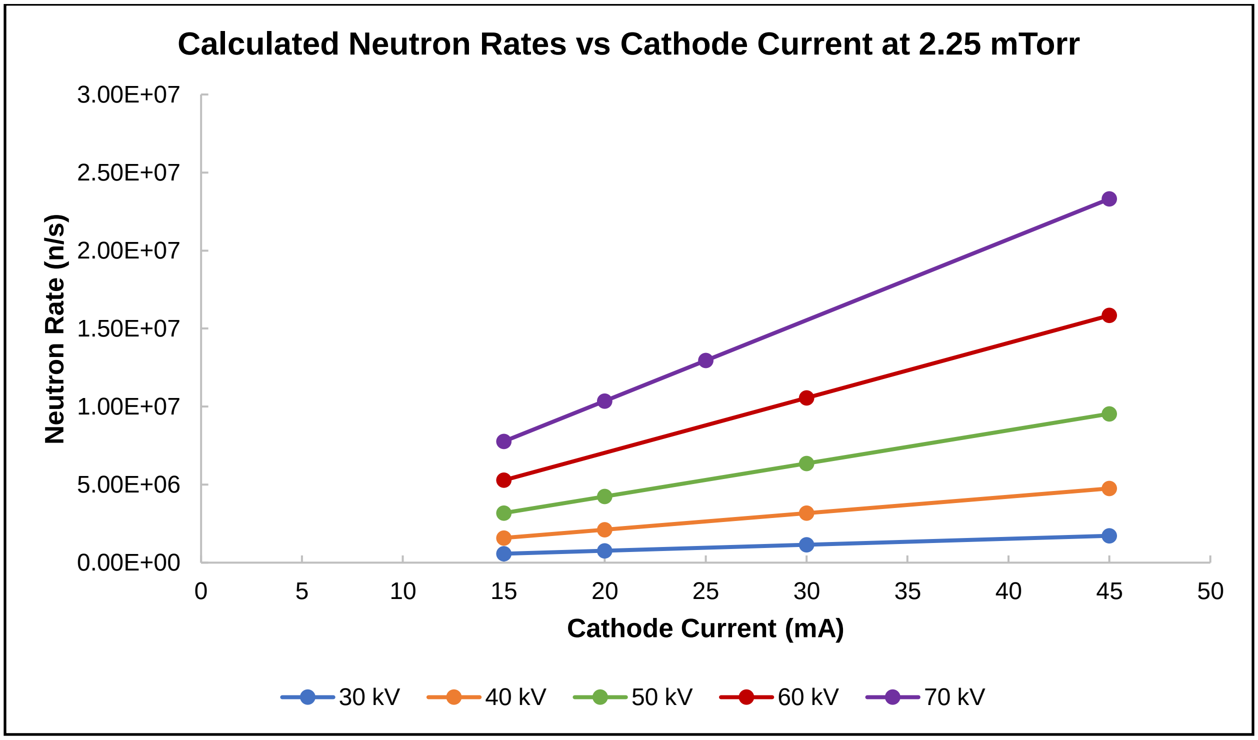

Figure 5-22. VICTER discharge predictions for the same run conditions as in Figure 5-19.

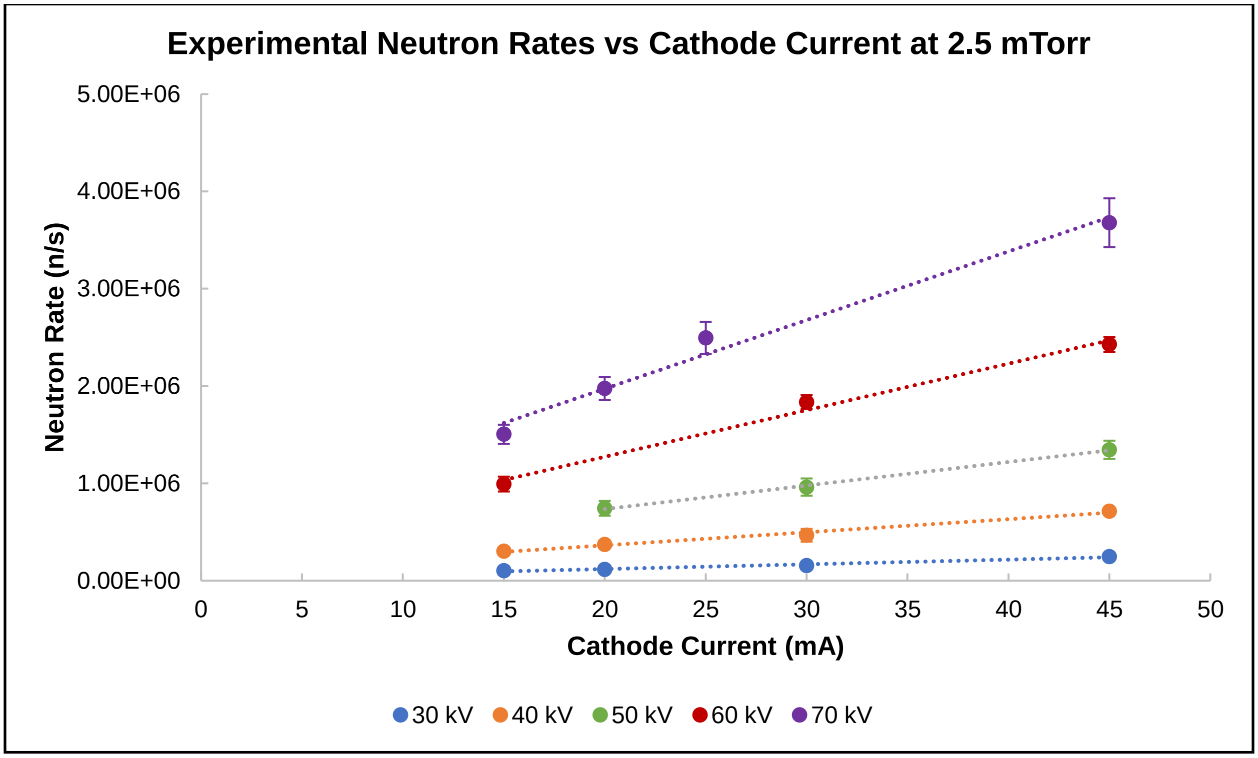

Figure 5-23. Experimental optimization for a cathode-anode separation of 3.75 cm, a cathode-cathode separation distance of 0.305m and a set deuterium pressure of 2.5 mTorr.

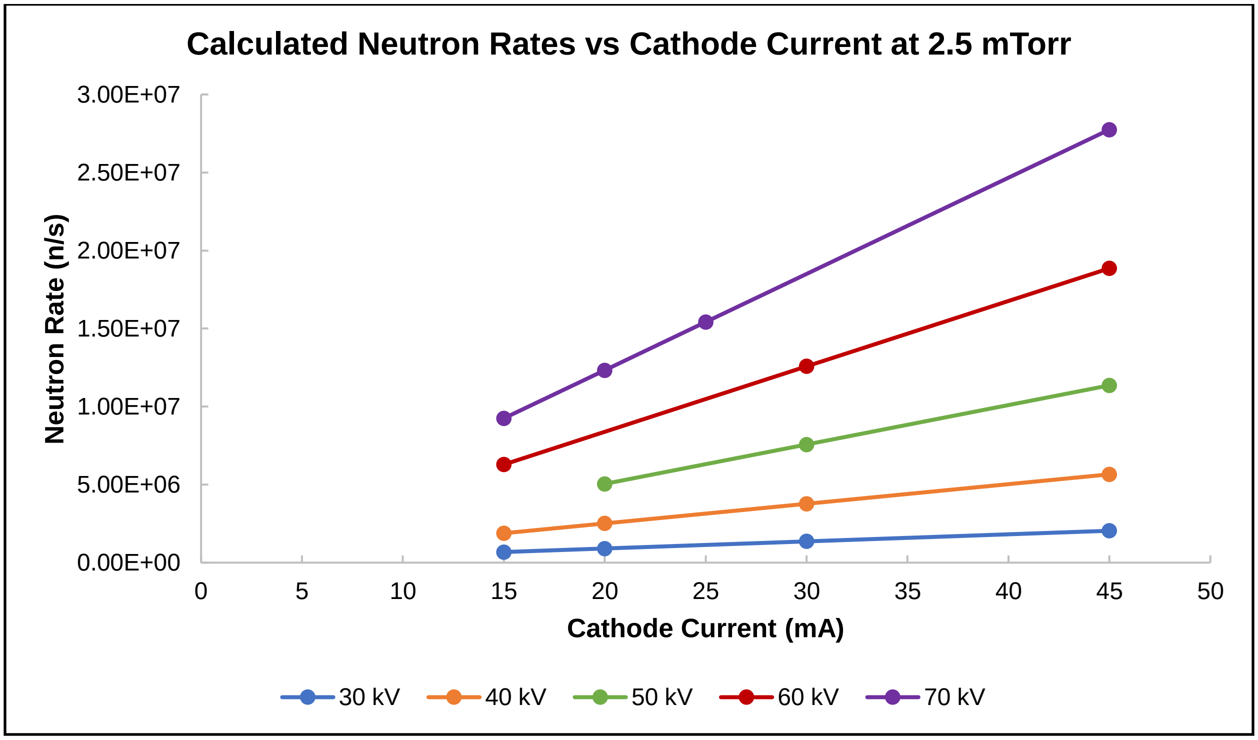

Figure 5-24. VICTER discharge predictions for the same run conditions as in Figure 5-21.

The data acquired reveals a few important observations for the current geometric configuration of the LUNA experiment. For pressures below 1.5 mTorr, it is difficult to sustain a plasma, or achieve any significant neutron rates. As mentioned before, the neutron rates in the experiment increase with cathode voltage and cathode current. A comparison between the VICTER data and the experimental data shows that the experimental neutron rates differ by almost a factor of 10, although the trends are similar. These results are also similar to those determined experimentally and computationally in HOMER [148]. This could be due to the assumptions gone into the VICTER model, and the simplification in the atomic and molecular processes described by it.

Another observation obtained from this data is the high-pressure limit of the device. In this experiment, a glow discharge occurred at pressures above 2.75 mTorr. When looking at the experimental data, the experimental neutron rates start to degrade when increasing the pressure from 2.25 to 2.5 mTorr, nearing the transition point to a glow discharge. This breakdown is not included in the VICTER code and is part of the processes that could explain the difference in the rates for varying cathode ion currents. The odd-numbered Figures from 5-25 through 5-33 present the rates as a function of pressure, and their corresponding VICTER results are presented in the even-numbered Figures from 5-26 through 5-34. For every pressure tested across several optimization parameters, the drop-off and softening of the spectrum is present, possibly indicating imminent gas breakdown in a glow discharge. This data is nonlinear as seen as well from the VICTER calculations, but because the breakdown physics is not included in VICTER, the shape of the curves is difficult to compare as well.

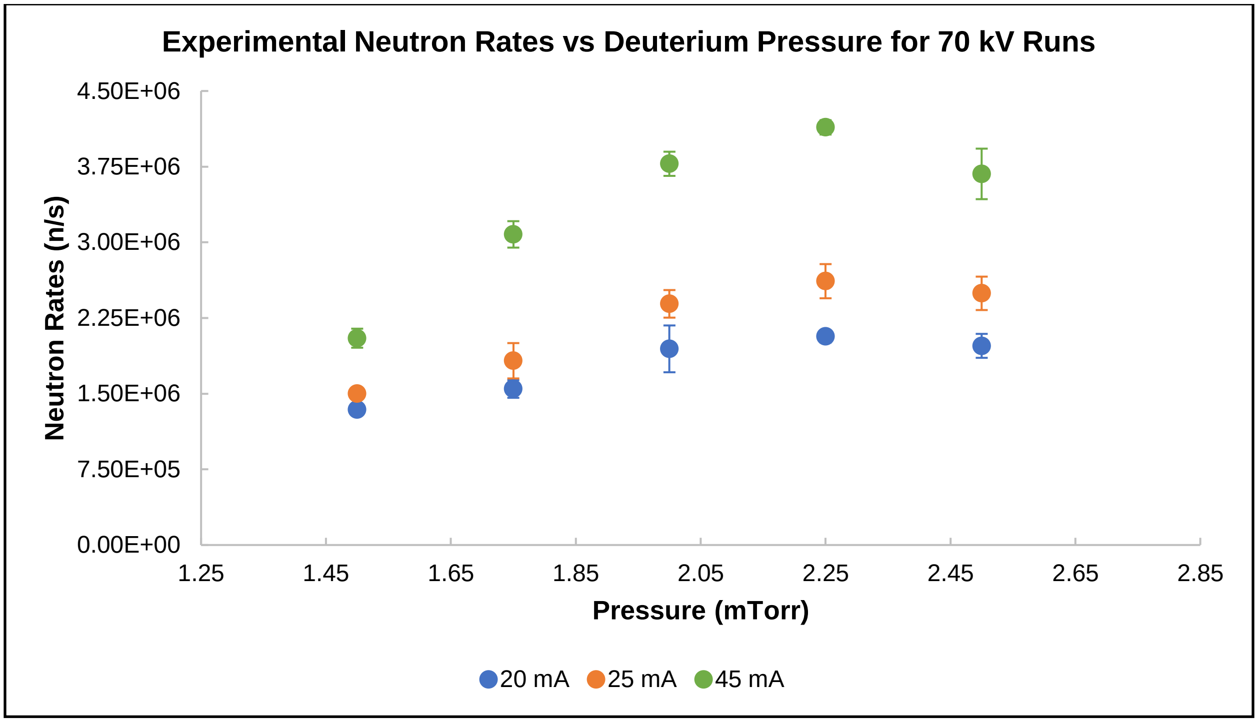

Figure 5-25. Experimental optimization for a cathode-anode separation of 3.75 cm, a cathode-cathode separation distance of 0.305m and a set cathode voltage of 70 kV.

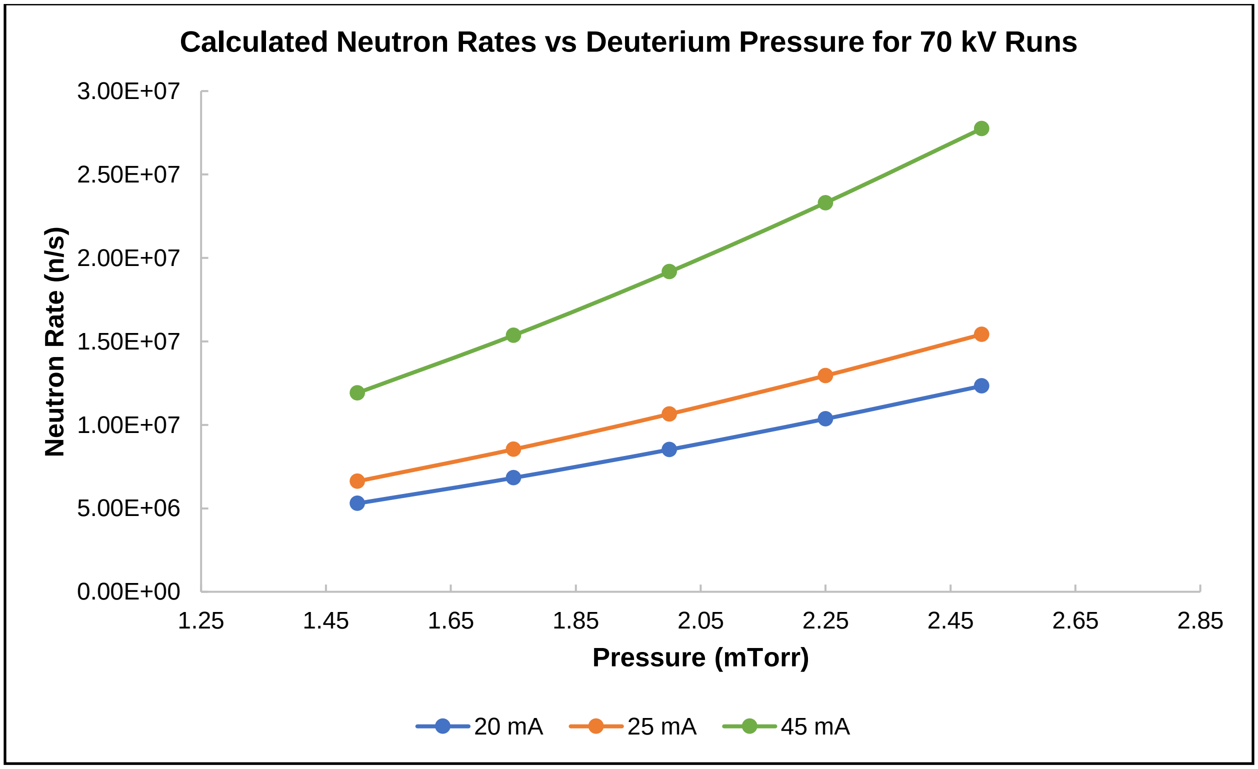

Figure 5-26. VICTER discharge predictions for the same run conditions as in Figure 5-23.

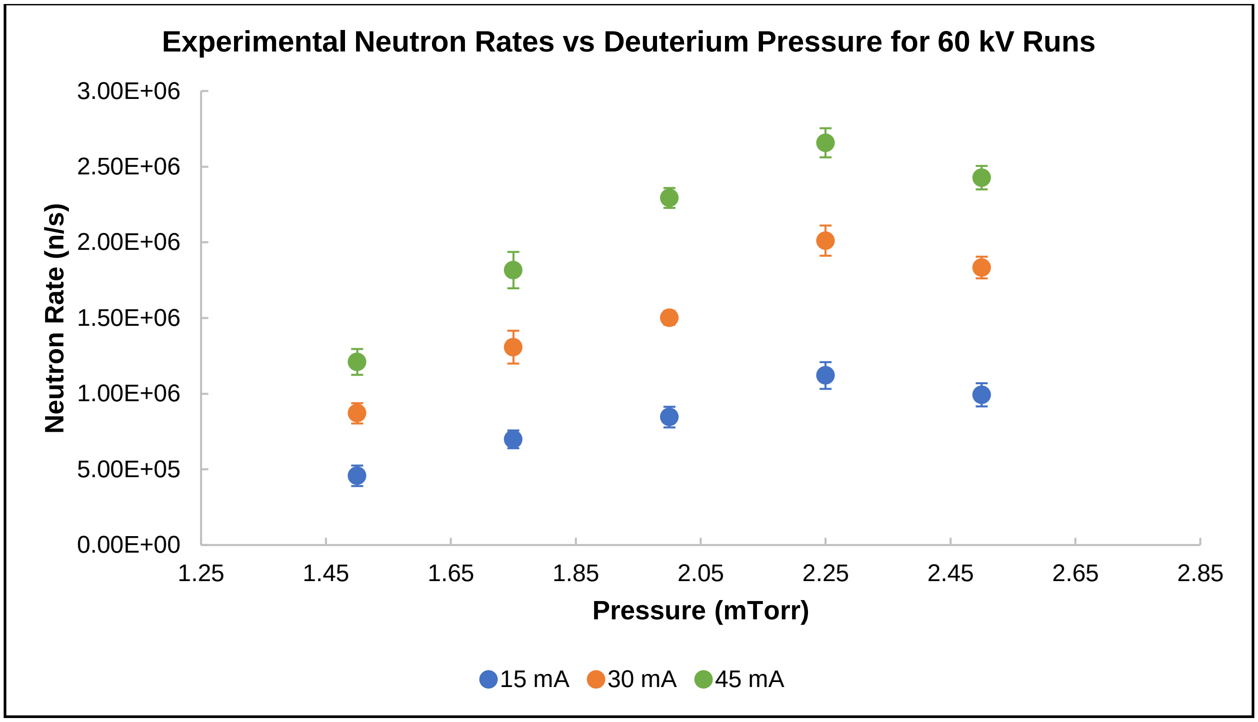

Figure 5-27. Experimental optimization for a cathode-anode separation of 3.75 cm, a cathode-cathode separation distance of 0.305m and a set cathode voltage of 60 kV.

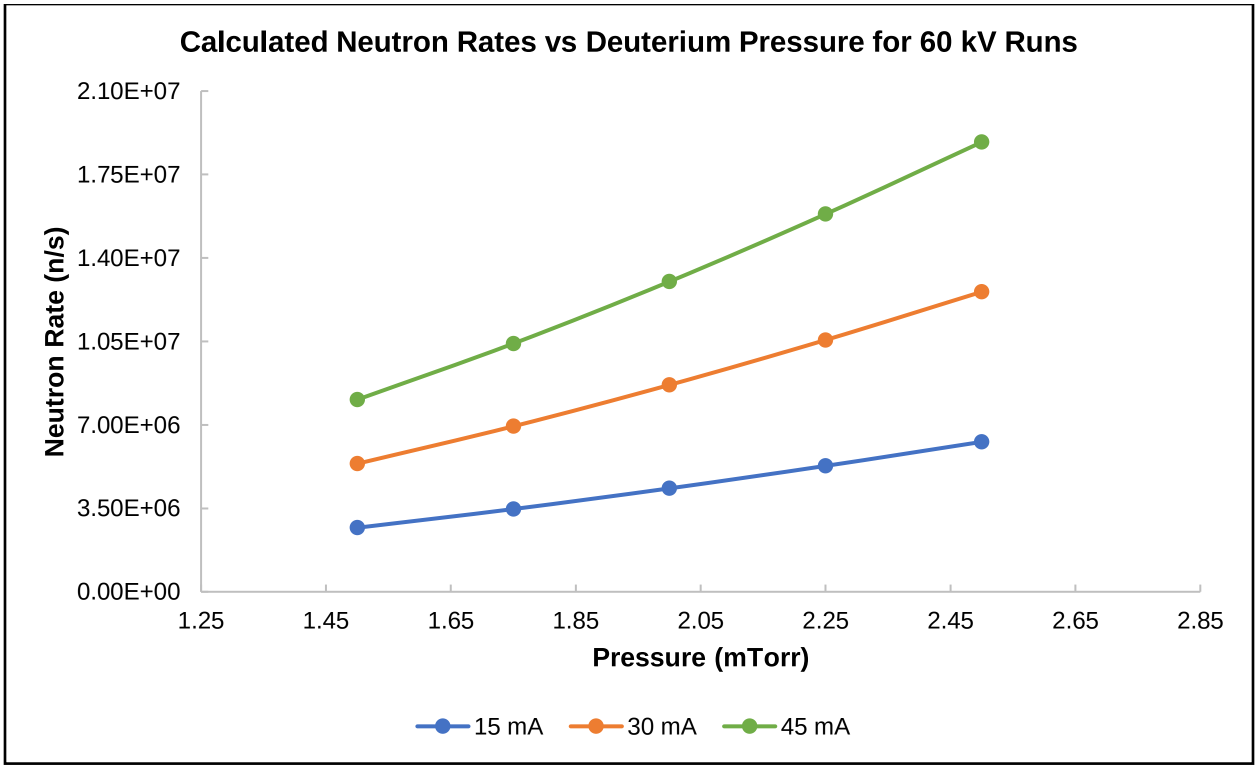

Figure 5-28. VICTER discharge predictions for the same run conditions as in Figure 5-25.

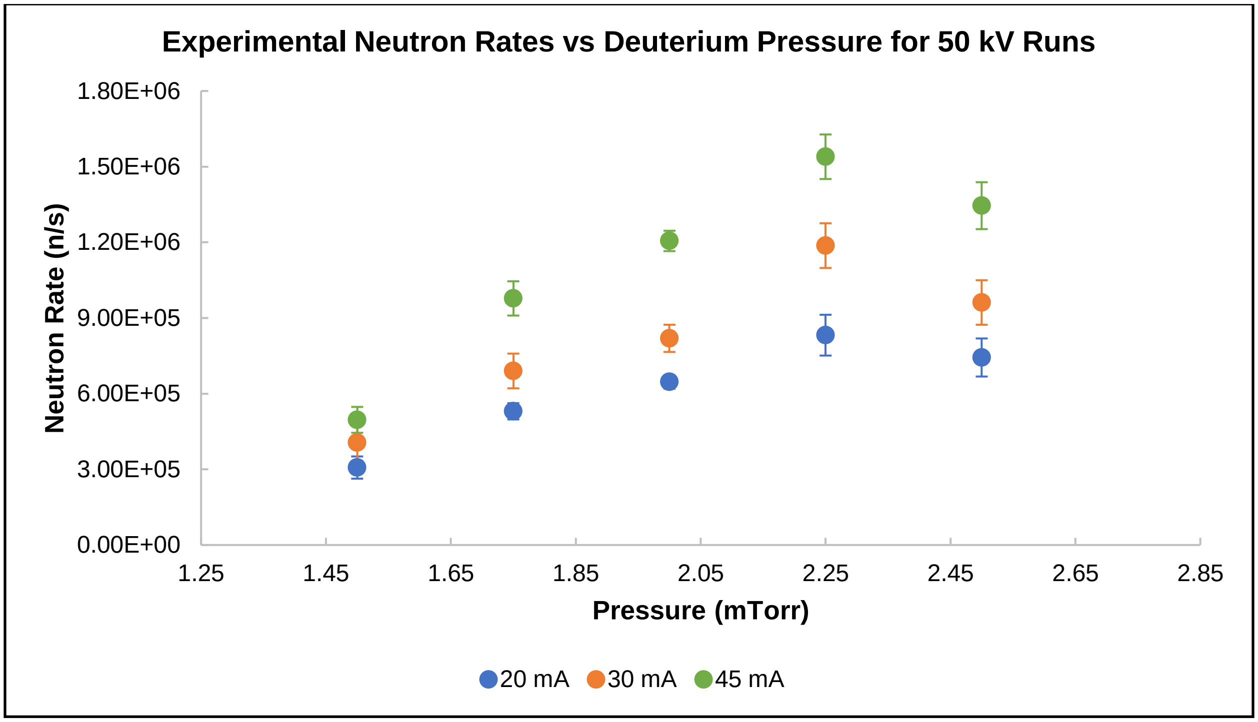

Figure 5-29. Experimental optimization for a cathode-anode separation of 3.75 cm, a cathode-cathode separation distance of 0.305m and a set cathode voltage of 50 kV.

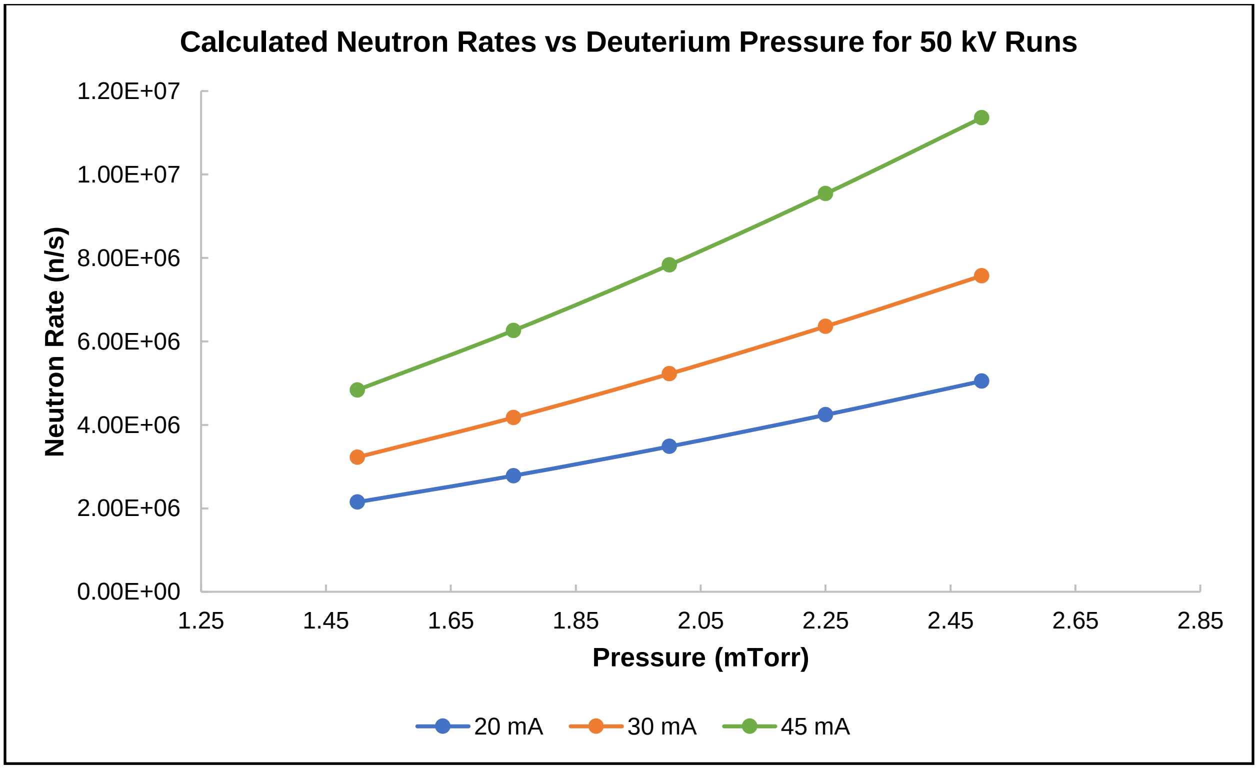

Figure 5-30. VICTER discharge predictions for the same run conditions as in Figure 5-27.

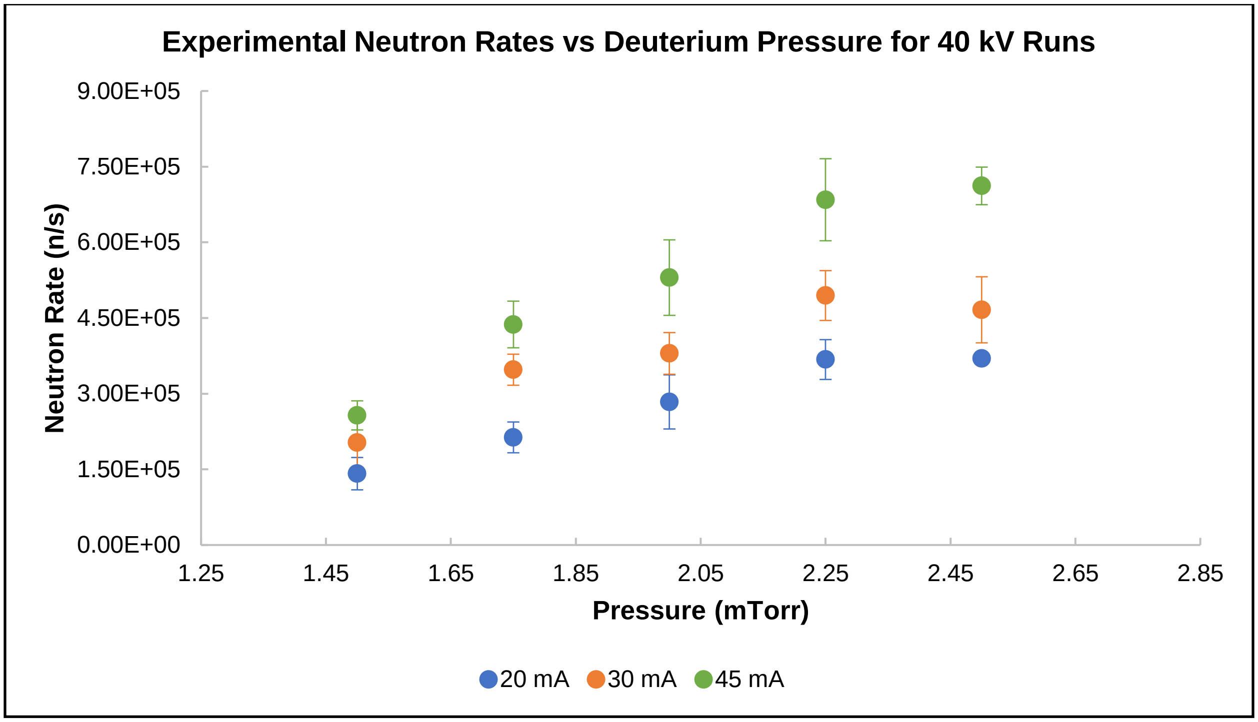

Figure 5-31. Experimental optimization for a cathode-anode separation of 3.75 cm, a cathode-cathode separation distance of 0.305m and a set cathode voltage of 40 kV.

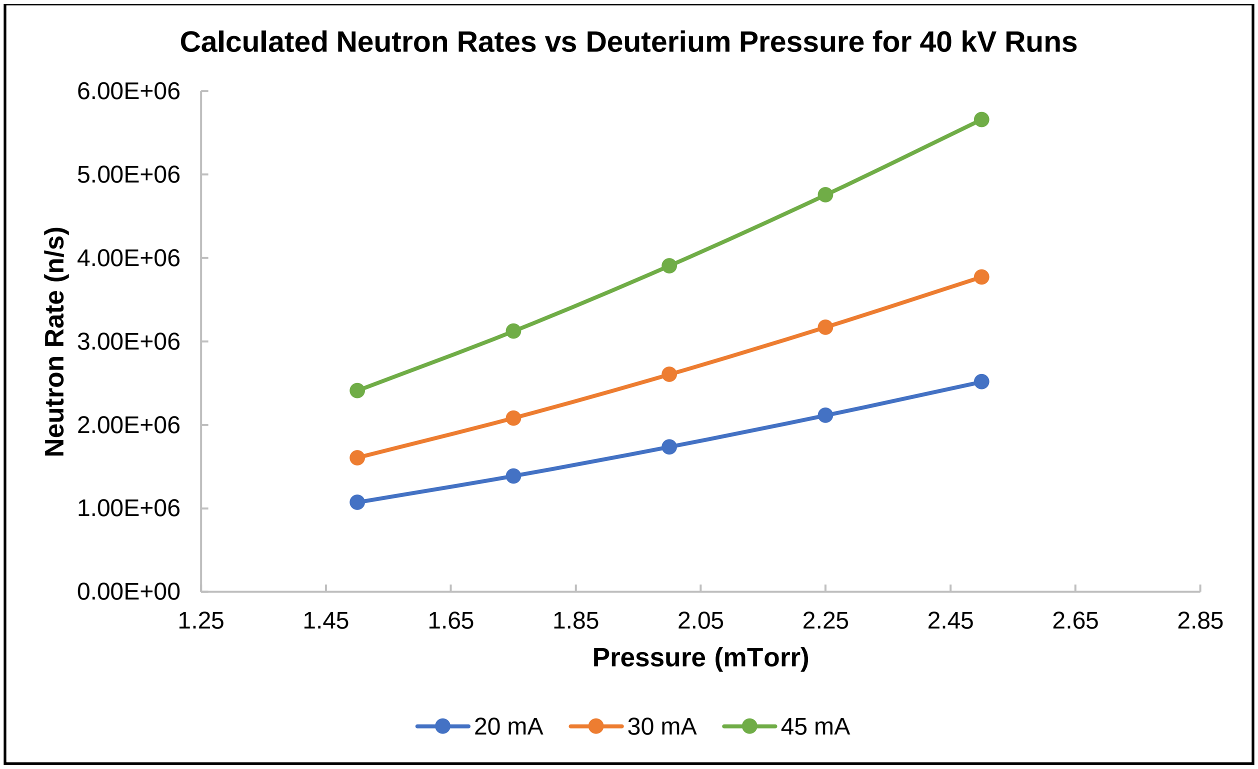

Figure 5-32. VICTER discharge predictions for the same run conditions as in Figure 5-29.

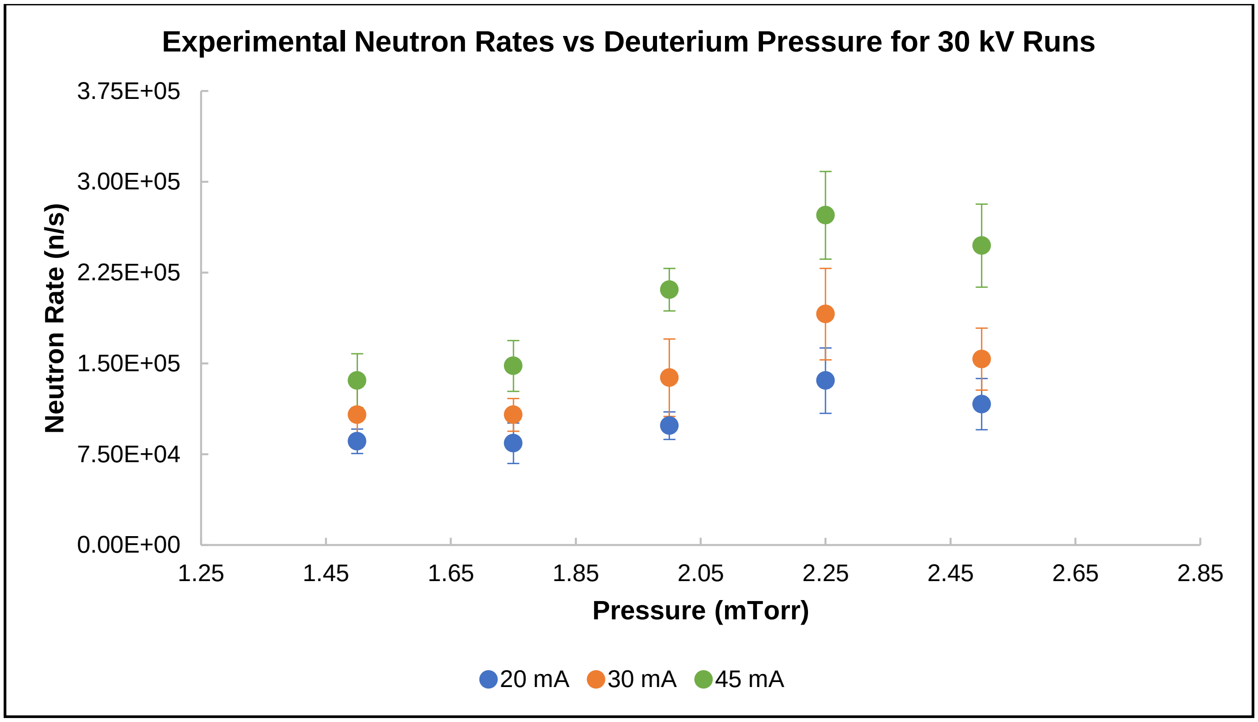

Figure 5-33. Experimental optimization for a cathode-anode separation of 3.75 cm, a cathode-cathode separation distance of 0.305m and a set cathode voltage of 30 kV.

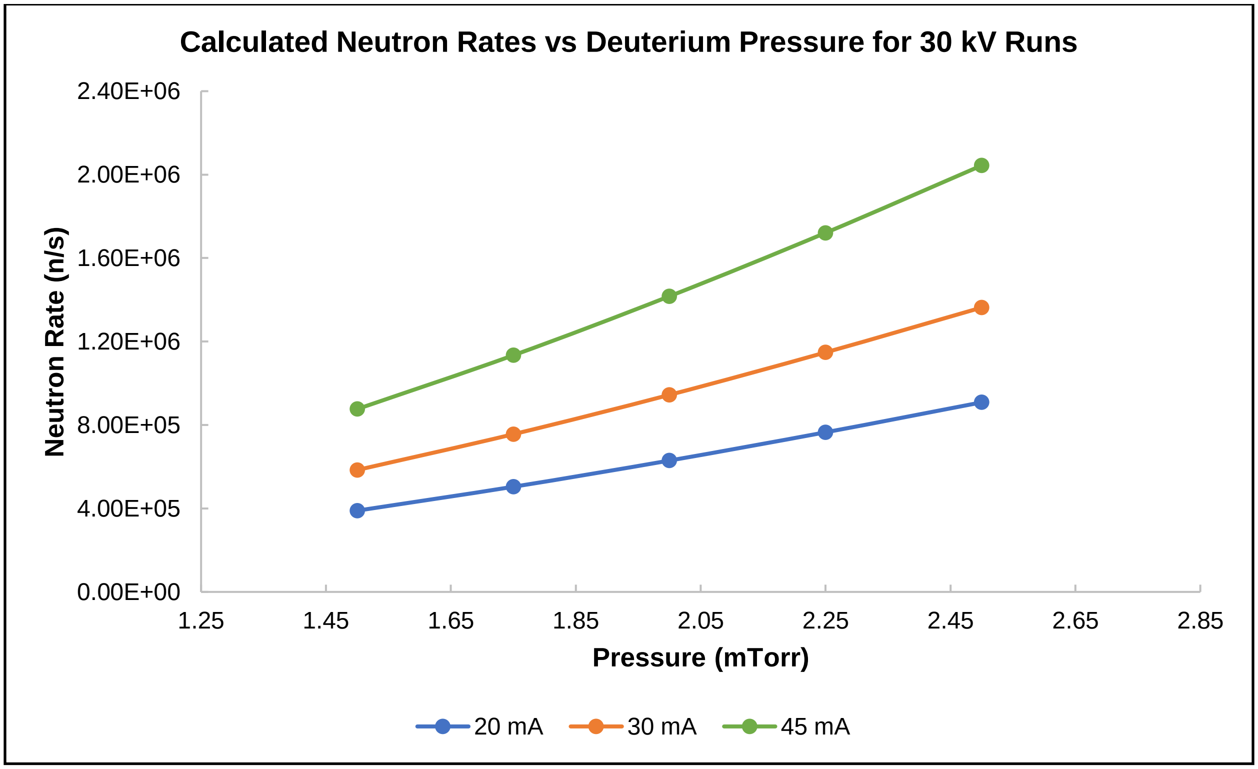

Figure 5-34. VICTER discharge predictions for the same run conditions as in Figure 5-31.

Although this experiment has begun producing neutrons, it is still a long way from achieving its expected optimal neutron generation. A neutron detector array is currently being constructed and installed near a moderating tank for a more detailed spatial description of the neutron distribution. A secondary filament supply has been installed to attempt to increase the source ion population and minimize secondary electrons. In general, VICTER showed that for every discharge, the secondary electron current is a large contributor to the cathode current (>50%). This is a large limiting factor not just for IEC devices but for any fusion confinement device that has surfaces being impacted by energetic ions or neutrals. The following chapter will discuss graphene's use as a PFC coating as well as its role in mitigating this secondary electron emission effect, thus possibly increasing the experimental neutron production rate.

This page is intentionally left blank.

Chapter 6 – Results for Graphene as a Coating for Plasma Facing Components

During the beginning of this project, the usage of graphene was initially intended towards its use in the LUNA experiment to maintain a pressure differential across a high-pressure and a low-pressure region. One of the materials considered as a support structure for the graphene was silicon due to its ease of fabrication and vast knowledge of etching properties to fit the specifications for many applications, in this case, a window with nanometer sized holes for neutrals to pass through without large energy losses. While this did not prove to be an efficient candidate, the following section summarizes the initial testing of a silicon oxide (SiO_2) solid substrate as a support for graphene in the MITE-E Irradiation Facility. The graphene damage results eventually led to the assessment of graphene as a coating for tungsten in three different facilities: MITE-E, PISCES, and C-2W which will be covered in the subsequent sections. Lastly, due to a number of studies demonstrating graphene as having an ultralow secondary electron emission, some experiments were performed on half-coated tungsten samples to measurements that allow the qualitative distribution of the secondary electron coefficient.

6.1 – Graphene on (100) Silicon Dioxide, SiO_2

Part of this study was to determine an appropriate candidate for a mesh to suspend graphene for its use as a membrane; firstly, to sustain a pressure difference and secondly, to minimize energy losses to the fusion products leaving LUNA through it. The original concept was to etch silicon dioxide because graphene's behavior on it has been well characterized. However, SiO_2 is extremely brittle, has very poor physical properties, and it etches in such a way that the transparency of the mesh would be too low for it to remain structurally stable [152–155]. Silicon sputtering also peaks at around the energies that we expect to run at and experiments were carried out for single and double layer graphene on a solid substrate to quantify some of its behavior under deuterium irradiation at various ion energies and no laser heating. Because the pyrometer only reads temperatures above 450 ºC, and the deuterium beam heats the sample poorly, we estimate the temperature of the substrates to be around 100 ºC. The results plotted on Figure 6-1 and Figure 6-2 are taken by averaging Raman measurements at various random locations over the substrate.

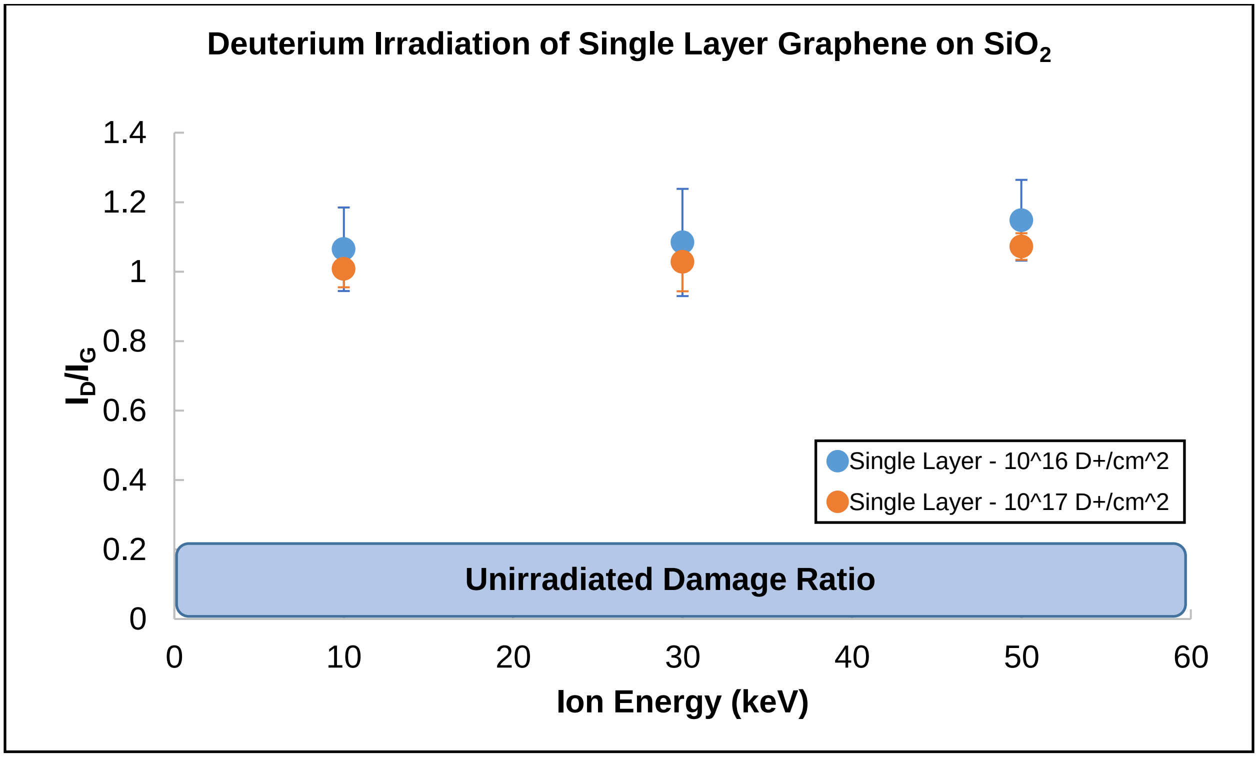

Figure 6-1. Vacancy ratio for irradiated single layer graphene (~100 °C through beam heating) on a silicon dioxide substrate with no additional laser heating. Statistics for these measurements do not show a large significance of ion energy on damage.

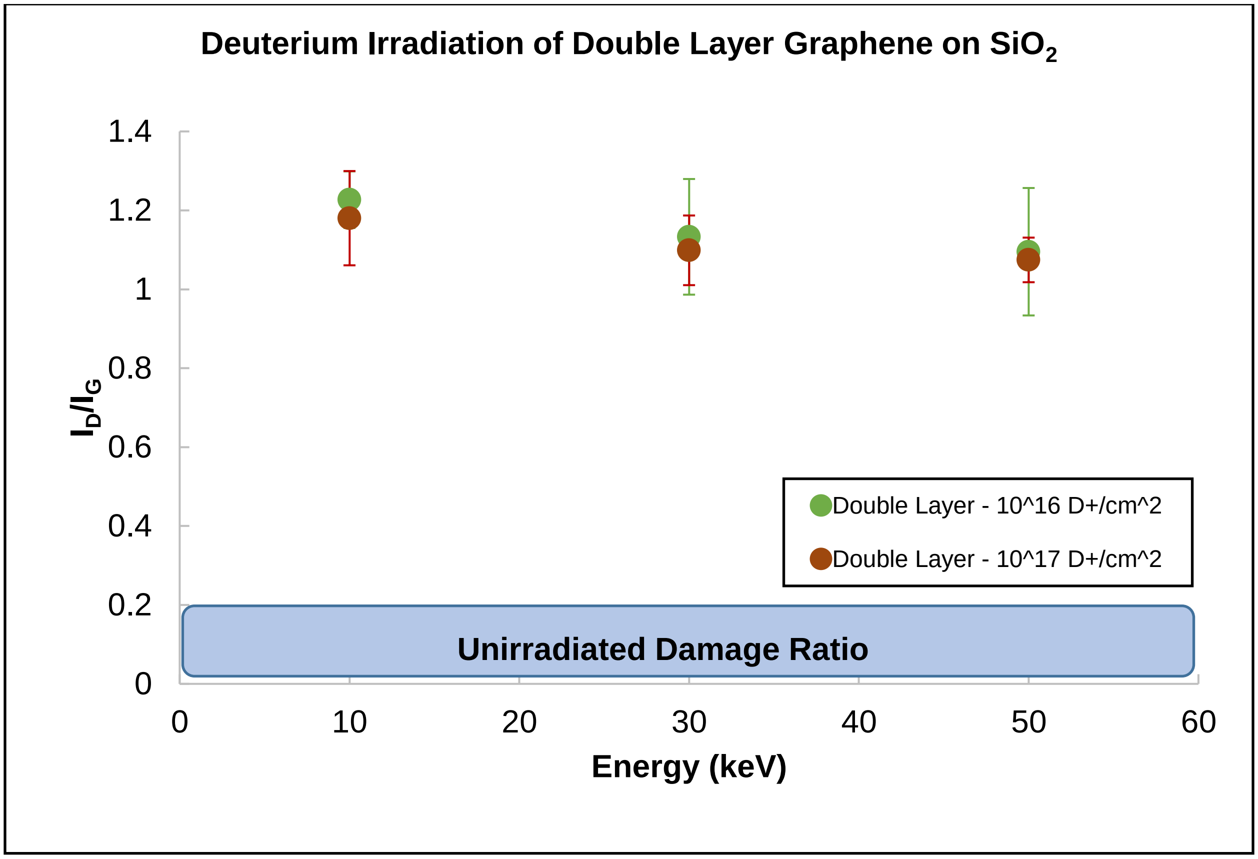

Figure 6-2. Vacancy ratio for irradiated double layer graphene (~100 °C through beam heating) on a silicon dioxide substrate with no additional laser heating. Statistics for these measurements do not show a large significance of ion energy on damage.

As seen in Figure 6-1 and Figure 6-2, although there is some damage to the graphene, increasing the ion energy does not seem to vary the degree of damage to the single and double layers on the silicon surface. For a free-standing sheet of graphene, the damage to the sheet is insignificant past ion energies of 1 keV [104]. This is due to the short interaction time between the energetic ion and the carbon atoms; the interaction is limited to deuterium with the electrons. What is causing significant damage is not ion impact on graphene but sputtering of the underlying substrate, possibly from the silicon. This also relates to why the fluence does not play a significant role at these energies; the graphene has been so damaged that silicon can escape the netting provided by the carbon lattice without damaging it further.

6.2 – Graphene on Heated Tungsten with Deuterium Gas Present

Due to the tendency of carbon-based materials to form hydrocarbons when exposed to hydrogen isotopes, it is of some importance to test graphene's robustness against such conditions. Previous studies have shown that graphene does have interactions with hydrogen, preferentially etching edges and defect sites (see 2.1.5 – Low Hydrogen Reaction Rate), as well as having peak hydrogen etch rates when the substrate on which the membranes are placed is heated to temperatures close to 500 °C; these etch rates decrease as the ambient temperature is increased above this value. Gas pressures were chosen such that they cover a range characteristic of plasma edge pressures in magnetic confinement devices [156–159], inertial electrostatic confinement devices [148,160], and plasma etching chambers [161]. A small vacuum chamber with a roughing pump, gate valve for gas flow, and a pressure gauge was used for this experiment. In order to heat the sample, MITE-E's laser setup was aligned to the sample stage from underneath and used to achieve a temperature of 500 °C. Tungsten samples used as substrates for the membrane were annealed under vacuum for 10 minutes prior to the start of the gas flow. Once annealed, the samples were exposed to a deuterium gas for 30 minutes. When the run was finished, the samples were left to cool for 4 hours before extracting them and performing post-mortem analyses.

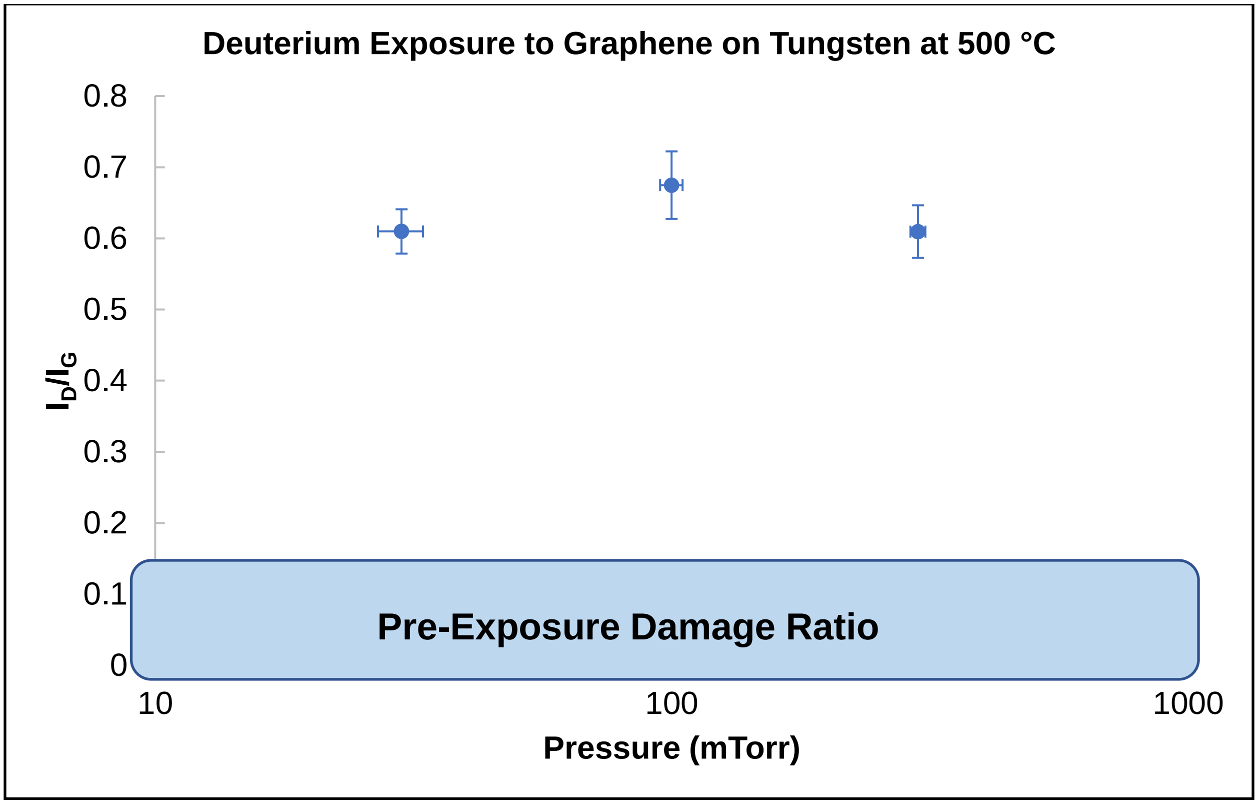

Figure 6-3. Deuterium damage to graphene under external laser heating and different neutral gas pressures.

Raman spectroscopy was performed on the samples after these exposures. Figure 6-3 shows data averaged over ten different regions and shows that defects were introduced into the membrane throughout the exposure. This is not a significant quantity since the membrane still retains its main crystalline features. Defect ratios (I_D/I_G) greater than 2 demonstrate a highly defective membrane. There does not appear to be a strong pressure dependence between pressure and defect production, although the damage to the graphene can saturate past a certain fluence.

6.3 – Graphene as a Surface Coating for Polycrystalline Tungsten, MITE-E Exposure

The results shown here build upon Lauren Garrison's thesis where the effect of ion irradiation on surface morphology of tungsten was studied [41]. In Table 6-1, the different exposure parameters for coated and uncoated tungsten are summarized. In order to track the fluence received by the sample, we measure the current to the sample with a fiber optic cable on the sample stage.

Table 6-1. Irradiation Conditions for samples exposures in MITE-E.

	Sample	Fluence (He/cm^2)	Energy (keV)	Temperature (°C)	Graphene
Garrison	P40	$6x10^{17}$	30	900	No
	P38	$1 x10^{18}$	30	900	No
	P37	$3x10^{18}$	30	900	No
	P39	$6 x10^{18}$	30	900	No
Navarro	P50	$6x10^{17}$	30	900	Yes
	P55	$1 x10^{18}$	30	900	Yes
	P54	$3x10^{18}$	30	900	Yes
	P35	$6 x10^{18}$	30	900	Yes

Secondary electron emission is an issue when trying to measure an accurate current. Samples P37-P40 were corrected for the secondary electron yields for tungsten (a value of 1.8 was used), the coated samples used the same correction for the yield.

$$I_{sample} = I_{measured}\left(\frac{1}{1+\gamma}\right) \qquad (6-1)$$

However, it is known that graphene has an extremely low secondary electron yield and has even been used to reduce this yield for other materials when used as a coating [91–93,162]. The correction used for the graphene coated samples is the same due to not having the data available for graphene on tungsten, which leads to the actual fluences for these samples to be slightly higher than reported in Figure 6-8 as well as for the comparison with samples P37-P40 in Table 6-1.

6.3.1 – Raman Spectroscopy of Graphene

Results show that, compared to the irradiated non-coated samples in Figure 6-4, the graphene has suppressed the fuzz/grass morphology on the surface of the tungsten. Using Raman spectroscopy (Figure 6-5 and Figure 6-6), the graphene coated W shows little to no sign of damage after being irradiated. This is of interest since it implies that at most, a small fraction of the carbon sputters off, which in turn, will reduce tungsten impurities eroding into the edge plasma and potentially transporting into the core plasma.

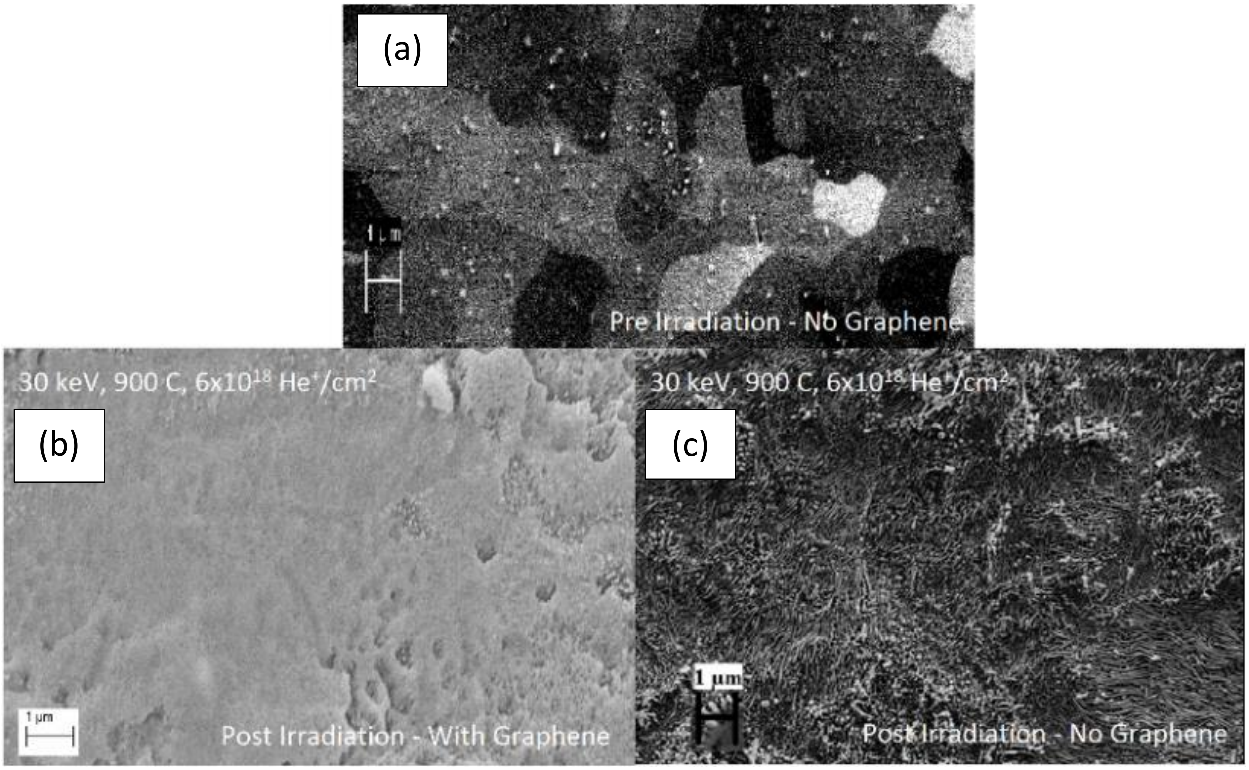

Figure 6-4. SEM image of W-Graphene sample P35 pre (a) and post (b,c) irradiation compared to W sample P39. Image (a) shows the surface finish of the sample before irradiation after being electropolished. The grass structures have been completely suppressed by the graphene coating in (b) near the center of the beam.

Figure 6-5 and Figure 6-6 show the Raman spectra of a W sample before and after being irradiated by the helium. Tungsten's Raman peak wave numbers are well below those of graphene and are omitted here. When comparing the I_D/I_G peak ratio for both cases, we see that there is essentially no change. One explanation is that, due to the self-healing properties of graphene [33], when bonds break and the hexagonal crystal structure is compromised, the graphene forms non-hexagonal structures in the lattice, preserving its 2-D form. Since graphene's I_D peak grows when it has an extra degree of freedom, and here the atoms are still bonded, but differently, this is not expected to change the Raman spectrum. However, explaining the formation of the different structures in the lattice is not something that can be derived from experiments at this time.

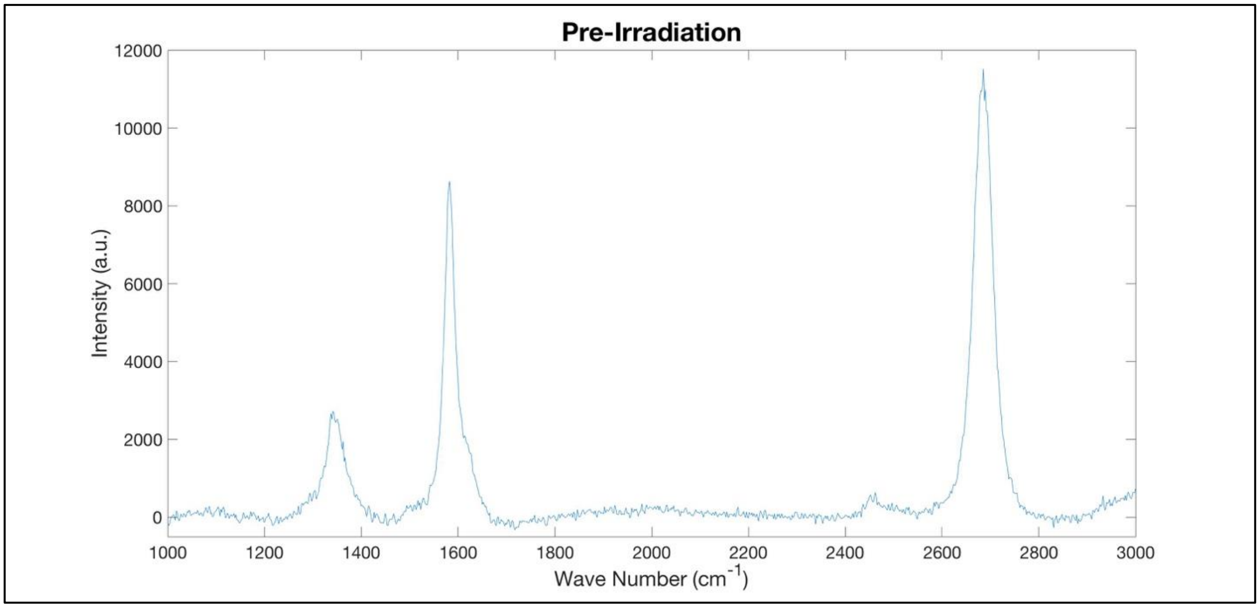

Figure 6-5. The Raman spectrum prior to irradiation shows the distinct 1550 and 2700 cm^{-1} graphene peaks. The lack of a peak at 1350 cm^{-1} indicates vacancies are insignificant compared to the intensity of 1550 cm^{-1}, implying a pristine sample.

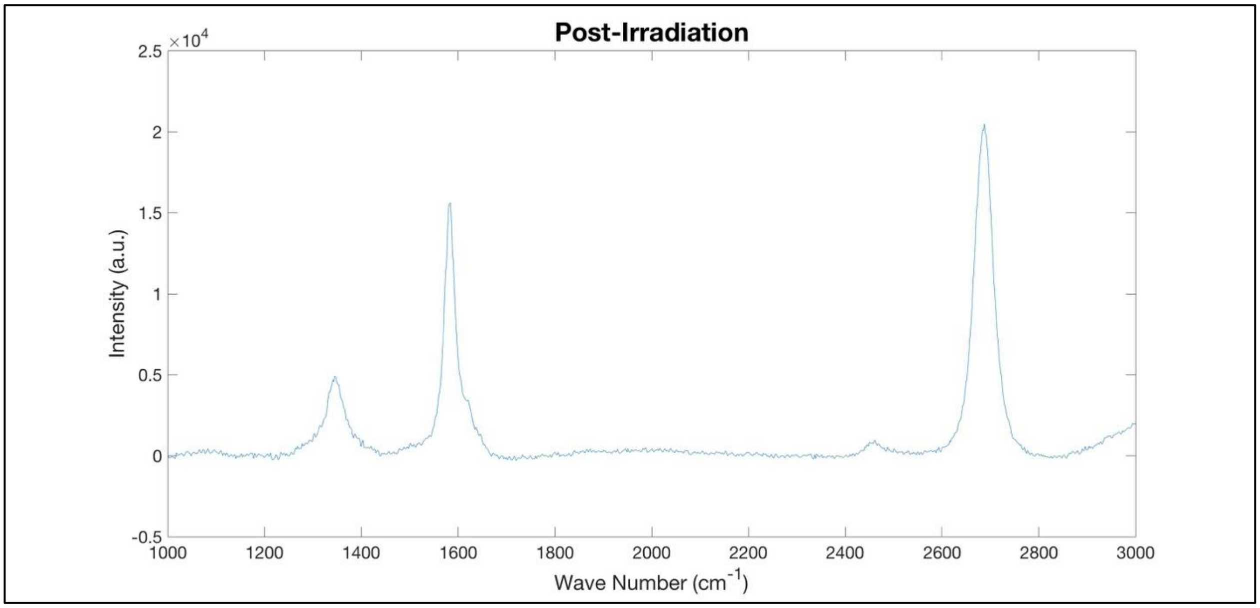

Figure 6-6. The Raman spectrum post irradiation for the most extreme conditions of 30 keV, 900°C, 6x10^{18} *He*$^{+}$*/cm*^{2}*, shows the 1550 and 2700 cm*$^{-1}$ *graphene peaks. The 1350 cm*$^{-1}$ *has not increased in relative size after irradiation meaning that the graphene has not suffered significant residual damage from the energetic helium.*

Graphene also, when grown somewhat beyond one layer, shows nearly ideal passivation behavior, because the second layer of graphene begins to grow at the grain boundaries of the first layer. This strengthening of the monolayer could also explain the low interaction with bombarding ions, making the sheet resistant to damage [141,163].

6.3.2 – SEM Analysis of Tungsten Surface

Figure 6-7 shows how the surface structure is affected due to irradiation of the samples. There is still some damage to the tungsten due to the implantation of ions, as seen for the high fluence case. For the lower fluence, the surface changes are not visible across the sample surface; the samples coated with the graphene show significant improvement on their surface morphology when compared to the bare tungsten, leading to a decrease in surface area, lower particle sputtering, and consequently, lower mass losses.

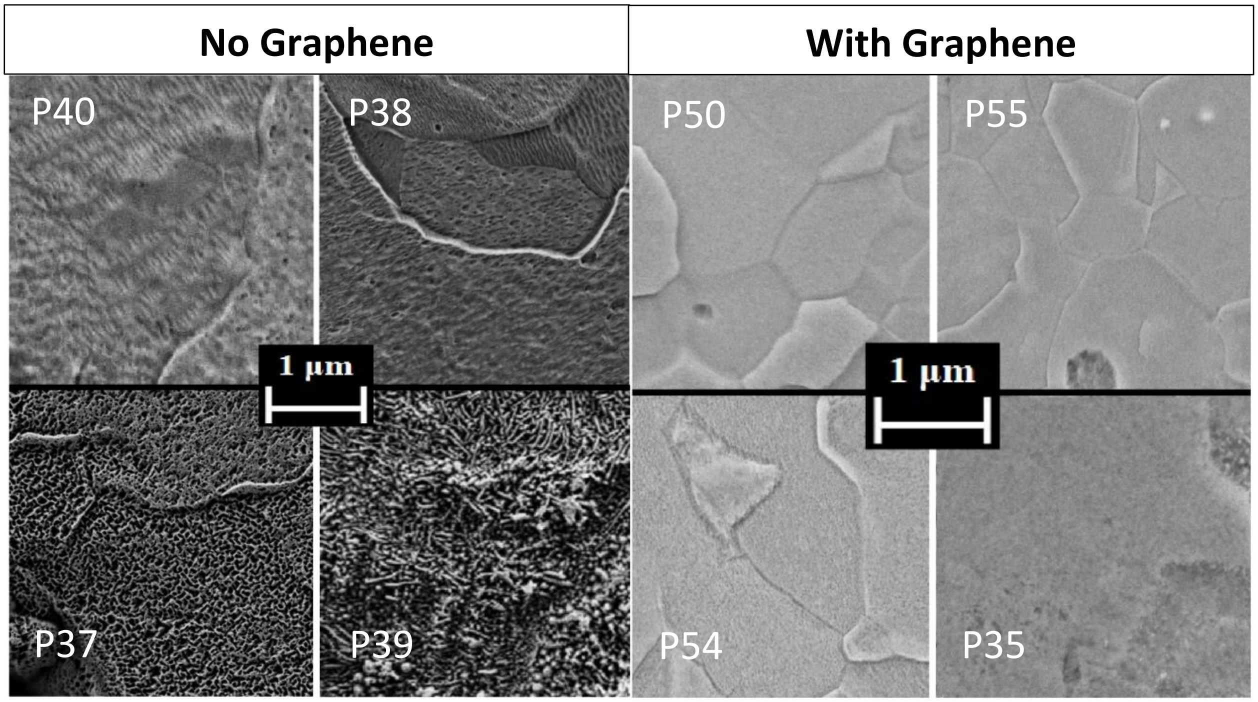

Figure 6-7. Surface morphology changes to the tungsten under intense helium irradiation at 30 keV, 900°C. The fluence conditions for the samples are summarized in Table 6-1.

6.3.3 – Mass Loss Analysis of Tungsten Samples

The SEM observations are supported by the mass losses as reported in Figure 6-8. At fluences ranging from $6\text{x}10^{17}$ $\text{He}^{+}/\text{cm}^{2}$ to $6\text{x}10^{18}$ $\text{He}^{+}/\text{cm}^{2}$, the mass losses are reduced almost by a factor of 10. These results imply that although the graphene may not entirely protect the tungsten from all damage, it might extend its lifetime to fluences at which a typical PFC would operate at.

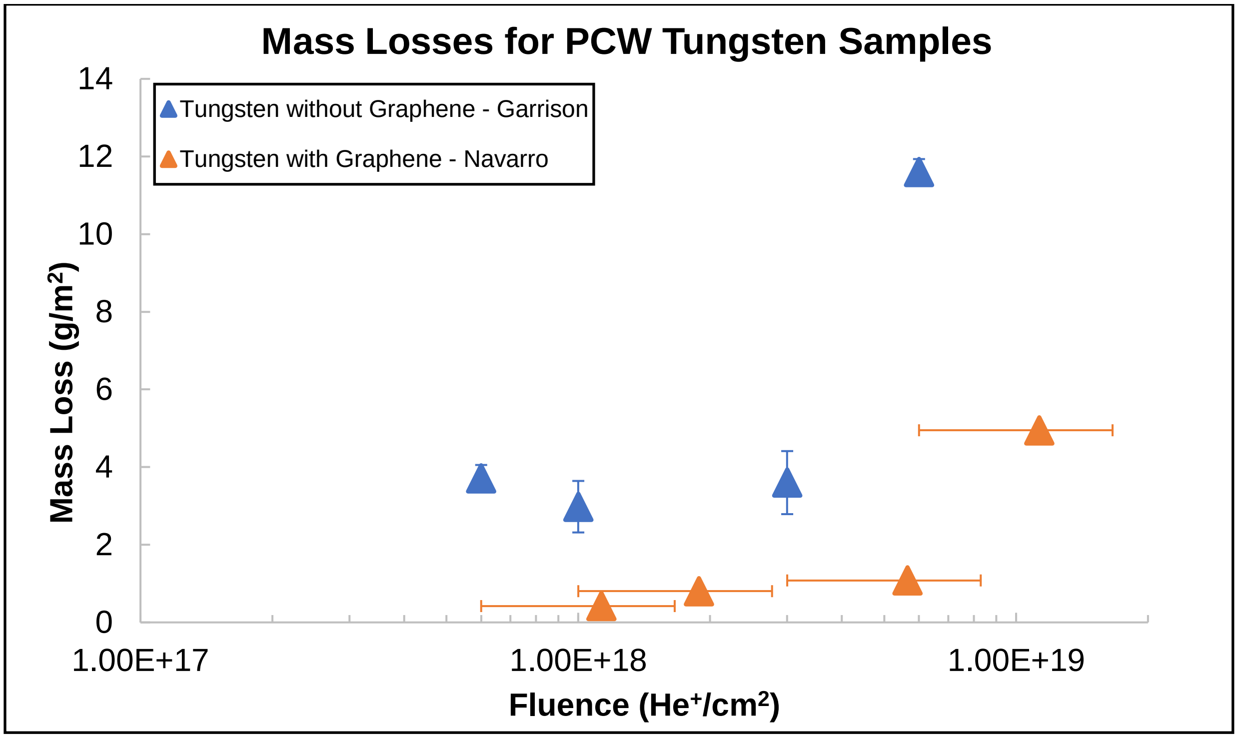

Figure 6-8. Mass losses of the graphene covered W compared to the mass losses of the bare W. There has been a significant reduction in the loss due to this coating, indicating a possible improvement in PFC lifetime.

When graphene is heated, instead of relaxing and expanding at high temperatures, it compresses, making the interatomic spacing narrower [92-93]. This is opposite to what happens to almost every other material, BCC tungsten or HCP titanium for example. Low-energy neutral atoms and molecules cannot penetrate undamaged graphene, although low-energy ions can generally pass through it. Helium implanted at low energy (<200 eV) into uncoated tungsten produces "fuzz", possibly due to helium diffusion and the resultant pressure at the surface producing tendrils of tungsten that grow beyond the original surface level [43]. Before graphene was discovered, 2D structures were thought to be unstable due to the dependence of the melting point on the thickness of a material [3], and this still holds for tungsten. However, the tungsten particulates cannot escape through the graphene, due to not having enough energy to break the carbon bonds, and because they are too massive to escape through the carbon lattice. Numerous studies have discussed the re-deposition and melting of tungsten particles due to their small size and direct contact with the heated substrates [8,9,115], the small amounts of tungsten particulates trying to escape could be diffusing back onto the surface, which would explain why the final exposed surface looks similar after heating and irradiation as well as why there's no significant damage on the graphene layer. This can explain why at the highest fluence, the surface looks smeared and there is zero organization and grains are difficult to identify; the tungsten particulates are diffusing back onto the surface instead of escaping.

6.4 – Graphene as a Surface Coating for Polycrystalline Tungsten, PISCES Exposure

Six samples were available for testing in the PISCES facility. These were 2.54 cm diameter disks with 2 mm thickness. Only half of all the sample surfaces were coated with single layer-graphene (Figure 6-9) in order to perform studies on the same surface.

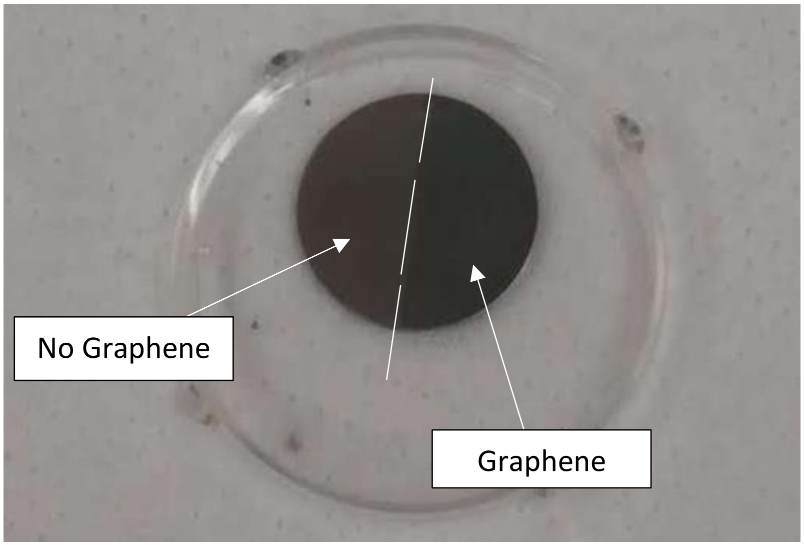

Figure 6-9. Tungsten disk samples for PISCES exposure.

The stage on which the samples were exposed on was negatively biased to 150 V or 50 V. The floating potential in the plasma amounts to -10 V, which, combined with the stage bias, imparts an energy of 140 and 40 eV to the ions bombarding the surface. The sample temperature was set through the plasma flux and the rate of cooling for the stage. Unfortunately, without actively cooling the stage, the experiment is not able to achieve the same fluxes between deuterium and helium, resulting in a lower substrate temperature for samples irradiated by deuterium.

Table 6-2. Sample Exposure Parameters for the surface of graphene half-coated tungsten samples.

Sample	**Species**	**Energy (eV)**	**Fluence (ions/cm^2)**	**Temperature (°C)**
GP1	He	140	$3.6\text{x}10^{21}$	800
GP2	He	140	$3.1\text{x}10^{20}$	800
GP3	He	40	$2.0\text{x}10^{20}$	800
GP4	D	140	$1.3\text{x}10^{21}$	600
GP5	D	140	$1.4\text{x}10^{20}$	600
GP6	D	40	$1.0\text{x}10^{20}$	600

6.4.1 – Raman Spectroscopy of Graphene

Because of the limited sample pool, there are pairs of samples for this analysis. Samples GP1 and GP2 are analyzed together due to the same exposure energy and varying fluence. GP2 and GP3 were exposed to the same fluence, but varying helium ion energies. This also applies for the deuterium exposures of sample pairs GP4-GP5 and GP5-GP6. In Figure 6-10, the damage ratio of similar fluence samples for different sample energies is examined. At lower energies, close to the binding energies of the carbon atoms in the membrane, the graphene damage for helium irradiated samples seems to increase as the energy is decreased due to the longer interactions at low energies. Deuterium damage remains nearly constant for 40-140 eV irradiation, similar to the laser heating tests of neutral deuterium in 0, although for those tests, the deuterium was not ionized.

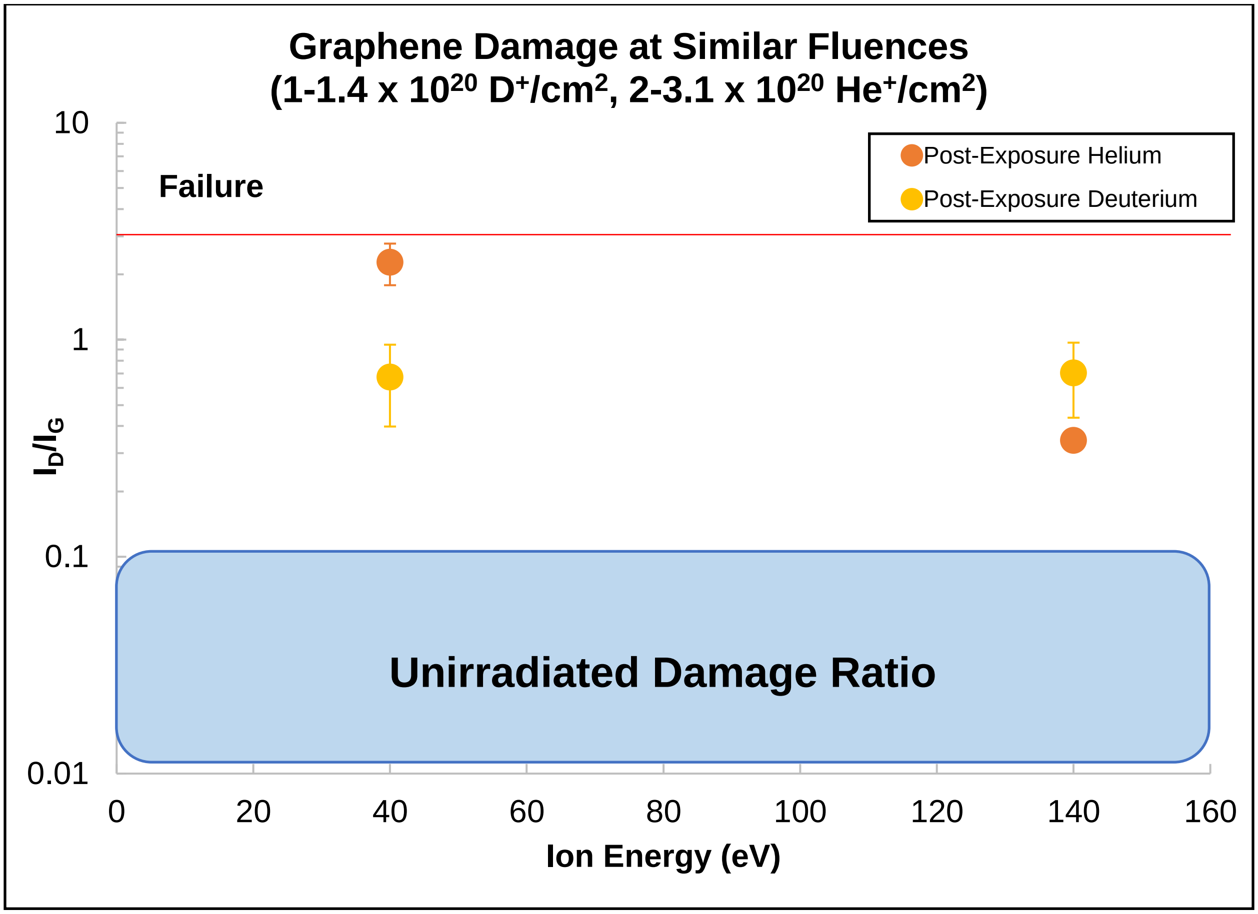

Figure 6-10. Graphene damage as a function of energy for PISCES samples. Similar fluences were used for deuterium and helium exposures. This data compares sample pairs GP2-GP3 and GP5-GP6.

In Figure 6-11 we examine pairs of samples for this analysis as well, in this case, we examine the damage ratio at 140 eV over different fluences. For this energy, the graphene damage for helium irradiated samples completely destroys the graphene film at the highest fluence, and a more significant dependence on this variable occurs. Deuterium damage to graphene seems to saturate as well after a certain fluence, similar to the laser heating tests of neutral deuterium exposure to graphene on tungsten discussed in 0.

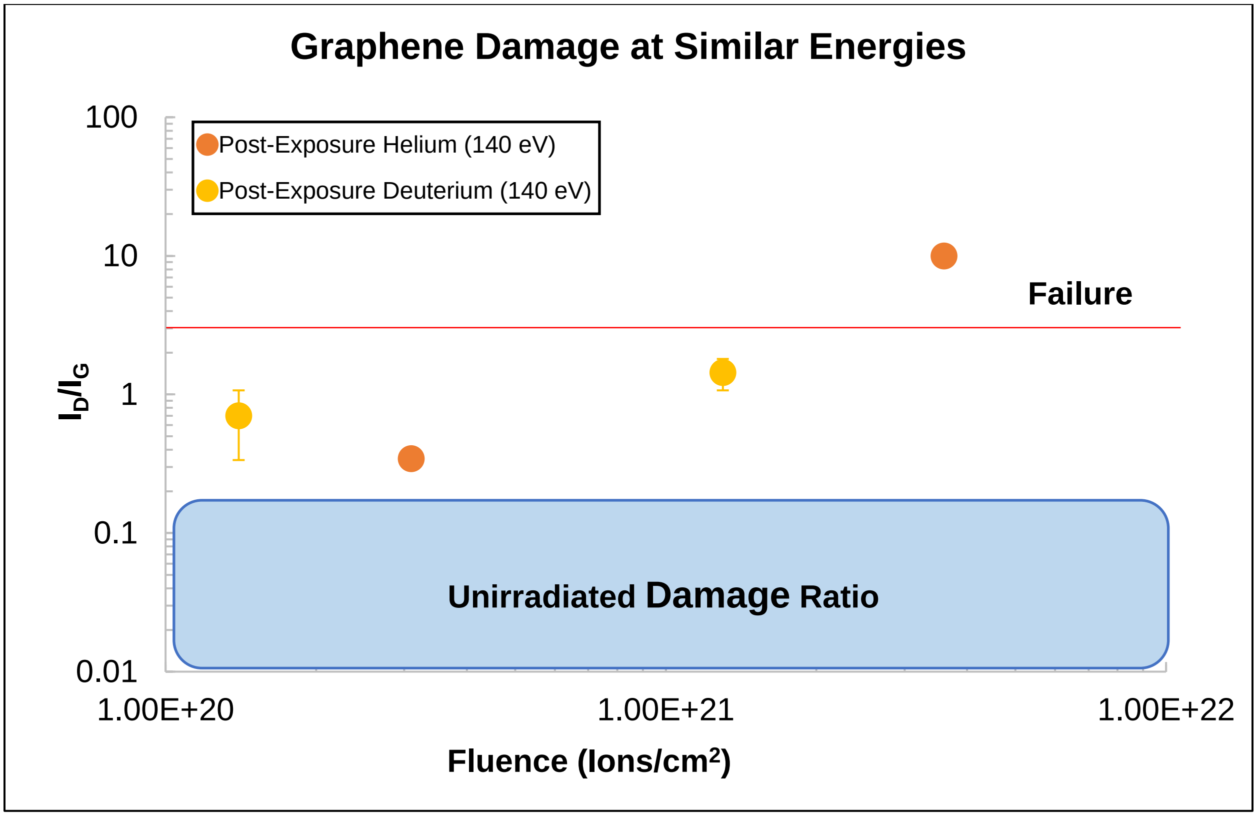

Figure 6-11. Graphene damage as a function of fluence for PISCES samples. This data compares sample pairs GP1-GP2 and GP4-GP5.

6.4.2 – SEM Analysis of Tungsten Surface (After exposure in PISCES)

Images were taken of the surfaces of these helium implanted samples at high magnification in order to see the morphology evolution on the samples. Figure 6-12, Figure 6-13 and Figure 6-14 demonstrate the fuzz growth with respect to the exposure energies and fluences. It is thought that these go through four implantation stages: roughening, bubble formation, bubble diffusion, and release of buildup, creating finer fuzz structures at higher fluences.

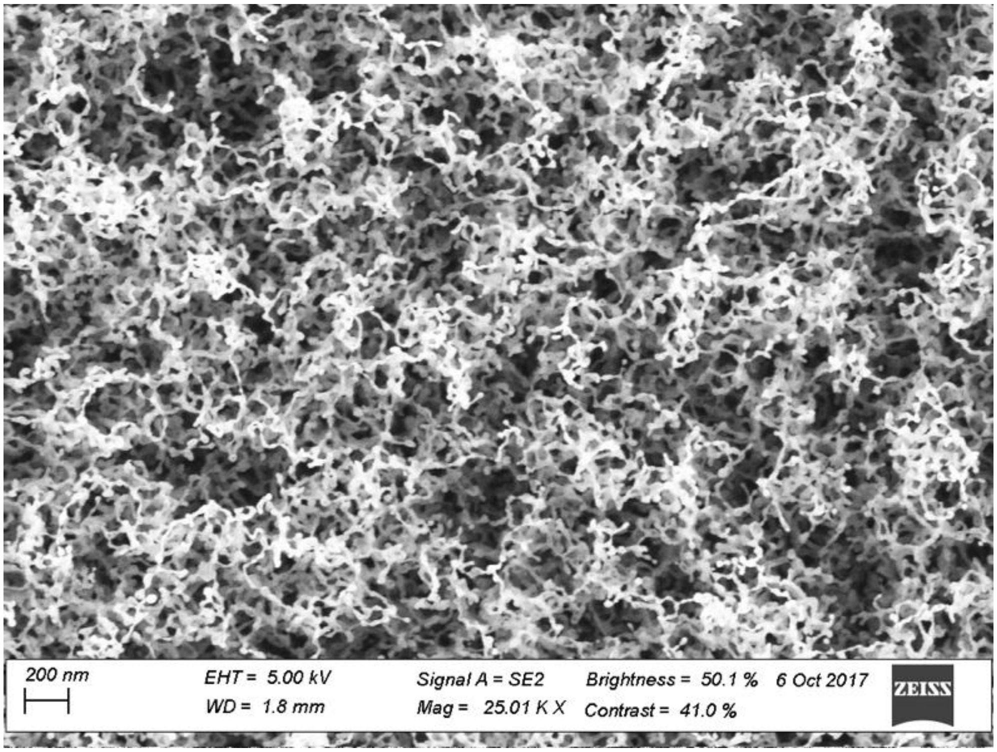

Figure 6-12. Surface morphology of uncoated side of GP1 (140 eV, 3.6x10^{21} He^+/cm^2, 800°C) after exposure in PISCES.

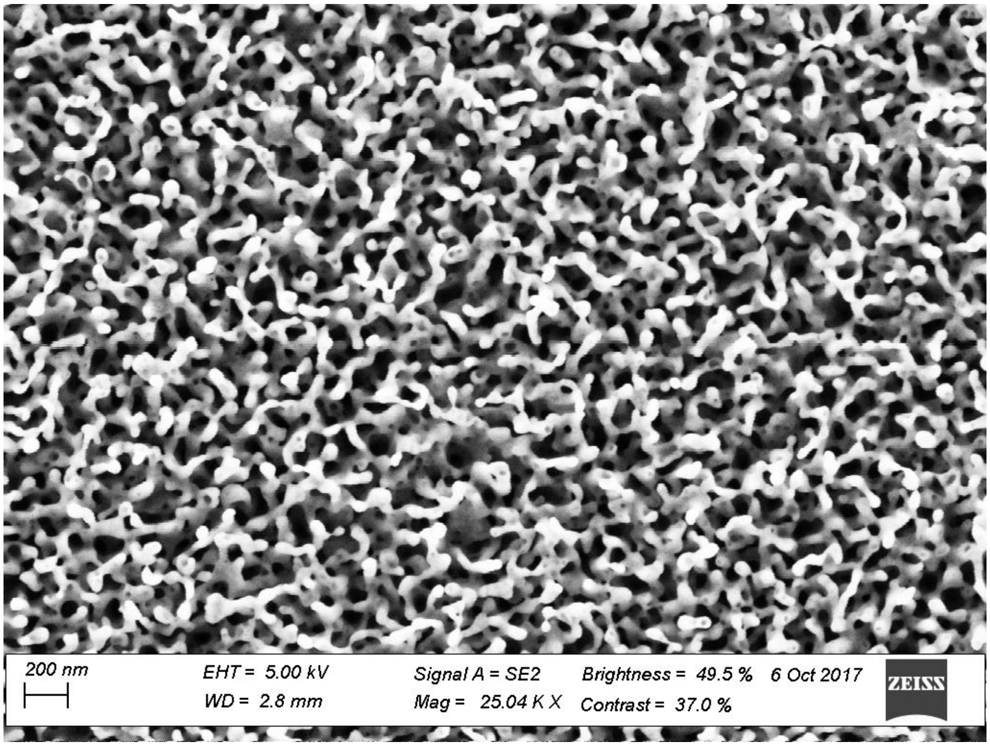

Figure 6-13. Surface morphology of uncoated side of GP2 (140 eV, 3.1x10^{20} He^+/cm^2, 800°C) after exposure in PISCES.

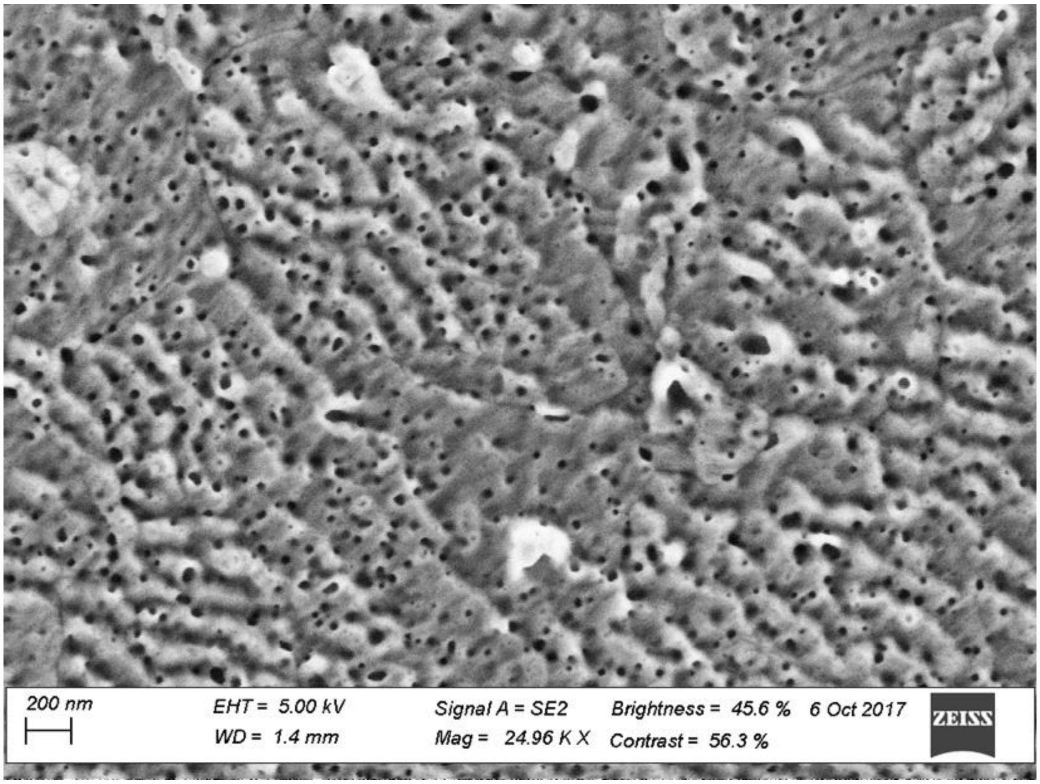

Figure 6-14. Surface morphology of uncoated side of GP3 (40 eV, 2.0x10^{20} He^+/cm^2, 800°C) after exposure in PISCES.

Images were taken of the surfaces of these deuterium implanted samples at high magnification in order to see the morphology evolution on the samples. Figure 6-15, Figure 6-16 and Figure 6-14 illustrate the roughening of the embrittled surface with respect to the exposure energies and fluences. Deuterium exposure does not create structures as dramatic as helium does, however it does contribute to some roughening of the surface, creating channels for helium to escape during operation of a fusion device.

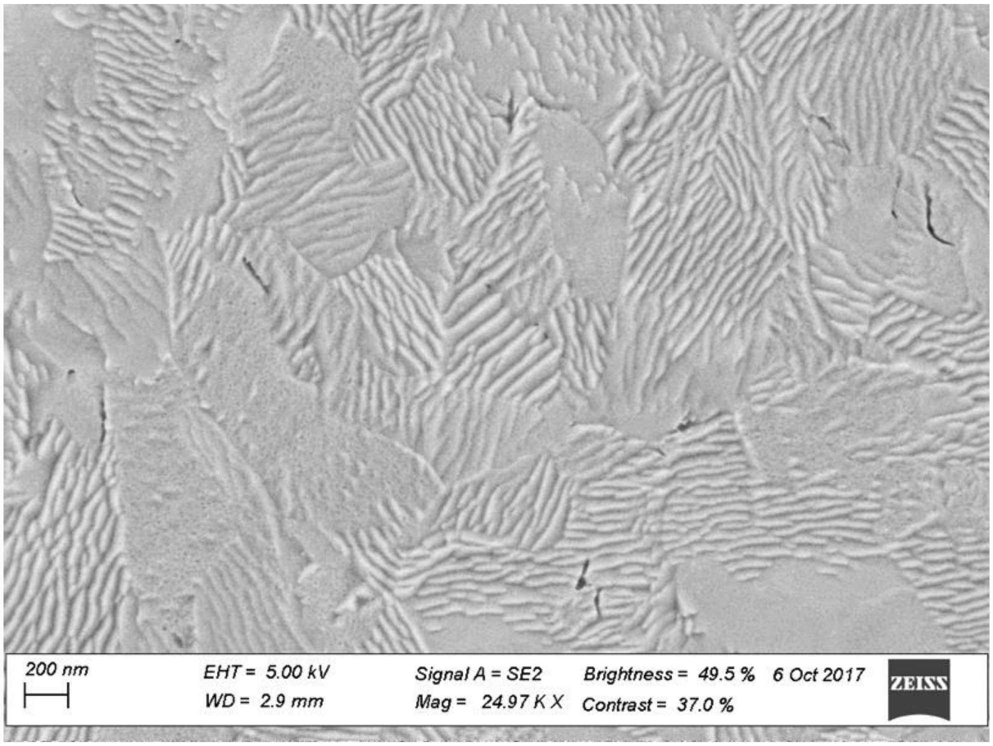

Figure 6-15. Surface morphology of uncoated side of GP4 (140 eV, 1.3x10^{21} D^+/cm^2, 600°C) after exposure in PISCES.

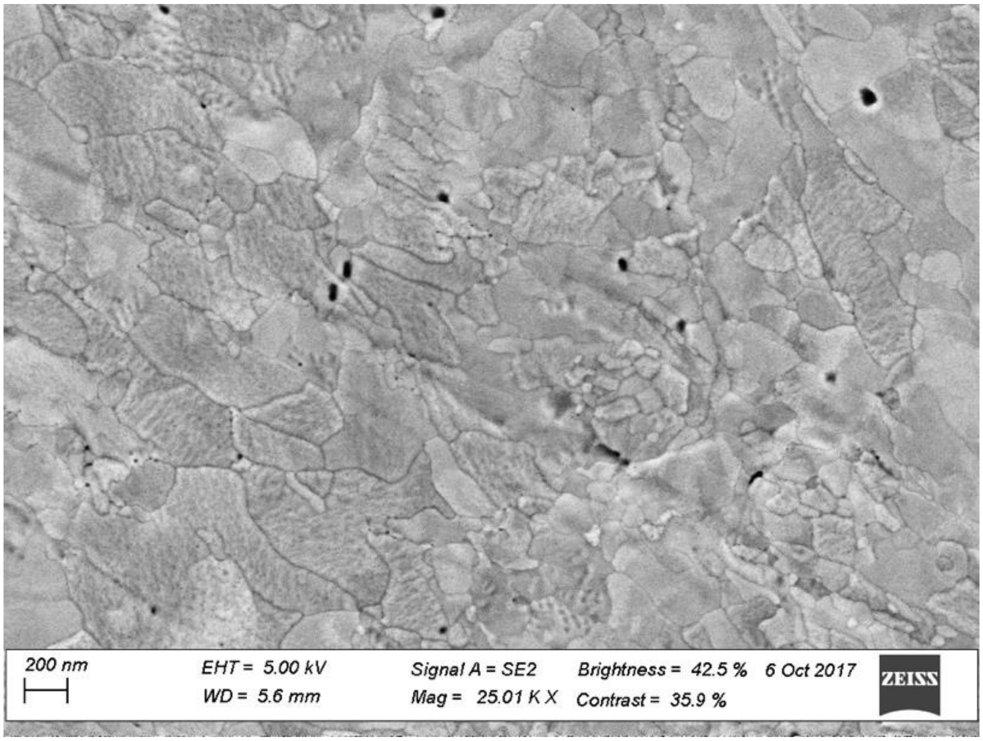

Figure 6-16. Surface morphology of uncoated side of GP5 (140 eV, 1.4x10^{20} D^+/cm^2, 600°C) after exposure in PISCES.

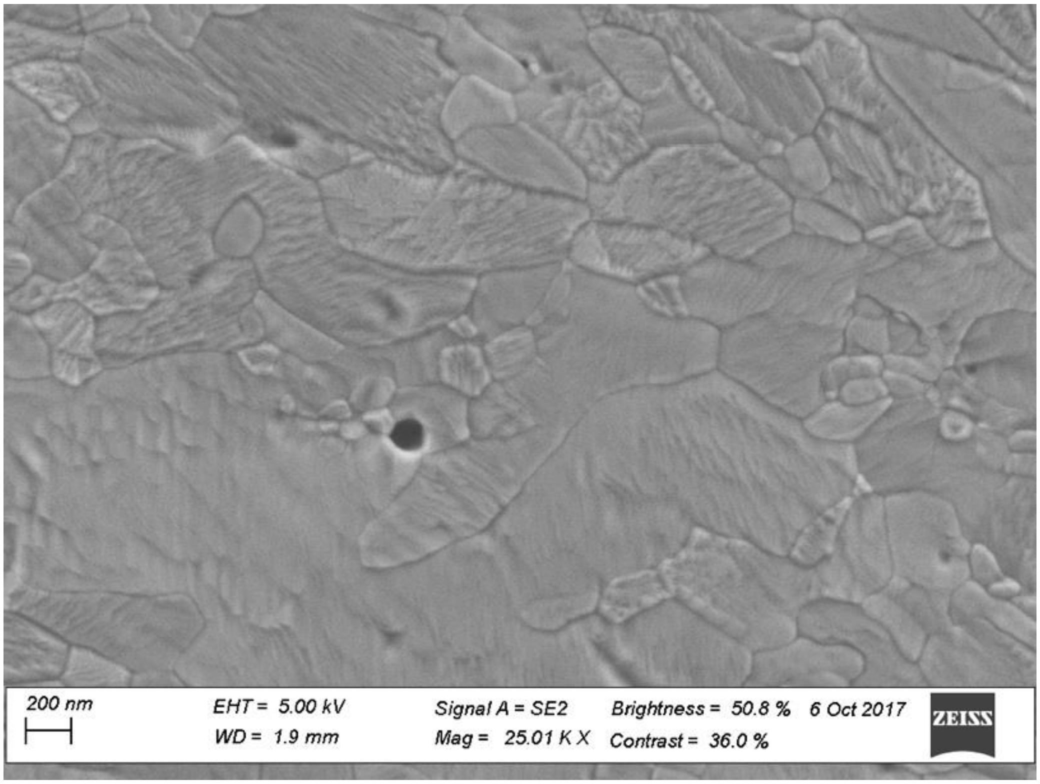

Figure 6-17. Surface morphology of uncoated side of GP6 (40 eV, 1.4x10^{20} D^+/cm^2, 600°C) after exposure in PISCES.

Much higher magnification image of samples GP1 and GP2 (Figure 6-18 and Figure 6-19) show the presence of helium nanobubbles within the fuzz tendrils. The structures also seem to "thin" out as the fluence is increased, which can eventually lead to a critical thickness, leading into evaporation. Although the goal was to prevent the fuzz growth on the graphene coated side, the Raman results show that for the high fluence case, the graphene membrane was completely destroyed, and did not prevent entirely the evolution of the fuzz formation.

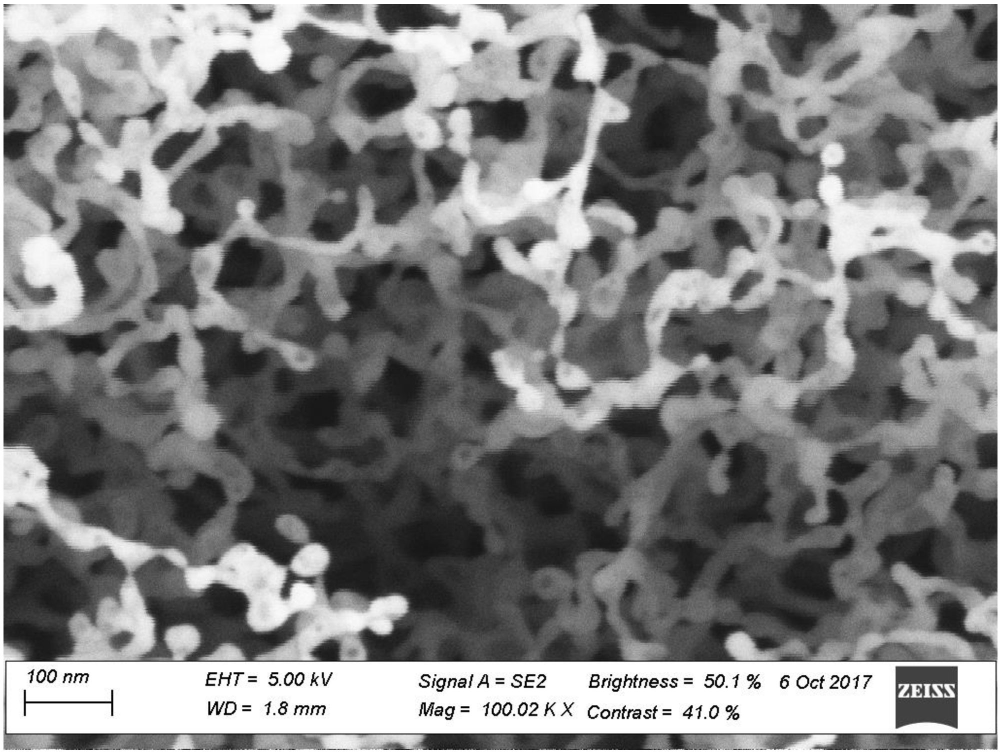

Figure 6-18. High Magnification image of tungsten fuzz on sample GP1 on the graphene coated region in PISCES.

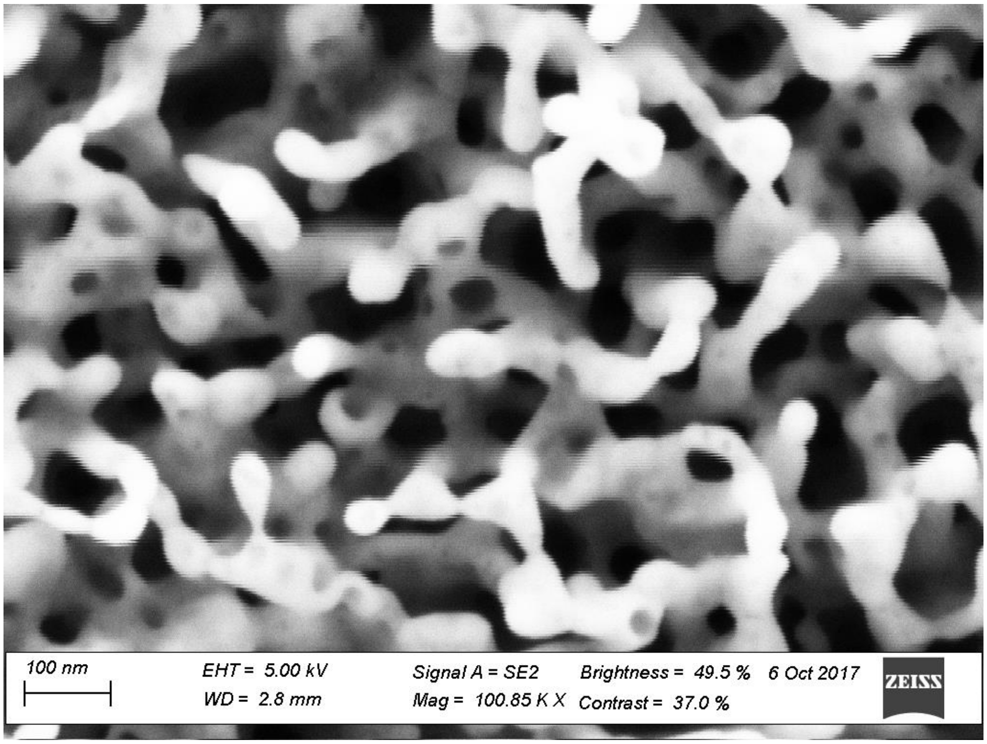

Figure 6-19. High Magnification image of tungsten fuzz on sample GP2 on the graphene coated region in PISCES.

6.4.3 Focused Ion Beam Analysis of Fuzz Growth

Although we still see fuzz forming on the surface of tungsten, the application of the graphene membrane did show some positive results. A focused ion beam was able to cut into the substrate revealing its cross section, allowing measurement of the thickness of these structures. Multiple areas were probed on both sides of the samples in order to average out thicknesses, and Figure 6-20 and Figure 6-21 demonstrate how some of these were cut into and measured. The graphene coated side for both GP1 and GP2 (the only samples with fuzz structures on the surface) slowed down the diffusion of helium and erosion of the tungsten. Table 6-3 summarizes the results of these measurements, revealing a significant slowing down of the growth.

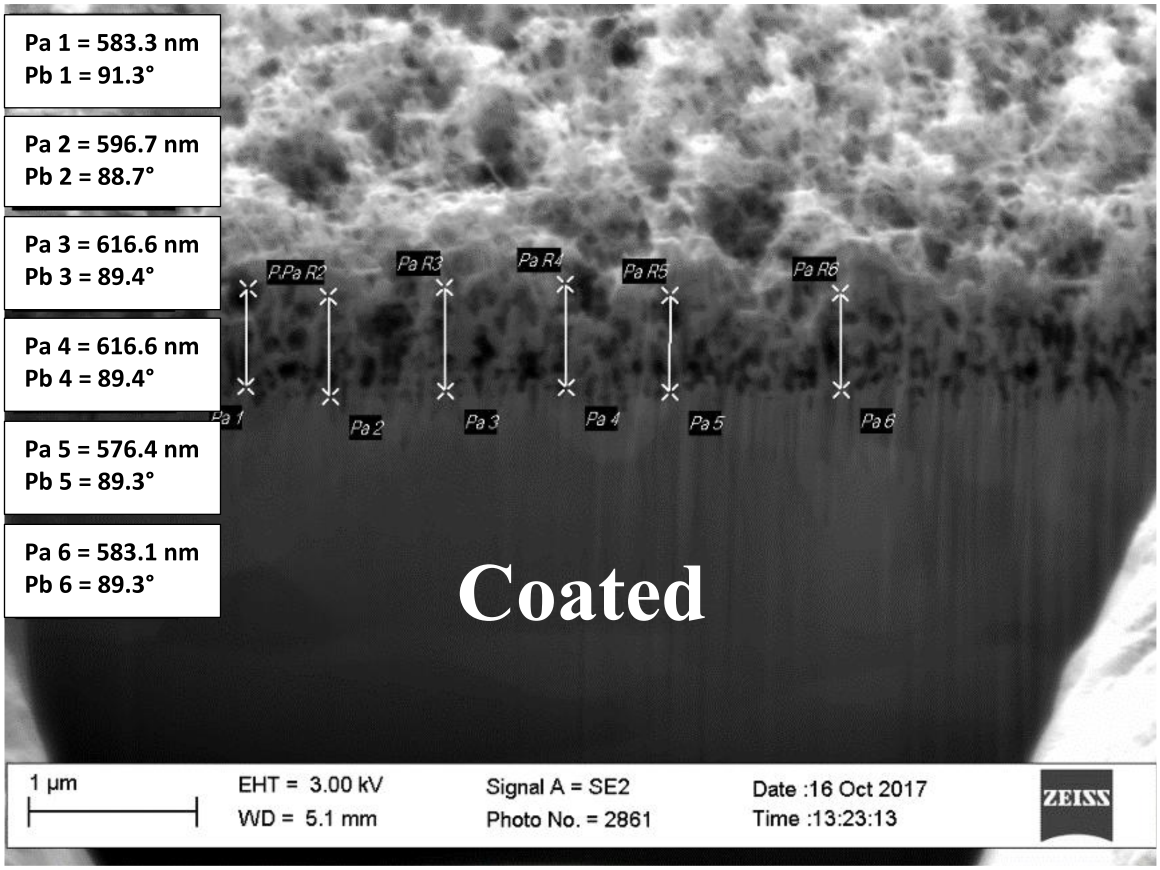

Figure 6-20. Measurement of fuzz thickness on the left side of the image performed on the Focused Ion Beam cut of the graphene coated region of sample GP1 in PISCES.

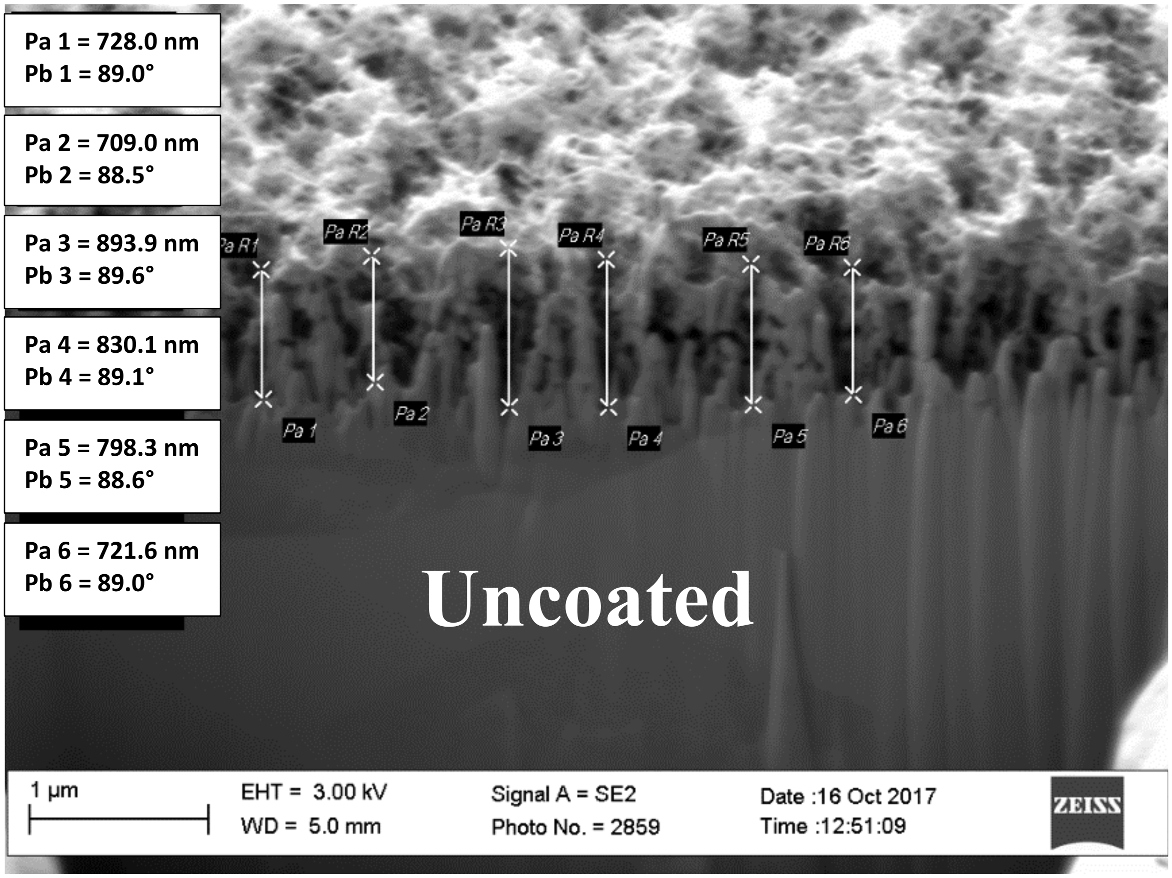

Figure 6-21. Measurement of fuzz thickness on the left side of the image performed on the Focused Ion Beam for the uncoated region of sample GP1 in PISCES.

Table 6-3. Measurements of fuzz thickness for PISCES samples.

Average Fuzz Thickness (nm)						
Sample Number	Energy (eV)	Fluence (He^+/cm^2)	Substrate Temperature (°C)	Coated Region	Uncoated Region	Percent Decrease
GP1	140	3.6×10^{21}	800	582 ± 41	784 ± 63	26 ± 8
GP2	140	3.1×10^{20}	800	240 ± 32	394 ± 28	39 ± 9

6.4.4 – Residual Strain Analysis on Half-Coated Graphene-Tungsten Samples

In order to perform a strain analysis on these samples, the X-ray exposure needs to occur at an angle close to normal to the sample surface. This is because the Poisson ratio is utilized in the analysis and it requires the cross-plane strain to determine the in-plane strain (i.e. in a state of biaxial stress, this is the strain which would cause cracking). 0 shows the procedure and methodology for performing these measurements. In order to determine if the stress is isotropic, the samples are rotated with respect to its axis of rotation ϕ at angles 0°, 45°, and 90°. These results showed that the interplanar spacing of crystallographic planes or d-spacing did not change with angle, so what remains is to change the tilt of the detector and X-ray source, called the angle ψ. Figure 6-22 shows how the residual stresses were determined for Sample GP5. The slope of these curves, long with the elastic properties of the material are used for the calculation.

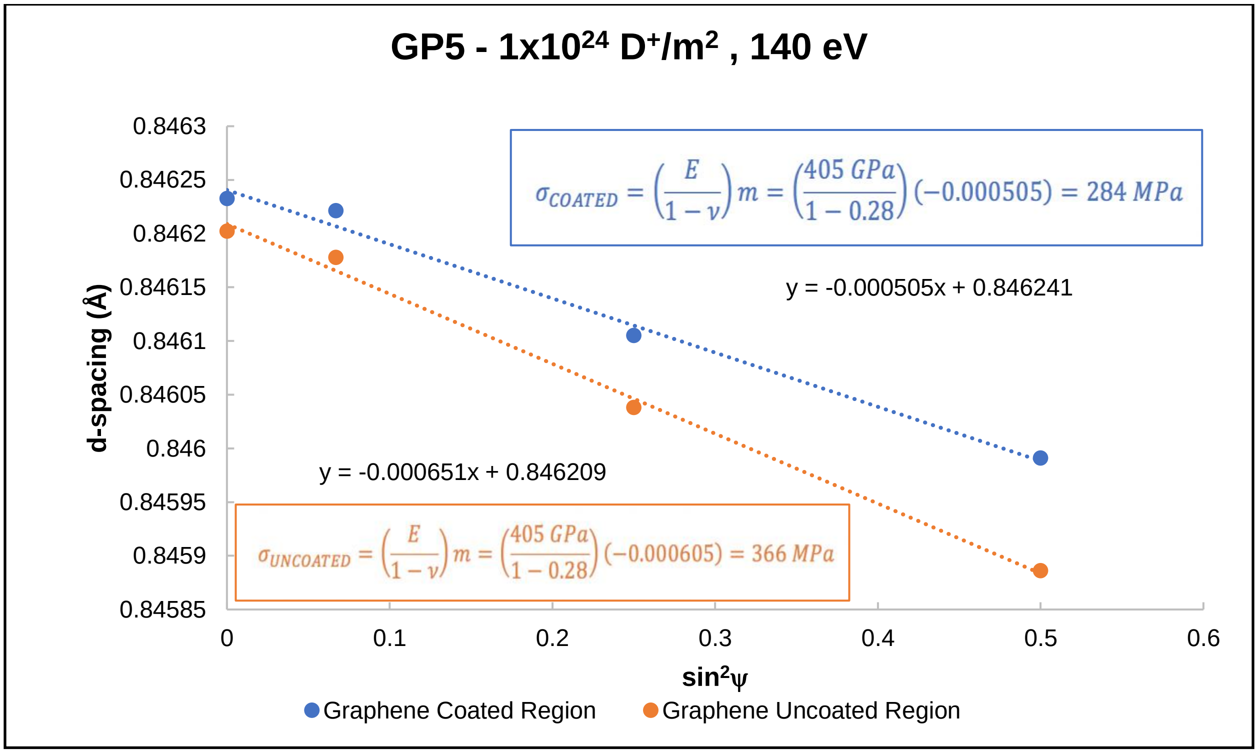

Figure 6-22. Measurement for a residual stress analysis of sample GP5 irradiated in PISCES.

Figure 6-23 shows the residual stresses for the helium implanted samples. Because the fuzz structures are still forming, there is no significant difference between stresses of the coated and uncoated sides in the bulk, so one can assume the helium is diffusing evenly across both the sample surface and bulk. However, there is a shift from compressive (negative) to tensile (positive) stresses in the material as the fluence is increased. Most materials that are irradiated are in a compressive state because its volume is not expanding while being implanted with helium, which is also true in this case. However, once the sample starts releasing these stresses in other ways (fuzz forming, removing excess material), these stresses shift to tensile and the structure relaxes. There is also a large difference between implantation at 40 and 140 eV due to the same number of atoms being implanted across a smaller distance, causing the helium density to be higher, leading to larger stresses.

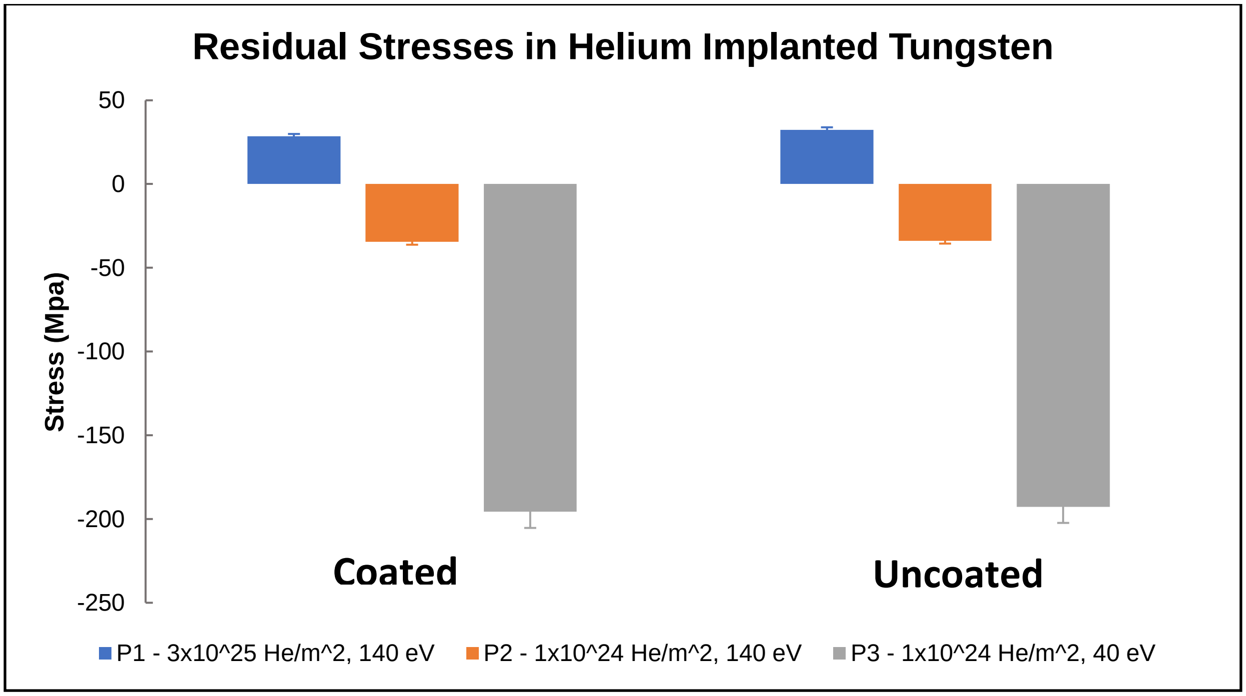

Figure 6-23. Residual stresses for helium implanted samples in PISCES. Of particular note is the transition from compressive to tensile stresses in the bulk as we increase the energy and fluence of the samples increases.

In the case of deuterium embrittlement (Figure 6-24), the change in residual stresses is somewhat more significant. The Raman data implies that the graphene is still acting as a barrier, and the residual stress data suggests that it prevents deuterium from implanting into the material, and this translates into the graphene coated tungsten side having lower residual stresses, as opposed to the bare tungsten. The ionization fraction in the plasma column is close to 10% (private discussion with Prof. Russ Doerner), which suggests that 90% of the deuterium implanted are neutral particles, and the graphene could potentially be blocking the neutral particles from penetrating into the tungsten as demonstrated in previous studies [96].

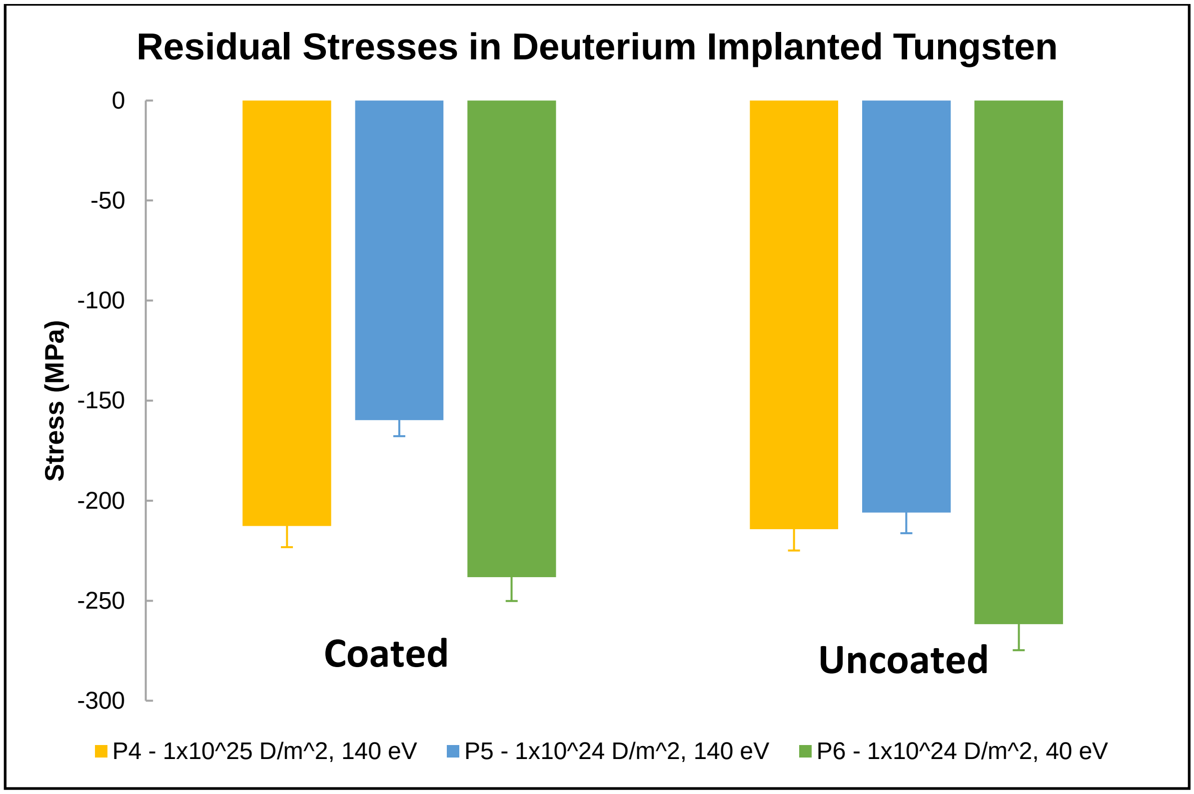

Figure 6-24. Residual stresses for deuterium implanted samples in PISCES. Of particular note is the reduction of stresses in the bulk, which leads to deuterium embrittlement.

6.5 – Graphene as a Surface Coating for Polycrystalline Tungsten, C-2W Exposure

6.5.1 – Raman Spectroscopy of Graphene

Two samples were placed side by side in the C-2W southern outer divertor (Figure 3-9). These were exposed over a period of two months at an average ion energy of approximately 100 eV to a fluence of 3.2x10^{22} D^+/m^2. The surface temperature data for these samples remained close to 0 ºC (at the temperature the cryopumps kept the chamber surfaces). These discharges also involve the introduction of numerous impurities onto the sample surface, as well as some damage to the graphene. Sample W2 was uncoated while sample W6 was fully coated with graphene and the exposures introduced more defects into its lattice, as summarized in Figure 6-25. Some sample shots of the raw and integrated data used to determine the deuterium ion temperature and flux is shown in Appendix B.

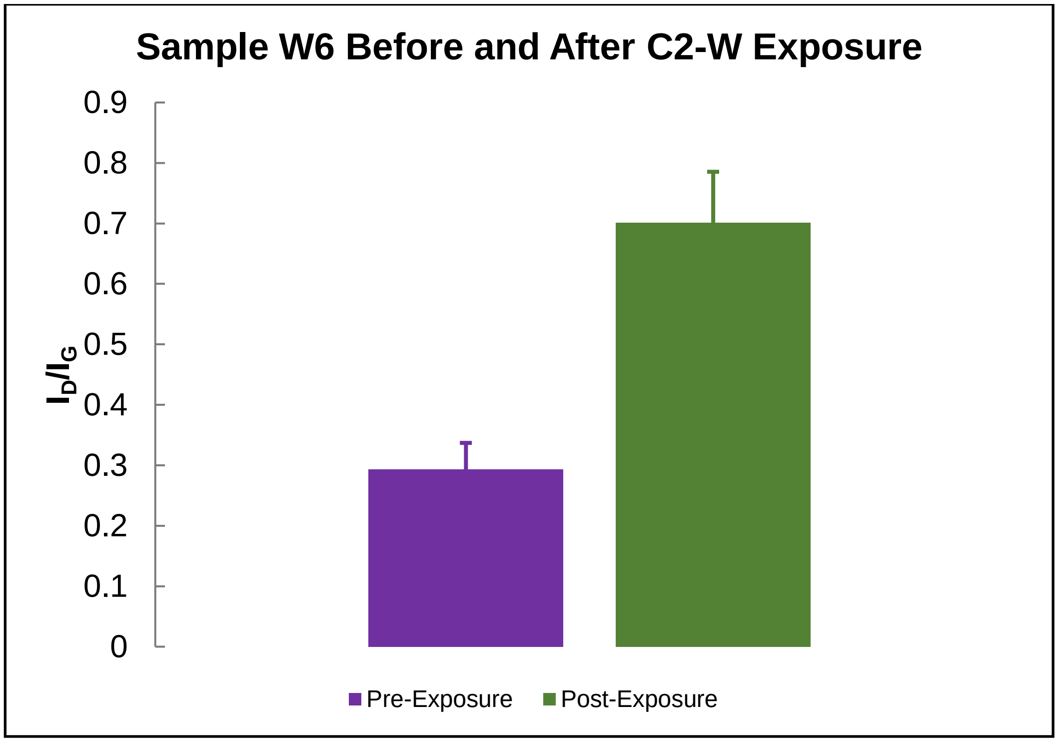

Figure 6-25. Graphene Damage ratio growth for sample W6 after C-2W exposure.

6.5.2 – SEM Analysis of Tungsten Surface

SEM analysis provides with an insight into surface morphologies and impurity deposition on the surface of these samples (Figure 6-26 and Figure 6-27). There are no morphologies developing on the surface of the tungsten on either surface. Initially, the grains are visible on both samples prior to the irradiations, but once the exposures are done, a thick layer of impurities covers the grains, and any information on the tungsten surface damage is lost. However, due to the samples being bombarded by deuterium, little change in the surface was expected, even at 2-3 orders of magnitude higher in fluence, as seen in the PISCES samples.

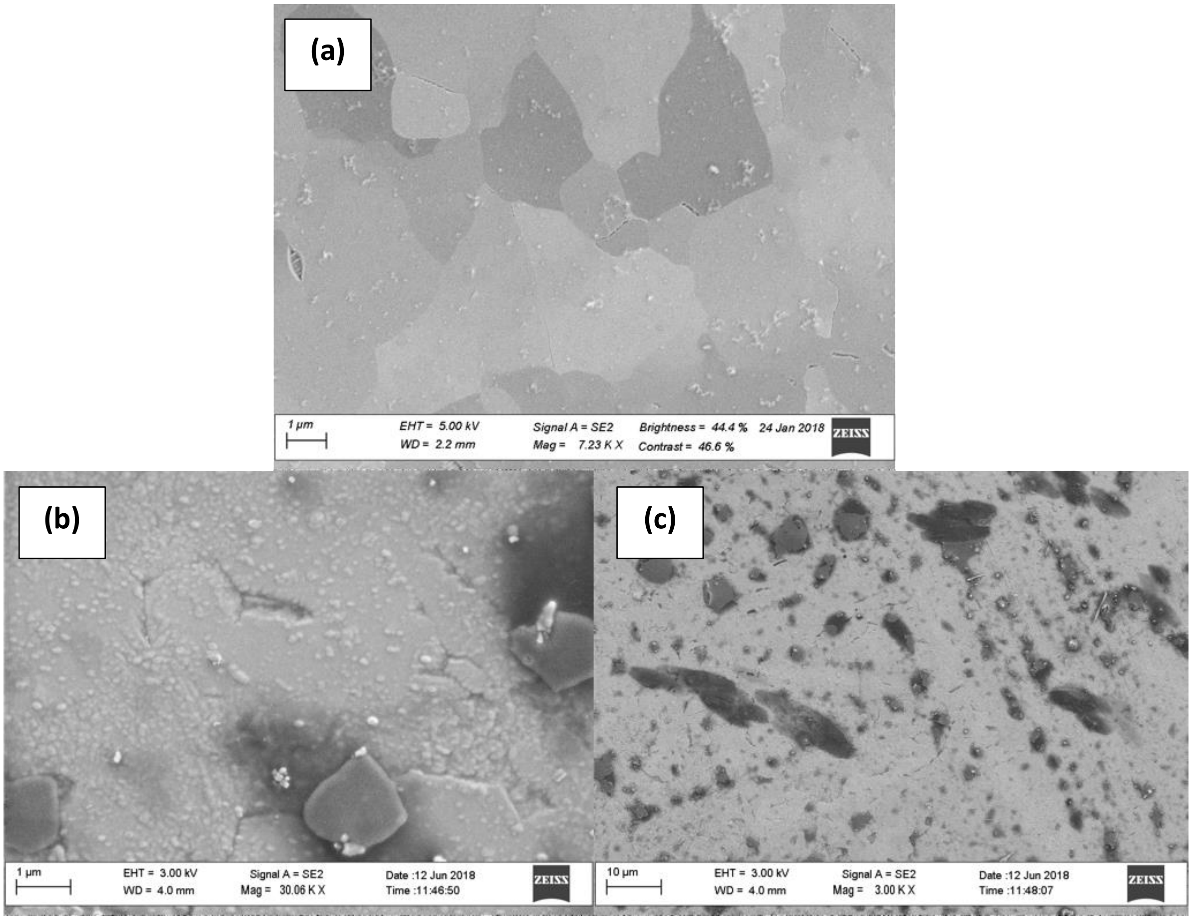

Figure 6-26. SEM image of W2 sample surface irradiated in C-2W. In general, the surface is much rougher and covered with more impurities than the graphene coated sample W6. (a) Unirradiated sample. (b) High magnification of irradiated sample surface. (c) Low magnification of irradiated sample surface.

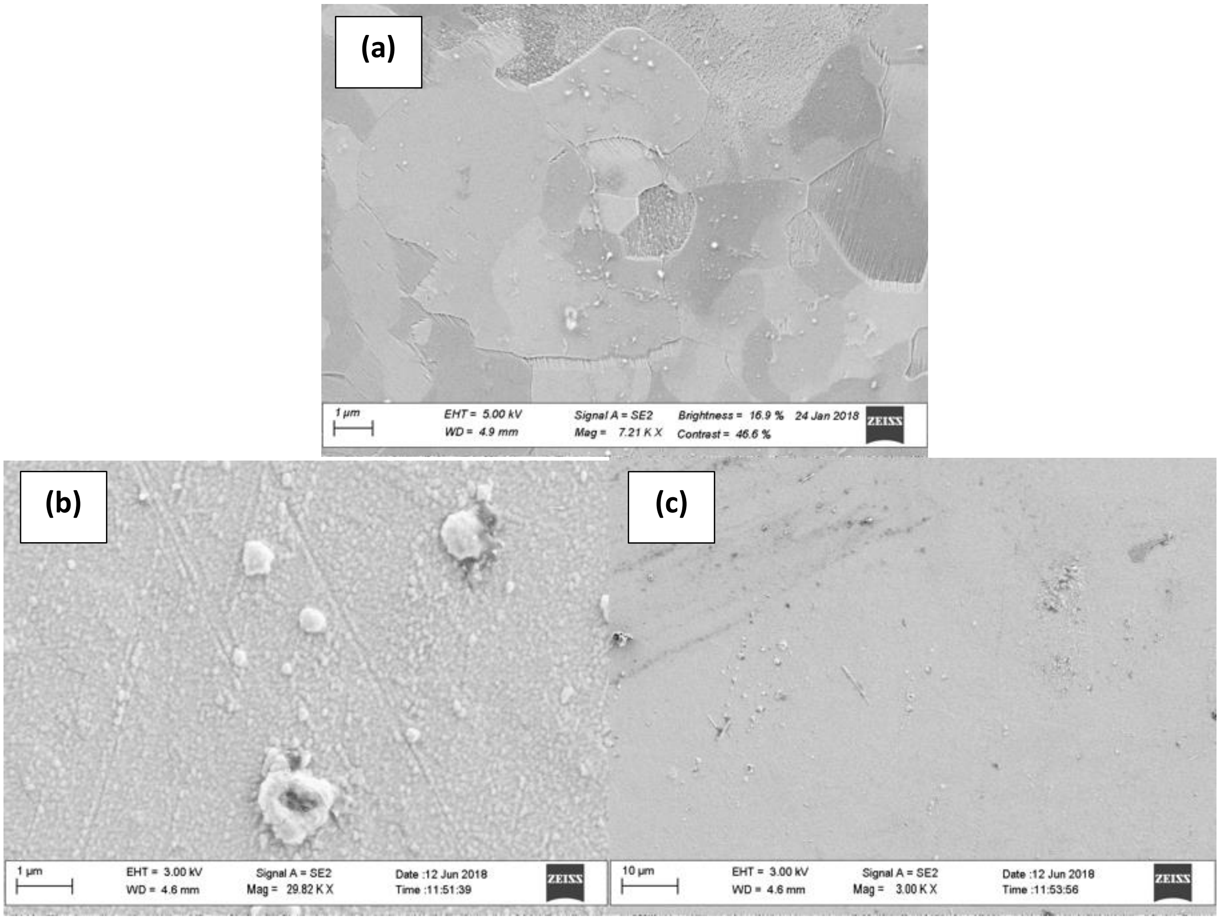

Figure 6-27. SEM image of W6 sample surface irradiated in C-2W. In general, the surface is much smoother and covered with less impurities than the uncoated sample W2. (a) Unirradiated sample. (b) High magnification of irradiated sample surface. (c) Low magnification of irradiated sample surface.

Overall, a comparison of different regions across both samples demonstrate that graphene-covered surfaces are much smoother than bare ones. This means that the amount of impurities present is less, and clustering of these is diminished.

6.5.3 – Mass Gain Analysis of Tungsten Sample

The samples were weighed before and after the exposure, and this revealed that the samples had in fact gained weight instead of losing it (Figure 6-28). These could have lost weight during the implantation and gained more weight due to impurity deposition, but deuterium exposures have not led to weight loss in past studies.

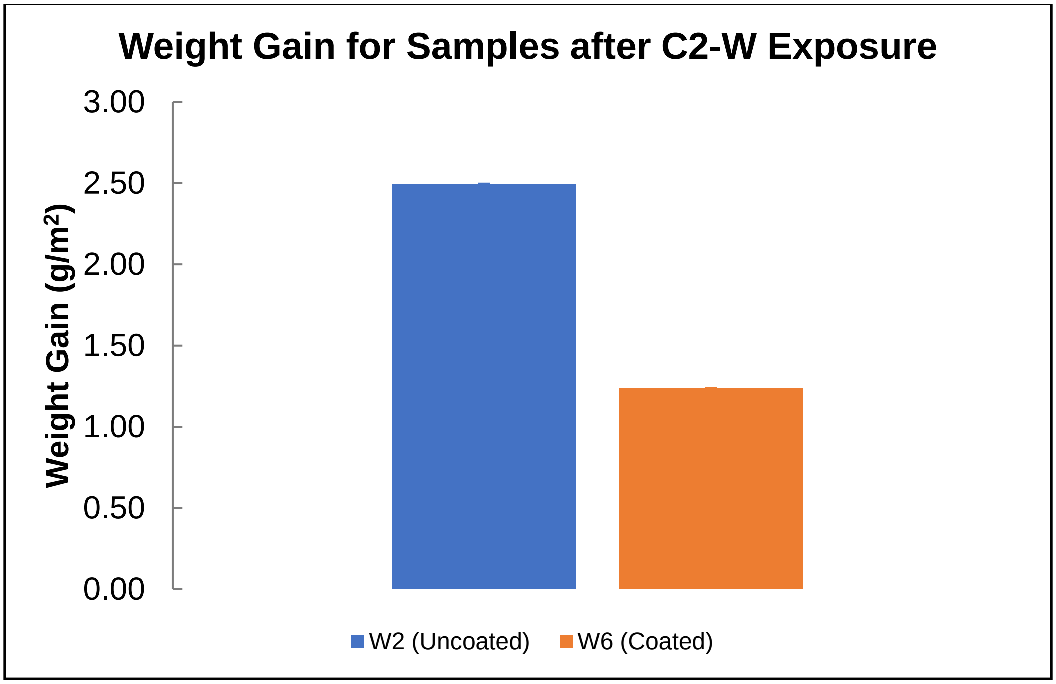

Figure 6-28. Weight gain comparison for exposed samples in C-2W.

6.5.4 – XPS Analysis of Impurity Layer on Sample Surface

Because of this mass gain, it is necessary to determine what impurities have been deposited onto the substrates. X-Ray Photoelectron Spectroscopy (XPS) is a straightforward way to test the composition of the samples. Before and after spectra of the samples (Figure 6-29) show the differences in the distribution of elements on the surfaces. Titanium is present due to its use as a getter for reaching ultra-high vacuum. The rest of the divertor is made out of stainless steel, which explains the presence of iron and chromium. Large carbon and oxygen impurities are always present on samples that have not been handled in a clean room. So far, there is no explanation for the presence of sodium. While tungsten was initially present in the spectrum, after exposure, the thickness of the impurity layer (262-528 nm) washes out the tungsten signal, since the resolution of the XPS is only about 10 nm, perpendicular to the surface (depth profile). With knowledge of material properties, the thickness of each layer can be estimated;

Table 6-4 summarizes the results. Many materials are not compatible with graphene growth onto them. This might explain why the impurity layer is much thinner for the graphene-coated sample.

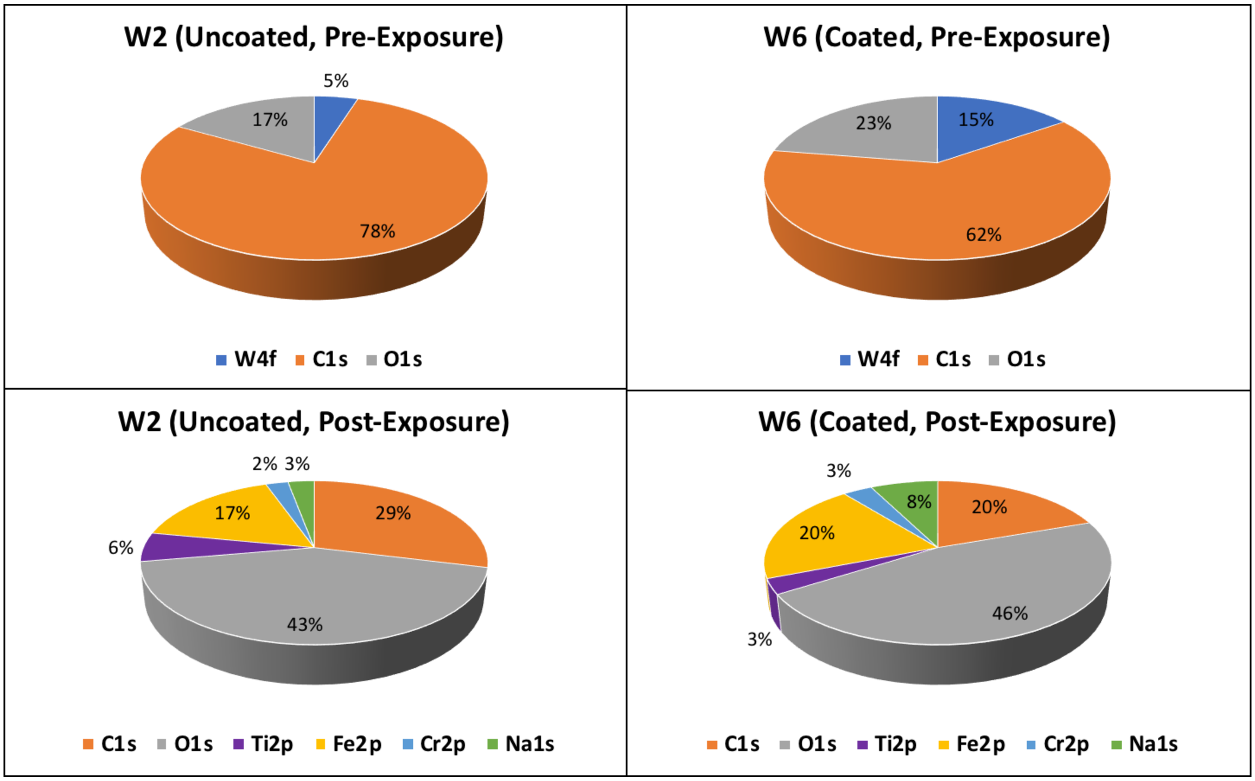

Figure 6-29. Compositional analysis of sample surfaces before and after exposure in C-2W. Oxygen was not considered in any analysis. This data was averaged over three randomly selected regions.

Table 6-4. Impurity layer thickness calculation for samples after exposure in C-2W.

Layer Thickness (nm)	
W2 (Uncoated)	W6 (Coated)
528±25	262±5

6.6 – Graphene for the Reduction of Secondary Electron Emission

Two samples were each half-coated with graphene in order to perform a contrast analysis to determine a virtual secondary electron yield (SEY) from the surfaces. The settings for the setup and data collection of the SEM are summarized in 0. A white light interferometer test was used to probe the surface to see if there were any significant features, such as slanting and mesas, that could affect the results. Across the marker points (cross in Figure 6-30) there are no significant changes in height or features that affect the results. All the dark spots are features introduced by polishing the surface. For data acquisition, primary electron energies in the SEM were varied from 800 eV up to 10 keV to produce secondary electrons. In order to introduce less variables in the comparison, all contrast and brightness data was fixed, as well as working distance for the samples. Image regions were then probed using ImageJ™ to determine contrast values for each area and the spread or standard deviation of the average measurement. These were then averaged from both samples and plotted in Figure 6-31.

At lower energies, the data shows that graphene appears to have a strong suppression effect on the secondary emission, as high as 53%. Tungsten secondary emission yields peak around 600 eV. It is due to the setup of the SEM settings that the SEY becomes more significant at energies approaching this value, there are more secondary than backscattered electrons, as opposed to the higher primary electron energies where backscattered electrons dominate, and the suppression effect due to the graphene membrane is less pronounced.

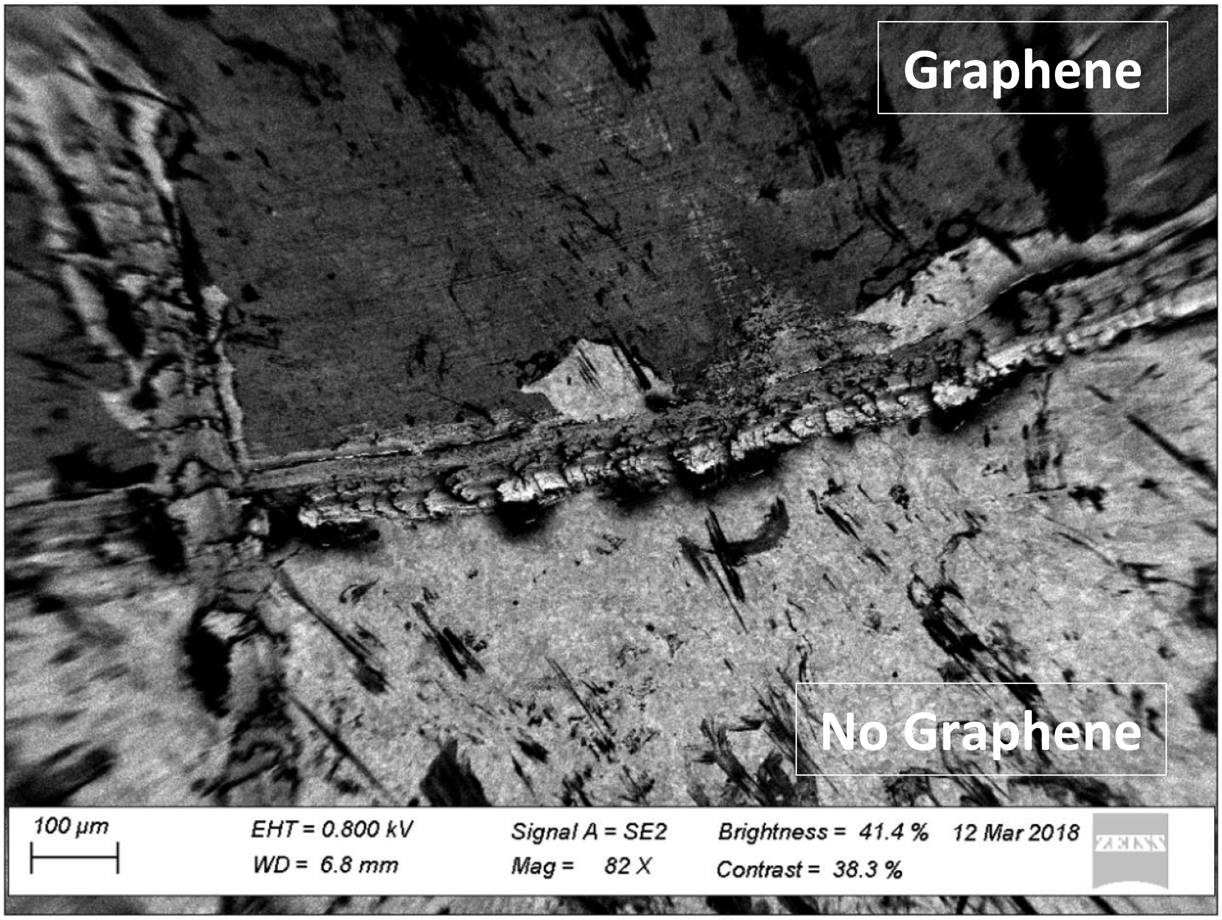

Figure 6-30. Unirradiated half-coated graphene sample for secondary electron emission measurements. Notice the darker region at the top due to the presence of the graphene impurity layer. A fiducial scratch mark separates the two regions.

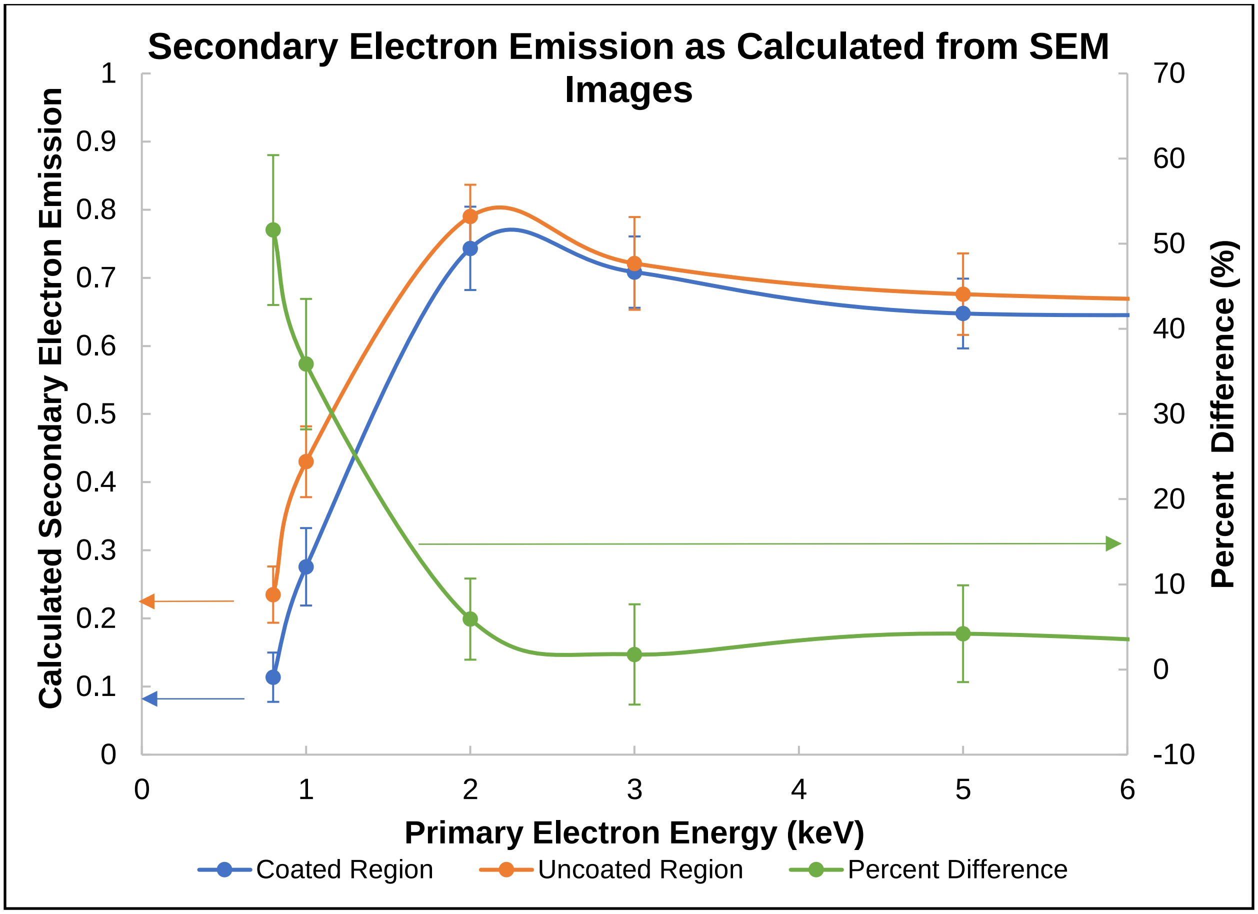

Figure 6-31. Calculated secondary electron emission determined from image contrast data on the SEM.

This page is intentionally left blank.

Chapter 7 – Discussion for Graphene as a Coating for Plasma Facing Components

The following chapter will address the results and interpretation for all the sections covered in Chapter 6. It will describe how these different studies come together to gain a better understanding of graphene's reaction to ion bombardment when placed on a solid substrate.

7.1 – Graphene on Silicon Oxide, SiO_2 (100)

Prior to testing graphene as a coating for low sputtering materials, a study performed here demonstrated its performance as a coating for a brittle substrate with a high level of sputtering and good semiconducting properties, SiO_2. However, silicon oxide's poor physical properties appear to be a limiting factor when submitted to high energy deuterium ions. Figure 6-1 and Figure 6-2 shows the defect ratio for single layer graphene and bilayer graphene on silicon dioxide, respectively. These exposures were performed without any additional laser heating, which would encourage additional etching of the carbon atoms by the deuterium gas. For single layer graphene, neither fluence nor energy appears to have a significant effect on defect formation on the membrane. The lack of dependence on either parameter suggests that there is either a damage saturation to the lattice, or that much longer exposures need to be performed in order for graphene to lose all its structural stability and features in the Raman spectra. Damage to the membrane is a nonlinear process (some of the data in this thesis, such as that one presented at the end of this chapter suggests it could be exponential or asymptotic depending on the experimental parameters). As a rough estimate, the graphene vacancy fraction introduced in the single layer graphene by the irradiation of a deuterium plasma is 27%, compared to the single layer membrane that had 6% vacancies prior to exposure, and 33% for bilayer graphene. Previous studies have shown that graphene can retain its structural stability with 40% vacancies per unit area [32], which is above what the damage threshold was predicted to be in the present experiments.

After the exposure, the silicon dioxide surface looks highly damaged, even demonstrating millimeter sized pits in the ion beam center, indicating a significant amount of sputtering of material. The low threshold energies for sputtering of silicon oxide and large energy transfer (almost 25% of the deuterium energy gets transferred to the silicon with each collision) by the deuterium ions contribute to large damage cascades of atoms and surface sputtering, which, in large concentrations could break the graphene mesh, introducing defects and increasing the damage ratio. High defect concentrations make it more difficult to knock out carbon atoms, which can lead to the reduced vacancy growth. The formation of oxygen radicals during the heating and bombardment can also enhance the removal of carbon atoms.

Prior to any exposure, all the G bands for the silicon oxide samples were centered around 1600 cm^{-1}, with a full sp^2 hybridization according to the amorphization trajectory model. One distinct feature that differentiates graphene from other nano-graphitic structures is that for a perfect structure, the D-band is small, with a correlation length of ~20 nm in the case of all the graphene samples on silicon oxide. During ion bombardment, a large amount of silicon could be attempting to leave the material, and this in turn would severely damage the graphene mesh. The red shift in the G band of graphene (from ~1600 cm^{-1} to ~1550 cm^{-1}) suggests that the graphene structure was severely damaged, meshed together into an amorphous carbon mesh, and that further irradiation would be needed to remove most of the atoms on the SiO_2 surface.

7.2 – Graphene on Heated Tungsten with Deuterium Gas Present

The setup for this experiment is described in Section 6.2, and Figure 6-3 summarizes the results of these exposures. Only neutral deuterium at various pressures was fed to the system while a laser provided heating of the substrate. After the deuterium gas exposure, Raman spectroscopy demonstrated an increase in the damage peak of graphene corresponding to a smaller correlation length of 15 nm. There was no red shift in the G band for the graphene (the peak remained at ~1600 cm^{-1}). This means that according to the model from Figure 4-7, as well as the amorphization trajectory model, only single vacancies are being produced, which cause disorder in the lattice. Due to the presence of the hydrogen isotope, some sp^3 hybridization may also be occurring on the surface, and consequently, broadening of the D and G peaks. While some defects were produced (~9%), there is still a significantly higher deuterium fluence required to completely eradicate the carbon atoms from the surface of the tungsten.

7.3 – Graphene as a Surface Coating for Polycrystalline Tungsten, MITE-E Exposure

7.3.1 – Raman Spectroscopy of Graphene

Raman spectra were taken before and after exposures for comparison of the samples. Prior to exposure, the red shift of the Raman spectrum G band (centered at ~1585 cm^{-1}) indicated some amorphization of the membrane, however, the lack of growth of the D band, or change in the 2D band implied no changes within the structure due to irradiation, as seen in Figure 6-5 and Figure 6-6 for sample P35, which is the highest fluence case that was studied. The Raman spectra for the lower fluence cases ($< 6x10^{18}$ He^+/cm^2) also showed no changes in the peak heights and position, indicating that the helium ions implanted in the sample had very little interaction with the carbon atoms, maintaining a low defect ratio in the graphene sheet and a large correlation length (>20 nm), which is an indicator of good crystallinity after irradiation.

7.3.2 – SEM Analysis of Tungsten Surface

Figure 6-7 demonstrates the effect of having graphene on a tungsten surface during high energy helium ion bombardment. On the left, the images show the evolution of the uncoated surface morphology as a function of ion fluence, leading from roughening, to porosity and eventual "grass" growth. Multiple detailed studies [40,41,47,164] discuss the formation of the surface structures, with a proposed model [41] suggesting increased channeling through the lattice near the {100} crystal orientation, and therefore development of the grass. On the right, graphene coated samples from the same sample lot were exposed to the same conditions in order to determine graphene's effect on the surface morphology evolution. Upon inspection, there are no highly disordered structures evident except for some roughening of the surface. Because these are high energy helium ions, and graphene's significantly strong interactions with ions only occur in nearly head-on collisions for impact energies closer to the binding energy of the atoms, the helium penetrates the graphene and is implanted into the tungsten lattice. A helium collision with a first layer tungsten atom, imparts a maximum energy close to 2.5 keV, which leaves the helium with 27.5 keV to either penetrate into the material or be backscattered through the membrane and reimplanted, repeating the process until the discharge is terminated. The probability of backscattering of first layer atoms is low, and bombardment by high Z metal ions is highly destructive to the graphene membrane at both high and low energies[139]. Also, from the graphene spectra it is known that there is an insignificant amount of defects introduced into the membrane during the present experiments. This suggests that the helium ions are penetrating deep into the tungsten and diffusing through the lattice, with those reaching the surface attempting to escape or attempting to push the tungsten atoms to escape. However, the damage cascade may not produce enough energetic tungsten to break through the membrane. The backscatter probability for these tungsten particles, including those in the first layer is extremely low [165–168], which makes it even more difficult for the particles to leave their positions. The presence of the strained graphene layer prevents helium escape from the surface and, consequently, the development of the surface morphology. All these effects are summarized in Figure 7-1 for bare tungsten and Figure 7-2 for coated tungsten.

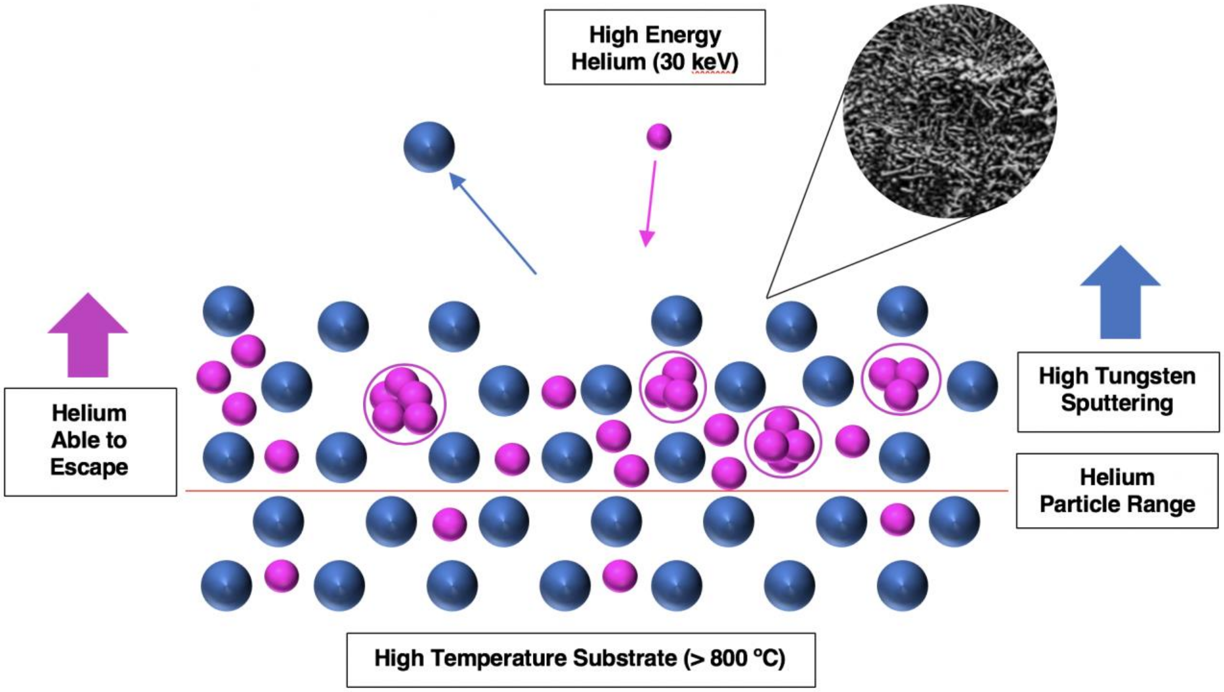

Figure 7-1. Helium ion bombardment of bare polycrystalline tungsten. A high energy helium ion has a small Coulomb cross section for scattering with tungsten atoms and slows down in the lattice due to electronic stopping. Helium builds up in the sub-surface layer and combined with high mobility due to high substrate temperatures, coalesces into helium bubbles. These bubbles diffuse to the surface and, combined with the sputtering of tungsten at high energies, creates "grass" structures along the surface. Enough helium needs to be implanted for these structures to develop, as much as 3x10^{18} *He*$^{+}$*/cm*^{2}*.*

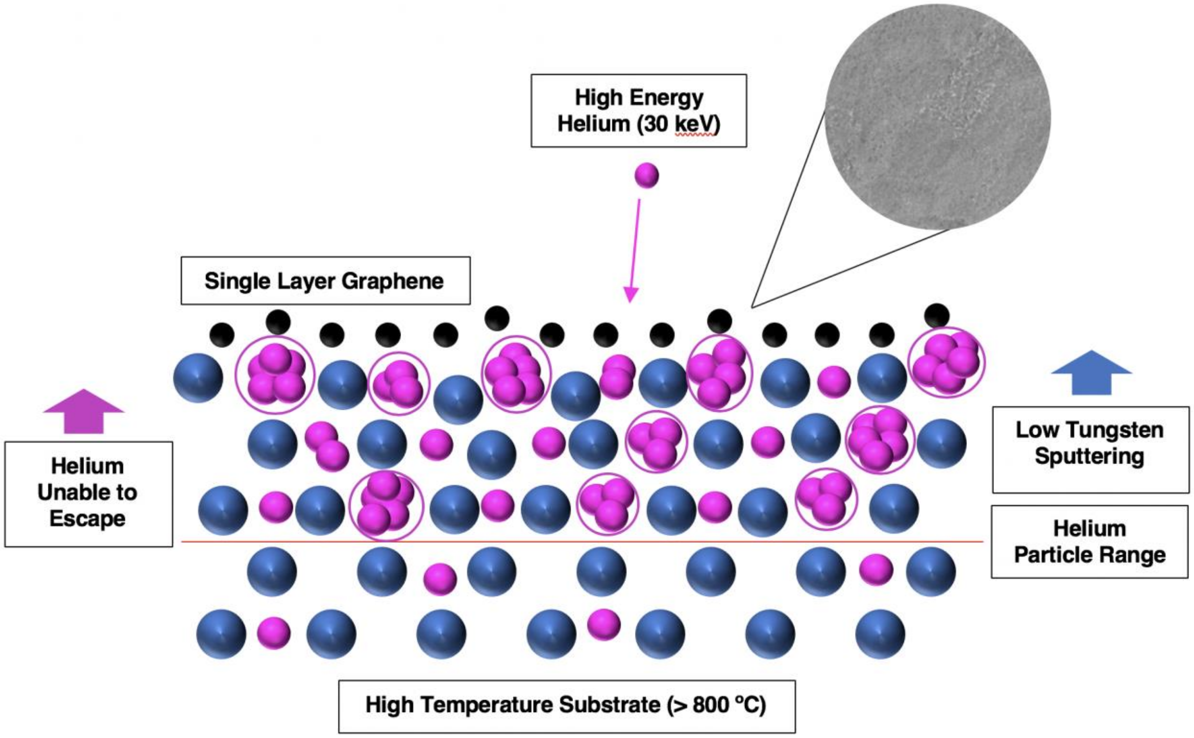

Figure 7-2. Helium ion bombardment of graphene-coated polycrystalline tungsten. A high energy helium ion has a small Coulomb cross section which decreases for scattering with tungsten and graphene carbon atoms and slows down in the lattice due to electronic stopping. Helium builds up in the sub-surface layer and, combined with high mobility due to high substrate temperatures, coalesces into helium bubbles. These diffuse to the surface but are prevented from escaping due to the added layer of the graphene atoms. This leads to a roughening of the surface but no large amounts of sputtering. The atoms attempting to escape do not have sufficient energy to introduce significant defects to the graphene membrane as demonstrated from the Raman spectra in Section 6.3.1.

The intermediate implantation fluences ($6\text{x}10^{17}$-$6\text{x}10^{18}$ He^+/cm^2) in these scans should lead to large helium clusters in the lattice, and some residual stresses. However, larger He fluences (> $1\text{x}10^{20}$ He^+/cm^2) are needed to have a statistically significant result and to justify the use of X-ray diffraction to determine these stresses. This type of analysis will be discussed in a subsequent section on the PISCES samples (Section 7.4.4), which were exposed to fluences at least two orders of magnitude larger than were the MITE-E samples.

7.3.3 – Mass Loss Analysis of Tungsten Samples

The main takeaway from the mass loss data of the samples is the diminished erosion caused by the graphene sheet. There is a lack of structures forming on the surface, but a significant mass loss (particularly for the higher fluence case) was measured. This is easily explained by the coverage area of the graphene. The circular ion beam covers an 8 mm diameter region [41] and the graphene sheet is 5 mm x 5mm square. Because of the 50% coverage fraction, there is still a significant part of the beam irradiating the bare tungsten, contributing to the mass loss of the sample at the high fluence (see Figure 6-8). The wide spread of the fluence data is a consequence of graphene’s hindering of secondary electrons from charged particle bombardment. For a secondary electron emission coefficient of γ secondary electrons per incident ion, the actual ion current is a fraction $1/(1+\gamma)$ of the measured (meter) current. However, the secondary electron emission is not known for helium on graphene coated tungsten so the lower limit ($\gamma = 0$) is used to give an upper limit on the fluence value, whereas the lower value is set from the correction used in the laboratory determined by Dev [169] ($\gamma = 0$).

7.4 – Graphene as a Surface Coating for Polycrystalline Tungsten, PISCES Exposure

7.4.1 – Raman Spectroscopy of Graphene

The exposures in the PISCES facility [20,42] were performed at extremely different conditions than those discussed in the previous section. Fluence values were at least two orders of magnitudes higher and the ion energies at least 2-3 orders of magnitude lower. Also, the MITE-E facility produces nearly monoenergetic ion beams, while the PISCES facility produces a spectrum of energies from a low-temperature plasma. These conditions induce a much different number of defects in the graphene. Figure 6-10 and Figure 6-11 show the change in the damage ratio as a function of energy or fluence, respectively. As the energies of the incoming helium ions approach the energy of the binding energy for the carbon atoms, the interaction between both particles becomes stronger and the damage ratio of the membrane increases. This follows the results from the previous section, discussing the low defect concentration due to high energy helium bombardment. Unfortunately, the highest fluence runs in PISCES completely destroyed the graphene membrane, introducing numerous defects, an extremely high damage ratio, and amorphizing the remaining carbon bonds (red shifting) spread across the substrate surface. The lower exposures maintained their G peak in the same position (~1600 cm^{-1}), indicating the single vacancy production regime for graphene may be dominant here. On the other hand, the deuterium exposure did not produce as large a number of defects into the membrane as might be expected, probably because of the ease of forming hydrocarbons with graphitic materials. The G-band for these exposures did not shift either, however it did broaden. This means that the deuterium ions is introducing defects into the membrane in the single vacancy regime, but the broadening of the G-band suggests that these ions are also amorphizing the graphene, forming bonds in the defect sites and stabilizing the structure [95,97,170] with correlation lengths close to 15 nm.

7.4.2 – SEM Analysis of Tungsten Surface

Previous PISCES studies have discussed the growth of tungsten fuzz on the surface, due to helium ions, and its mechanisms and dependence of exposure time on $\sqrt{t}$ [43,45,46,111,117,119] indicating a diffusive process. Low energy helium atoms cluster together, migrates and diffuses to grain boundaries or to the surface. This is not a sputtering process, it is a diffusive and erosive process. These fuzz structures only occur over a certain window of operation (low ion energies and high fluences and high substrate temperatures). Figure 6-12, Figure 6-13, and Figure 6-14 show the different stages of these structures, as a function of fluence and energy, ranging from a highly porous surface, to the onset of growth of thicker coral structures (Figure 6-18) , and finally the much finer tungsten fuzz (Figure 6-19). Because of the different experimental conditions, and the discussion from the previous subsection, the graphene was not able to prevent the growth of the tungsten fuzz, but it was able to reduce the growth rate of this phenomenon. Unlike helium, deuterium does not cause significant surface changes aside from some roughening of the surface as demonstrated in Figure 6-15, Figure 6-16, and Figure 6-17. However, it could contribute more significantly to the embrittlement of the material.

7.4.3 – Focused Ion Beam Analysis of Fuzz Growth

Cross sectional cuts with a focused ion beam (FIB) of the fuzzy structures on samples GP1 and GP2 were used to determine if the graphene had any significant impact on the structure evolution. To recall, only half of the surface of these samples was coated with graphene, while the other half was bare tungsten. Figure 6-20 and Figure 6-21 show one sample cross section of multiple ones used for the measurement of the fuzz thickness on sample GP1 using the FIB built-in analysis functions. The first picture shows one region of the graphene coated area, and the second one shows the bare tungsten region. Measurements averaged across multiple regions for sample GP1 showed that the growth rate of the fuzz in the graphene-coated area is reduced by approximately 30%. This effect is further seen on sample GP2, where, for a lower fluence, the fuzz thickness is reduced by close to 40%. Once the graphene was completely destroyed in GP1 (termination of region 3 in the amorphization of graphene), it was easier for the fuzz to grow and helium to escape. While sample GP2 also demonstrated an increase in the graphene damage ratio, the correlation length and G-band position for such damage corresponds to region 2 of the ion irradiation of graphene scheme proposed in previous sections (Section 4.1.5). This indicates that the removal of carbon from graphene is destroying the hexagonal lattice, introducing some amorphous structures in it, but not to the degree of GP1, where the fuzz is much thicker. As expected, the relation of thickness to exposure time remains the same after eradication of the graphene, but with different initial conditions due to the growth that took place when the membrane was present. The mechanisms for tungsten erosion for a bare and a graphene coated sample are summarized in Figure 7-3 and Figure 7-4 respectively.

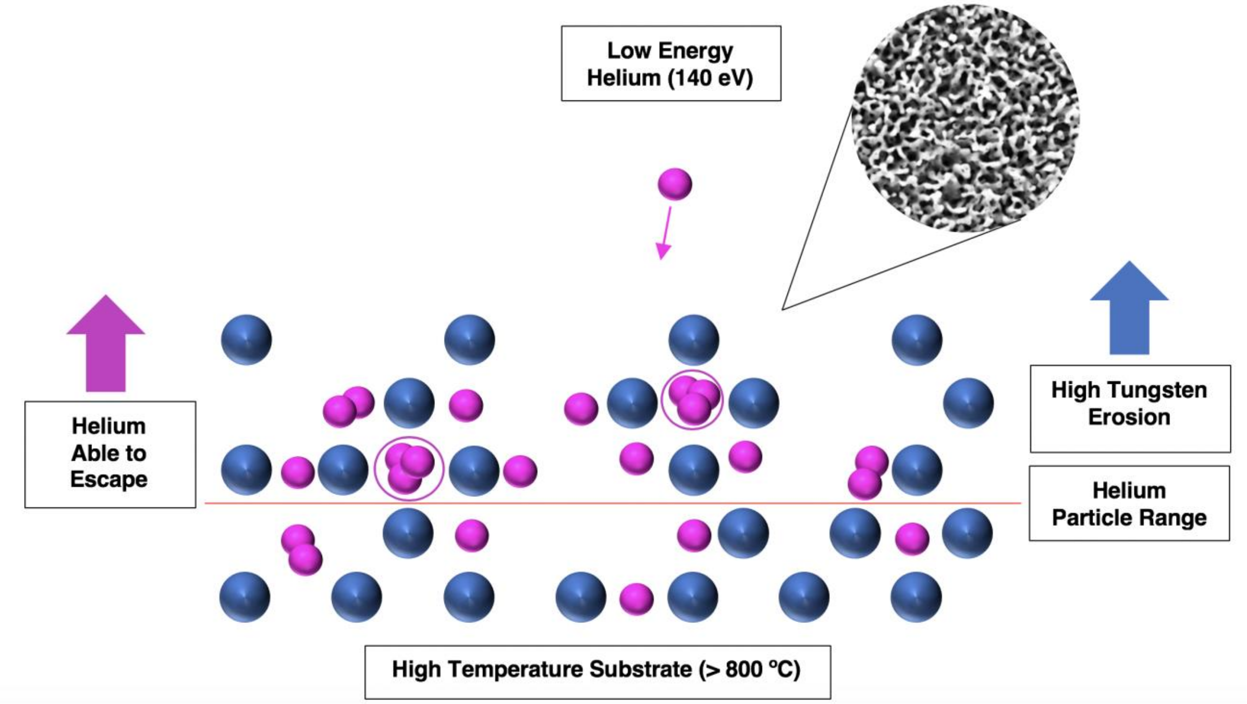

Figure 7-3. Helium ion bombardment of bare polycrystalline tungsten. A low energy helium ion has a large Coulomb cross section for scattering with tungsten atoms, and slows down in the lattice due to nuclear stopping. Helium builds up in the sub-surface layer and, combined with high mobility due to high substrate temperatures, coalesces into helium bubbles. These diffuse to the surface and create thin "fuzz" tendrils due to enhanced helium mobility along the surface, and a thick fuzz layer. Enough helium needs to be implanted for these structures to develop, as much as $1x10^{20}$ *He*$^{+}$*/cm*^{2}*.*

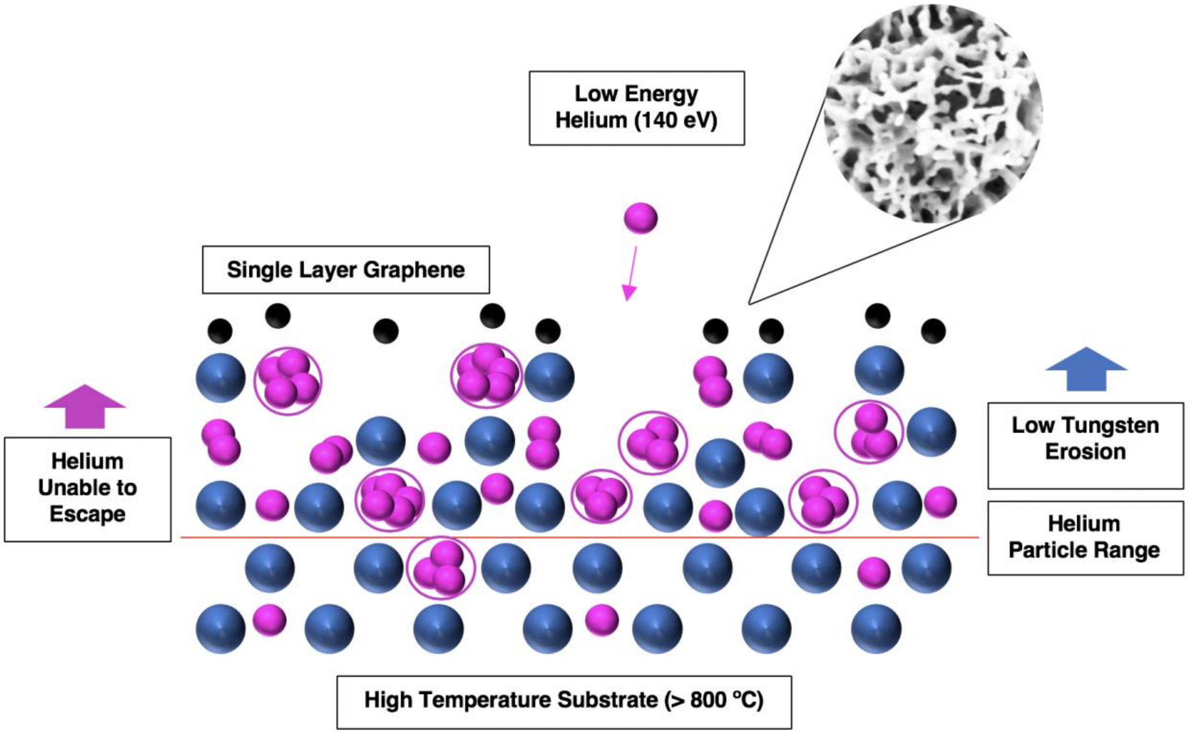

Figure 7-4. Helium ion bombardment of graphene-coated polycrystalline tungsten. A low energy helium ion has a large Coulomb cross section for scattering with tungsten atoms, and slows down in the lattice due to nuclear stopping. These ions can also easily interact with the carbon atoms in the graphene membrane, transferring enough energy to create single vacancy defects. In addition to creating these defects, helium also builds up in the sub-surface layer and, combined with high mobility due to high substrate temperatures, coalesces into helium bubbles. These nanoscale bubbles diffuse to the surface but are prevented from escaping due to the added layer of the graphene atoms, creating a rough surface, and as more defects are introduced, thick fuzz tendrils and a thin fuzz layer. Eventually, due to extremely high fluences and low energy ion bombardment, the entire graphene layer fails, and the tungsten fuzz starts to grow at the same rate as it would for bare tungsten.

7.4.4 – Residual Strain Analysis on Half-Coated Graphene-Tungsten Samples

Because these samples were exposed to significantly higher fluences than those performed at the UW-IEC Laboratory, there is a possibility that the stresses within the sample shifted and the particle bombardment is contributing to the embrittlement of the bulk material. In order to test this, a residual stress analysis was performed on all the samples at high diffraction angles ($2\theta = 131°$) for reasons explained in 0. Figure 6-23 demonstrates that graphene does not have much of an impact on residual stresses due to helium bombardment. Of note, there is a change from compressive to tensile stress within the lattice which correlates with the destruction of the graphene, thicker fuzz growth and tungsten expansion. Just at the onset of the fuzz growth, there is still significant helium in the tungsten leading to a compressive stress state. For the low energy, low fluence case, there is no release of tungsten, and the trapped particles contribute to the higher negative (compressive) stresses. Deuterium appears to have a higher retention in tungsten and does not leave the bulk as easily as helium bubbles can, possibly due to the graphene membrane. The stabilization of defect sites by other deuterium molecules could prevent the deuterium in the surface of the substrate from escaping though the graphene pores. This leads to larger residual stresses in the samples, with some significant difference between the graphene coated and uncoated sides. The samples are large enough that the spot sizes for the analysis do not overlap the two different regions. Figure 6-24 shows lower residual stresses for the graphene coated areas than for the bare tungsten regions. Previous results for these samples (0) showed that the deuterium introduces defects and stabilizes those vacancy sites by forming sp^3 bonds with the carbon atoms [57], which can lead to less deuterium becoming implanted in the bulk material and lower residual stresses.

7.5 – Graphene as a Surface Coating for Polycrystalline Tungsten, C-2W Exposure

7.5.1 – Raman Spectroscopy of Graphene

Deuterium ion energies for exposures on the C-2W divertor at TAE Technologies [44,171] can vary significantly, however average ion energies in the edge plasma range from 20 ± 15 eV over 2,000+ plasma discharges performed over the 2-month period. Section 7.5.2 discusses surface changes due to impurity deposition on the surface of tungsten. While the surface of tungsten was not visible, there is no significant roughening of the surface as seen in samples GP4-6 in the PISCES exposures. This information can be used to extrapolate a fluence of approximately in the range of 10^{18}-10^{19} D^+/cm^2 for those exposure energies, a range where no surface effects would normally be seen on the tungsten. For these conditions, the Raman data correlates with the deuterium exposures done in PISCES. There is a growth in the damage ratio for graphene with fluence (Figure 6-25) and no shift of the G-band implying that the exposure only caused single vacancies in the membrane. There is also stabilization (sp^3 bonding) of defect sites by the deuterium ions. The correlation length is still high (~15 nm), and the residual defect density introduced by the exposure is small (~15%).

7.5.2 – SEM Analysis of Tungsten Surface

A survey of the surface of these samples through the SEM revealed some interesting features. Figure 6-26 shows the surface of the bare tungsten after the exposure. There are large traces of impurities on the surface, and a more visible morphology change on sample W2 (bare) than in sample W6 (coated). No useful information can be extracted for tungsten irradiated in C-2W due to thick layers of impurities on the surface (notice the disappearance of all grain boundaries). However, the much smoother graphene coated surface and mass gain information discussed in the next section provide some insight regarding these phenomena. Overall, graphene has a much lower surface energy [172,173] than tungsten [174,175]. This makes graphene incompatible with growth of thin films on the graphene surface due to cracking, ripples and film warping. Consequently, deposition and growth on the graphene would be more difficult than on a bare tungsten substrate, which could lead to a lower mass gain as discussed in the next section.

7.5.3 – Mass Gain Analysis of Tungsten Sample

As mentioned before, there is a significantly higher mass gain for the bare tungsten sample than for the graphene coated sample, by a factor of approximately 2. A reasonable inference from this mass gain analysis is that there is no erosion of the tungsten, and other metal impurities accumulate on the surface when exposed to deuterium due to the gas' low energy transfer to tungsten particles (with an energy transfer factor of 0.005). This makes it impossible at low fluences to displace tungsten from its lattice with its high displacement energy threshold (215 eV for deuterium on tungsten according to the Semi-Empirical sputtering yield model [176]), and this energy transfer factor will remain low for any large-mass atoms. More importantly, this gain poses a question on the sources of the impurities deposited on the samples. Fortunately, an X-ray photoelectron spectroscopy (XPS) analysis can be used to determine the distribution, identity and composition of particles on these surfaces.

7.5.4 – XPS Analysis of Impurity Layer on Sample Surface

The initial analysis via XPS for the samples exposed in C-2W revealed carbon and oxygen impurities, which are always present in any sample that has been exposed to atmosphere, as well as the substrate itself (W). After the exposure, the examination demonstrated the lack of tungsten in the surface compositional analysis. Since the perpendicular resolution of the diagnostic is 10 nm, all that the X-rays are probing are the surface impurities, revealing the different amounts of the elements shown in Figure 6-29. The presence of all the elements is explained in 0 as well. With knowledge of the physical properties of these components, it was possible to calculate the layer thicknesses, which for the bare tungsten sample is twice as large as for the graphene coated tungsten. These results suggest that graphene can be a good candidate for minimizing impurity collection on plasma facing component surfaces.

7.6 – Graphene for the Reduction of Secondary Electron Emission

Secondary electron emission is a large concern in plasma confinement devices due to its ability to hinder plasma performance. Previous studies have shown that for electron bombardment of graphene on different surfaces, the membrane is able to suppress some of the secondary electron emission.[82-83,153,168].

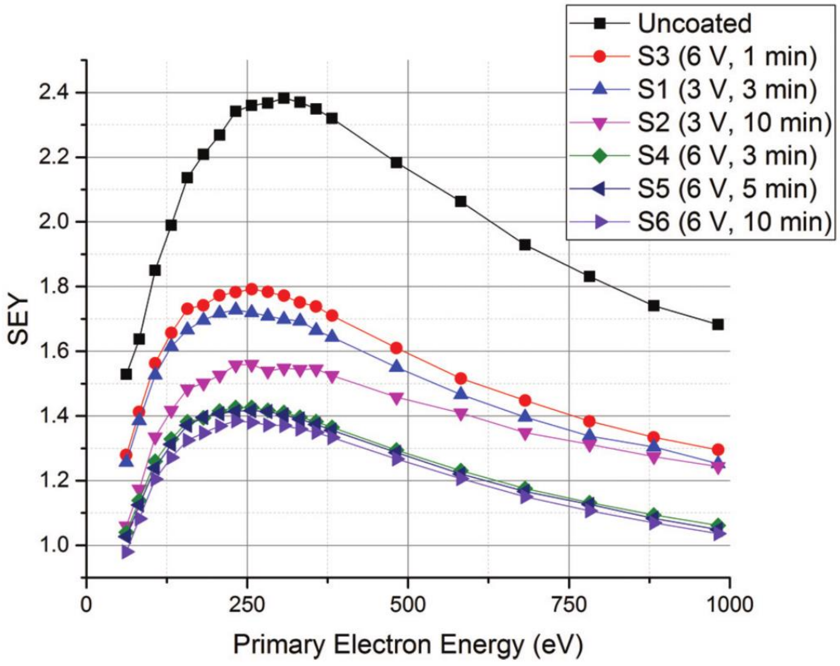

Figure 7-5. The secondary electron yield (SEY) data for stainless steel coated with graphene [162].

Section 6.6 gives an overview of the setup and procedure for acquiring the results for secondary electron suppression on tungsten surfaces, similar to an analysis performed by Hiura et al [178], where they used contrast to determine the numbers of graphene layers in reference to bare surfaces. Measuring the true secondary electron current for the determination of the emission coefficient was not determined, but the relative difference in contrast change between the coated and uncoated regions are calculated to determine the effect of the graphene membrane on a tungsten surface. Due to the limitations of the scanning electron microscope, data points for energies where tungsten's secondary electron emission peaks (400-600 eV) [179] due to primary electrons were not collected. As mentioned in the previous results chapter, the curve in Figure 6-31 is shifted due to backscattered electrons contributing more to the collected signal at high energies. As the energy of the primary beam is decreased, there is a more defined splitting of the curves, showing a significant drop in the secondary electron emission, by as much as 50% for the lower energies. At these lower primary electron energies, SEY production is higher and the image is largely generated by these kinds of electrons, whereas at higher energies, the SEY production falls and the backscattered electron production rises (see description in 0). This can explain the large difference in emission yields between the two sample regions. These results are encouraging and support the trends seen in the studies mentioned at the beginning of this section. Therefore, due to the large repulsive forces from the different hybridization states of the electron bonds in the graphene membrane, secondary electrons from the underlying substrate (tungsten) cannot escape as easily as they would for an uncoated material.

7.7 – Summary and Implications of this Work

Throughout this thesis, graphene has been tested as a coating for a tungsten PFC over several facilities and irradiation conditions. Overall, graphene has performed well under irradiation, and has been able to dampen the evolution of the surface morphology for the refractory metal with different degrees of success. The first significant result is that, unless graphene is freestanding, the damage to the sheet will be dependent on the sputtering surface below the graphene. Therefore, materials with lower threshold energies for sputtering will damage the membrane more easily. Another major conclusion to draw from these studies is the resemblance of a $1/E^{\frac{3}{2}}$ dependence on the damage ratio, which alludes to the same dependence with correlation length (L_D) discussed in previous chapters and seen in Figure 7-2.

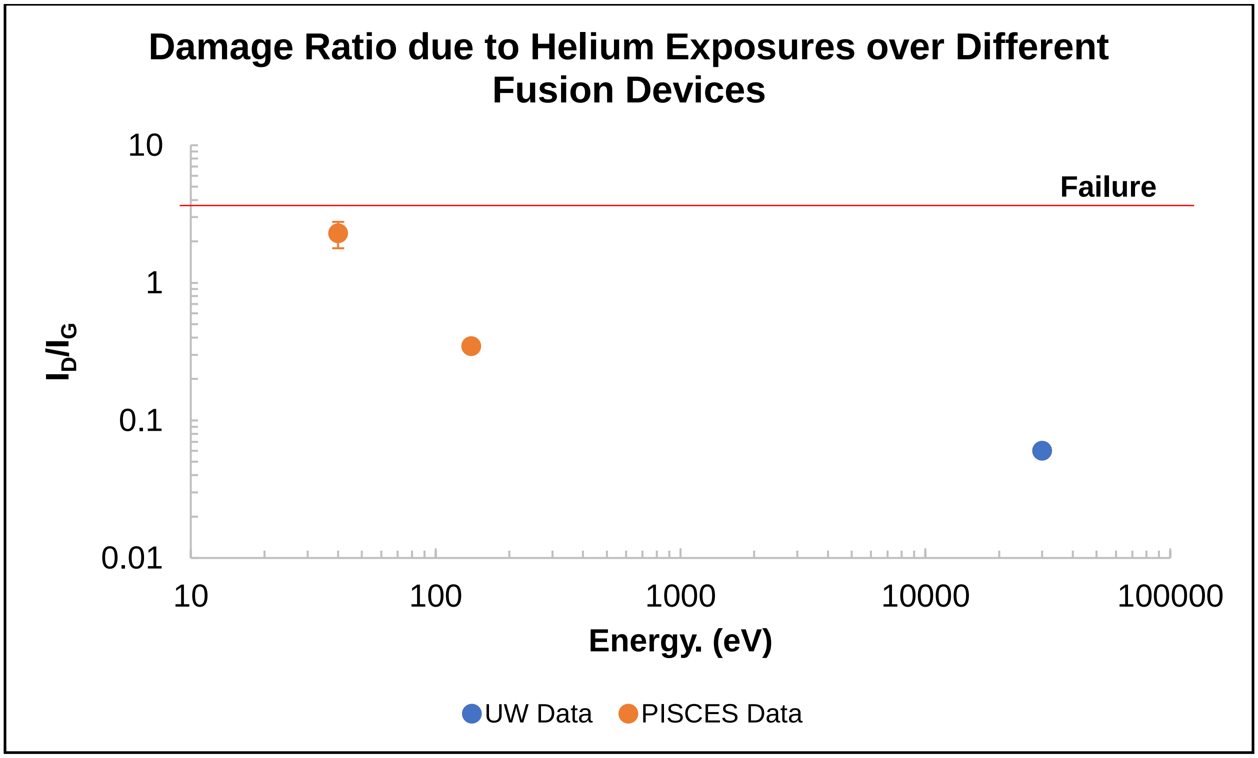

Figure 7-6. Graphene damage as a function of the helium ion energy for similar fluences (~1x10^{19}-1X10^{20} He^+/cm^2) and substrate temperatures (800-900°C) for MITE-E and PISCES.

As the ion bombardment energy approaches the binding energy of the carbon atoms in the hexagonal structure, the interaction between particles becomes stronger, making it easier to create vacancies in the structure. However, for a fixed fluence to the plasma facing component, a higher helium ion bombardment energy can make the graphene more durable, extending its lifetime. For tungsten as a PFC, this also assists in reducing the development of surface morphologies which are detrimental to plasma performance in those extreme environments. High helium fluences also appear to have an effect on the damage to the membrane, but the destructive dose is highly dependent on ion energy as expected. Figure 7-3 shows the combined effect of fluence and energy, with lower energies limiting the failure fluence, and much higher energies, possibly extending the failure fluence significantly.

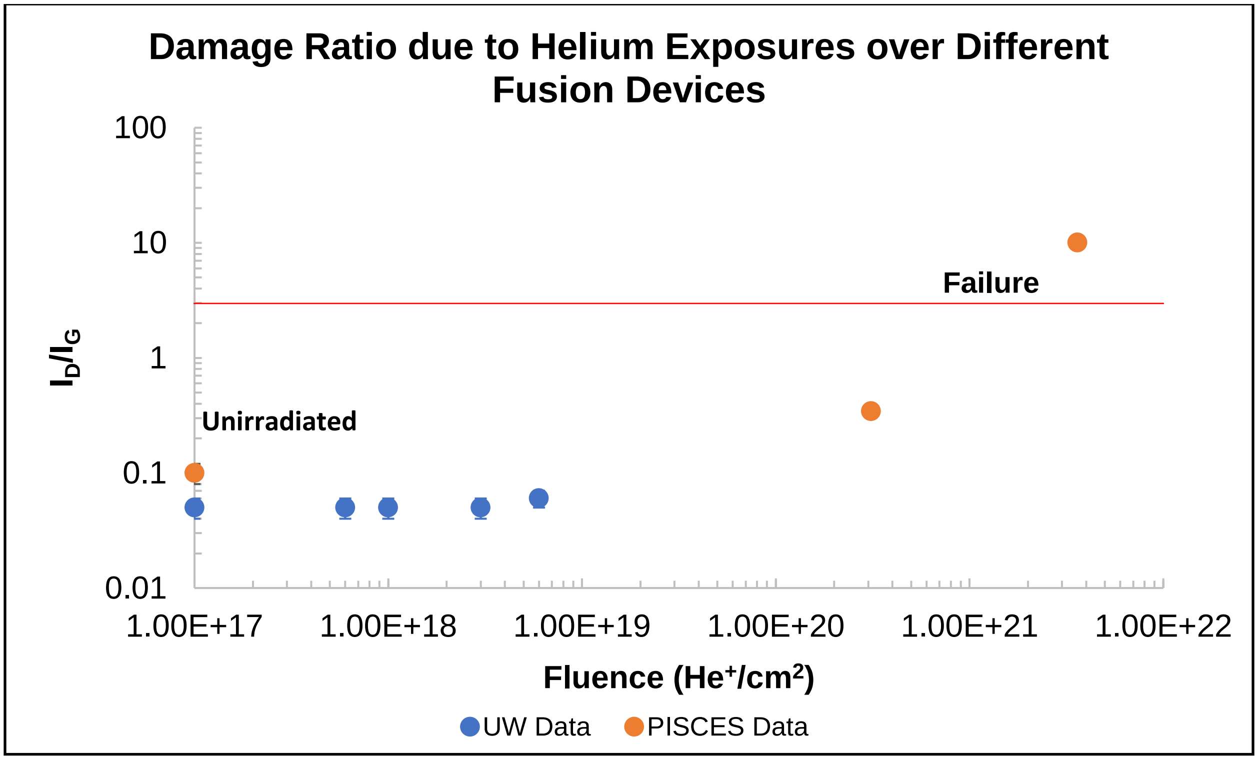

Figure 7-7. Graphene damage as a function of fluence for similar energies (30 keV for UW and 140 eV for PISCES data) and substrate temperatures (800-900°C) for different fusion devices across the USA. The unirradiated label corresponds to the damage ratio prior to irradiation.

Unfortunately, this limit has not been experimentally determined at this time due to limitations in the experimental setup. The durability of the graphene sheet will also have an impact on the mass loss of the sample, slowing down the sputtering of the substrate material and increasing the eventual failure fluence.

Deuterium exposure seems to have a different effect on damaging the graphene due to the hydrogen isotopes ability to produce defects as well as stabilizing the defect site by forming sp^3 bonds with the carbon atoms. One of the first results for this kind of interaction is that neutral hydrogen pressure seems to saturate damage to a heated membrane. During a deuterium plasma exposure, the graphene damage does not change significantly as a function of energy for low incoming energies. Figure 7-4 shows this effect for samples tested in both PISCES and TAE fusion facilities. This figure indicates that the limiting species for a fusion plasma exposure is helium, not deuterium. Unfortunately, all the deuterium fluences explored (Figure 7-9) did not reveal the failure limit for the membranes, but this is something to address in future projects.

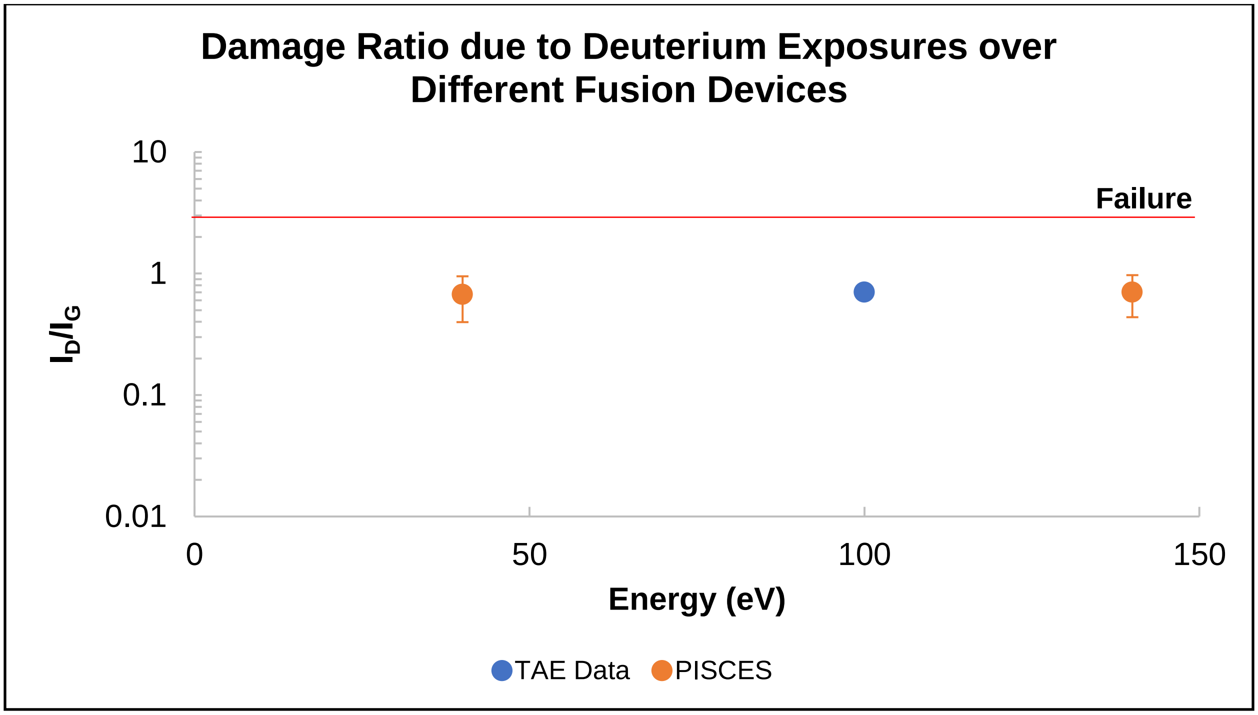

Figure 7-8. Graphene damage as a function of the deuterium ion energy for similar fluences (~1x10^{19}-1X10^{20} D^+/cm^2) and substrate temperatures (600°C) for different fusion devices across the USA.

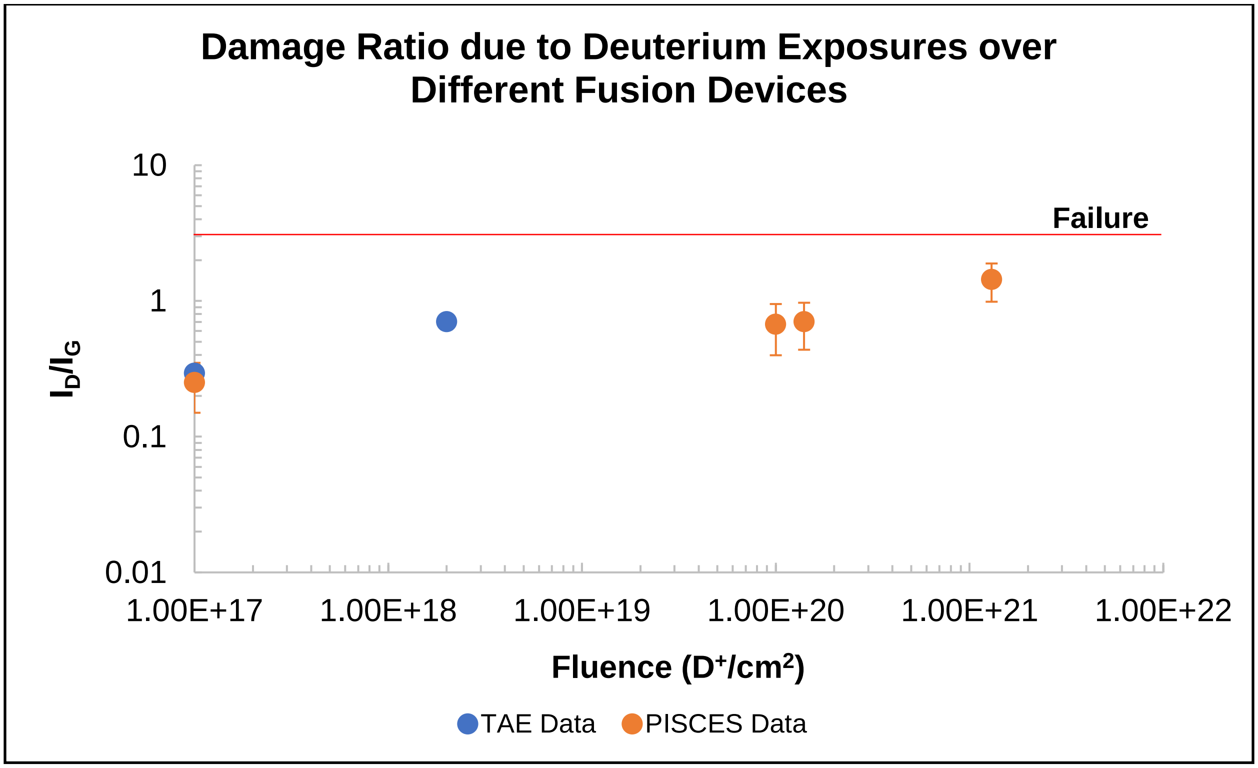

Figure 7-9. Graphene damage as a function of deuterium fluence for similar energies (25 eV for TAE and 40-140 eV for PISCES data) and substrate temperatures (600°C) for different fusion devices across the USA.

Lastly, the implementation of graphene appears to have an effect on the bulk properties of its substrate material, being able to reduce residual stresses in the bulk due to deuterium exposure. Due to its low surface energy, having a graphene membrane on a PFC makes it difficult for impurities to adhere to the sheet, reducing their quantity on the surface and in turn, their secondary electron emission, which for some impurities are much higher than for the PFC and in high quantities can significantly affect plasma performance. Luckily, the last major result is graphene's ability to suppress secondary electrons from a primary electron bombardment, which might translate as well into ion bombardment, for energies close to peak emission yields in tungsten.

This page is intentionally left blank.

Chapter 8 – Conclusions

The dual goal of this work was to 1) determine if graphene was a suitable candidate as a coating for plasma facing components (PFC's) in fusion devices and 2) to understand the operation characteristic of the linear neutron source experiment (LUNA). In order to determine the viability of using a single layer of graphene (one atomic carbon membrane) as a coating on PFC's, one needs to consider the plasma exposure parameters, the damage to the graphene, and the damage to the underlying substrate (tungsten in this work), and the interaction between these materials and the plasma. Below is a summary of the main conclusions drawn from this work:

- When irradiated, substrates with poor physical properties can contribute to introducing large damage ratios into a graphene membrane, regardless of the sheet being single layer, or bilayer graphene.
- Oxygen impurities on the surface can contribute to the formation of CO_2, and thereby introducing defects into the graphene sheet due to the radicals being released during substrate heating and irradiation.
- Graphene exposed to heated (500 °C) neutral deuterium introduces relatively few defects into a graphene membrane. However, the pressure of the neutral gas in the chamber (30-300 mTorr) does not have a significant effect in the defect concentration.
- High energy (30 keV) helium ions and neutrals appears to introduce significantly less defects into a graphene membrane than low energy helium ions (<200 eV).
- Graphene seems to suppress or slow down the development of surface morphologies on tungsten surfaces during high energy helium irradiation. Graphene coatings also may

contribute to lower erosion yields of these exposed surfaces due to the added impurity layer (as much as by a factor of 10 for 30 keV helium ions).

- During low energy helium exposures, for ion/neutral energies close to the displacement energy of graphene atoms, it appears to be easier to introduce defects into the carbon membrane.
- The failure limit for graphene exposed to low energy helium (<200 eV) appears to be occur past fluences greater than $1x10^{25}$ He^{+}/m^{2}.
- Low energy deuterium exposures (<200 eV) introduce larger defect densities into a graphene membrane but appears to have a higher failure limit than helium. Unfortunately, failure limits of the graphene for deuterium exposures were not determined in this thesis.
- For half graphene coated tungsten samples, after low energy helium exposures (<200 eV) the membrane seems to slow down the growth of tungsten fuzz by 30-40% in the coated areas.
- Low energy ion/neutral deuterium exposures cause large residual stresses in tungsten probably due to the graphene membrane preventing any neutral deuterium in the substrate from escaping.
- Coating a tungsten surface with a graphene membrane may reduce the amount of impurities collected on the surface. This could be due to graphene’s low surface energy, which make it difficult for impurities to wet the membrane’s surface, as opposed to the higher impurity content collected in bare tungsten, which has a higher surface energy.
- Graphene has a low secondary electron yield. This property can also assist in suppressing the secondary electron yield from the underlying substrate by as much as 53% in this work. This also contributes to smaller secondary electron coefficient corrections for ion fluxes.

- For the present configuration of the linear IEC experiment (LUNA), the system cannot produce significant neutron rates below pressures of 1.5 mTorr.
- LUNA will transition into a glow discharge mode for pressures above 2.75 mTorr, severely dropping the neutron rates.
- The LUNA experiment follows the same linear dependence for the neutron rates on cathode current as the spherical IEC device, HOMER.
- LUNA has comparable neutron rates to HOMER at the same operating voltages and currents, despite the difference in particle path lengths between the cathodes and anodes.

This page is intentionally left blank.

Chapter 9 – Recommendations for Future Work

The studies performed throughout this thesis are of significant interest for applications which make use of plasma environments, whether they are plasma processing technologies, or fusion devices. While there were experiments covering a wide range of effects of interest in having a graphene coating, the survey data is not enough to generalize to every device and experimental ranges. These following bullet points summarize recommendations for work in the field:

- Investigate graphene's effect on different substrate materials (such as stainless steel and other alloys) due to their different sputtering threshold energies.
- Explore the effect for different ion species, Helium, Deuterium, Argon and Xenon, which cover species for various plasma applications.
- Perform a parametric study of energy and fluence for such species, in order to determine failure criteria for different applications.
- Determine if bilayer, or trilayer graphene will perform better, since multilayer graphene appears to demonstrate significantly more structural stability.
- Characterize the effect of these studies on the bulk properties of the substrate materials.
- Eliminate the possibility of defect introduction into a substrate due to the transfer process by growing directly on the substrate of interest.
- Manufacture graphene composite structures and study their durability in extreme environments.
- Due to the high temperatures during irradiation, it is not possible to take the tungsten samples out immediately after irradiation for study. One way to bypass this to would be to have a Raman laser which could make in-situ measurements of the sample before, during,

and after irradiation. This would allow us to keep track of the damage and record this self-healing property as a function of time, energy and fluence.

- In the future, the physics studied should be extrapolated to D-^{3}He fusion, with the one goal of using it for the generation of PET radioisotopes.
- The data extracted here could also be used to implement p-B^{11} fusion.

This page is intentionally left blank.

Chapter 10 – References

1. Peierls, R. Quelques propriétés typiques des corps solides. *Ann. l'I.H.P.* **5,** 177–222 (1935).
2. Landau, L. D. Zur Theorie der phasenumwandlungen II. *Phys. Z. Sowjetunion* **11,** 26–35 (1937).
3. Mermin, N. D. Crystalline order in two dimensions. *Phys. Rev.* **176,** 250–254 (1968).
4. Novoselov, K. S. *et al.* Electric Field Effect in Atomically Thin Carbon Films. *Science (80-.).* **306,** 666–669 (2004).
5. Novoselov, K. S. *et al.* Two-dimensional atomic crystals. *Proc. Natl. Acad. Sci.* **102,** 10451–10453 (2005).
6. Nelson, D., Piran, T. & Weinberg, S. *Statistical Mechanics of Membranes and surfaces. World Scientific* (2004). doi:10.1017/CBO9781107415324.004
7. Geim, A. K. & Novoselov, K. S. The rise of graphene. *Nat. Mater.* **6,** 183–191 (2007).
8. Muroga, T., Gasparotto, M. & Zinkle, S. J. Overview of materials research for fusion reactors. *Fusion Eng. Des.* **61–62,** 13–25 (2002).
9. Zinkle, S. J. Advanced materials for fusion technology. *Fusion Eng. Des.* **74,** 31–40 (2005).
10. Zinkle, S. J. Fusion materials science: Overview of challenges and recent progress. *Phys. Plasmas* **12,** 1–8 (2005).
11. Cook, I. Materials research for fusion energy. *Nat. Mater.* **5,** 77 (2006).
12. Roth, J. *et al.* Recent analysis of key plasma wall interactions issues for ITER. *J. Nucl. Mater.* **390–391,** 1–9 (2009).
13. Atsumi, H. Hydrogen retention in graphite and carbon materials under a fusion reactor environment. *J. Nucl. Mater.* **313–316,** 543–547 (2003).
14. Atsumi, H., Tanabe, T. & Shikama, T. Bulk hydrogen retention in neutron-irradiated graphite at elevated temperatures. *J. Nucl. Mater.* **390–391,** 581–584 (2009).
15. Franzen, P., Garcia-Rosales, C., Plank, H. & Alimov, V. K. Hydrogen trapping in and release from tungsten: Modeling and comparison with graphite with regard to its use as fusion reactor material. *J. Nucl. Mater.* **241–243,** 1082–1086 (1997).
16. Roth, J. & García-Rosales, C. Analytic description of the chemical erosion of graphite by hydrogen ions. *Nucl. Fusion* **36,** 1647–1659 (1996).
17. Sunyaev, R. A. The Interaction of Radiation and Matter in a Hot-Model Universe. *Astrophys. Space Sci.* **4,** 301–316 (1969).
18. Bakhtiari, M. *et al.* Role of bremsstrahlung radiation in limiting the energy of runaway electrons in tokamaks. *Phys. Rev. Lett.* **94,** 2–5 (2005).
19. Pease, R. S. Equilibrium characteristics of a pinched gas discharge cooled by bremsstrahlung radiation. *Proc. Phys. Soc. Sect. B* **70,** 11–23 (1957).
20. Baldwin, M. J., Doerner, R. P., Nishijima, D., Tokunaga, K. & Ueda, Y. The effects of high fluence mixed-species (deuterium, helium, beryllium) plasma interactions with tungsten. *J. Nucl. Mater.* **390–391,** 886–890 (2009).
21. Conn, R. W., Doerner, R. P. & Won, J. Beryllium as the plasma-facing material in fusion energy systems—experiments, evaluation, and comparison with alternative materials. *Fusion Eng. Des.* **37,** 481–513 (1997).
22. Skinner, C. H. *et al.* Recent advances on hydrogen retention in iter's plasma-facing materials: Beryllium, carbon. And tungsten. *Fusion Sci. Technol.* **54,** 891–945 (2008).

23. Solonin, M. I. *et al.* Present status and future prospect of the Russian program for fusion low-activation materials. *J. Nucl. Mater.* **287,** 1468–1472 (2000).
24. Mas de les Valls, E. *et al.* Lead-lithium eutectic material database for nuclear fusion technology. *J. Nucl. Mater.* **376,** 353–357 (2008).
25. Pozio, A., Carewska, M., Santucci, A. & Tosti, S. Behaviour of hydrogenated lead–lithium alloy. *Int. J. Hydrogen Energy* **42,** 1053–1062 (2017).
26. Lee, D. W., Hong, B. G., Kim, S. K. & Kim, Y. Design and preliminary safety analysis of a helium cooled molten lithium test blanket module for the ITER in Korea. *Fusion Eng. Des.* **83,** 1217–1221 (2008).
27. Aiello, G. *et al.* Development of the Helium Cooled Lithium Lead blanket for DEMO. *Fusion Eng. Des.* **89,** 1444–1450 (2014).
28. Kondo, M., Nakajima, Y., Tsuji, M. & Nozawa, T. Evaluation of thermal conductivity for liquid lead lithium alloys at various Li concentrations based on measurement and evaluation of density, thermal diffusivity and specific heat of alloys. *Fusion Eng. Des.* **109–111,** 1345–1350 (2016).
29. Charpin, J. *et al.* Investigation of γ lithium aluminate as tritium breeding material for a fusion reactor blanket. *Fusion Eng. Des.* **8,** 407–413 (1989).
30. Balandin, A. A. *et al.* Superior thermal conductivity of single-layer graphene. *Nano Lett.* **8,** 902–907 (2008).
31. Lee, J. U., Yoon, D., Kim, H., Lee, S. W. & Cheong, H. Thermal conductivity of suspended pristine graphene measured by Raman spectroscopy. *Phys. Rev. B - Condens. Matter Mater. Phys.* **83,** 1–4 (2011).
32. Kumar, S., Tripathi, A., Khan, S. A., Pannu, C. & Avasthi, D. K. Radiation stability of graphene under extreme conditions. *Appl. Phys. Lett.* **105,** (2014).
33. Zubeltzu, J., Chuvilin, A., Corsetti, F., Zurutuza, A. & Artacho, E. Knock-on damage in bilayer graphene: Indications for a catalytic pathway. *Phys. Rev. B - Condens. Matter Mater. Phys.* **88,** 1–11 (2013).
34. Cançado, L. G. *et al.* Quantifying Defects in Graphene via Raman Spectroscopy at Different Excitation Energies. *Nano Lett.* **11,** 3190–3196 (2011).
35. Song, W., Lee, S. Il, Kim, Y. & Jung, D. S. Effect of MeV Electron Beam Irradiation on Graphene Grown by Thermal Chemical Vapor Deposition Effect of MeV Electron Beam Irradiation on Graphene Grown by Thermal Chemical Vapor Deposition. *Jpn. J. Appl. Phys.* **125104,** (2013).
36. Lehtinen, O., Kotakoski, J., Krasheninnikov, A. V & Keinonen, J. Cutting and controlled modification of graphene with ion beams. *Nanotechnology* **22,** 1–13 (2011).
37. Leenaerts, O., Partoens, B. & Peeters, F. M. Graphene: A perfect nanoballoon. *Appl. Phys. Lett.* **93,** 1–4 (2008).
38. Wang, L., Williams, C. M., Boutilier, M. S. H., Kidambi, P. R. & Karnik, R. Single-Layer Graphene Membranes Withstand Ultrahigh Applied Pressure. *Nano Lett.* **17,** 3081–3088 (2017).
39. Boddeti, N. G. *et al.* Graphene blisters with switchable shapes controlled by pressure and adhesion. *Nano Lett.* **13,** 6216–6221 (2013).
40. Zenobia, S. J., Garrison, L. M. & Kulcinski, G. L. The response of polycrystalline tungsten to 30 keV helium ion implantation at normal incidence and high temperatures. *J. Nucl. Mater.* **425,** 83–92 (2012).
41. Garrison, L. M. Improving the Materials Irradiation Experimental Facility and Increasing

Understanding of Helium Irradiation of Tungsten. (2013).

42. Baldwin, M. J. & Doerner, R. P. Helium induced nanoscopic morphology on tungsten under fusion relevant plasma conditions. *Nucl. Fusion* **48,** (2008).
43. Baldwin, M. J. & Doerner, R. P. Formation of helium induced nanostructure ‘fuzz’ on various tungsten grades. *J. Nucl. Mater.* **404,** 165–173 (2010).
44. Binderbauer, M. W. *et al.* Recent breakthroughs on C-2U: Norman’s legacy. *AIP Conf. Proc.* **1721,** 1–12 (2016).
45. Doerner, R. P., Baldwin, M. J. & Stangeby, P. C. An equilibrium model for tungsten fuzz in an eroding plasma environment. *Nucl. Fusion* **51,** (2011).
46. Petty, T. J., Baldwin, M. J., Hasan, M. I., Doerner, R. P. & Bradley, J. W. Tungsten ‘fuzz’ growth re-examined: The dependence on ion fluence in non-erosive and erosive helium plasma. *Nucl. Fusion* **55,** (2015).
47. Jasica, M. J. *et al.* Preliminary Results of He Implantation in Tungsten at Angled Incidence in DAISIE Preliminary Results of He Implantation in Tungsten at Angled Incidence in DAISIE. *Fusion Sci. Technol.* **72,** 719–725 (2017).
48. Wong, C. P. C. *et al.* Divertor materials evaluation system at DIII-D. *J. Nucl. Mater.* **196–198,** 871–875 (1992).
49. Luxon, J. L. A design retrospective of the DIII-D tokamak. *Nucl. Fusion* **42,** 614 (2002).
50. Bolt, H. *et al.* Materials for the plasma-facing components of fusion reactors. *J. Nucl. Mater.* **329–333,** 66–73 (2004).
51. Herrmann, A. *et al.* Energy Flux to the ASDEX Upgrade Divertor Plates Determined by Thermography and Calorimetry. *Plasma Phys. Control. Fusion* **37,** 17–29 (1995).
52. Pitts, R. A. *et al.* Material erosion and migration in tokamaks. *Plasma Phys. Control. Fusion* **47,** (2005).
53. Greuner, H. *et al.* Final design of W7-X divertor plasma facing components - Tests and thermo-mechanical analysis of baffle prototypes. *Fusion Eng. Des.* **66–68,** 447–452 (2003).
54. Cooper, D. R. *et al.* Experimental review of graphene. **2012,** (2011).
55. Geim, A. K. Nobel Lecture: Random walk to graphene. *Rev. Mod. Phys.* **83,** 851–862 (2011).
56. Hu, S. *et al.* Proton transport through one atom thick crystals. *Nature* **516,** 227–230 (2014).
57. Pimenta, M. A. *et al.* Studying disorder in graphite-based systems by Raman spectroscopy. *Phys. Chem. Chem. Phys.* **9,** 1276–1290 (2007).
58. Ferrari, A. C. & Basko, D. M. Raman spectroscopy as a versatile tool for studying the properties of graphene. *Nat. Nanotechnol.* **8,** 235–246 (2013).
59. Kim, K. *et al.* High-temperature stability of suspended single-layer graphene. *Phys. Status Solidi - Rapid Res. Lett.* **4,** 302–304 (2010).
60. Li, X. *et al.* Large area synthesis of high quality and uniform graphene films on copper foils. *Science* **324,** 1312–1314 (2009).
61. Lin, Y. C. *et al.* Clean transfer of graphene for isolation and suspension. *ACS Nano* **5,** 2362–2368 (2011).
62. Suk, J. W. *et al.* Transfer of CVD-grown monolayer graphene onto arbitrary substrates. *ACS Nano* **5,** 6916–6924 (2011).
63. Li, X. *et al.* Transfer of Large-Area Graphene Films for High-Performance Transparent Conductive Electrodes. (2009). doi:10.1021/nl902623y

64. Kirkland, N. T., Schiller, T., Medhekar, N. & Birbilis, N. Exploring graphene as a corrosion protection barrier. *Corros. Sci.* **56,** 1–4 (2012).
65. Sun, W. *et al.* Inhibiting the corrosion-promotion activity of graphene. *Chem. Mater.* **27,** 2367–2373 (2015).
66. Prasai, D., Tuberquia, J. C., Harl, R. R., Jennings, G. K. & Bolotin, K. I. Graphene: Corrosion-inhibiting coating. *ACS Nano* **6,** 1102–1108 (2012).
67. Zhou, F., Li, Z., Shenoy, G. J., Li, L. & Liu, H. Enhanced room-temperature corrosion of copper in the presence of graphene. *ACS Nano* **7,** 6939–6947 (2013).
68. Hsieh, Y. P. *et al.* Complete corrosion inhibition through graphene defect passivation. *ACS Nano* **8,** 443–448 (2014).
69. Böhm, S. Graphene against corrosion. *Nat. Nanotechnol.* **9,** 741–742 (2014).
70. Schriver, M. *et al.* Graphene as a long-term metal oxidation barrier: Worse than nothing. *ACS Nano* **7,** 5763–5768 (2013).
71. Lee, C., Wei, X., Kysar, J. W. & Hone, J. Measurement of the Elastic Properties and Intrinsic Strength of Monolayer Graphene. *Science (80-.).* **321,** 385–388 (2008).
72. Gao, Y. & Hao, P. Mechanical properties of monolayer graphene under tensile and compressive loading. *Phys. E Low-Dimensional Syst. Nanostructures* **41,** 1561–1566 (2009).
73. Frank, I. W., Tanenbaum, D. M., van der Zande, A. M. & McEuen, P. L. Mechanical properties of suspended graphene sheets. *J. Vac. Sci. Technol. B Microelectron. Nanom. Struct.* **25,** 2558 (2007).
74. Min, K. & Aluru, N. R. Mechanical properties of graphene under shear deformation. *Appl. Phys. Lett.* **98,** 1–4 (2011).
75. Graphene, L. *et al.* Enhanced Mechanical Properties of. *ACS Nano* **3,** 3884–3890 (2009).
76. Scarpa, F., Adhikari, S. & Srikantha Phani, A. Effective elastic mechanical properties of single layer graphene sheets. *Nanotechnology* **20,** (2009).
77. Bunch, J. S. *et al.* Impermeable atomic membranes from graphene sheets. *Nano Lett.* **8,** 2458–2462 (2008).
78. Koenig, S. P., Wang, L., Pellegrino, J. & Bunch, J. S. Selective molecular sieving through porous graphene. *Nat. Nanotechnol.* **7,** 728–732 (2012).
79. Boutilier, M. S. H. *et al.* Implications of permeation through intrinsic defects in graphene on the design of defect-tolerant membranes for gas separation. *ACS Nano* **8,** 841–849 (2014).
80. Drahushuk, L. W. & Strano, M. S. Mechanisms of gas permeation through single layer graphene membranes. *Langmuir* **28,** 16671–16678 (2012).
81. Sun, C. *et al.* Mechanisms of molecular permeation through nanoporous graphene membranes. *Langmuir* **30,** 675–682 (2014).
82. Suk, M. E. & Aluru, N. R. Water transport through ultrathin graphene. *J. Phys. Chem. Lett.* **1,** 1590–1594 (2010).
83. Cohen-Tanugi, D. & Grossman, J. C. Water desalination across nanoporous graphene. *Nano Lett.* **12,** 3602–3608 (2012).
84. Cohen-Tanugi, D. & Grossman, J. C. Water permeability of nanoporous graphene at realistic pressures for reverse osmosis desalination. *J. Chem. Phys.* **141,** (2014).
85. Goenka, S., Sant, V. & Sant, S. Graphene-based nanomaterials for drug delivery and tissue engineering. *J. Control. Release* **173,** 75–88 (2014).
86. Liu, J., Cui, L. & Losic, D. Graphene and graphene oxide as new nanocarriers for drug

delivery applications. *Acta Biomater.* **9,** 9243–9257 (2013).
87. Sun, X. *et al.* Nano-graphene oxide for cellular imaging and drug delivery. *Nano Res.* **1,** 203–212 (2008).
88. Bonaccorso, F., Sun, Z., Hasan, T. & Ferrari, A. C. Graphene photonics and optoelectronics. *Nat. Photonics* **4,** 611–622 (2010).
89. Nair, R. R. *et al.* Fine structure constant defines visual transparency of graphene. *Science (80-.).* **320,** 1308 (2008).
90. Langendorf, S. & Walker, M. Effect of secondary electron emission on the plasma sheath. *Phys. Plasmas* **22,** (2015).
91. Luo, J. *et al.* Ultralow secondary electron emission of graphene. *ACS Nano* **5,** 1047–1055 (2011).
92. Cao, M., Zhang, X. S., Liu, W. H., Wang, H. G. & Li, Y. D. Secondary electron emission of graphene-coated copper. *Diam. Relat. Mater.* **73,** 199–203 (2017).
93. Cazaux, J. Calculated dependence of few-layer graphene on secondary electron emissions from SiC. *Appl. Phys. Lett.* **98,** 1–4 (2011).
94. Hiura, H., Miyazaki, H. & Tsukagoshi, K. Determination of the number of graphene layers: Discrete distribution of the secondary electron intensity stemming from individual graphene layers. *Appl. Phys. Express* **3,** 2–5 (2010).
95. Despiau-Pujo, E. *et al.* Elementary processes of H2 plasma-graphene interaction: A combined molecular dynamics and density functional theory study. *J. Appl. Phys.* **113,** 114302 (2013).
96. Boukhvalov, D. W., Katsnelson, M. I. & Lichtenstein, A. I. Hydrogen on graphene: Electronic structure, total energy, structural distortions and magnetism from first-principles calculations. *Phys. Rev. B - Condens. Matter Mater. Phys.* **77,** (2008).
97. Xie, L., Jiao, L. & Dai, H. Selective etching of graphene edges by hydrogen plasma. *J. Am. Chem. Soc.* **132,** 14751–14753 (2010).
98. Diankov, G., Neumann, M. & Goldhaber-Gordon, D. Extreme monolayer-selectivity of hydrogen-plasma reactions with graphene. *ACS Nano* **7,** 1324–1332 (2013).
99. Mounet, N. & Marzari, N. First-principles determination of the structural, vibrational and thermodynamic properties of diamond, graphite, and derivatives. *Phys. Rev. B - Condens. Matter Mater. Phys.* **71,** 1–14 (2005).
100. Lui, C. H., Liu, L., Mak, K. F., Flynn, G. W. & Heinz, T. F. Ultraflat graphene. *Nature* **462,** 339–341 (2009).
101. Su, Y. *et al.* Exceptional negative thermal expansion and viscoelastic properties of graphene oxide paper. *Carbon N. Y.* **50,** 2804–2809 (2012).
102. Yoon, D., Son, Y. W. & Cheong, H. Negative thermal expansion coefficient of graphene measured by raman spectroscopy. *Nano Lett.* **11,** 3227–3231 (2011).
103. Fasolino, A., Los, J. H. & Katsnelson, M. I. Intrinsic ripples in graphene. *Nat. Mater.* **6,** 858–861 (2007).
104. Åhlgren, E. H., Kotakoski, J., Lehtinen, O. & Krasheninnikov, A. V. Ion irradiation tolerance of graphene as studied by atomistic simulations. *Appl. Phys. Lett.* **100,** (2012).
105. Lehtinen, O. *et al.* Effects of ion bombardment on a two-dimensional target: Atomistic simulations of graphene irradiation. *Phys. Rev. B - Condens. Matter Mater. Phys.* **81,** 1–4 (2010).
106. Mathew, S. *et al.* The effect of layer number and substrate on the stability of graphene under MeV proton beam irradiation. *Carbon N. Y.* **49,** 1720–1726 (2011).

107. Herbig, C. & Michely, T. Graphene: The ultimately thin sputtering shield. *2D Mater.* **3,** (2016).
108. Ahlberg, P. *et al.* Defect formation in graphene during low-energy ion bombardment. *APL Mater.* **4,** 046104 (2016).
109. Yang, Q. *et al.* Microscopic evolution of pre-damaged and undamaged tungsten exposed to low-energy and high-flux helium ions. *Nucl. Instruments Methods Phys. Res. Sect. B Beam Interact. with Mater. Atoms* **325,** 73–78 (2014).
110. Sakaguchi, W., Kajita, S., Ohno, N., Takagi, M. & Kurishita, H. Formation Condition of Fiberform Nanostructured Tungsten by Helium Plasma Exposure. *Plasma Fusion Res.* **5,** S1023–S1023 (2010).
111. El-Atwani, O. *et al.* Ultrafine tungsten as a plasma-facing component in fusion devices: Effect of high flux, high fluence low energy helium irradiation. *Nucl. Fusion* **54,** (2014).
112. Miyamoto, M. *et al.* Observations of suppressed retention and blistering for tungsten exposed to deuterium-helium mixture plasmas. *Nucl. Fusion* **49,** (2009).
113. Kajita, S., Sakaguchi, W., Ohno, N., Yoshida, N. & Saeki, T. Formation process of tungsten nanostructure by the exposure to helium plasma under fusion relevant plasma conditions. *Nucl. Fusion* **49,** (2009).
114. Yoshida, N., Iwakiri, H., Tokunaga, K. & Baba, T. Impact of low energy helium irradiation on plasma facing metals. *J. Nucl. Mater.* **337–339,** 946–950 (2005).
115. Tokunaga, K. *et al.* Synergistic effects of high heat loading and helium irradiation of tungsten. *J. Nucl. Mater.* **329–333,** 757–760 (2004).
116. Iwakiri, H., Yasunaga, K., Morishita, K. & Yoshida, N. Microstructure evolution in tungsten during low-energy helium ion irradiation. *J. Nucl. Mater.* **283–287,** 1134–1138 (2000).
117. Martynenko, Y. V. & Nagel', M. Y. Model of fuzz formation on a tungsten surface. *Plasma Phys. Reports* **38,** 996–999 (2012).
118. Garrison, L. M. & Kulcinski, G. L. Irradiation resistance of grains near {0 0 1} on polycrystalline tungsten under 30 keV He+ bombardment at 1173 K. *Phys. Scr.* **T159,** (2014).
119. Meyer, F. W. *et al.* Flux threshold measurements of He-ion beam induced nanofuzz formation on hot tungsten surfaces. *Phys. Scr.* **2016,** (2016).
120. Kulcinski, G. L. *et al.* Progress in the understanding of gridded inertial electrostatic confinement devices at the university of Wisconsin. *Fusion Sci. Technol.* **68,** 314–318 (2015).
121. Kulcinski, G. L. *et al.* Recent advances in iec physics and technology at the university of wisconsin. *Fusion Sci. Technol.* **64,** 373–378 (2013).
122. Emmert, G. A. & Santarius, J. F. Atomic and molecular effects on spherically convergent ion flow. I. Single atomic species. *Phys. Plasmas* **17,** 1–12 (2010).
123. Emmert, G. A. & Santarius, J. F. Atomic and Molecular Effects on Spherically Convergent Ion Flow II : Multiple Molecular Species. *Phys. Plasmas* **17,** 013503 (2010).
124. Kim, K. S. *et al.* Large-scale pattern growth of graphene films for stretchable transparent electrodes. *Nature* **457,** 706–710 (2009).
125. Mattevi, C., Kim, H. & Chhowalla, M. A review of chemical vapour deposition of graphene on copper. *J. Mater. Chem.* **21,** 3324–3334 (2011).
126. Lahiri, J. *et al.* Graphene growth and stability at nickel surfaces. *New J. Phys.* **13,** (2011).
127. Wimmer, E. *et al.* Temperature-dependent diffusion coefficients from ab initio

computations: Hydrogen, deuterium, and tritium in nickel. *Phys. Rev. B - Condens. Matter Mater. Phys.* **77,** 1–12 (2008).

128. Gullapalli, H., Mohana Reddy, A. L., Kilpatrick, S., Dubey, M. & Ajayan, P. M. Graphene growth via carburization of stainless steel and application in energy storage. *Small* **7,** 1697–1700 (2011).
129. John, R., Ashokreddy, A., Vijayan, C. & Pradeep, T. Single-and few-layer graphene growth on stainless steel substrates by direct thermal chemical vapor deposition. *Nanotechnology* **22,** (2011).
130. Zou, Z. *et al.* Uniform single-layer graphene growth on recyclable tungsten foils. *Nano Res.* **8,** 592–599 (2015).
131. Egle, B. J. Nuclear Fusion of Advanced Fuels Using Converging Focused Ion Beams. (2010).
132. Tynan, G., Doerner, R. & Najmabadi, F. *The PISCES Program FY04-06 Progress Report*. (2006).
133. Tuszewski, M. Field reversed configurations. *Nucl. Fusion* **28,** 2033–2092 (1988).
134. Steinhauer, L. C. Review of field-reversed configurations. *Phys. Plasmas* **18,** 1–38 (2011).
135. Santarius, J. F., Kulcinski, G. L., El-Guebaly, L. A. & Khater, H. Y. Could Advanced Fusion Fuels Be Used with Today's Technology? *J. Fusion Energy* **17,** 33–40 (1998).
136. Neto, A. H. C., Guinea, F., Peres, N. M. R., Novoselov, K. S. & Geim, A. K. The electronic properties of graphene. **81,** (2007).
137. Malard, L. M., Pimenta, M. A., Dresselhaus, G. & Dresselhaus, M. S. Raman spectroscopy in graphene. *Phys. Rep.* **473,** 51–87 (2009).
138. Ferrari, A. C. & Robertson, J. Interpretation of Raman spectra of disordered and amorphous carbon. *Phys. Rev. B* **61,** 14 295 (2000).
139. Buchheim, J., Wyss, R. M., Shorubalko, I. & Park, H. G. Understanding the interaction between energetic ions and freestanding graphene towards practical 2D perforation. *Nanoscale* **8,** 8345–8354 (2016).
140. Lucchese, M. M. *et al.* Quantifying ion-induced defects and Raman relaxation length in graphene. *Carbon N. Y.* **48,** 1592–1597 (2010).
141. Delgado, R. R. The Physical Electronics of Graphene on Germanium. (2017).
142. Fitzpatrick, M. *et al.* Determination of Residual Stresses by X-ray Diffraction - Issue 2. *Meas. Good Pract. Guid.* 74 (2005). doi:10.1007/s00028-005-0194-y
143. Shen, Y. G. *et al.* Residual stress, microstructure, and structure of tungsten thin films deposited by magnetron sputtering. *J. Appl. Phys.* **87,** 177–187 (2000).
144. Badawi, K. F. & Naudon, A. Residual stress determination thin films by X-ray diffraction in tungsten. *Appl. Surf. Sci.* **65/66,** 99–105 (1993).
145. Durand, N., Badawi, K. F. & Goudeau, P. Residual stresses and microstructure in tungsten thin films analyzed by x-ray diffraction-evolution under ion irradiation. *J. Appl. Phys.* **80,** 5021–5027 (1996).
146. Cullity, B. D. & Stock, S. R. *Elements of X-ray diffraction, 3rd edition*. *Prentice Hall* (2001). doi:citeulike-article-id:3998040
147. Dekker, A. J. Secondary Electron Emission. *Solid State Phys.* **Volume 6,** 251–311 (1958).
148. Fancher, A. N. Fusion Neutron Production using Deuterium Fuel in an Inertial Electrostatic Confinement device at 10 to 200 Kilovolts. (2018).
149. Boris, D. R. & Emmert, G. A. Composition of the source region plasma in inertial electrostatic confinement devices. *Phys. Plasmas* **15,** (2008).

150. Alderson, E. C. Experimental and Theoretical Characterization of Negative Deuterium Ion Distributions in a Gridded Inertial-Electrostatic Confinement Device. (2012).
151. Emmert, G. A. & Santarius, J. F. Atomic and molecular effects on spherically convergent ion flow. I. Single atomic species. *Phys. Plasmas* **17,** (2010).
152. Ligenza, J. R. Silicon oxidation in an oxygen plasma excited by microwaves. *J. Appl. Phys.* **36,** 2703–2707 (1965).
153. Pliskin, W. A. & Lehman, H. S. Structural Evaluation of Silicon Oxide Films. *J. Electrochem. Soc.* **112,** 1013–1019 (1965).
154. Bean, K. E. & Bean, K. E. Anisotropic etching of silicon. *IEEE Trans. Electron Devices* **25,** 1185–1193 (1978).
155. Barone, M. E. & Graves, D. B. Chemical and physical sputtering of fluorinated silicon. *J. Appl. Phys.* **77,** 1263–1274 (1995).
156. Suttrop, W. *et al.* Identification of plasma-edge-related operational regime boundaries and the effect of edge instability on confinement in ASDEX Upgrade. *Plasma Phys. Control. Fusion* **39,** 2051–2066 (1997).
157. Chu, M. S. *et al.* Plasma shaping, edge ballooning stability and elm behaviour in diii-d. *Nucl. Fusion* **30,** 1425–1432 (1990).
158. Lao, L. L. *et al.* Dependence of edge stability on plasma shape and local pressure gradients in the DIII-D and JT-60U tokamaks. *Nucl. Fusion* **41,** 295–300 (2001).
159. Evans, T. E. *et al.* Edge stability and transport control with resonant magnetic perturbations in collisionless tokamak plasmas. *Nat. Phys.* **2,** 419–423 (2006).
160. Boris, D. R. *et al.* Deuterium anions in inertial electrostatic confinement devices. *Phys. Rev. E - Stat. Nonlinear, Soft Matter Phys.* **80,** 1–9 (2009).
161. Tachi, S., Tsujimoto, K. & Okudaira, S. Low-temperature reactive ion etching and microwave plasma etching of silicon. *Appl. Phys. Lett.* **52,** 616–618 (1988).
162. Sian, T. *et al.* Graphene coating for the reduction of the secondary electron yield. *IPAC 2016 - Proc. 7th Int. Part. Accel. Conf.* 3688–3690 (2016).
163. Roy, S. S. Synthesizing High-Quality Graphene Membranes for Engineering Diffusion Barriers. (2015).
164. Garrison, L. M. & Kulcinski, G. L. The effects of tungsten's pre-irradiation surface condition on helium-irradiated morphology. *J. Nucl. Mater.* **466,** 302–311 (2015).
165. Grahmann, H., Feuerstein, A. & Kalbitzer, S. Critical channeling angles of low energy ions in tungsten. *Radiat. Eff.* **29,** 117–119 (1976).
166. Teo, B. K., Averill, B. A. & Antonio, M. R. Tungsten as a Weak Backscatterer: An Example of Information Loss in Extended X-ray Absorption Fine Structure (EXAFS) Spectroscopy. Tungsten and Iron EXAFS Studies of Tungsten-Iron-Sulfur Clusters Containing the WS2Fe Unit. *J. Am. Chem. Soc.* **107,** 3583–3590 (1985).
167. Ohya, K. *et al.* Related content Ion Backscattering and Sputtering of Plasma- Irradiated Carbon and Tungsten Surfaces in an Oblique Magnetic Field. (1995).
168. Herlt, H.-J., Feder, R., Meister, G. & Bauer, E. G. Experiment and theory of the elastic electron reflection coefficient from tungsten. *Solid State Commun.* **38,** 973–976 (1981).
169. Dev, B. Statistics of secondary electrons from W induced by He ions and atoms at 0° -90° incidence. *Appl. Surf. Sci.* **40,** 319–326 (1990).
170. Boukhvalov, D. W., Katsnelson, M. I. & Lichtenstein, A. I. Hydrogen on graphene: Electronic structure, total energy, structural distortions and magnetism from first-principles calculations. *Phys. Rev. B - Condens. Matter Mater. Phys.* **77,** 1–7 (2008).

171. Binderbauer, M. Progress at Tri Alpha Energy Michl Binderbauer Tri Alpha Energy. (2015).
172. Shin, Y. J. *et al.* Surface-energy engineering of graphene. *Langmuir* **26,** 3798–3802 (2010).
173. Wang, S., Zhang, Y., Abidi, N. & Cabrales, L. Wettability and surface free energy of graphene films. *Langmuir* **25,** 11078–11081 (2009).
174. Kumar, R. & Grenga, H. Surface Energy Anisotropy of Tungsten. *Surf. Sci.* **59,** 612–618 (1976).
175. Hodkin, E. N., Nicholas, M. G. & Poole, D. M. The surface energies of solid molybdenum, niobium, tantalum and tungsten. *J. Less-Common Met.* **20,** 93–103 (1970).
176. Nastasi, M., Mayer, J. & Hirvonen, J. Ion-Solid Interactions - Fundamentals and Applications. *Ion-Solid Interactions - Fundamentals and Applications* 88–145 (1996).
177. Riccardi, P., Cupolillo, A., Pisarra, M., Sindona, A. & Caputi, L. S. Primary energy dependence of secondary electron emission from graphene adsorbed on Ni(111). *Appl. Phys. Lett.* **101,** (2012).
178. Hiura, H., Miyazaki, H. & Tsukagoshi, K. Determination of the number of graphene layers: Discrete distribution of the secondary electron intensity stemming from individual graphene layers. *Appl. Phys. Express* **3,** (2010).
179. Chang, H. Y., Alvarado, A. & Marian, J. Calculation of secondary electron emission yields from low-energy electron deposition in tungsten surfaces. *Appl. Surf. Sci.* **450,** 190–199 (2018).

Chapter 11 – Appendices

Appendix A - Neutron Calibration for LUNA

Unlike HOMER with its concentric spherical grids, LUNA has a different spatial distribution of the neutrons due to its linear geometry, which makes its calibration procedure more difficult and different. A PuBe neutron source with a source strength of 2.2×10^6 n/s was placed at locations in 5 different regions along the chamber as shown in Figure A-1.

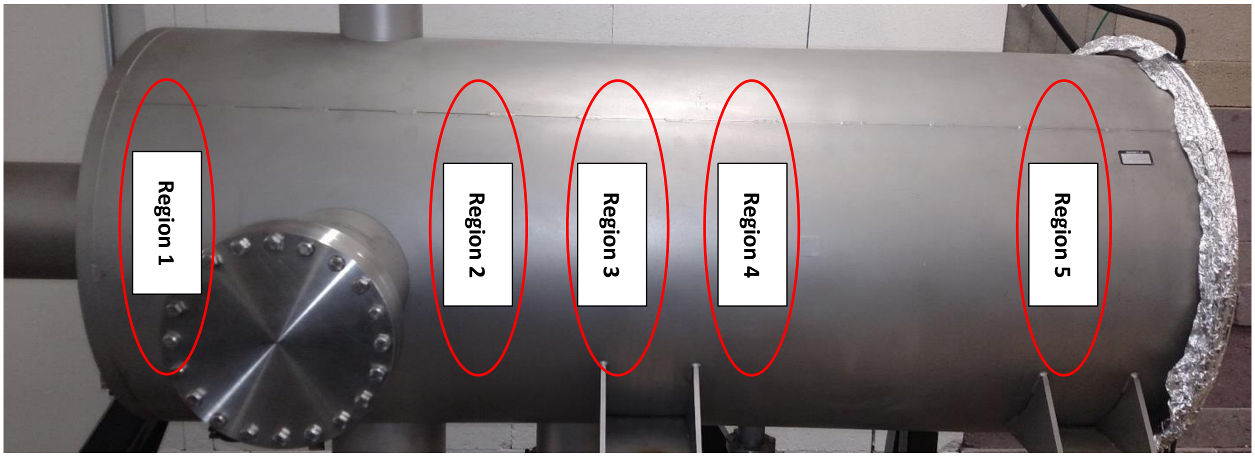

Figure A-11-1. Placement of PuBe neutron source along the axis of the LUNA experiment. Regions 1 and 5 correspond to the ends of the vacuum vessel, regions 2 and 4 correspond to anode locations and region 3 to the center of the cathode.

On each region, counts are taken for 60 seconds, until more than 10,000 counts are collected. These are then averaged to find the neutron rate of the region. The weights for the different regions where the PuBe source was placed are determined using a neutron distribution predicted by the VICTER code, such as the one shown in Figure A-2.

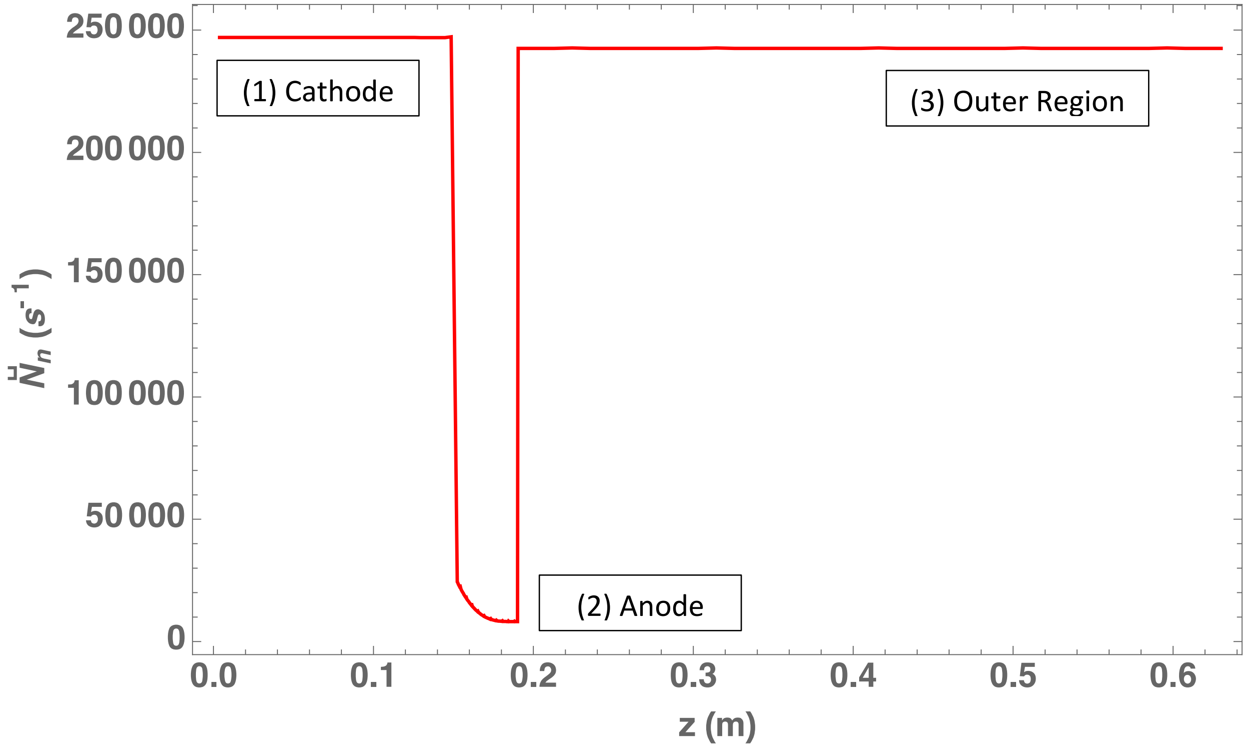

Figure A-11-2. Neutron Distribution of half of the LUNA experiment for a cathode voltage of 70 kV, a cathode ion current of 45 mA, and a D_2 pressure of 2.25 mTorr. The profile is presumed to be symmetric along the center axis. Courtesy of John Santarius.

The neutron rate data is normalized, to the center region (cathode), where the counts are highest. These can then be used to set up a system of equations for determining the weights per region. For the present geometry, $M = 28.65$ and $N = 1.022$. The first equation in the set corresponds to all the weights adding up to 1, and the other equations correspond to the normalization and relation of the other two regions to the maximum neutron rate.

$$\begin{gathered} x + 2y + 2z = 1 \\ y = \frac{x}{M} \\ z = \frac{x}{N} \end{gathered} \qquad (A-1)$$

$$M = \frac{\text{Value}(\mathit{Cathode\ Center})}{\text{Value}(\mathit{Anode\ Location})} \qquad (A-2)$$

$$N = \frac{\text{Value}(Cathode\ Center)}{\text{Value}(Outer\ Location)} \qquad (A-3)$$

The variable x corresponds to (1) in Figure A-1, y corresponds to (2), and z corresponds to (3). The current cathode is 0.3048 m in length, which corresponds to 0.1524 m in the neutron profile, the anode-cathode separation is 0.01905 m, and therefore the second position corresponds to 0.1715 m. The last region (3) is the vacuum chamber wall set at 0.6415 m from the center of the chamber. The rate values used for the calibration are the ones corresponding to this position. With these, the calibration weights are found, and multiplying them to the corresponding neutron rate determined from the PuBe source and adding them together, the correct calibration factor is found for LUNA. The corresponding weights were $(1) = 0.330, (2) = 0.011, (3) = 0.323$. These correspond to a calibration factor of 48,483.

Appendix B – Ion Flux and Energy Spectrum at the Location of the First Graphene Sample Exposure in the C-2W Device at TAE Technologies

The following data acquisition and analysis were provided by Dr. Martin Griswold from TAE Technologies. The first graphene sample was exposed to the C-2W plasma between Feb. 2nd and April 11th, 2018 (shots #104339 - 105549). The samples were installed on electrode plate #2 of the south outer divertor, as indicated in the figure below.

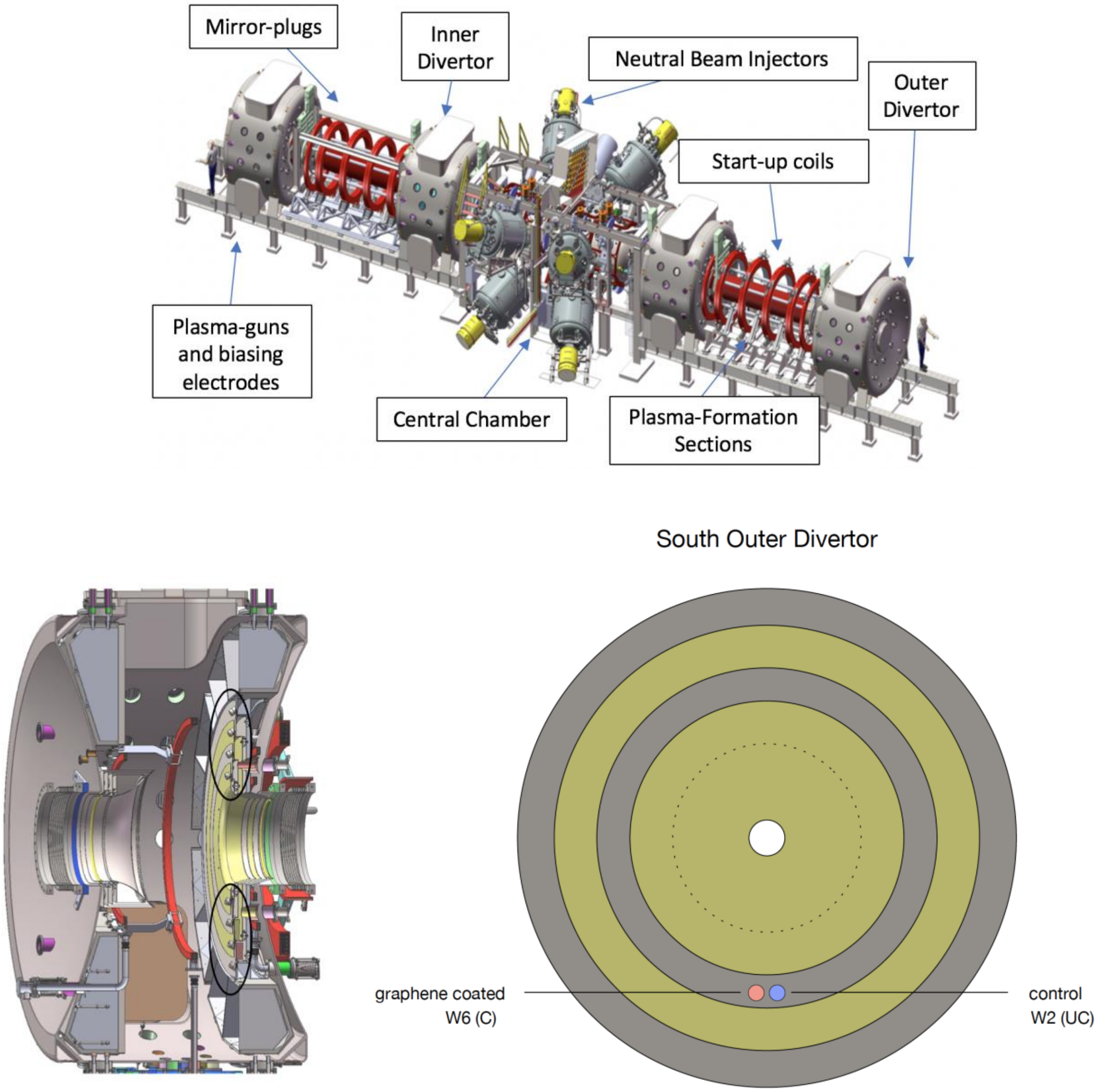

Figure B-1. Axial and radial location of samples in the outer divertor of C-2W.

An energy analyzer installed at the same location, but on the north side of the machine (C2W diagnostic #DEA03), can measure the ion particle flux and energy distribution incident on that location. Unfortunately, this diagnostic was not operational until after the exposure of the first sample. We do have measurements from later shots that could give a rough estimate of the ion fluxes and energies seen by the sample. These measurements are shown for four representative shots in Figures B2-B5. The sample location sees average ion current densities of roughly 0.02-0.07 A/cm^2 for the duration of each shot (1-6 ms), and typical average energies of 50-150 eV.

Shot #107527
Outer Divertor Electrode Plate 2

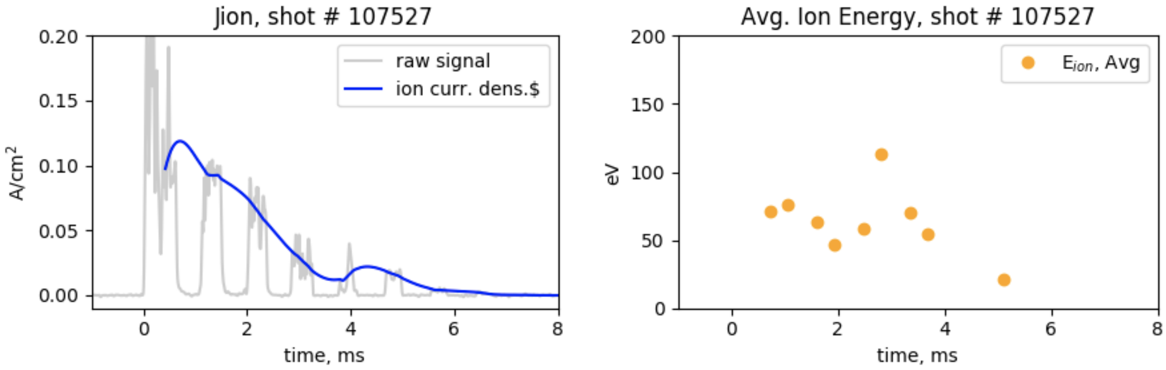

Ion Energy Distribution, shot #107527

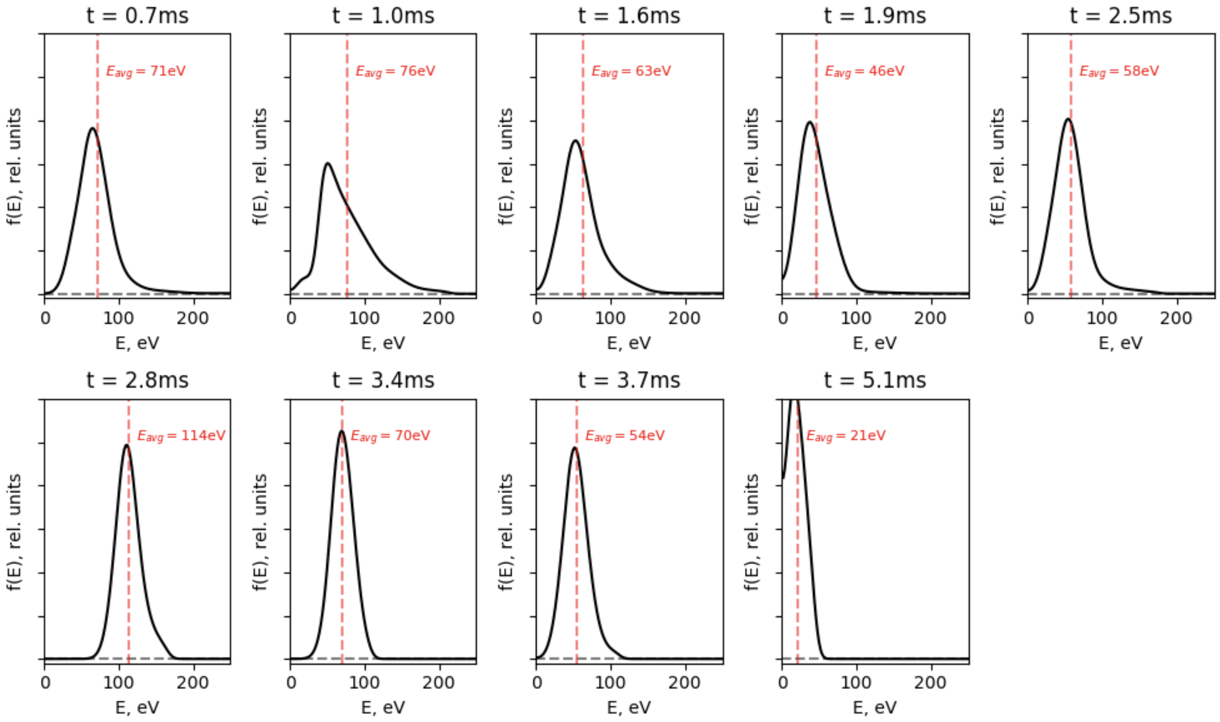

Figure B-2. Integrated current profile, ion energy changes over the discharge duration and Maxwellian distribution of the deuterium plasma at different time intervals during shot 107527.

Shot #107533
Outer Divertor Electrode Plate 2

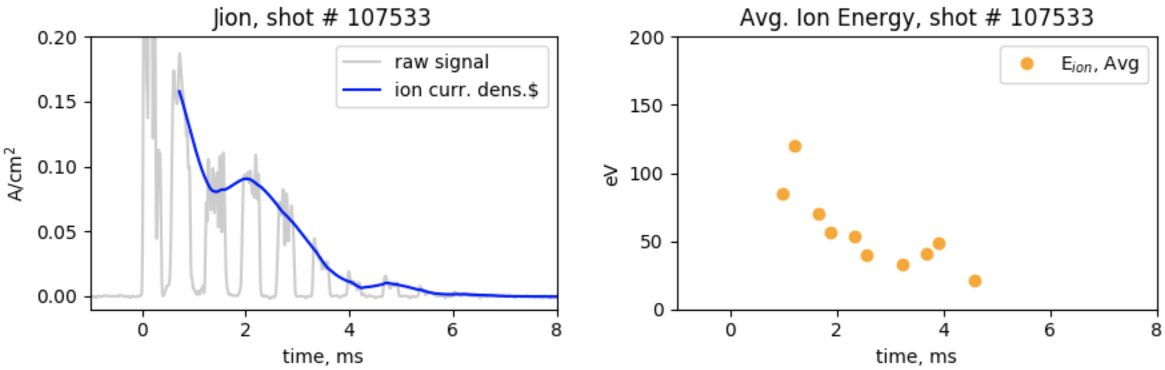

Ion Energy Distribution, shot #107533

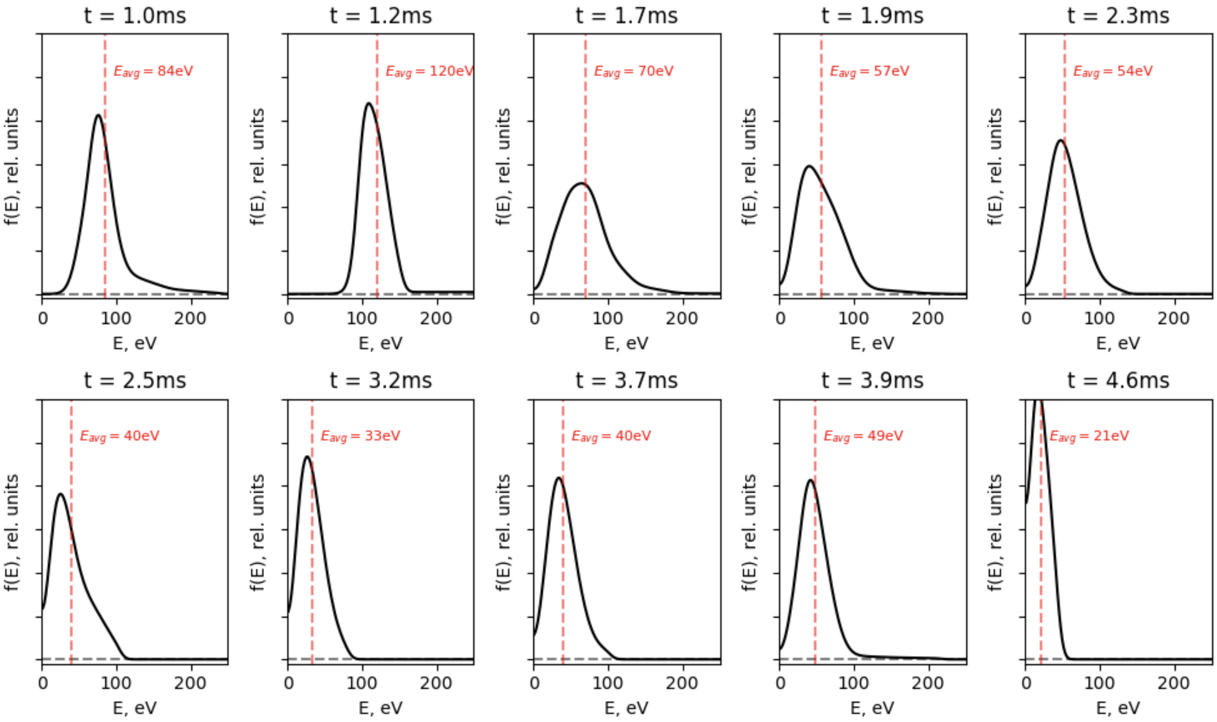

Figure B-3. Integrated current profile, ion energy changes over the discharge duration and Maxwellian distribution of the deuterium plasma at different time intervals during shot 107533.

Shot #107534
Outer Divertor Electrode Plate 2

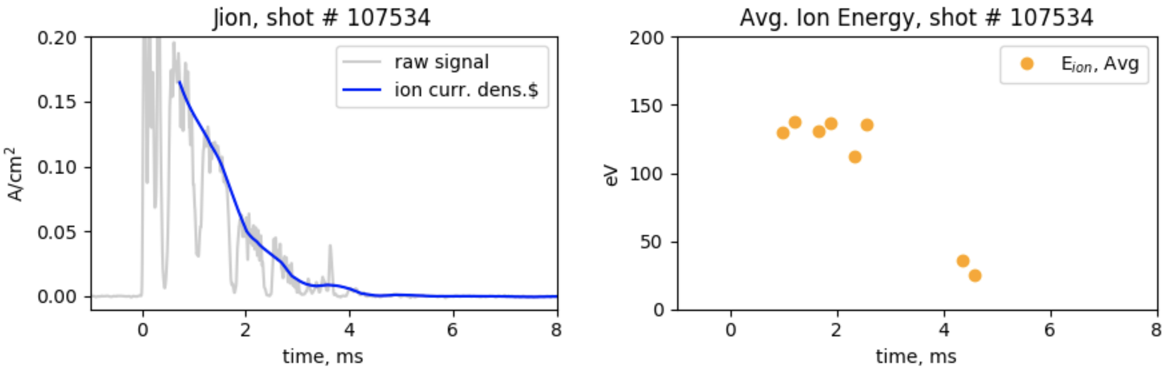

Ion Energy Distribution, shot #107534

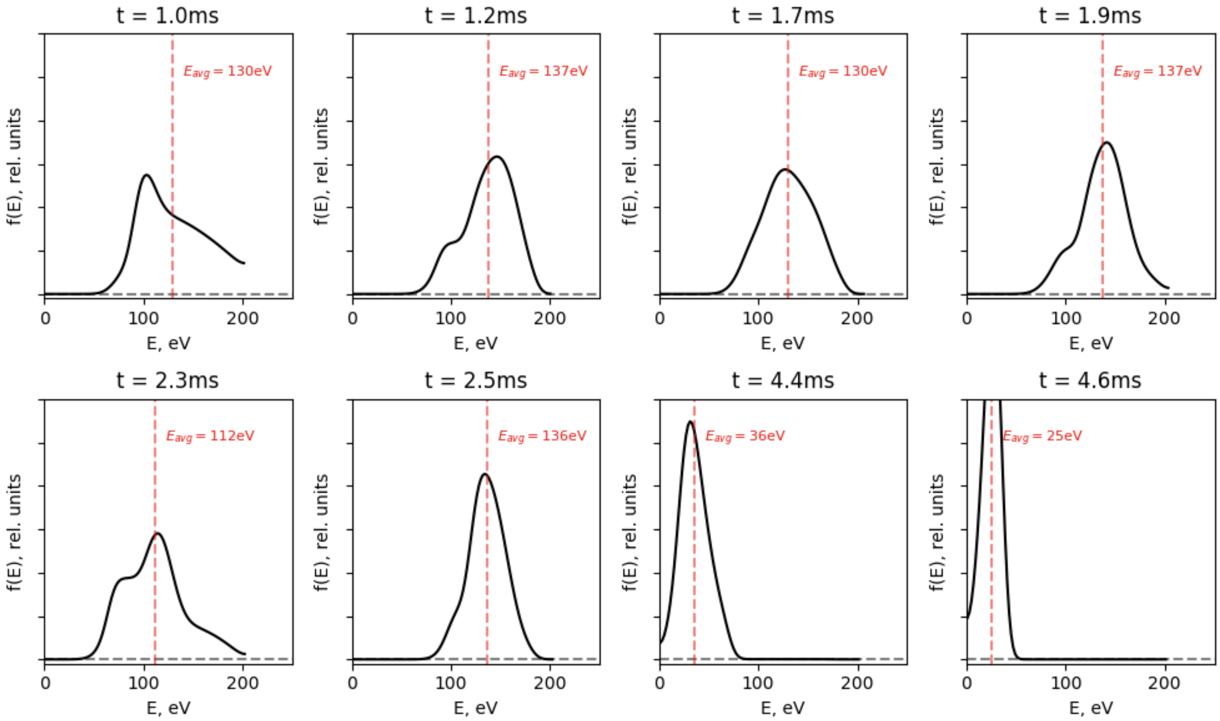

Figure B-4. Integrated current profile, ion energy changes over the discharge duration and Maxwellian distribution of the deuterium plasma at different time intervals during shot 107534.

Shot #107677
Outer Divertor Electrode Plate 2

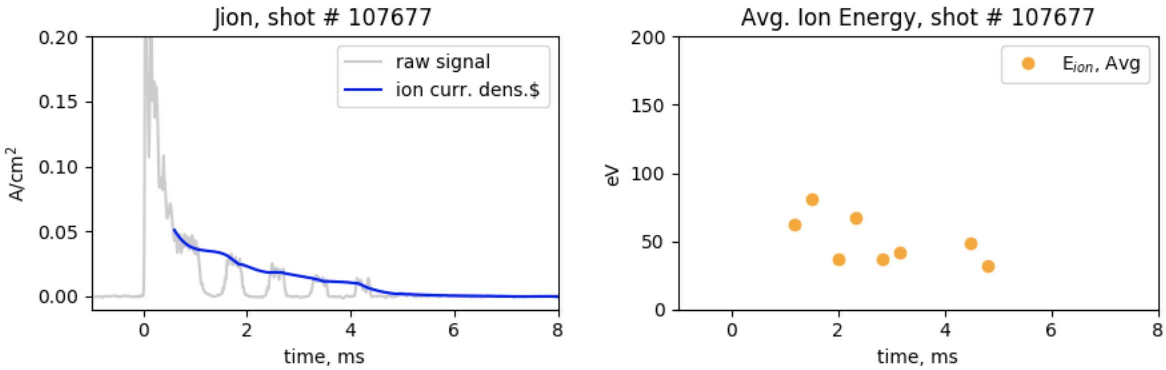

Ion Energy Distribution, shot #107677

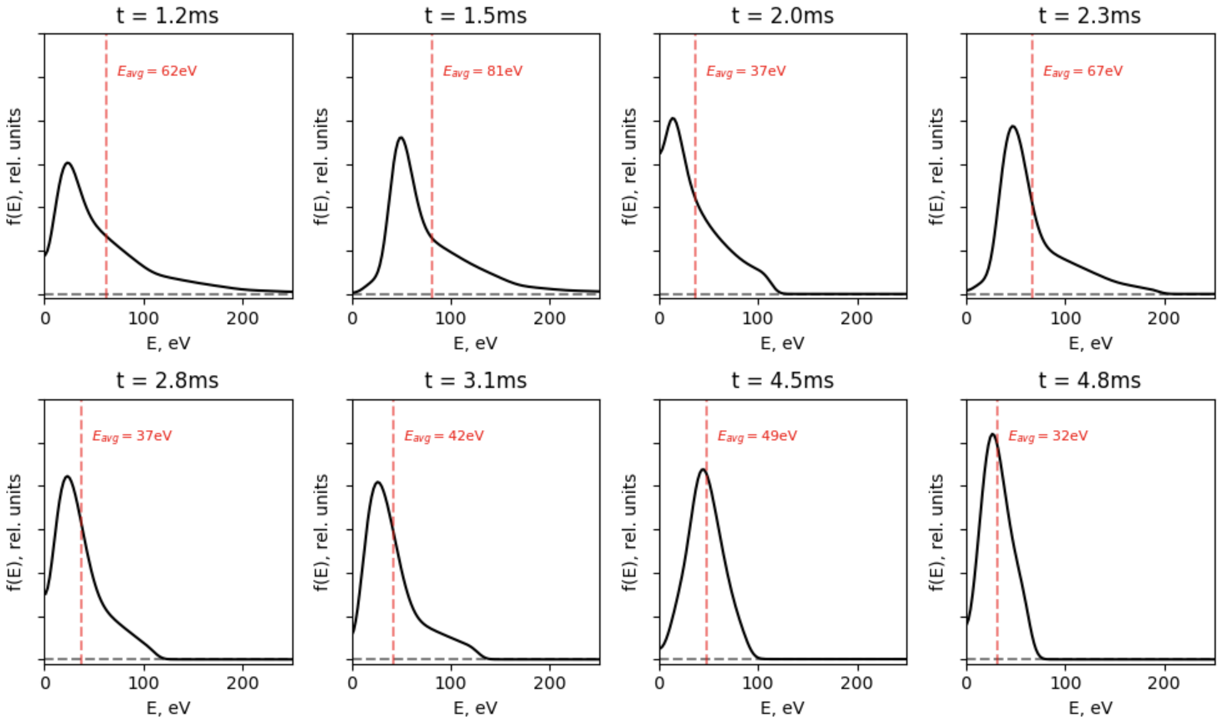

Figure B-5. Integrated current profile, ion energy changes over the discharge duration and Maxwellian distribution of the deuterium plasma at different time intervals during shot 107677.

The fluence data was calculated from the average current density data provided previously.

$$\Phi = \frac{Jt}{Ze} \times (number\ of\ shots) \qquad (B-1)$$

where *J*, is the current density, *t* is the discharge duration, *Ze* is the effective charge of deuterium (*Z=1*). Knowing that $e = 1.602 \times 10^{-19} C$, we can calculate the maximum expected fluence for 1210 shots:

$$\Phi = \frac{0.07\ \left(\frac{A}{cm^2}\right) \times 6\ (ms)}{1.602 \times 10^{-19} (C)} \times (1210) \times \frac{1s}{1000\ ms} = \mathbf{3.2 \times 10^{18}\ \frac{D^+}{cm^2}}$$

This fluence is similar to those explored in the MITE-E helium exposures. This exposure give some insight on deuterium damage to graphene due to a low temperature-low fluence Maxwellian plasma.